Measurement and Modelling of Bistatic Sea Clutter

Waddah Ali Mohammed Al-Ashwal

A dissertation submitted in fulfillment

of the requirements for the degree of

Doctor of Philosophy

of the

University College London.

Department of Electronic and Electrical Engineering

University College London

2011

I, Waddah Ali Mohammed Al-Ashwal, confirm that the work presented in this thesis is my own. Where information has been derived from other sources, I confirm that this has been indicated in the thesis.

Abstract

There is a growing interest in bistatic radars; however, such systems cannot reach their full potential unless the designer has a proper understanding of the environment in which they operate. Rather little information has been published on bistatic clutter and out-of-plane bistatic sea clutter in particular. This is due to a number of factors including the inherent complexity of conducting bistatic radar trials and the resulting lack of high quality bistatic data.

In this thesis the collection and analysis of a unique set of bistatic sea clutter data is described. To achieve this objective a novel multistatic radar system was developed. The nodes do not need to be physically connected. This system has a peak transmitted power of more than $500\,\mathrm{W}$. Synchronisation in time and frequency was achieved using GPS disciplined oscillators built and designed at the University of Cape Town.

Using the above system simultaneous bistatic and monostatic sea clutter and target signatures were recorded in the UK and South Africa at various geometries and weather conditions. Parts of this unique data set related to out-of-plane bistatic sea clutter was analysed in this thesis. The data covered both co- and cross-polarised sea clutter data at low grazing angles with bistatic angles between $30°$ and $120°$. Data sets covering a range of conditions with sea states from 2 – 5.

Using the recorded data it was shown that the ratio of the bistatic normalised radar cross section to the monostatic normalised radar cross section dropped as the scattering angle was increased until the scattering angle was around $90°$. Furthermore, the cross-polarised bistatic normalised radar cross section was found to be larger than the cross-polarised monostatic normalised radar cross section when the scattering angle was around $90°$.

A new empirical model for predicting bistatic normalised radar cross section has been developed. The model is applicable to both in-plane and out-of-plane geometries. The model was able to provide a good fit to both UCL and external data.

The temporal correlation properties of both monostatic and bistatic data were studied. It was found that the speckle component of both bistatic and monostatic clutter decorrelated in tens of milliseconds, with the decorrelation time longer for bistatic clutter. The texture of both bistatic and monostatic clutter had similar autocorrelation functions and had similar decorrelation times. By comparing the texture and

intensity autocorrelation functions it was concluded that the compound model still holds.

It was also found that bistatic clutter was less 'spiky' than monostatic clutter particularly at horizontal polarisation. This was due to the reduction in the intensity of the spikes due to specular reflections. By combing the effects of the reduction in reflectivity and spikiness it was shown that a bistatic radar would require a smaller signal to interference ratio than a monostatic radar for the same probability of detection and probability of false alarm. This was more evident at angles close to 90° and for horizontal polarisation.

In summary this thesis reports the collection and analysis of novel simultaneous monostatic and bistatic sea clutter and target data. This was achieved by the development of a unique multistatic radar system. This work has resulted in significant advances in both netted radar technology and understanding of bistatic sea clutter.

Acknowledgements

I would like to express my utmost gratitude to my supervisors Dr. Karl Woodbridge, Prof. Hugh Griffiths and Prof. Chris Baker for their inestimable support and guidance.

I would like to also thank the UK Ministry of Defence for providing the initial funding for the project. I would like to gratefully acknowledge the US Office of Naval Research Global (ONRG), Thales UK and Thales Netherlands for generously supporting the experimental part of this work. I would like to acknowledge the logistical support provided by the South African Council for Scientific and Industrial Research (CSIR). Wave and wind data for the Cape Point area in October 2010 was supplied by the CSIR, Stellenbosch, which was collected on behalf of the Transnet National Port Authority (TNPA).

I would like to extend my deepest appreciation to Dr. William Miceli from Quibis LLC, Prof. Simon Watts and Dr Andy Stove from Thales UK, and Dr. Keith Ward and Dr. Robert Tough from Igence for their help in planning and conducting the trials.

The experimental part of this work would not have been possible without the support of many of my colleagues from UCL and the University of Cape Town. From UCL I would like to thank Dr. Alessio Balleri, Dr Kevin Chetty, Dr. Graeme Smith, Dr. Shaun Doughty and Mr. Matthew Ritchie.

From the University of Cape Town I am grateful to Prof. Mike Inggs for his invaluable advice. I am also indebted to Mr. Stephan Sandenbergh, he tirelessly worked with me to integrate his clocks with my radar. I would also like to thank the Postgraduate students at the Radar Remote Sensing Group in the University of Cape Town for their support in conducting the trials and their hospitality during my stay there.

I am also grateful to my friends at UCL for making this journey such an enjoyable one. In particular I would like to thank Dr. Yanchuan Hang, Dr. Daniel O'Hagan, Dr. Alex Charlish, Mr. Matthew Ash and Mr. James Brown.

I would like to thank my wife, Dalal, to whom I am infinitely grateful for her unconditional support and encouragement. I would also like to thank my daughter whose beautiful face gave me the will the continue this endeavour. Last but not least, I would like to express my greatest appreciation and gratitude to my parents for their long-standing unwavering support of my education.

Publications List

Th work described in this thesis has led to the following publications:

1. W. Al-Ashwal, C. Baker, A. Balleri, H. Griffiths, R. Harmanny, M. Inggs, W. Miceli, M. Ritchie, J. Sandenbergh, A. Stove, R. Tough, K. Ward, S. Watts, and K. Woodbridge, "Statistical analysis of simultaneous monostatic and bistatic sea clutter at low grazing angles," *Electronics Letters*, vol. 47, no. 10, pp. 621 – 622, May 2011.

2. M. Inggs, J. Sandenbergh, G. Inggs, W. Al-Ashwal, K. Woodbridge, and H. Griffiths, "Multistatic networked radar for sea clutter measurements," in *Proc. IEEE International Geoscience and Remote Sensing Symposium (IGAARS)*, Vancouver, Canada, Aug. 2011.

3. W. Al-Ashwal, A. Balleri, H. Griffiths, R. Harmanny, M. Inggs, , M. Miceli, W. Ritchie, J. Sandenbergh, A. Stove, R. Tough, K. Ward, S. Watts, and K. Woodbridge, "Measurement of bistatic radar sea clutter," in *Proc. IEEE Radar Conference RadarCon*, Kansas City, Missouri, May 2011.

4. J. Sandenbergh, M. Inggs, and W. Al-Ashwal, "Evaluation of coherent netted radar carrier stability while synchronised with GPS disciplined oscillators," in *Proc. IEEE Radar Conference RadarCon*, Kansas City, Missouri, May 2011.

5. M. Inggs, H. Griffiths, K. Woodbridge, W. Al-Ashwal, J. Sandenbergh, and G. Inggs, "Experimental coherent networked radar using GPS-disciplined reference oscillators," in *Proc. Cognitive systems with Interactive Sensors (COGIS)*, Crawley, UK, Nov. 2010.

6. H. Griffiths, W. Al-Ashwal, K. Ward, R. Tough, C. Baker, and K. Woodbridge, "Measurement and modelling of bistatic radar sea clutter," *IET Radar, Sonar & Navigation*, vol. 4, no. 2, pp. 280–292, Apr. 2010.

Contents

List of Figures

List of Tables

List of Symbols and Abbreviations

ΔR	Range resolution
$\Gamma(\cdot)$	Gamma function
β	Bistatic angle
γ	Gamma clutter model constant
λ	Generalised Pareto distribution scale parameter
λ	Wavelength
ν	Shape parameter of the compound K distribution
ν_{BW}	KA distribution shape parameter for Bragg and whitecap scattering
ω_w	Water frequency
ϕ	Azimuth angle
ϕ_s	Scattering angle
ψ	Grazing angle
σ	Log-normal distribution shape parameter
σ	Radar cross section
σ°	Normalised radar cross section
σ_h	Root mean square wave height
σ_{BW}	Mean Bragg and whitecap intensity
σ_{SP}	Mean burst spike intensity
τ	Compressed pulse length
τ	Sea clutter texture

θ	Elevation angle
θ_{3dB}	One-way antenna 3 dB beamwidth
θ_{3dB}	Two-way antenna 3 dB beamwidth
θ_{SW}	
2D	two dimensional
3D	Three dimensional
a	Semimajor axis
a	Weibull distribution scale parameter
A_c	Clutter cell area
ACF	Autocorrelation function
ADC	Analog to digital converter
AUT	Antenna under test
$_B$	Bistatic radar quantities
b	Scale parameter of the compound K distribution
b	Semiminor axis
B	Byte
BAM	Breaking area model
c	Speed of propagation of radio waves in vacuum$\approx 2.997\,924\,58 \times 10^8\,\mathrm{m\,s^{-1}}$
c	Weibull distribution shape parameter
ccdf	Complimentary cumulative distribution function
COTS	Commercial off the shelf
CSM	composite-surface scattering model (CSM)
d	Water depth
DDS	Direct digital synthesis
EIRP	Effective isotropic radiated power

EM	Electromagnetic
Erf	Error function
ESR	Effective series resistance
F	Propagation factor
$f(\cdot)$	Antenna propagation pattern
f_d	Doppler shift
FPGA	Field-programmable gate array
G	Antenna gain
g	Acceleration due to gravity $\approx 9.8\,\mathrm{m\,s^{-2}}$
Gi	Gibi = 1×2^{30}
GNSS	global navigation satellite system
GO	Geometric optics
GPSDO	GPS disciplined oscillator
GPS	Global Positioning System
G_{rx}	The receiver chain gain.
$H_{1/3}$	Significant wave height
h_{av}	Average wave height
h_{av}	Average wave height
HPA	High power amplifier
$\Im$	Real part of an imaginary number
I	Inphase component
k	Generalised Pareto distribution shape parameter
KA	Kirchhoff approximation
k_B	Bragg wave number
K_{mf}	Compression gain

k_r	Radar wave number
L	Baseline length
L	System losses > 1
LNA	Low noise amplifier
LVDS	Low-voltage differential signalling
$_M$	Monostatic radar quantities
MBET	Monostatic bistatic equivalence theorem
Mi	Mebi = 1×2^{20}
MLE	Maximum likelihood estimation
MoM	Method of moments
NetRAD	UCL netted radar
NF	Noise figure
NRCS	Normalised radar cross section
NRCS	cross section
NTP	Network time protocol
OCXO	Ovenised oscillator
pdf	Probability density function
Pd	Probability of detection
Pfa	Probability of false alarm
P_I	Probability of the interference
P_{S+I}	Probability of the signal + interference
PLL	Phased locked Loop
p_n	Receiver noise power
PoE	Power over Ethernet
PO	Physical optics

P_r	Received Power
PRF	Pulse repetition frequency
PRI	Pulse repetition interval
P_T	Transmitted Power
Q	Quadrature component
$\Re$	Real part of an imaginary number
$_R$	Receiver quantities
R_B	Bistatic range
RCS	Radar cross section
rms	Root mean square
R_R	Distance between the target and the transmitter
R_T	Distance between the target and the transmitter
RTI	Range time intensity
Rx	Receiver
S	Wave spectrum
SIRP	Spherical invariant random process
SIR	Signal to interference ratio
SPDT	Single pole double throw
SPM	Small perturbation method
SPST	single pole single throw
SSA	Small slope approximation
stdev	Standard deviation
$_T$	Transmitter quantities
Tx	Transmitter
U_a	The wind speed a metres above the sea level

UAV	Unmanned air vehicle
UCL	University College London
UCT	University of Cape Town
UHF	Ultra high Frequency
UTP	Unshielded twisted pair
v_d	Drift velocity
VHDL	Very high speed integrated Circuits hardware description language
VHF	Very high Frequency
v_o	Orbital velocity
x	Complex envelope of the sea returns
x	local mean power of the Bragg and whitecap scattering
z	Intensity of the sea returns

Chapter 1

Introduction

1.1 Overview

The term bistatic radar generally means that the transmitting and receiving antennas are separated sufficiently such that the path by which the target echo travels is significantly different from the monostatic geometry. Although the first radars were bistatic, soon after the duplexer was invented most research and development shifted into monostatic radars. There have been a few periods of resurgence during the past 70 years [1]. As can be seen from Fig. 1.1 the percentage of published works on bistatic radar has been increasing steadily in recent years after the local minimum in 2005. The plot was generated by searching the Compendix data base[1] for works which contain the phrase 'bistatic radar' in the subject, title or abstract, then normalised by the total number of works which contains only 'radar' in the same fields. Some of the reasons for this interest are:

1. Bistatic radar has potential advantages in detection of stealthy targets which are shaped to scatter energy in directions away from that of the transmitter. In addition, radar absorbing materials are not effective in forward scattering geometries.

2. The receiver is passive, hence more immune to countermeasures.

3. The absence of the transmitter makes it more suitable when size and weight are at a premium such as on unmanned air vehicles (UAVs).

4. The extra degrees of freedom may make it easier to extract information from bistatic clutter for remote sensing applications and from targets for automatic target classification.

5. The receiver design is simplified, due to the lack of transmit receive switching.

After the development of the isolator most of the development has been geared towards monostatic radars. This is because of the extra complexity of bistatic radars. The main issues with bistatic radars are:

[1] The data was retrieved on 12-July-2011 using The Engineering Village http://www.engineeringvillage2.org/

1. The transmitter and receiver nodes need to be synchronised in both frequency and time.

2. It is necessary to acquire knowledge of the location of both the transmitter and receiver and their relative bearing.

3. Data communications between the two nodes needs to be established, in a cooperative bistatic radar configuration.

4. The overall coverage volume is geometry dependant and may be reduced compared to the monostatic case.

5. The increased complexity due to the use of multi-beam receive antenna or pulse chasing to overcome the coverage area limitation.

6. Calibration of bistatic radars is much more difficult than monostatic radar.

7. There is a lack of reliable theoretical information and experimental data on the properties of bistatic radar clutter.

Monostatic sea clutter can be very 'spiky'[2] especially at low grazing angles and high seas. The longer tail of the probability density function of spiky clutter increases the probability of false alarm which could be detrimental to the radar performance. This is particularly true at horizontal polarisation. Studies of land bistatic SAR images suggested that the amplitude statistics of the clutter were shorter tailed in bistatic SAR compared to monostatic SAR [2]. The same could be true for sea clutter. In addition, from the study of the spatial correlation of sea clutter at small bistatic angle, it can be concluded that spikes are decorrelated [3]. However, the above does not provide conclusive evidence to whether or not the above assumption is true. Until the question is answered it is very difficult to imagine real advances being made in marine and naval bistatic radar.

Two key advances in technology in recent years could help pave the way to the development of high performance bistatic and multistatic radar systems:

1. Global navigation satellite systems, such as Global Positioning System (GPS) can provide frequency and time synchronisation without the need for wires between the nodes.

2. Advances in digital electronics have made it possible to implement complex algorithms in real-time or near real time. Such processing power is necessary to process bistatic data particularly if the data is to be fused as part of a multi-sensor system.

[2] Clutter spikiness is discussed in Section 2.2.1 on page 54

1.2 Objectives

The research reported in this thesis has addressed the above issues as outlined below:

- The technological advances mentioned above have been utilised to build the UCL netted radar system (NetRAD). GPS disciplined oscillators were used to provide frequency and time synchronisation, and the built-in GPS was used to provide location information. The advances in digital electronics and computing power made it economical to use a high resolution fast analogue to digital converter, to perform rudimentary data analysis in the host nodes, and to process most of the data on personal computers.

- Using this system unique simultaneously gathered monostatic and bistatic sea clutter and marine target data was collected. Field trials were planned and carried out in the UK and SA. The sea clutter data was obtained at different geometries and at different environmental conditions. The target data covered different geometries and target types ranging from sail boats and inflatables to large ships.

A key aim of this study of bistatic sea clutter was to provide the foundations necessary to improve the detection of low visibility targets in sea clutter. This could have profound implications in detecting small low visibility boats used by pirates and human traffickers. In addition, this could aid in search and rescue operations.

Furthermore, the extra degrees of freedom offered by bistatic geometry could open new fronts in remote sensing and oceanography. There could be certain bistatic geometries which might reduce the dependency of the radar returns on some environmental conditions hence making it possible to estimate other parameters.

This works aims to be a starting point to kick off active research into bistatic sea clutter. Due to the dire lack of experimental data, it was necessary to collect the data. The required hardware had to be developed in house. UCL netted radar system (NetRAD) was enhanced to enable the simultaneous monostatic and bistatic sea clutter and small target data at ranges up to 2 km. To enable arbitrary baseline operation NetRAD was integrated with University of Cape Town GPS disciplined oscillators to provide a common time and frequency reference. Initial trials were carried out in the UK and the main trials were carried out in South Africa.

1.3 Novel Contributions

The main novel contributions of this work include:

1. *Enhancement of a Novel Multistatic Radar System*

   Further development of the UCL coherent multistatic netted radar system to enable complete wireless operation at transmitted power more than $500\,\mathrm{W}$. The main aim of the development was to

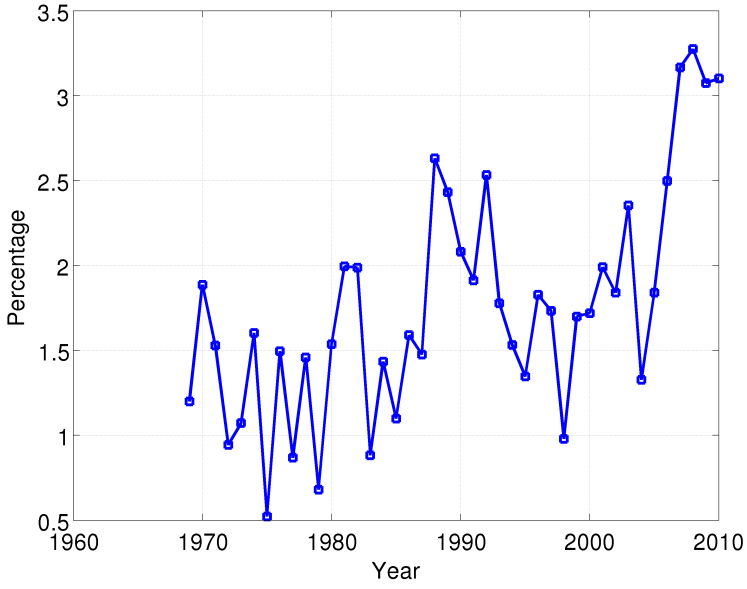

Figure 1.1: Percentage of the publications containing the word 'bistatic radar' in the title , subject or abstract to those containing 'radar between' 1965 to 2010.

facilitate the simultaneous recording of the first publicly available monostatic and bistatic sea clutter and marine target data. This included modifications to the hardware, firmware and software and integrating the radar system with University of Cape Town GPS discipline oscillators. The new system was fully characterised and calibrated. Algorithms were developed reduce the effect of the frequency drift the tracking of the GPS on the Doppler spectrum and in-band interference.

2. *Planing and Execution of a Major Overseas Multinational Multistatic Radar Trial*

   The research directly involved planning and execution of a unique set of multinational set of trials to measure simultaneous monostatic and bistatic sea clutter, and marine target signature in both the UK and South Africa. The gathered data was unique in many ways: 1) the bistatic and monostatic data were simultaneously recorded, 2) it covered a range of bistatic angles not reported before in open literature, 3) it contained cross-polar measurements, 4) some of data was recorded in littoral waters which is not available in open literature even for monostatic geometries and 5) the target data contains various examples ranging form large ships to inflatables undertaking various manoeuvres such as spirals and circles.

3. *Obtaining and Analysing Unique Results Pertaining to the Determination of the Variation of Radar Cross Section with Bistatic Angle*

   Average simultaneously recorded normalised bistatic and monostatic sea clutter data was analysed and compared to published data. It was shown for the first time that the normalised bistatic radar cross section was equal to or smaller than the monostatic one for backscattering geometries for out-

of-plane bistatic angles up to $120°$. Cross-polarised data was also analysed and it was demonstrated for the first time that cross-polarised bistatic sea clutter had larger normalised radar cross section than cross-polarised normalised radar cross section for monostatic radar around a bistatic angle of $90°$.

4. *Development of a New Bistatic Clutter Model by the Author*

   A new empirical model for describing average normalised radar cross section of both in-plane and out-of-plane bistatic sea clutter has been developed. The model is an extension of Barton's model for surface bistatic clutter. It takes into account the effects of the geometry on the scattering and cross-polarised clutter. The model was successfully fitted to published data and UCL data.

5. *First Published Analysis of Amplitude Statistics Sea of Bistatic Sea Clutter*

   The amplitude statistics of recorded bistatic data was analysed, for the first time. It was found that bistatic clutter was less spiky than monostatic clutter even at small bistatic angles even when there was little difference in the average normalised radar cross section. Furthermore, it was shown that the main reason for the reduction in spikiness was that the amplitude of burst spikes was attenuated due to the bistatic geometry in most cases. It was also shown that the current distributions that are used to describe monostatic clutter can still be used to model the statistics of bistatic clutter. This data was best described by the KA distribution. It was also shown the drop in the radar cross section and the reduction in the spikiness could improve the performance of bistatic radars compared to monostatic radars particularly at bistatic angles close $90°$ and at horizontal polarisation.

6. *First Published Temporal Correlation Study of Bistatic Sea Clutter*

   The autocorrelation function of simultaneously recorded monostatic and bistatic sea clutter, including those recorded at shallow depths were computed. It was shown that autocorrelation function of the speckle was different between monostatic and bistatic clutter but in all cases the speckle decorrelated in tens of milliseconds. However, the texture seemed to be correlated. By comparing the texture and the intensity autocorrelation function it was shown that the bistatic and littoral sea clutter can still be represented by the compound model.

1.4 Thesis Outline

An overview of the rest of the thesis is as follows:

The next chapter starts with an overview of the main concepts of bistatic radar. This is followed by an analytical review of the theory of monostatic sea clutter. Finally an up-to-date critical review of bistatic sea clutter theory and experiment is presented.

The third chapter describes the UCL netted radar system in some detail. It provides a brief review of the original system, followed by a discussion of the re-design and development as part of this research. Finally, the various integration tests and calibrations are presented.

Chapter 4 gives an account of the field trials and the data collection methodology both in the UK and South Africa. This is followed by a description of the data processing challenges and procedures.

In chapter 5 the average bistatic and monostatic normalised radar cross section of the measured sea clutter is analysed. Two sea states are studied for both horizontally and vertically polarised clutter, and a cross-polarised measurement. A new model for bistatic sea clutter is introduced.

Chapter 6 investigates temporal correlation properties of monostatic and bistatic sea clutter. In addition the applicability of various distributions to both littoral monostatic and bistatic sea clutter is also discussed. The effect of the change in the statistical properties of in bistatic sea clutter compared to monostatic radar on the performance of radar systems is studied.

Chapter 7 concludes the thesis by providing a concise summary of the results and achievements presented in the previous chapters and discussion of future work in the area of bistatic sea clutter and netted radar development.

Three appendices are included at the end of the thesis covering the basics of sea surface hydrography, the Georgia Institute of Technology monostatic sea clutter model and the development of the method used to derive the variation of the bistatic angle in the clutter area.

Chapter 2

Background Theory and Literature Review

This chapter provides an overview of the background theory necessary to understand this work and also reviews the relevant theory in monostatic and bistatic sea clutter. The chapter is divided into four sections. The first section will be concerned with the current theory of bistatic radar and its properties and how they relate to monostatic radar. A detailed discussion of monostatic sea clutter will then be presented in the next section. This will include a brief examination of the electromagnetic (EM) scattering theory as applied to sea surface scattering. The general properties of monostatic sea clutter are then discussed, followed by a detailed examination of the amplitude statistics. The spatial and Doppler properties are also reviewed.

In the third part of this chapter a detailed critique of bistatic sea clutter literature will be presented. This will include analytical and empirical modelling of bistatic sea clutter and a review of publicly available measurements of bistatic sea clutter. The chapter concludes with a summary which will highlight the research issues in the field of bistatic sea clutter.

2.1 Basic Principles of Bistatic Radar

This section provides a brief introduction to bistatic radar. The subject is discussed in great detail in the literature [4–7]. In its broadest sense a radar is a device that detects and locates targets by measuring and processing there reflected electromagnetic waves. Radars can be classified by a number of parameters, particularly frequency, bandwidth, waveform, and receiver and transmitter configuration. Conventional monostatic radars send and receive electromagnetic energy using a common antenna or collocated antennas. If the receiving and transmitting antennas are sufficiently separated such that the transmitting and receiving antennas have different views of the target the system is called a bistatic radar [8]. If the individual radars, either monostatic or bistatic, can communicate and share data then the system can be called a netted radar system. The physical separation of the transmitter and receiver leads to the need for the transmitter and receiver pair to be synchronised in time and in frequency if coherent detection is required.

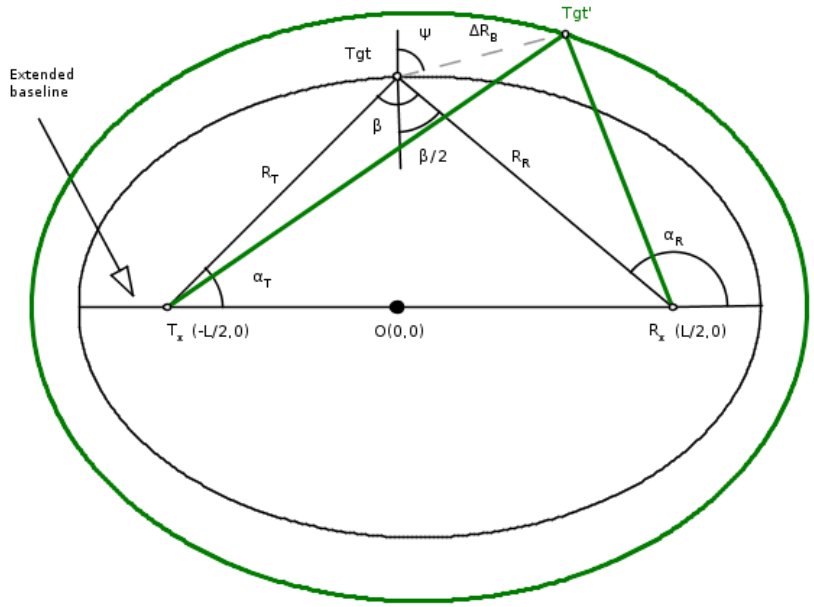

Figure 2.1: Bistatic radar geometry

2.1.1 The Bistatic Radar Equation

In general the bistatic geometry is a three dimensional (3D) problem [9]. The choice of the number of coordinate systems, their type and the origins will depend on the application. Since a plane is completely defined by two lines, when the target, transmitter and receiver are stationary a two dimensional (2D) coordinate system can be used. The North-referenced coordinate system is the one most commonly used [4, 7]. A slightly modified version of the North-referenced coordinate system is shown in Fig. 2.1; the main difference being is that the angles are referenced to the baseline rather than North. It is clear that if the baseline length, which is defined as the distance between the transmitter and the receiver (L), is shrunk to zero, the system will reduce to a monostatic radar. All bistatic radar equations must reduce to those of the equivalent monostatic radar when $L = 0$. The equivalent monostatic radar is placed on the bisector of the bistatic angle β. The time delay measured at the passive receiver is the time it takes the signal to travel from the transmitter to the target then to the receiver. Thus the bistatic range R_B (also known as the range sum, two way range or the total range) is the sum of the distance between the target and the transmitter R_T and the target and the receiver R_R:

$$R_B = R_T + R_R \tag{2.1}$$

The locus of points with a constant bistatic range is known as the isorange contour. In bistatic geometries the locus of the isorange contour is an ellipsoid. The intersection of the bistatic plane with the ellipsoid is an ellipse. It can be completely described by R_B and L.

With reference to Fig. 2.1, the required L to achieve a bistatic angle β given R_T and R_R is given

by [4, 7]:

$$L = R_T^2 + R_R^2 - 2R_T R_R \cos(\beta) \tag{2.2}$$

The bistatic angle β is given by:

$$\beta = |\alpha_T - \alpha_R| \tag{2.3}$$

For a given isorange surface the maximum bistatic angle is achieved when the bistatic triangle is isosceles.

For simplicity the origin of the coordinate system can be assumed to be at the centre of the coordinate system and the baseline on the x-axis. The semimajor axis, a is just half the bistatic range

$$a = \frac{1}{2} R_B \tag{2.4}$$

the semiminor axis, b, is given by

$$b = \sqrt{a^2 - \frac{L^2}{4}} \tag{2.5}$$

The monostatic radar can be thought of as a special of the bistatic radar, with $L = 0$ and $\beta = 0°$. In this case the isorange contour is a circle with a radius equal to the monostatic range R_M.

The bistatic radar equation for a point target can be written as:

$$P_r = \frac{P_T G_T G_R G_{rx} \lambda^2 F_T^2 F_R^2 \sigma_B K_{mf}}{(4\pi)^3 R_T^2 R_R^2 L_T L_R L_P} \tag{2.6}$$

where:

P_T: is the transmitted power, in Watts.

P_r: is the received power after pulse compression, in Watts.

G: is the antenna gain, in natural units.

λ: the wavelength, in metres.

F: is the field propagation factor, in natural units.

L: is the system losses > 1, in natural units.

$_T$: denote quantities related to the transmitter.

$_R$: denote quantities related to the receiver.

σ_B: is target bistatic radar cross section in m^2.

K_{mf}: is the matched filter (compression) gain.

G_{rx}: is the receiver chain gain.

L_p: processing loss, in natural units > 1.

Unlike monostatic radar changing the position of the target within the isorange contour changes P_r; since the detection contours and the isorange contours are not collinear in bistatic radar. Because the

receiver noise is constant the P_r contours are the same as the signal-to-noise ratio (SNR) contours, and are given by Cassini Ovals [10].

2.1.2 Bistatic Radar Cross Section

When an electromagnetic wave impinges on a target, in general, some of the energy will be absorbed and some will be scattered. The absorption and scattering mechanisms are governed by Maxwell's equations under the relevant boundary conditions. The radar cross section (RCS) is a measure of the intensity of the power reflected from the target towards the receiver in the polarisation of the receiver. It is defined as [11]:

$$\sigma_{Bvu} = \lim_{R_R \to \infty} 4\pi R_R^2 \frac{|\mathbf{E}_u^{sc}|^2}{|\mathbf{E}_v^{in}|^2} \tag{2.7}$$

where:

σ_{Buv}: is the bistatic radar cross section (BRCS).

$\mathbf{E}_u^{sc}$: is the u-polarised scattered electric field.

$\mathbf{E}_v^{in}$: is the v-polarised incident electric field. u and v: are any two orthogonal frequencies. The RCS is a function of the look angle and the radar frequency. Except for very simple targets approximate methods are used to compute the RCS.

It should be noted here that the BRCS is a function of both the incident wave direction and the scattered wave direction. In monostatic radar cross section (MRCS) the scattered wave direction is opposite to that of the incident wave. For forward-scattering the scattered wave has the same direction as the incident wave. Thus they can be considered as special cases of the BRCS.

A review of some of BRCS results is provided in [12]. Kell [13] approximated the BRCS as that seen by a monostatic radar at the bisector of the bistatic angle, at a frequency reduced by $\cos(\beta/2)$. This method is known as monostatic bistatic equivalence theorem (MBET). Kell's results require a smooth surface, and the absence of shadowing. Furthermore, the applicability of this method is limited by the angular width of the individual scatterers making up the target. Hence it cannot be applied to complicated targets or clutter.

In forward-scattering the BRCS can be very large as, predicted by Babinet's principle, even for targets covered with radar absorbing materials [14]. The peak forward-scatter σ_F is approximately given by:

$$\sigma_F = \frac{4\pi A^2}{\lambda^2} \tag{2.8}$$

where A is the target silhouette area. To be able to detect the target reliably at forward-scattering geometries it is necessary for it to have a large scattering angular width. The angular width will be of the order λ/d(rad), where d is the target dimension. Griffiths [15] showed that optimum frequency to detect aircraft would be in the VHF and UHF bands. Given the reduction in the range resolution Eq. (2.9), it

would be difficult to locate the target at best.

Since the main objective of this work is the measurement and statistical analysis of bistatic and monostatic sea clutter returns. This subject will not be explored in any more depth. A more detailed treatment is provided in [11, 16–18]

2.1.3 Bistatic Radar Resolution

Typically radars can resolve targets in angle, time (range) and/or Doppler. The minimum required target separation, in any dimension, is known as the radar resolution. Unlike monostatic radar the resolution is geometry dependant [19].

The range resolution ΔR_B is reduced approximately by $\cos(\beta/2)$ compared to the equivalent monostatic radar. If the line connecting the two targets makes an angle φ with the bistatic angle bisector, ΔR_B can be found from the approximate relation:

$$\Delta R_B = \frac{c}{2\tau \cos(\beta)\cos(\varphi)} \tag{2.9}$$

where c is the speed of propagation of radio waves in vacuum$\approx 2.997\,924\,58 \times 10^8\,\mathrm{m\,s^{-1}}$.

Ignoring relativistic effects the Doppler shift in bistatic radar is related to the bistatic range sum by [20]:

$$f_d = \frac{\partial R_T}{\partial t} + \frac{\partial R_R}{\partial t} \tag{2.10}$$

defining the velocity vectors as in Fig. 2.2, the Doppler shift can be written as

$$f_d = \frac{1}{\lambda}[2V_{tgt}\cos(\delta_{tgt})\cos(\beta/2) + V_T\cos(\delta_T - \alpha_T) + V_R\cos(\delta_R - \alpha_R)] \tag{2.11}$$

where V is the speed, δ_{tgt} is the angle the velocity makes with the bistatic bisector, δ_T and δ_R are the angles the transmitter and receiver motion vectors make with the baseline. The subscripts T, R and tgt denote the transmitter, receiver and target related quantities respectively.

When the transmitter and receiver are stationary and the target moving f_d

$$f_d = \frac{2V_T}{\lambda}\cos(\delta_{tgt})\cos(\beta/2) \tag{2.12}$$

If the target is stationary then Eq. (2.11) reduces to:

$$f_d = \frac{V_T\cos(\theta_T - \delta_T) + V_R\cos(\theta_R - \delta_R)}{\lambda} \tag{2.13}$$

As in monostatic radar Doppler resolution is defined as the reciprocal of the coherent integration

time. The minimum speed required to achieve such resolution is given by:

$$\Delta V_B = \frac{\lambda}{2T\cos(\beta/2)} \tag{2.14}$$

Similar to the isorange contours the isodoppler contours can be determined for the bistatic radar. For example, given a stationary target and a moving transmitter and receiver, isodoppler for a flat earth is a function of V_T, V_R, δ_T and δ_R and unlike the monostatic isodoppler the loci are not conic sections.

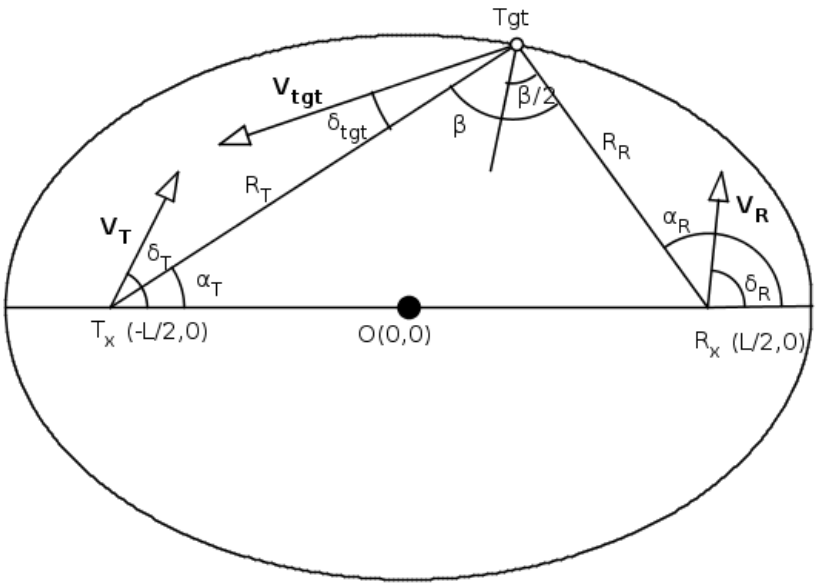

Figure 2.2: Schematic for the geometry of bistatic Doppler

The angle resolution is a term used to describe the minimum change in angle required to separate two targets which will be otherwise ambiguous. A drop of 6 dB from the peak power is usually enough to separate two targets of similar RCS. In monostatic radar this usually translates to a change of 3 dB in the one way pattern. In bistatic radar this might not be the case since the transmitter and radar range and beamwidth are usually different. The cross range, $R\theta_B$, is usually used to account for the angle resolution as it includes the effect of the range, where θ_B is the beamwidth.

Numerical methods can be used to estimate cross range based on the drop in the received power, beyond a certain threshold, taking into account the antenna pattern. If the cross range of the transmitter and receiver are very different, the smaller of them is used. If they are approximately equal then either of them can be use. Assuming that the receiver has a smaller cross range the required physical separation is:

$$R_\psi = R_R\theta_{BR}\cos\left(\beta/2\right) \tag{2.15}$$

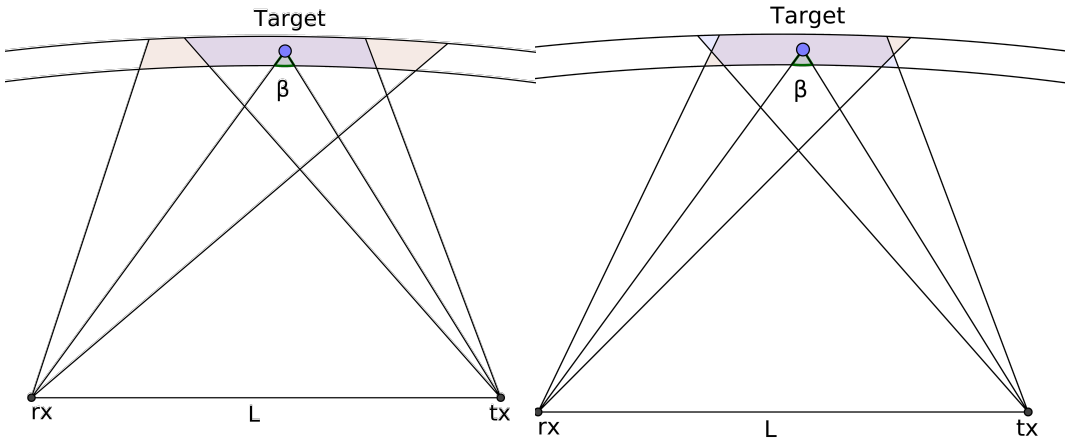

(a) Limited by transmitter (b) Equal cross range

Figure 2.3: The dependency of the clutter area on the cross range.

2.1.4 Bistatic Clutter Cell Area

The sea surface represents a distributed target and thus the received signal is the coherent sum of many discrete scatterers. Because of the finite pulse length and antenna beamwidth it is impossible to resolve such scatterers. Such targets are known as extended targets. If the target is extended in two dimensions, it is known as surface clutter. It is customary to normalised the radar cross section by dividing it by the clutter area.

The clutter cell area A_c is defined as the smallest of the antenna footprints, range cell and Doppler cell [21]. In most cases, A_c for pulsed radar will be limited by the range cell. It is given by the product of the range resolution and cross range resolution. A_c is limited generally by the smaller of the transmitter and receiver cross ranges. In Fig. 2.3a, the transmitter beamwidth is smaller than the receiver beamwidth, hence the clutter area is defined by the transmitter beamwidth. Figure 2.3b shows the case when the transmitter and receiver cross ranges are almost equal. For sufficiently high grazing angles and very long pulses pulsed radar can be limited by the antenna beamwidth. Finally A_c can be limited by the intersection of the isodoppler and the cross range resolution. In most cases A_c is usually calculated using numerical techniques. For small grazing angles the clutter area can be approximated by [21, 22]:

$$A_{cB} \approxeq \Delta R_B \Delta R_\psi \tag{2.16}$$

Weiner [23] derived more accurate approximations for the low grazing case. Moyer [24] developed a formula for the clutter area when either the transmitter or receiver antenna has a broad azimuth beam. In this thesis the clutter area was estimated numerically. For extended targets such as sea clutter normalised

radar cross section (NRCS) σ° is usually used, which is defined as:

$$\sigma_B^\circ = \frac{d\sigma_B}{dA_c} \tag{2.17}$$

Thus the received power will be given by

$$P_R = \int_{A_c} \frac{P_T G_T G_R G_{rx} \lambda^2 \sigma_B^\circ K_{mf}}{(4\pi)^3 R_T^2 R_R^2 L_T L_R L_p} \, dA_c \tag{2.18}$$

In most clutter measurements it is difficult to estimate the propagation factors, and they are implicitly included in the σ_B°. Given that $G = G_\circ f^2(\phi, \theta)$,$f(\phi, \theta)$ is the antenna propagation pattern as a function of the azimuth and elevation angles from the target to the antenna in the antenna reference frame.

$$P_R = \frac{P_T G_{T\circ} G_{R\circ} G_{rx} \lambda_r^2 \sigma_B^\circ K_{mf}}{(4\pi)^3 L_T L_R L_p} \int_{A_c} \frac{f_T^2(\phi_T, \theta_T) f_R^2(\phi_R, \theta_R)}{R_T^2 R_R^2} \, dA_c \tag{2.19}$$

by setting $K_A = \frac{P_T G_{T\circ} G_{R\circ} G_{rx} \lambda^2 K_{mf}}{(4\pi)^3 L_T L_R L_P} \, \sigma_B^\circ$ is given by

$$\sigma_B^\circ = \frac{K_A P_R}{I} \tag{2.20}$$

where I is given by

$$I = \int_{A_c} \frac{f_T^2(\phi_T, \theta_T) f_R^2(\phi_R, \theta_R)}{R_T^2 R_R^2} \, dA_c \tag{2.21}$$

The integration limits are defined by the isorange contour and the range resolution. In Cartesian coordinates $dA_c = dxdy$ and

$$I = \int_x \int_y \frac{f_T^2(\phi_T, \theta_T) f_R^2(\phi_R, \theta_R)}{R_T^2 R_R^2} \, dxdy \tag{2.22}$$

which can be approximated by:

$$\hat{I} \approx \begin{cases} \sum_i \sum_j \frac{f_T^2(\phi_{Tij}, \theta_{Tij}) f_R^2(\phi_{Rij} \theta_{Rij})}{R_{Tij}^2 R_{Rij}^2} \Delta x_i \Delta y_j & \text{if } |R_{Tij} + R_{Rij} - R_\circ| \leq \tau c \\ 0 & \text{if } |R_{Tij} + R_{Rij} - R_\circ| > \tau c \end{cases} \tag{2.23}$$

where $R_\circ$ is the two-way range at which the clutter power is to be computed, τ is the compressed pulse length including the effect of windowing.

Provided that the range variation within the clutter area is small, the clutter area can be approximated by:

$$A_{cB} \approxeq R_{T\circ}^2 R_{R_\circ}^2 I \tag{2.24}$$

where $R_{T\circ}$ and $R_{R_\circ}$ are the transmitter and receiver one way range to the centre of the clutter patch.

For monostatic radar assuming antennas with Gaussian beam pattern Eq. (2.27) can be written as:

$$A_{cM} = R_{T\circ}^4 \int_{\phi=0}^{\phi=2\pi} \int_{r_1}^{r_2} \frac{f_t^2(\theta-\theta_t', \phi-\phi_t') f_r^2(\theta-\theta_r', \phi-\phi_r')}{r^4} r\, dr d\phi \tag{2.25}$$

where $r_1 = R_{T\circ} - \Delta R_M/2$ and $r_2 = R_{T\circ} + \Delta R_M/2$ For low grazing angle the effect of the change in elevation can be ignored within the same clutter area. The antenna pattern can be written as:

$$f(\phi) = \exp - \left(\left(\frac{K_g \phi}{\phi_{3dB}} \right)^2 \right) \tag{2.26}$$

where ϕ_{3dB} is the one way 3 dB bandwidth and $K_g = 1.17742$. evaluating the above integral results in

$$A_{cM} = \frac{8\sqrt{\pi} r_\circ^5 \Delta R \phi_{3dB} \mathrm{Erf}\left(\frac{2\mathrm{K_g}\pi}{\phi_{3\mathrm{dB}}}\right)}{K_g \left(4r_\circ^2 - \Delta R^2\right)^2} \tag{2.27}$$

where Erf is the error function. Since the argument of Erfc$(\cdot)$ >1 it is almost equal to unity. In addition, $\left(4R_{M\circ}^2 - \Delta R_M^2\right)^2 \approxeq 16 R_{M\circ}^4$. Thus Eq. (2.27) can be approximated by:

$$A_{cM} \approxeq 0.7527 \phi_{3dB} R_{M\circ} \Delta R_M \tag{2.28}$$

The monostatic clutter area has been approximated by:

$$A_{cM} = \phi_{3dB2} R_{M\circ} \Delta R_M \tag{2.29}$$

where ϕ_{3dB2} is the two way 3 dB pattern which is related to the one way 3 dB beamwidth for a Gaussian pattern by

$$\phi_{3dB2} = \frac{\phi_{3dB}}{\sqrt{2}} \tag{2.30}$$

which very close to the exact result.

It can be easily shown that the clutter power will drop proportional to R^3 whereas the target echo power will drop proportional to R^4:

$$P_R = \frac{P_T G^2 \lambda^2 \sigma_M^\circ c\tau \phi_{az}}{2(4\pi)^3 R^3} \tag{2.31}$$

Although using the geometry presented in Fig. 2.1 might be convenient, it is inadequate for use when modelling extended targets. This is because it relies on the bistatic angle which can only give a complete description if the geometry or the target's polar diagram under consideration is two dimensional. There exist an infinite number of possible geometries which could generate the same bistatic

angle but could be illuminating very different scatterers within the target, and thus have very different RCS. Traditionally, the scattering angle has been measured from the y-axis, i.e. if the transmitter was in the xz-plane at forward-scattering the receiver will have a scattering angle $\phi_{sR} = 0°$ and for in-plane backscatter measurement $\phi_{sR} = 180°$ [25]. This convention is counter intuitive, since if the grazing angle of the transmitter and receiver are very small and the transmitter is located on the xz-plane then for a small scattering angle will translate into a large bistatic angle. Furthermore, it does not map directly to the right-handed coordinate systems used in scattering and modelling. In this work the scattering angle is equal to the azimuth angle and is measured from the x-axis and an object on the xz-plane will have and azimuth angle of zero degrees, as shown in Fig. 2.4. Using vector algebra the bistatic angle can be given by:

$$\begin{aligned}\beta = \arccos\big[&\cos(\psi_T)\cos(\phi_T)\cos(\theta R)\cos(\phi_{sR}) + \\ &\cos(\theta T)\sin(\phi_{sT})\cos(\theta R)\sin(\phi_{sR}) + \sin(\theta T)\sin(\theta R)\big]\end{aligned} \tag{2.32}$$

where ϕ_s is the scattering angle, $0° \leq \phi_s \leq 360°$ and ψ is the elevation angle, $-90° \leq \psi \leq 90°$, $\psi < 0°$ if the radar is looking downwards, $\psi > 0°$ if the radar is looking upwards, and $\psi = 0°$ at grazing incidence.

To simplify the mathematics it might be convenient to place the transmitter in the xz-plane, (2.32) reduces to

$$\beta = \arccos\big[\cos(\theta T)\cos(\theta R)\cos(\phi_{sR}) + \sin(\theta T)\sin(\theta R)\big] \tag{2.33}$$

At low grazing angles β reduces to:

$$\arccos\big[\cos(\phi_{sT})\cos(\phi_{sR}) + \sin(\phi_{sT})\sin(\phi_{sR})\big] = |\phi_{sT} - \phi_{sR}| \tag{2.34}$$

2.2 Theory of Monostatic Sea Clutter

The importance of understanding sea returns for naval and marine radars cannot be overestimated. Several books, book chapters and review papers have been dedicated to the subject [26–29]. In this section the theory of monostatic sea clutter is reviewed. A brief review of the hydrographical properties of the sea is presented in Appendix A. In this section is only concerned with sea returns for radars operating between bands L – K (1 GHz to 12 GHz) [30].

Radar returns from the sea remain to pose a real challenge to operational radars. Although sea clutter is generally weaker than land clutter the non-stationary nature of the problem makes it more complex to model. Depending on the radar frequency, polarisation, the geometry and the weather conditions σ°_M could vary between $-90\,\text{dB}\,\text{m}^2/\text{m}^2$ to $-20\,\text{dB}\,\text{m}^2/\text{m}^2$ [29]. Of particular interest, the sea returns

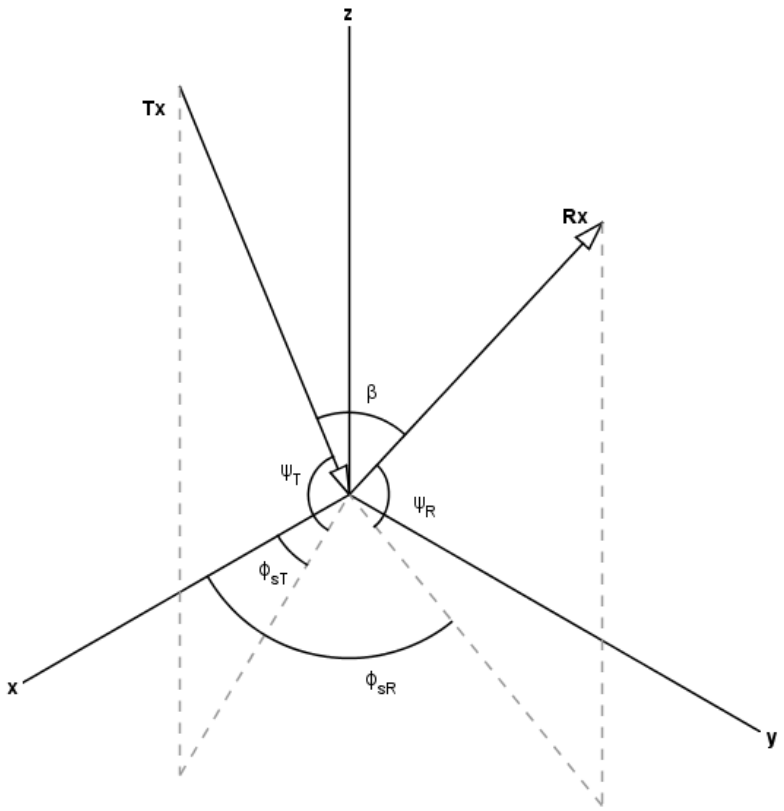

Figure 2.4: Clutter centred coordinate system

can have large excursions from the mean particularly when using horizontal polarisation at low grazing angles and heavy sea state. Furthermore, sea clutter does not only depend on the radar parameters, but also on the long term and short term environmental conditions. Several theories have been proposed to explore the nature of sea clutter and to model it, some of which are discussed below.

2.2.1 The Compound Nature of Sea Clutter

By the 1960s it was recognised that the σ°_{HH} is lower than σ°_{VV} for calm seas, and that as the depression angle is decreased and the wind is increased the probability that $\sigma^{\circ}_{HH} > \sigma^{\circ}_{VV}$ is increased. Long [31,32] studied the polarisation properties of sea backscatter and proposed a two scatter model:

1. A fast varying speckle-like component due to wind driven ripple component.

2. A slow fluctuating gross sea structure.

The above assumptions were based on the observation that the cross-polar reflectivity was independent of wave height but was a function of the wind speed.

Wright [33] argued that sea backscatter at microwave frequencies and higher is mainly due to short gravity and capillary waves which are modulated by larger gravity waves. The tilt with respect to incident wave caused the difference in HH and VV backscatter characteristics. The model was a better fit for

σ°_{VV} than σ°_{HH}. A similar model was developed by Brown [34], which divides the sea structure into two zones, see Section 2.2.2 for more details.

Although the above theory could explain, to some degree, the non-Gaussian nature of the sea returns it failed to explain the presence of discrete spikes. Lee *et al.* [35] reported that Goldstein (1951) was the first to note that from rough seas σ°_{MHH} could be greater than σ°_{MVV}. In 1974 Long [32] reported that particularly for horizontal polarisation there is strong correlation between the presence of spikes and 'single-peaked wave crests which become unstable and break to form a whitecap'. Wetzel [36] attributed the presence of spikes at very low grazing angles to shadowing which leads to intermittent illumination of the waves.

Ward [37] used frequency agile radar to decorrelate the fast fluctuation component of the sea returns. The slow moving component was fitted to the gamma distribution. The large gravity waves modulate the noise-like speckle.

It is generally accepted that sea returns are made up of three components [28, 38]:

1. Smooth modulation: These rise from Bragg scattering by short gravity and capillary waves, which are modulated by longer gravity waves. They give rise to speckle and are decorrelated by frequency agility from pulse to pulse [1] and have local Gaussian statistics. The backscatter due to speckle is higher for vertical polarisation than horizontal polarisation.

2. Burst scattering: scattering from the crest of the waves, just before they break giving rise to specular reflections of short duration, around 200 ms. The returns are much higher in horizontal polarisation compared to vertical polarisation. They seem to be created by the constructive multipath between the direct illumination and the forward scattering by the sea surface. They do not decorrelate by frequency agility.

3. Whitecap scattering: those seem to arise from the rough waves as they break. They RCS is roughly equal in both polarisations. They decorrelate within a few milliseconds but could last for a few seconds.

Lee *et al.* [35, 40] used Fourier analysis to isolate the clutter returns into fast and slow returns. The slow returns were found to be due to Bragg scattering. The fast returns were both due to Bragg scattering and specular reflections. The relation between the Doppler spectrum and the compound representation is discussed further in Section 2.2.7.

In this work the terminology introduced in the above bullet points are used; this is very similar to that used by Ward *et al.* [28]. It can be linked to that of Lee and his co-workers. The subevents are due to bounded Bragg scatterers which could be whitecaps. In the above notation, the whitecaps have almost

[1] The frequency difference Δf should be greater than the radar bandwidth [39].

equal RCS in both polarisations. In this work the term 'spike' will be used to denote large excursions from the mean clutter intensity. In some works the term spikes is used for burst scattering components only, and the term Bragg scattering is used for smooth noise-like speckle and range extended whitecaps.

McLaughlin *et al.* [41] used fully polarimetric X-band high resolution data, to study the polarisation of sea backscatter at low grazing. They concluded that the vertically polarised returns did not change much between spiking and non-spiking events. On the other hand horizontally polarised returns were much small there than vertically polarised returns for non-spiking events and of similar or larger amplitude during spiking event. The difference was around 7 dB. In almost all cases σ°_{MVH} was almost equal to σ°_{MHV}. In non-spiking measurements σ°_{MHH} was sometimes smaller than the cross-polarised components. They suggested that σ°_{MHH} are due to independent discrete scatterers.

2.2.2 Modelling Monostatic Sea Clutter

To properly model the sea surface returns it is essential to first understand the behaviour of the sea itself. A review of sea surface modelling is presented in Appendix A. The main definitions are repeated below for completeness. The definitions below are based on [29].

Sea state A measure of the roughness of the sea. There are many definitions for the sea state, in radar usually Douglas hydrographic scale is used. It relates the sea roughness to the wind speed and the significant wave height, Table A.1.

of the waves. It is denoted by h_{av}.

Root mean square wave height Used to estimate the roughness of the sea surface. It is related to h_{av} by:

$$h_{av} = \sqrt{2\pi}\sigma_h \tag{2.35}$$

Significant wave height The average of the heights of the one-third highest waves. It is related to h_{av} and σ_h by:

$$H_{1/3} = 1.6h_{av} \tag{2.36}$$

$$H_{1/3} = 4\sigma_h \tag{2.37}$$

Period The time it takes two consecutive crests or troughs to cross a fixed point. It is denoted by T.

Water frequency The water frequency in rad s^{-1} is given by:

$$\omega_w = \frac{2\pi}{T} \tag{2.38}$$

Water wavelength The distance between two consecutive crests from the same wave, it is denoted by λ_w.

Water Wavenumber This is related to the wavelength by

$$k_w = \frac{2\pi}{\lambda_w} \tag{2.39}$$

Fetch and duration They are defined as the horizontal distance (fetch) along which a nearly constant wind has been blowing for a length of time (duration).

Fully developed sea A sea surface which has reached a state of equilibrium after a constant wind has been blowing for a certain fetch and duration. The required fetch and duration can be very long. For example, a constant wind of $7\,\mathrm{m\,s^{-1}}$ will need to blow for a duration of $20\,\mathrm{h}$ and a fetch of $120\,\mathrm{nmi}$ or $222\,\mathrm{km}$ [42].

Wind waves Waves which are or just have been generated by local winds.

Swell Waves which were excited by wind but have moved out from the area where they originated.

Gravity waves Waves which the damping mechanism is gravity.

Capillary waves Waves which the restoring force is due to surface tension.

Phase velocity The velocity at which the phase of the waves travel, given by:

$$v_p = \frac{\omega_w}{k_w} \tag{2.40}$$

The sea surface is usually modelled as a stochastic rough surface. In monostatic sea clutter, the omnidirectional wave spectrum usually suffices [43]. This section will only provide an overview of the problem; scattering from the sea surface is discussed in more detail in [44, 45]. Generally the scattered field is calculated by solving the Stratton-Chu integrals.

When the scatterer has a large curvature compared to the electromagnetic wavelength the fields on the surface maybe approximated by the fields that would be present on a tangent plane at every point on the surface. This is known as physical optics (PO) or Kirchhoff approximation (KA). In the limit the wavelength vanishes and the geometric optics (GO) limit is reached. When PO is applied to finite rough surfaces the resulting RCS is independent of the polarisation [45]. This model is only applicable at high grazing angles.

At medium grazing angles the sea backscatter is polarisation dependent and the KA fails to predict such behaviour. It has been postulated that the scattering is due to Bragg scattering, thus the relation

between the water wavelength and the radar wave length is given by:

$$\lambda_r = 2\lambda_w \cos(\psi) \tag{2.41}$$

where λ_r and λ_w are the radar and water wavelengths respectively and ψ is the local grazing angle. At microwave frequencies, it is small gravity and capillary waves (ripples) that are responsible for the Bragg scattering. The small perturbation method (SPM) can be used to predict the scattering from such small structures. To apply SPM to sea surface Wright [33] formulated the composite-surface scattering model (CSM) or the two scale model, in which the ripples which are responsible for scattering ride on larger waves. The ripples are tilted by the larger wave and thus their local grazing angle is changed, hence changing their resonant wavelength. The model provided a good fit for σ°_{VV} particularly at lower frequencies. A similar method was developed by Brown [34] in which the surface was modelled by two independent Gaussian variables depending on the wave number, one representing the low frequency large waves and the other the high frequency small structures. Voronovich [46] proposed the use of small slope approximation (SSA) method to calculate the σ°_M. This method can be applied to scatterers of arbitrary sizes. Voronovich reported good agreement between simulation and experimental results at Ku- and C-bands for high and medium grazing angles.

At low grazing angles, the composite model fails to predict the RCS of the sea surface. It over estimates the polarisation ratio and has little change with the sea state. Including the effect of breaking waves, shadowing and multipath will increase the accuracy of the results, however, it will greatly increase the complexity of the equations, especially since at low grazing angle the clutter area is much larger and thus more computationally demanding.

To include the effects of breaking waves the sea surface is modelled as a Gaussian surface. The wave break when the downward acceleration exceeds $g/2$ where g is the gravitational acceleration $\approx 9.8\,\mathrm{m\,s^{-2}}$.. The breaking waves give rise to the spikes found in the horizontal polarisation. After the waves have broken the whitecaps are created and give noise-like, speckle, returns which are roughly equal in both polarisations [47, 48]. Voronovich [46] included the effect of breaking waves into the SSA model by calculating the distribution function of the specular reflections from the breaking waves from the difference between the theoretical measurement and the SSA simulation results at HH.

The above models are primarily aimed at open seas. There is little work reported on undeveloped seas and littoral waters. Ward and Tough [49, 50] used Creamer's model to describe the sea surface. In this study the finite depth of the sea was also taken into account.

2.2.3 Properties of the Average Monostatic Sea Backscatter

Since the clutter returns are generally noise-like, an average is used to describe to describe the general qualities of the clutter returns. Both the mean and the median have been used. Care must be taken

when comparing different results that the same average is being compared. The mean is usually higher by around $1.6\,\mathrm{dB}$ [27]. Although, the mean (median) does not provide a full description of the clutter return, it is a good indicator of the general behaviour under certain conditions.

At near normal incidence σ°_M drops rapidly with decreasing grazing angle from its peak at $90°$, the returns are almost independent of frequency and polarisation. As the grazing angle (ψ) is decreased at about $60°$ the drop in σ°_{MVV} is much slower than σ°_{MHH}. This region is sometimes known as the plateau zone because σ°_M is almost independent of the grazing angle or related to $\sin(\psi)$ [51].

At small grazing angles, σ°_M drops faster with decreasing ψ due to shadowing and multipath. The returns are spikier especially for the horizontal polarisation which increases σ°_{MHH}. The critical angles which determine the above mentioned scattering regions are dependent on the radar frequency and the roughness of the surface. As ψ is decreased further, the drop in σ°_M is more rapid, It has been found that below the critical angle the received power varies as R^{-7}. At small grazing angles the angle is approximately equal to the ratio of antenna height to the range, σ°_M will vary as ψ^4. Katzine [52] suggests this is because of interference between direct reflected EM signals. Wetzel [27, 36] suggests that the decrease is due to shadowing.

It is difficult to characterise the dependency of the sea clutter with wind speed, as it is not only a function of the wind speed but also the fetch and duration. At high grazing angles the clutter returns has weak dependency on the wind speed. According to [27] this is due to the balancing act between the increase in surface roughness as the wind speed is increased and reducing the specular reflections, and the increase in the number of scattering facets. It is extremely difficult to accurately characterise the dependency of σ°_M with wind and sea at medium and low grazing angles. Not the least of these difficulties is the accurate measurements of the relevant surface parameters. σ°_M does not only depend on the magnitude of the wind velocity, wave height, but also on their direction and their temporal and spatial properties. Moreover, breaking waves give rise to whitecaps and bursts which have a profound effect on the σ°_M. For example a strong wind will give rise to spray which could increase the σ°_M. However, the wave height also depends on the time the wind has been blowing. Generally, σ°_M increases with wind speed until saturation is reached. Furthermore, higher wind speeds over an extended area for a long time would results in larger wave height, rougher seas, which in turn results in a higher σ°_M. The σ°_{MVV} to σ°_{MHH} ratio decreases with increased roughness and wind speed due to the increased probability of breaking waves. The effect of wind on sea clutter has been modelled using a power law [53]. However, this model does not take into account the saturation effects at high winds. A model based on the wave height spectrum was proposed [54]. In this model a cut-off wind speed is proposed below which the returns are very low. Above the threshold the returns rise sharply towards saturation.

It is generally accepted that looking up-wind results in higher σ°_M. In the plateau region the backscatter is higher at upwind direction and minimum for cross-wind direction. At low grazing an-

gles, σ°_{M} is highest when looking up-wind and minimum when looking downwind.

At high grazing angle σ°_{M} is almost independent of the radar frequency. However, σ°_{M} is more dependent on frequency as the depression angle is decreased [27]. It tends to increase with increasing frequency [27] this can also be inferred from Nathanson's tables [29]. The variation with frequency does not depend on the EM wave frequency only, but also on the environment, since it also influenced by the nature of the scatterers and the propagation environment.

At low grazing angles propagating radio waves are sensitive to permittivity inhomogeneity, which leads to the increase in the local grazing angle and the wave propagate beyond the optical horizon. This phenomenon is known as ducting [29, 55].

Since at the frequency of interest the echoes are due to wind waves, the presence of contaminants on the surface of the sea could reduce the σ°_{M} [56].

Rain also affects the radar backscatter from the sea surface. Laboratory experiments with artificial rain suggest that at light winds the rain increases the backscatter, and little change was observed for strong winds [57]. Measurements at Ku-band confirmed these findings [58]. Wetzel [27] reported (Hansen 1984) that even light rain can case high frequency components in the spectrum of sea backscatter. It was also reported that the rain decreased the correlation time of the clutter.

2.2.4 Empirical Modelling of Monostatic Sea Clutter

It is very difficult to determine quantitative relationships that describe the relation between the backscatter, the environmental conditions, the radar geometry and the radar parameters. Several empirical models have been proposed to predict the average σ°_{M} of sea clutter. Nevertheless, since these models were developed based on finite sets of measurements, under different conditions and using different approximations their results do not always agree. Therefore it is important to know the limits and applicability of the model [38]. Nathanson and Reilly [29] complied a comprehensive summary of sea backscatter measurement is presented, for grazing angles between 0.1° to 30°, at frequencies from $0.5\,\text{GHz}$ to $35\,\text{GHz}$, for both vertical and horizontal polarizations.

Several empirical models have been proposed to represent sea monostatic clutter. Probably the simplest of these is the constant gamma model which was first proposed for land clutter but has been applied to sea backscatter as well, particularly in the plateau. The reflectivity is given by [51]:

$$\sigma^{\circ} = \gamma \sin(\psi) \tag{2.42}$$

More accurate models which link σ°_{M} to the environment and the radar parameters have been developed such as Georgia Institute of Technology (GIT) model [59], the Hybrid model [29, 55] and Royal Radar Establishment (RRE) model [60]. Leonard *et al.* [61] showed that using the different models and the same sea conditions could lead to different results. In addition, using different models to predict

unavailable sea parameters could results in different results, even if the same σ°_{M} model is used.

Although, the GIT model has its imperfections, most authors who have developed or used other models have included the GIT model in their discussion. Thus GIT model is therefore the only model which will be described in some detail in this thesis, Appendix B.

Although the full scattering matrix of the sea returns have been measured [27,41,62] only very few models have been proposed to predict the cross-polarised returns of the sea surface. Long [31] proposed a model which relates the cross-polarised components to the wind speed and the look angle

$$\sigma^{\circ}_{Mc}(\text{dB}) = 29.8\log((V_w/0.51444)) + 6\cos(\phi_w) - 84.7 \tag{2.43}$$

2.2.5 Amplitude statistics

Since the sea surface is an extended surface, the returned clutter power is due to a large number of scatterers. If there is no dominant scatterer then according to the central limit theorem the returns from a fixed range will follow the Gaussian distribution, whose probability density function (pdf) is given by:

$$P(E_I, E_Q) = \frac{1}{\pi x}\exp\left(-\frac{E_I^2 + E_Q^2}{x}\right), \qquad -\infty \leq E_I, E_Q \leq \infty \tag{2.44}$$

where, E_I, E_Q are the in-phase and quadrature components of the received signal respectively, and x is the average intensity. After envelope detection the amplitude is Rayleigh distributed and the power (intensity) is an exponential random variable.

$$P(E) = \frac{2E}{x}\exp\left(\frac{-E^2}{x}\right), \qquad E = \sqrt{E_I^2 + E_Q^2} \tag{2.45}$$

$$P(z) = \frac{1}{x}\exp\left(\frac{-z}{x}\right), \qquad z = E^2 \tag{2.46}$$

where E is the amplitude and z is the intensity of the received signal.

This model was found to be a good fit for low resolution radars. It was assumed that returns were due to Bragg scattering from the gravity waves. However, it failed to explain longer tails of higher resolution measurements specially at low grazing angles and rough seas. Furthermore, at microwave frequencies the Bragg scatterers are the capillary waves not the gravity waves. This phenomenon is more evident in HH polarisation. This section will mainly concentrate on low grazing high resolution monostatic sea clutter.

Long [63] stated that MacDonald (1957) reported the presence of some target-like returns in the sea clutter. This spikiness tends to increase with decreasing depression angle and increasing resolution. It is more evident in horizontal polarisation. Trunk [64] fitted sea clutter returns to log-normal and contaminated normal distributions they both provided a better fit compared to the Rayleigh distribution. Trunk

reported that Ballard (1966) proposed to use the log-normal distribution to model sea clutter [64]. In a later paper Trunk [65] attributed the non-Gaussian nature to the special variation of σ°_{M}. He concluded that the returns would fit a gamma distribution; however, since there was no physical explanation for the use or occurrence of the gamma distribution he suggested the use of the Rice distribution, the source of the strong scatterer was not identified. The horizontally polarised returns were closer to the Rice distribution while the vertically polarised returns were closer to the Rayleigh distribution.

Valenzuela and Laing [66] calculated the statistics of the sea returns based on Wright's composite surface model [33]. They concluded that as the roughness of the surface is increased the amplitude pdf develops a longer tail. The sea clutter returns were neither exponential nor log-normal.

Sea clutter has been also fitted to the Weibull distribution. The Weibull distribution and its application to radar clutter and detection is discussed in great detail in [67]. The intensity pdf of the Weibull distribution is given by:

$$p_Z(z) = \frac{cz^{c-1}}{a^c} \exp\left(-\left(z/a\right)^c\right), \qquad z \geq 0 \tag{2.47}$$

where z is the intensity of the returns, c is the shape parameter, and a is the scale parameter. Schleher [68] fitted sea clutter data to the Weibull distribution. The distribution is between the log-normal and the exponential distribution, which makes it a better fit for a wider range of conditions. When $c = 1$, Eq. (2.47) reduces to that of the exponential distribution.

Jakeman and Pusey [69] extended the method used by [66] further by taking into account the fluctuations in the number of discrete scatterers rather than assuming a single patch scatterer is illuminated by the radar. The distribution of each scatterer was assumed to be K-distributed, thus the overall distribution of the sum of the scatterers was also K-distributed. The compound K-distribution was first proposed by Ward [37]. The compound formulation allowed the extension of the K-distribution to include noise, target and the effects of breaking waves. The K-distribution will explored in more detail in Section 2.2.5.1

The compound K-distribution belongs to a class of distributions known as compound Gaussian models. The distribution is the result of a Gaussian speckle component being modulated by a texture. In the K-distribution the texture is gamma distributed. Other textures have been used. For example, the inverse gamma has been proposed to model the texture [70].

Conte and Longo [58] modelled sea clutter as a complex spherical invariant random process (SIRP). An SIRP is a generalisation of the Gaussian mixture process. It is defined as a process in which the linear mean square estimate is the optimum mean square estimate [71]. It can be seen by using the representation theorem [72] that K-distributed and other Gaussian compound distributed random variables are special cases of the SIRP.

Anastassopoulos and co-workers [73, 74] proposed the use of a generalised compound probability distribution function (GC-pdf). As the clutter area decreases the number of scatterers decreases and the speckle is not Gaussian. They proposed that both the speckle and the texture are modelled by a generalised gamma process. It was also shown that the Weibull and K-distributions are special cases of the GC. The effects of thermal noise can be also included. The model would obviously provide a better fit than both the Weibull and the K-distribution as it is a more general distribution and has six free parameters.

Azzarelli [75] modelled sea clutter amplitude as being composed of a number of discrete scatterers. Those are grouped into different groups based on their statistical properties and the number distribution function. In this paper all the scatterers were assumed to be Gaussian. The resulting pdf is a weighted sum of Gaussian pdfs. If there is only one scatterer the resulting pdf is that of an SIRV. To fit low grazing sea clutter the negative polynomial was used to describe the number probability function.

Recently, there has been some interest in using the generalised Pareto distribution to model sea clutter as it more tractable than the K-distribution. It has been fitted to both low grazing [76] and high grazing X-band sea clutter [77]. The pdf of the generalised Pareto distribution is given by [78]:

$$p(z) \begin{cases} \frac{1}{\lambda}\left(1 - k\frac{z}{\lambda}\right)^{\frac{1}{k}-1} & \text{when } k \neq 0 \\ \frac{1}{\lambda}\exp(\frac{-z}{\lambda}) & \text{when } k = 0 \end{cases} \tag{2.48}$$

where λ is the scale parameter and k is the shape parameter. When $k > 0$ the domain of z is $0 \leq z \leq \frac{k}{\lambda}$ and $0 \leq z \leq \infty$. The exponential distribution is a special case of the generalised Pareto distribution with $k = 0$. For sea clutter applications k is defined between $-0.5 \leq k \leq 0$.

Most of the current sea clutter statistical analysis uses either the Weibull or K-distribution. The K-distribution provides the middle ground between the other more general models and the simplicity of the Weibull distribution. It is far more extensible to model coherent clutter, pulse integration and the effect of thermal noise as has been shown by Ward and Watts [79]. The compound nature of the K-distribution makes it possible to extend the model to coherent clutter, and to include the effect of noise and burst spikes.

Weibull, K- and log-normal fit to sea clutter data was examined in [80]. It was reported that the log-normal was the best fit for more than half the data. There were low clouds and some rain during the measurements. Furthermore the data covered different sea states 2-5. Given the above condition, there could be an increase in the number of spikes due to breaking waves, such events are not accounted for by either the K-distribution or the Weibull distribution. The paper did not relate the fits to the ground truth. Such events can be modelled by the K+A distribution as discussed in Section 2.2.5.1. Beside the original I-band data that was used to derive the K-distribution, it has been used, or one of its variants, to

fit other clutter data such as the IPIX data [81, 82].

Very low grazing angle data $\psi < 0.5^\circ$ was fitted to log-Weibull [83]. The authors reported that the log-Weibull was a better fit than log-normal, Weibull and K-distribution at such low angles.

2.2.5.1 The Compound K-Distribution

Since the sea is modelled as consisting of independent small scale structures which are modulated by large scale structures. Even at high resolution radar, the number of small scale structure is large enough such that they can be described by Gaussian statistics. The modulation results in the change of the local power. Since speckle can be decorrelated by frequency agility [39], it is possible to have many independent looks at the local power. It has been found that they can be fitted into a gamma distribution, the resulting distribution is known as the compound K-distribution. The compound K-distribution has been examined in great detail in [37, 84, 85]. Given that the speckle is locally Gaussian the pdf of the envelope and intensity are given by:

$$p(E) = \frac{2E}{x}\exp(-E^2/x), \qquad -\infty < E < \infty \tag{2.49}$$

$$p(z) = \frac{1}{x}\exp(-z/x), \qquad 0 \leq z \tag{2.50}$$

Given that the speckle is modulated by the texture which has a pdf $P_c(x)$, for sea clutter it has been found that $P_c(x)$ is gamma distributed

$$p_c(x) = \frac{b^\nu}{\Gamma(\nu)}x^{\nu-1}, \qquad 0 \leq x \tag{2.51}$$

and the envelope and intensity pdfs are given by

$$p(E) = \frac{4b^{(\nu+1)/2}E^\nu}{\Gamma(\nu)}\mathrm{K}_{\nu-1}(2E\sqrt{b}), \qquad -\infty < E < \infty \tag{2.52}$$

$$p(z) = \frac{2b^{(\nu+1)/2}z^{(\nu-1)/2}}{\Gamma(\nu)}\mathrm{K}_{\nu-1}(2\sqrt{bz}), \qquad 0 \leq z \tag{2.53}$$

where ν is the shape parameter and b is the scale parameter of the underlying gamma distribution, and $\mathrm{K}_{\nu-1}$ is the modified Bessel function of the second kind of the order $\nu - 1$.

Normalised intensity moments are usually used to test for the normality of the pdf. For Gaussian clutter or noise the normalised intensity moments are given by:

$$M_{n=}\frac{\langle z^n \rangle}{\langle z \rangle^n} = n! \tag{2.54}$$

for K-distribution with shape parameter ν it is given by:

$$M_{n=}\frac{\langle z^n \rangle}{\langle z \rangle^n} = n!\frac{\Gamma(n+\nu)}{\Gamma(\nu)\nu^n} = n!\prod_{k=1}^{n-1}(1+k/\nu) \tag{2.55}$$

The shape parameter is related to the spikiness of the sea clutter and is limited by $0.1 \leq \nu \leq \infty$. For values of $\nu < 1$ the sea clutter is considered to be very spiky as $\nu \to \infty$ the pdf tends to that of a Rayleigh distribution.

The above model does not take into account the effect of noise on the measured data. Watts [86] extended the compound K-distribution to include the effect of thermal noise. In the presence of thermal noise the pdf of the local mean power is given by:

$$p(E|p_n, x) = \frac{2E}{p_n + x}\exp(-E^2/(p_n + x)), \qquad -\infty < E < \infty \tag{2.56}$$

$$\tag{2.57}$$

The overall pdf of the clutter and thermal noise can be given by :

$$p(E) = \frac{2Eb^\nu}{\Gamma(\nu)}\int_0^\infty \frac{x^{\nu-1}\exp(-bx)}{x+p_n}\exp(-E^2/(x+p_n))\,dx, , -\infty < E < \infty \tag{2.58}$$

Lamont-Smith [87] suggested that a better fit was achieved by adding a Rayleigh component that is higher than the noise power.

The previous development can be used to model Bragg scattering from short gravity waves and capillary waves. However, discrete spikes cannot be model in this manner as they do not have a speckle component. The discrete spikes are modelled as a Poisson distribution $P_m(m)$ including the effects of noise the pdf is given by:

$$p(z) = \frac{1}{m\sigma_{sp} + p_n}\exp\left(\frac{-z}{m\sigma_{sp} + p_n}\right), 0 \leq z \tag{2.59}$$

where m is the number of spikes, σ_{sp} is the mean spike intensity.

Including the effect of speckle we arrive at the KA distribution which is given by [48]:

$$\begin{aligned} p(z|x) &= \sum_{m=0}^{\infty}\frac{1}{x+p_n+m\sigma_{sp}}\exp\left(\frac{-z}{x+p_n+m\sigma_{sp}}\right)P_m(m), \quad 0 \leq z \\ p_c(x) &= \frac{x^{\nu-1}}{\Gamma(\nu)}\left(\frac{\nu}{\sigma_{BW}}\right)^\nu \exp\left(\frac{-\nu x}{\sigma_{BW}}\right), \qquad 0 \leq x \\ P(z) &= \int_0^\infty P(z|x)P_c(x)\,dx \end{aligned} \tag{2.60}$$

where:

x: is the local mean power of the Bragg and range extensive whitecap scattering.

z: is the intensity of the received signal.

σ_{BW}: is the mean Bragg and whitecap intensity, it given by $\sigma_{BW} = \nu/b$

m: is the number of spikes in a range cell

ν: is the shape parameter for Bragg and whitecap scattering.

p_n: is the noise power

$\overline{N}$: is the average number of spikes per range cell.

$p_m(m)$: is the pdf of the number of spikes in a range cell.

Since the average number of spikes is assumed to be very small $\bar{N} \ll 1$, $p_m(m)$ is given by:

$$\begin{aligned} p_m(0) &= 1 - \bar{N} \\ p_m(1) &= \bar{N} \\ p_m(m \geq 2) &= 0 \end{aligned} \tag{2.61}$$

The mean intensity of the received signal is given by:

$$\langle z \rangle = \sigma_{BW} + \bar{N}\sigma_{sp} + p_n \tag{2.62}$$

and the noise-to-clutter ratio(CNR) is:

$$C/N = \frac{\sigma_{BW} + \bar{N}\sigma_{sp}}{p_n} \tag{2.63}$$

It is worth noting that most of the above presented material is discussed in greater detail in the in [88].

2.2.6 Spatial Properties

Using the compound model for sea clutter, it can be seen that either by averaging or frequency agility, the speckle component will be decorrelated. Burst spikes are range limited and will not decorrelate in time. The underlying texture is correlated in both time and space. The correlation properties of the texture cannot be ignored if the separation between the two range bins is less than the decorrelation length of the texture.

An understanding of how the spatial properties of the underlying texture could help in predicting the radar performance and give insight into the properties of the swell. Watts and Ward [89] argued that averaging the radar returns spatially has a similar effect to that of reducing the radar resolution. Hence these results can be used to predict the radar performance when using longer pulse lengths.

In [90] the autocorrelation functions of the mean clutter intensity of different data sets were plotted after the removal of speckle. It was found that the normalised autocorrelation functions were different

for all data sets. Furthermore, it was concluded that for short averaging times the data exhibits periodic behaviour. When the averaging period is extended the periodic behaviour ceases. It has been suggested that this is due to transient coherent structures. Furthermore, it has been reported in [3] that even a small bistatic angle could cause some decorrelation in the discrete spikes found in the amplitude of horizontally polarised sea clutter.

2.2.7 Doppler Spectrum

The coherent properties of the sea backscatter are expressed in terms of its power Doppler spectrum. Because the sea was thought to be made of two components, small scale scatterers riding on larger waves, the spectrum was assumed to be made of two components, one due to the orbital velocity of the large gravity waves and another related to the wind spray [91].

Pidgeon [92] studied the Doppler shift of the sea surface at low grazing angle using a coherent pulsed C-band radar. He reported that for horizontal polarisation the Doppler spectrum of sea backscatter is dependent on the orbital velocity of gravity waves, the wind speed, and the wave height. For vertical polarisation it is a function of the wave orbital velocity which is a function of the wave height. This was attributed to the Brewster effect since the vertically polarised waves will penetrate the upper layer of the waves and are reflected from just below the sea surface which is moving at the orbital velocity. The dependency of the Doppler shift on the viewing angle, angle between the radar line of sight and the wind and wave direction appears to follow a cosine law; however, the shape and bandwidth seems to be independent of the viewing angle. In addition, it was noticed that the Doppler spectrum bandwidth is larger for horizontal polarisation.

Trizna [93] argued that the crest of the heights waves are the preferential scatterers, which is more constant with the Bragg scattering from the crest than Pidgeon's ideas of below the surface scattering in vertical polarisations. The velocity and height of the highest waves were used for calculating the Doppler shift and not the average values. In estimating the Doppler velocity the effects of the capillary wave phase velocity, the gravity waves orbital velocity, Stoke's drift velocity and the wind drift were included. The model is a bad fit for horizontal and cross polarised waves. The author suggested taking breaking waves into account.

Lee and his co-workers [94, 95] examined the spectral lines of the Doppler spectra. They proposed three spectrum broadening mechanisms, Gaussian, Lorentzian and Voigtian profiles. The Gaussian profile is due to a spread of scatterer velocities, i.e. Bragg scatterers; while the Lorentizian is due to finite-scatterer lifetime, such as non-Bragg scatterers. Voigtian is the convolution of the former two profiles, Gaussian scatterers with limited lifetime. The Gaussian profile was related to the speed variations of the large scale waves. It was the dominant line shape in VV returns. The Lorentz profile is due to the sudden appearance and disappearance of scatterers, this was related to the peaks in horizontally polarised

returns. Finally Voigtian spectral lines are due to an ensemble of facet-like scatterers, or a short-lived Bragg scatterer. It was also noticed that horizontally polarised returns when averaged over time tend to a Voigtian profile. In most cases a combination of the all three profiles provided a better fit than a single profile. For example, using a Lorentizian profile provides a good fit for the σ°_{MHH} around the peak, but a combined fit will provide a good fit in the peak and at the sides as well.

Walker [96–98]. modelled the spectrum of the sea clutter as the sum of weighted Gaussian random variables. Walker measured σ°_{MHH} and σ°_{MVV} returns and used range time intensity plots in conjunction with Doppler profiles to draw his conclusions. The spectrum was found to be composed of three components:

1. The Bragg scattering was due to the capillary waves which are slower than the large waves. It was higher in VV returns compared to HH returns as predicted by the two scale model. The Doppler shift corresponded to the sum of the drift velocity and orbital velocity given by the gravity-capillary dispersion equation.

2. Burst scattering component, Walker used the term spikes in which the HH component was much higher than VV was identified, but were localised in rage. It had a higher Doppler frequency shift, approximately equal to the gravity waves phase velocity.

3. Whitecap scattering component, they were also localised in range with peaks around the wave phase velocity. The σ°_{MHH} and σ°_{MVV} returns were almost equal.

Assuming that all the components are Gaussian the following equations can be written for σ°_{MHH} and σ°_{MVV} return Doppler spectra respectively:

$$\Psi_v(\nu) = B_v\Psi_B(\nu) + W\Psi_W(\nu) \tag{2.64}$$

$$\Psi_H(\nu) = B_H\Psi_B(\nu) + W\Psi_W(\nu) + S\Psi_S(\nu) \tag{2.65}$$

and

$$\Psi_B(\nu) = \exp(\frac{-(\nu-\nu_B)^2}{w_B^2}) \tag{2.66}$$

$$\Psi_W(\nu) = \exp(\frac{-(\nu-\nu_P)^2}{w_W^2}) \tag{2.67}$$

$$\Psi_S(\nu) = \exp(\frac{-(\nu-\nu_P)^2}{w_S^2}) \tag{2.68}$$

where:

ν_B is the Doppler frequency shift corresponding to the Bragg resonance including the effects of Stoke drift and orbital velocities.

ν_P is the Doppler frequency shift corresponding to the gravity waves phase velocity.

w: is the spectrum bandwidth.

the subscripts B, W and S denote Bragg, whitecap and spike (burst) scattering respectively.

B_H, B_V are the Bragg scattering coefficients for σ°_{MHH} and σ°_{MVV} respectively. It is worth noting that there is a typographical error in equations (3) and (4) in [98].

Other models have been proposed for modelling the Doppler spectrum. However, those are beyond the scope of this work [99].

2.3 Review of Bistatic Sea Clutter

In this section bistatic sea clutter measurements and modelling are reviewed and analysed. As will be shown in the following subsections the EM scattering mechanisms are not well understood. This is partly due to the complexity of the problem and to the lack of the experimental data. The lack of the experimental data is due to the complexities inherent in building bistatic radar systems and carrying out bistatic sea clutter measurements, these include

1. Synchronisation of the transmitter and receiver in both time and frequency.
2. Correct alignment of both transmit and receiver antennas.
3. Data communication between the radar nodes and the radar operators at both sites.
4. Site selection is further complicated by the constrained imposed by synchronisation and communication requirements.
5. It is more difficult to calibrate bistatic radars.

2.3.1 Analytical Modelling of Bistatic Sea Clutter

Modelling bistatic sea clutter is more complicated than that of monostatic sea clutter since many of the assumptions used in solving the scattering problem are no longer valid. Valenzuela and Laing [66] derived their model for scattering from the sea surface for the bistatic geometry; however, the final solution was provided for the monostatic case. Some work has been done on extending the models used, or rather by removing the simplifications when the equations were used to solve for monostatic radar, to model monostatic scattering to the bistatic domain [100]. Generally speaking σ°_B decreases with increasing bistatic angle in backscatter geometries, and increases with increasing bistatic angle in the forward scattering geometries until it reaches the peak around 180° [101, 102].

Awada *et al.* [102] compared the theoretical results related to bistatic scattering from sea surfaces using both SSA and CSM. Numerical results were similar at vertical polarisation but were different at HH polarisation and at high wind speeds. It should be noted that these simulation results did not agree

with the limited published results, Section 2.3.2, and there is no justification for the increase in the σ_B° at backscattering geometries at scattering angles less than 20°. Furthermore, the paper did not take into account the effect of non-Bragg scattering.

Comblet and Khenchaf [103] reviewed 6 different methods for the 2D scattering from ocean surfaces and applied them to bistatic radar geometries. They also compared the numerical results of some of the results. However, some of the plots are the same as those in [102].

Arnold-Bos and co-workers, develop what they described as a general polarimetric bistatic simulator [104, 105], they applied the simulator to the problem of radar signals scattering from the sea surface. The theoretical background was presented in [104]. The orbital velocity was considered to be the source of the Doppler shift, non-linear effects were ignored. The composite model was used to compute the radar cross section. The authors showed that the co-polarised σ_B° was a minimum at a scattering angle of 90°. However, due to the lack of experimental bistatic sea clutter data the simulator could be only be validated in the monostatic geometry [105].

2.3.2 Experimental Measurements and Empirical Modelling

Unlike monostatic radar sea clutter, bistatic sea clutter has not been studied extensively. There are five major published reviews of bistatic sea clutter, viz.: Nathanson [29], Willis [25], Long [26], Weiner in *Advances in Bistatic Radar* [22] and Griffiths *et. al* [106]. The study by Weiner [22] gives a comprehensive review of the results, it counts 9 measurement programmes only; 4 of which are on sea clutter. Only a single out-of-plane sea clutter measurement was reported. It is worth noting that a more detailed analysis of some of the results is given in [25]. Only measurement programmes related to sea clutter will be discussed in this section. None of the reported measurement did any statistical analysis of the data. It is worth noting that the statistical properties of foliage were studied in [107] and the clutter amplitude statistics were found to be non-Gaussian, it is not clear what was the best fit distribution of the equivalent monostatic clutter.

2.3.2.1 In-Plane Backscatter Measurements

Pidgeon [108] did not reference any papers on bistatic sea clutter and this seems to be the first publicly available paper on the bistatic backscatter of the sea surface. The measurements were made using a land based cooperative C-band CW illuminator and an airborne receiver. Monostatic data was also recorded. However, it is not clear if the recordings were simultaneous or not. The bistatic angle was changed by changing the receiver and transmitter depression angle. The results were presented as a function of the transmitter depression angle, and for sea states 1, 2 and 3 and wind speeds 5 kn, 20 kn to 30 kn and 10 kn respectively, which indicates that the at least sea state 2 measurements were of an undeveloped sea. The sea state was determined by measuring the wave height using a wave gauge. For sea state 3 σ_B° was 10 dB higher than that of sea state 1. Although the wind speed was higher for the sea state 2 measurements,

the backscatter for sea state 2 was smaller than that for sea state 3. This led Pidgeon to suggest that local wind might not have any effect on σ°, but this conclusion cannot be drawn from his measurements. Sea state data for a fully developed sea needs to be compared to those of the same significant wave height but at a higher wind speed to support such claims. All the data was recorded with the radars looking cross wind except for those of sea state 3. Given that the bistatic depression angles were much larger than those of the transmitter, these relatively small changes in the transmitter depression angle will have a small effect on the bistatic angle. The σ_B° was relatively independent of receiver depression angles between 10° and 90° and the transmitter depression angles were between 0.1° and 4°. It is also claimed that the results were very close to those of monostatic measurements under similar conditions.

When studying the Doppler properties of bistatic sea clutter Pidgeon [92] reported that the bistatic geometry had no significant effect on the Doppler shift or Doppler spectrum. This is the only reported measurement of simultaneous bistatic and monostatic sea clutter. A C-band coherent land based pulsed radar was used. The transmitter and receiver were separated vertically. It is not clear what bistatic angles were used. The main contribution of this paper is that σ_B° was similar σ_M° for those measurements, where the bistatic depression angle was much larger than the monostatic depression angle. However, since the measurements did not include other geometries the relationship between the two cannot be analysed further.

Domville [109, 110] recorded the most comprehensive data set for in-plane land and sea bistatic clutter measurements. Some data was recorded for small out-of-plane clutter as well, but the data set is small. Furthermore, algorithms were devised to predict σ_B°. He used a CW X-band transmitter and a receiver. The transmitter and receiver were carried on separate aircrafts. Both forward scattering and backscatter σ_B° were recorded. The wave height was not measured and the wind speed at the sea was taken from Meteorological Office data. The measurements were made at different look angles with respect to the wind and sea directions. As in [108] Domville concluded that the receiver grazing angle had little effect on σ_B°. The σ_B° was determined by the σ_M° of the antenna with smaller grazing angle. Two examples of the data set are shown in Fig. 2.5 , both in both plots the wind speed was approximately $20\,$kn. Willis [25] fitted Domville's backscattering data for angles up to 15°, using Barton's model for bistatic land clutter, discussed in Section 2.3.3. Willis reported the error to be less than ± 5 dB. A specular ridge was noticed at forward scattering geometry. Kochanski *et al.* [111] used a CW horizontally polarised land based transmitter operating in the X-band and an airborne receiver with a coplanar co-polarised array antenna to measure the in-plane backscattering σ_B° of the sea surface at low transmitter grazing angles. The transmitter's grazing angle was fixed at 0.3° while the receiver's varied from 5° to 40°. The transmitter was aligned using a C-band beacon on a low RCS fibreglass dinghy. Good surface truth was recorded and the sea was reported to be fully developed sea state 1. The mean σ_B° was reported to be about -45 dB, with a spread of around 10 dB. The amplitude statistics were fitted to log-normal

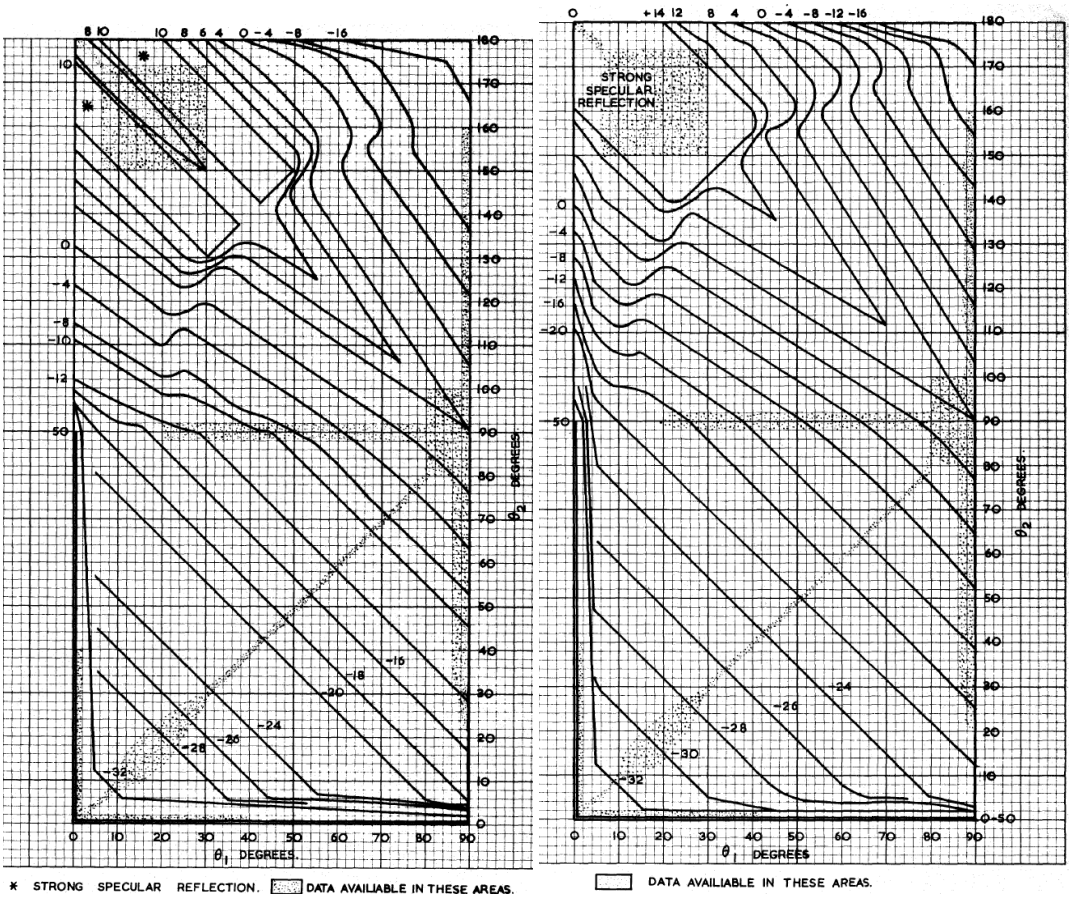

(a) Vertically polarised (b) Horizontally polarised

Figure 2.5: Two example of in-plane sea clutter, the wind speed was 20 kn, source [110].

distribution using Kolmogorov-Smirnov (K-S) test.

2.3.2.2 Out-of-Plane Experiments

One of the very few openly available bistatic sea clutter measurements are those by Ewell and Zehner which are described in [112, 113]. It is worth noting that a few typographical errors were made in some of the equations in [112]; however, those were corrected in [113]. In these trials an X-band land based coherent pulsed monostatic node and bistatic receiver were used. The baseline length was $3.5\,\mathrm{km}$. The transmitter bearing was fixed at 90° or 150°, the range gate and angle of receiver were changed to change the bistatic angle. A dihedral corner reflector was used to calibrate both the monostatic and bistatic systems, as an additional aid a trihedral corner reflector was used in calibrating the monostatic radar. The data was represented as the ratio of the median reflectivities of bistatic and monostatic sea clutter and plotted as a function of the environment and bistatic angle. The amplitude of the data was fitted to a log-normal distribution. In almost all cases the $\sigma^\circ_M > \sigma^\circ_B$ with the ratio decreasing more as β is increased.

As part of Rome Laboratory adaptive multimode bistatic (AMBIS) program. Clancy and Len [114] conducted bistatic sea clutter measurements for both land and sea (Florida Keys area) environments. They used S-band pulsed radar with staggered PRF. The data is reduced by rejecting cells outside of the receiver beam, and those with low clutter to noise ratio. They calculated the average reflectivity and plotted the averages against the out-of-plane angle, grazing angle and terrain type, which included ocean and gulf terrains. Only a few examples of different terrain types were provided in this report. In this work, as typical in forward scattering experiments, forward scattering is achieved when the out-of-plane angle $= 0$. In gulf the terrain example, with wave heights $0\,\mathrm{m}$ to $4\,\mathrm{m}$, the peak reflectivity was found around forward scattering. A plateau was found between $35^\circ - 145^\circ$. The minimum was between $85^\circ - 95^\circ$, however, the variation in this plateau region is around 10°. The minima was reached around 90°. The reflectivity increased sharply until about 100°, Finer variations cannot be discerned due to the limited resolution in the plot. Examples of other terrain types such as scrubs and weeds showed a shaper peak around 90°.

In addition to the above mentioned programmes, Other experiments have used global navigation satellite system (GNSS) signals to measure the wave height and wind speed [115–119]

2.3.3 Empirical Models

Although most of the experiments described in the previous sections were accompanied by some form of empirical models, most of these models did not agree with the presented data. Barton [120] proposed an extension to the constant gamma model and used it to model surface land clutter

$$\sigma^\circ_B = \gamma\sqrt{\sin(\psi_T)\sin(\psi_R)} \tag{2.69}$$

where ψ_T and ψ_R are the transmitter and receiver grazing angles respectively, γ is a constant that depends on the terrain, the environment and the radar parameters. The model is only valid for in-plane backscatter geometries. Willis [25] fitted Domville's results for sea surface backscatter [109, 110] using (2.69).

Domville [109, 110] developed regression models to fit his measured data. However, no other use of this model was found in the literature. Since they are linear model, it will be difficult to extend them to different sea conditions and radar parameters. This model is only applicable to in-plane geometries.

No empirical models for modelling out-of-plane bistatic sea clutter were found in the open literature.

2.4 Summary

In this chapter the fundamentals of bistatic radar have been introduced including discussion of the bistatic radar equation for point and extended targets. The important concepts of bistatic radar resolution and clutter area have also been reviewed. A comprehensive survey of monostatic sea clutter literature was also presented including a brief overview of scattering theory, and a detailed analysis of the amplitude statistics. Emphasis was placed on discussing the compound nature of sea clutter and the compound K-distribution. The sea clutter Doppler spectrum is important in this work and its literature and theory were reviewed and linked to the compound sea clutter model.

Finally the limited information on bistatic sea clutter was discussed. Only a handful of measurement programmes have been dedicated to bistatic sea clutter most of these studies are more than 20 year old. It is clear that there is a pressing need for more experimental bistatic sea clutter data to verify the existing scattering theory based models. New bistatic data will also be critical to the development new physical and empirical models to better understand bistatic sea clutter.

It is clear from this that the development of reliable models to predict the performance of bistatic radar in the marine environment has been hindered by the lack of experimental data. Although, the analysis part of this work has focused on the average reflectivity and statistical properties, the results will undoubtedly help to give more insight into the scattering mechanisms in out-of-plane and in-plane bistatic geometries. This will pave the way for the development of more accurate analytical and statistical models of bistatic sea clutter.

Chapter 3

NetRAD System Development and Testing

As discussed in the previous chapter there is a pressing lack of experimental data to validate and create accurate models for bistatic sea clutter. It was therefore necessary to develop a system that is capable of recording monostatic and bistatic data. In this chapter the UCL netted radar (NetRAD) will be introduced. The system formed the basis for the data collection presented in this thesis. The chapter begins with a brief review of the original system. The main drawbacks of that system were its limited baseline and limited peak output power. The second section is concerned with the hardware and software development of the current system. It starts with a discussion of the drawbacks of the original system and how the proposed changes were implemented. The following section is concerned with the calibration method used to evaluate the system performance and insure that it works as expected. The chapter concludes with a summary of the main features and specifications of NetRAD.

3.1 Historical Overview of NetRAD

This section provides a very brief description of the NetRAD system. A fuller treatment is available in [121, 122]. NetRAD was designed as a low power, coherent netted radar system, which can operate in monostatic, netted monostatic, bistatic and netted bistatic modes. It was developed using commercial off the shelf (COTS) components. The netted radar consists of three nodes; each node was capable of transmission and reception.The maximum theoretical bandwidth was $50\,\text{MHz}$ [1]. The user controlled the radar and set the parameters using a graphical user interface (GUI) designed using C#.

One of the main difficulties in bistatic and multistatic radar system is the synchronisation and coherence of the nodes. In NetRAD a common $100\,\text{MHz}$ clock, was generated in node 1 which was the master node and was converted to Low-voltage differential signalling (LVDS) then transmitted using $50\,\text{m}$ high quality (category 6) unshielded twisted pair (UTP) cables to nodes 2 and 3 (Fig. 3.1). This signal was then used in a phased locked loop (PLL) to generate the carrier at $2.4\,\text{GHz}$, and to clock the field programmable gate array (FPGA), direct digital synthesis (DDS) and capture card. The same cable was also

[1] Because zero IF was used the maximum band width was less than half the clock frequency ($100\,\text{MHz}$) which limited the maximum practical bandwidth to $45\,\text{MHz}$. In addition, the ADC had a maximum frequency of $100\,\text{MHz}$.

used to send the synchronisation signal, and LDVS trigger pulse which starts the transmission/recording process in the radar. Data communication between the nodes was achieved using wired Ethernet, with the master node acting as a server, as shown in Fig. 3.1. In addition the FPGA was responsible for conveying control commands and data between the host PC and the other hardware components. The FPGA was programmed using very high speed integrated circuits hardware description language (VHDL). The DDS was used to generate the inphase and quadrature components of the transmitted signal which modulate the carrier to generate the transmitted signal. To reduce the effect of aliasing the output of the DDS output was filtered before it was mixed up and amplified. However, since zero-IF was used this process did not completely eliminate the lower sideband. The signal was amplified by 25 dB and transmitted using a 24 dBi gain antenna. Separate antennas were used for transmission and reception. The main characteristics of the original radar system are shown in the Table 3.1[2].

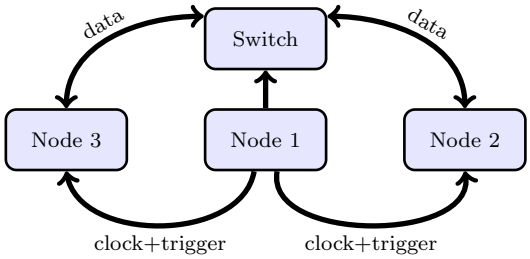

Figure 3.1: Block diagram of the original NetRAD data communication, clock distribution and triggering paradigm.

Property	Value
Carrier frequency	2.4 GHz
Noise at ADC input with receive match terminated (in the lab)	−34.5 dBm
Noise figure (measured in the lab)	5.64 dB
Peak transmitted power	23 dBm
Antenna beamwidth	10° × 10°
Antenna gain	24 dBi
Maximum bandwidth	50 MHz
Nominal range resolution	3 m
Measured range resolution (45 MHz chirp)	4.35 m
Pulse lengths	0.1 µs - 10 µs
Average receiver gain	56.5 dB
1 dB compression point (at output)	7 dBm

Table 3.1: Specifications of the original NetRAD system.

In the receiver chain the received signal was amplified by the low noise amplifier (LNA), then mixed down directly to baseband. Then the signal was filtered and amplified by a two stage baseband amplifier. Finally the signal was passed through an anti-aliasing filter before being sampled at 100 MHz using a

[2]Antenna data was taken from the manufacturer's datasheet available at `www.stelladoradus.com/pdfs/2.4/24.SD27.(12-08-08).pdf`

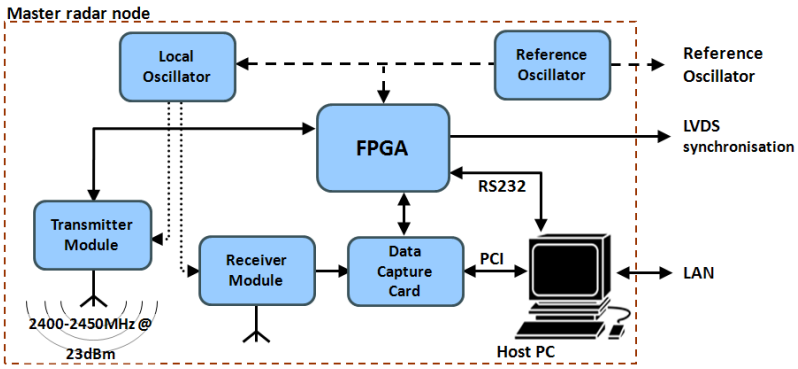

(a) Block diagram of the master node

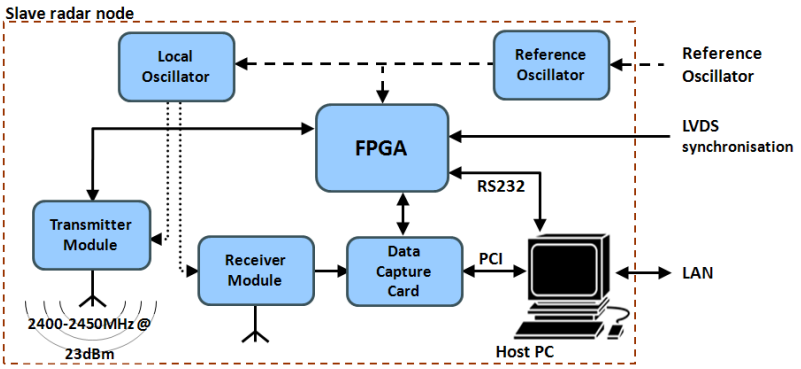

(b) Block diagram of a slave node

Figure 3.2: Functional block diagram of the original NetRAD nodes

capture card. The capture card had a word size of 14 bit and interfaces with the host computer using PCI. The capture card had a 512 MiB onboard memory [3] which was used to store the recorded data. Since each captured sample was stored as 2 B, the maximum number of recorded samples was 256 MiS. The data was sampled at 100 MHz using a single channel. The complex signal was recovered by using the Hilbert transform.

All the nodes were powered from 12 V lead-acid batteries. Each node consists of two 2U 19 in rack-mounts in a case which could hold up to three such rack-mounts. The battery was connected to the lower rack-mount which housed dedicated 6 V and 16 V power supplies and the host PC. The host PC mini-itx power supply was used to supply 5 V and 12 V. These voltages were used to power the network switch and monitor (when connected), and were also connected to the upper rack-mount, where they powered the FPGA and the cooling fans. The upper rack-mount housed the receiver, transmitter, FPGA, and the power supplies and regulators necessary for powering the components not powered from the min-itx power supply. Communication between the FPGA and the host PC was achieved by using RS-232 via the host PC serial port.

[3] To avoid confusion the IEEE Std 1541-2002 [123] will be used, M $= 1 \times 10^6$ while Mi $= 1 \times 2^{20}$.

3.2 System Development

The goal of this hardware upgrade is to be able to simultaneously record coherent monostatic and bistatic sea and small target data at ranges up to 3 km using arbitrary baselines. The main deficiencies of the original system for this application were:

1. Output power was too low.
2. The dynamic range was limited.
3. The maximum baseline was limited to 100 m.
4. The antennas were not robust enough for sea clutter field work.
5. Directional control of the antennas was inaccurate.
6. The above developments necessitated a complete rewrite of the software interface.

3.2.1 Increasing the Transmitted Power

The peak transmitted power of the original system was 0.2 W. This greatly limited the range of the radar as illustrated below:

> Assuming the radar parameters provided in Table 3.1 and a cable loss of 2 dB, sea state 3, a grazing angle of 3° ($\sigma^{\circ}_{M} = -50\,\mathrm{dB\,m^2/m^2}$ [29]) and a pulse length of 1 µs, the maximum noise limited monostatic range is about 208 m (using Eq. (2.31) on page 52). Thus it is clear that a substantial increase in the output power is needed for adequate sea clutter measurements.

The output power was increased by using external pulsed high power amplifiers (HPA). Two amplifiers were purchased; the main HPA has a nominal output power of 450 W (Microwave Amplifiers Ltd. AM85-2.45S-57-57), the backup amplifier has a peak power of 200 W (Microwave Amplifiers Ltd. AM82-2.5S-45-53). The main properties of these amplifiers are shown in Table 3.2[4].

Increasing the transmitted power increases the level of interference between the transmitter and receiver. This is particularly true in the monostatic node. It was found in field measurements that antenna separation of the order of 100 m might cause the bistatic receiver to saturate; however, it recovered almost immediately thus not affecting the quality of the measurement. The sidelobe breakthrough proved to be a good reference for calibrating the phase and range of the passive node as shown in Chapter 4

As far as the monostatic node was concerned the three options were considered for isolating the transmitter and receiver, see Fig. 3.3. The three options are:

[4]The nominal data was taken from the manufacturers datasheet or measurements, the output power was measured in the laboratory as detailed in Section 3.3.1.3

Property	Main HPA	Backup HPA
Output power	57.7 dBm	54.3 dBm
Input power for rated output	5 dBm	10 dBm
Control signal	TTL	TTL
Control pulse rise time	5 µs	10 µs
Control pulse fall time	5 µs	10 µs
Positive bias	12 V	12 V
Negative bias	−12 V	−12 V
Peak positive supply current	120 A	60 A
Standby current	1400 mA	183 mA
Maximum duty cycle	10 %	10 %

Table 3.2: Main and secondary high power amplifiers specifications.

1. To use a single antenna for transmission and reception and a high power single pole double throw (SPDT) switch to isolate the receiver from the transmitter (Fig. 3.3a).

2. To use a single antenna for transmission and reception and a circulator to isolate the transmitter and the receiver (Fig. 3.3b).

3. To use two closely spaced antennas, one for transmission and the other for reception (Fig. 3.3c).

The cost of buying a high power fast SPDT switches was prohibitive so this option was not pursued any further. Thus only the last two options were investigated experimentally as discussed below:

1. Isolating the receiver using a circulator. In this configuration a single antenna was used, followed by a circulator, the circulator which is connected directly to the HPA in the transmitter path and to a limiter followed by a SPST switch on the receiver side, as illustrated in Fig. 3.3b. The circulator provided 23 dB isolation. Assuming an antenna reflection coefficient of around −15 dB and two-way cable loss of 4 dB the actual loss was around 19 dB. To protect the receiver a limiter (Herotek LP2040) was installed. In addition, a SPST) absorptive switch (AtlanTekRF APS-1005-A) with 50 ns fall/rise time was used. The switch provides 80 dB isolation and an insertion loss of 1.6 dB. Although, the isolation was more than enough, it was found in field and laboratory measurements that the received data suffered from substantial interference even after the pulse has been transmitted. After examining the problem further it was found that whenever there was a dc path between the transmitter and receiver the receiver signal was corrupted even if the transmitter was not active.

2. Isolating the receiver using two closely spaced antennas. In this configuration one antenna was used for transmission and the other for reception. The separation between the antennas was kept small compared to the target range. In field trials this was kept between (3 m to 6 m). The SPST switch discussed in the previous point was used to prevent the receiver from saturating. In addition an identical switch was used to prevent the local oscillator leakage from being amplifier while the HPA is being switch off between transmissions. This option eliminates the dc path between the

transmitter and receiver, thus eliminating low frequency interference; furthermore since there was not a risk of reflection power damaging the receiver a limiter was not needed, improving the noise figure of the receiver as compared to the other option. On the other hand it was not true monostatic since two antennas were used; however for a separation of $4\,\text{m}$ and equidistant target range of $300\,\text{m}$ the bistatic angle is $0.76°$. On balance this option was the best alternative and was used in the field trials.

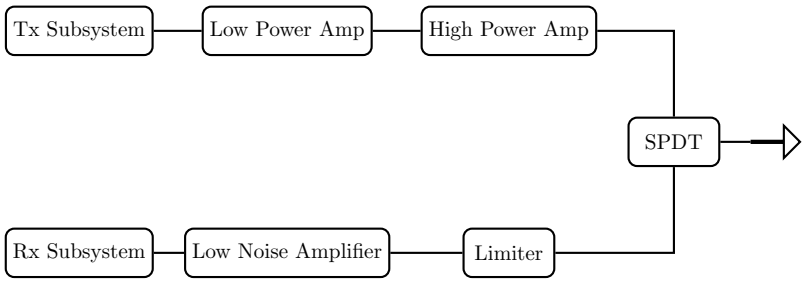

(a) Using one antenna and an SPDT switch

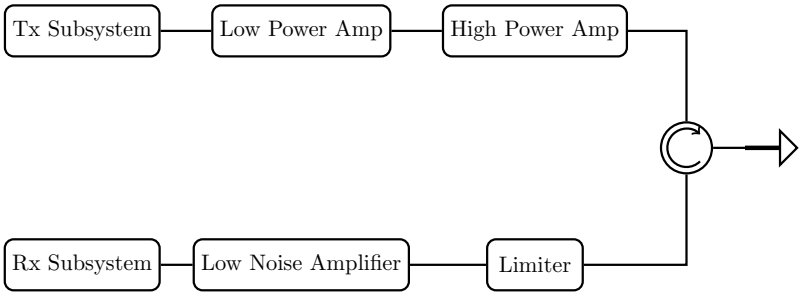

(b) Using one antenna and a circulator

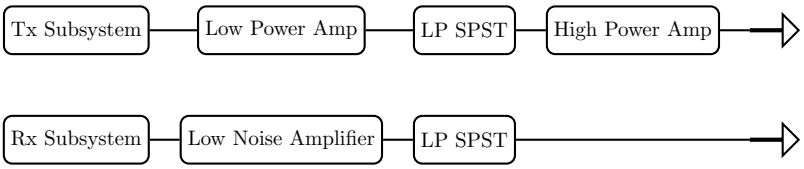

(c) Using two antennas and two SPST switches

Figure 3.3: Block diagram of the isolation strategies in the active node. The last option was used in all field trials.

Although the two amplifiers have different input power requirements, a similar design methodology was used, in order to ensuring maximum portability between the two devices. It is discussed in the following enumerated points[5].

1. When the amplifier is not transmitting it consumes very little current. Hence, the peak current is much larger than the mean current, and this is clearly shown in Table 3.2. It would have been an overkill to use a power supply capable of supplying the peak current on a continuous basis.

[5]For values used in the following bullet points please refer to Table 3.2.

Electrolytic capacitors with low effective series resistance (ESR) were used to store enough charge to provide the required bias current during the operation of the amplifier. When the amplifier is switched off the capacitor will charge. When transmitting the discharge must be minimal such that the bias voltage remains unchanged. The capacitor was placed as close as possible to the dc-bias terminals of the amplifier to reduce ohmic losses.

2. Two 12 V lead-acid batteries were connected in series to provide 24 V input power.

3. This was converted to 12 V using 24-to-12 V using Moonraker 24 V to 12 V dc-dc converter.

4. Because the current from the negative power supply is much smaller than that of the positive power supply a dedicated inverting power supplied was used.

5. The amplifiers were cooled by mounting a heat sink on the amplifiers. Two fans were also used to further reduce the risk of overheating when operating in hotter climates. To reduce the load on the power supply, the fans were powered from 24 V available from the input socket.

6. Both amplifiers have a D-sub connector which was used to receive the control signal, negative bias, and monitor the over-temperature and duty cycle trips.

7. The amplifiers were housed in 3U 19 in rack-mounts. Identical heavy duty power sockets were mounted on the front panel of each rack-mount. In addition, chassis monitors for the input voltage, the positive bias and the negative bias were installed. Two LEDs were also used to indicate the duty cycle and the over-temperature trips.

8. Both amplifiers required that the negative bias is switched on first then the positive bias finally the RF input could be connected to the input of the HPA. The HPA power supplies were wired such that the positive bias could not be applied without switching on the negative bias.

9. The HPA has a relatively long fall times of the HPA (5 µs to 10 µs), during which the noise and local oscillator leakage would be amplifier and transmitted. They would pose a significant interference source for the monostatic node. A switch was installed, in the monostatic node, between the last low power amplifier and the output of the node. The switch is identical to that used in the receiver path (Fig. 3.4).

From the above it can be seen that there are two identical switches installed in the monostatic node. The switches required ± 5 V. The positive supply was taken from the existing 5 V power supply. The -5 V was provided by using an inverted dc-dc power supply. A block diagram of the current transmitter and receiver subsystems are shown in Figs. 3.4 and 3.5 respectively.

Both the transmitter and receiver switches were controlled from the FPGA. To reduce the risk of human error, a single module in the FPGA timer control core was used to generate the pulse that controls

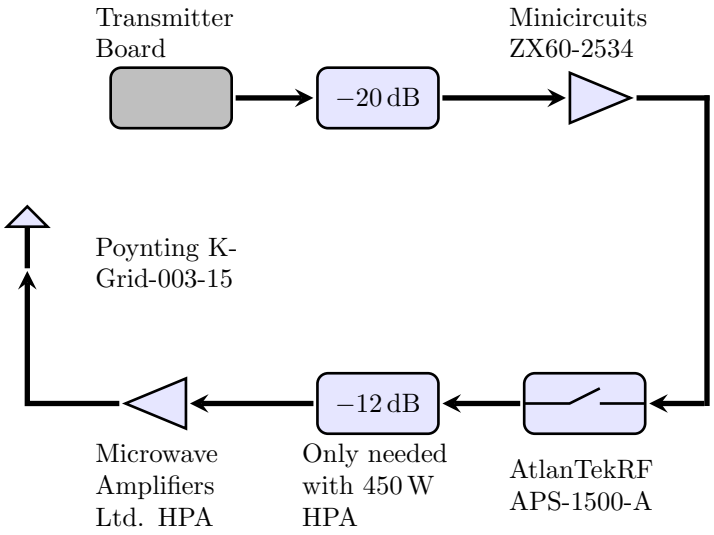

Figure 3.4: NetRAD transmitter subsystem, the blocks in light gray represent the new components

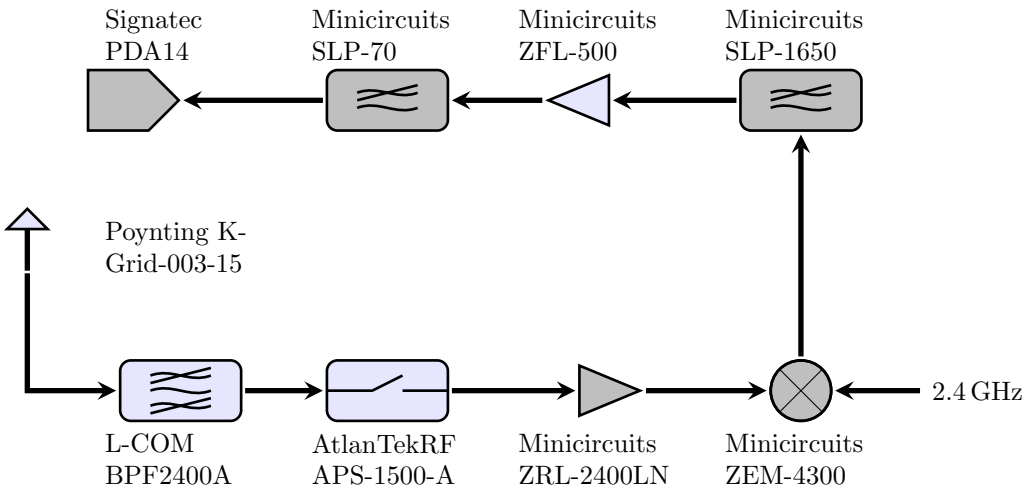

Figure 3.5: NetRAD receiver subsystem, the blocks in light gray represent the new components

the receiver and transmitter switches. The transmitter switch control pulse was generated by inverting the receiver switch control pulse. The start times of most of the control pulses can be controlled via pre-delay counters, the user can set these values as appropriate using the graphical user interface. The minimum switch duration is set equal to the transmitted pulse length. A block diagram of the FPGA timer module is shown in Fig. 3.6.

The HPA was also controlled from the FPGA. The HPA rise time was taken into account when in the main loop of the timer core. The on-time was set equal to the pulse length, see Fig. 3.6.

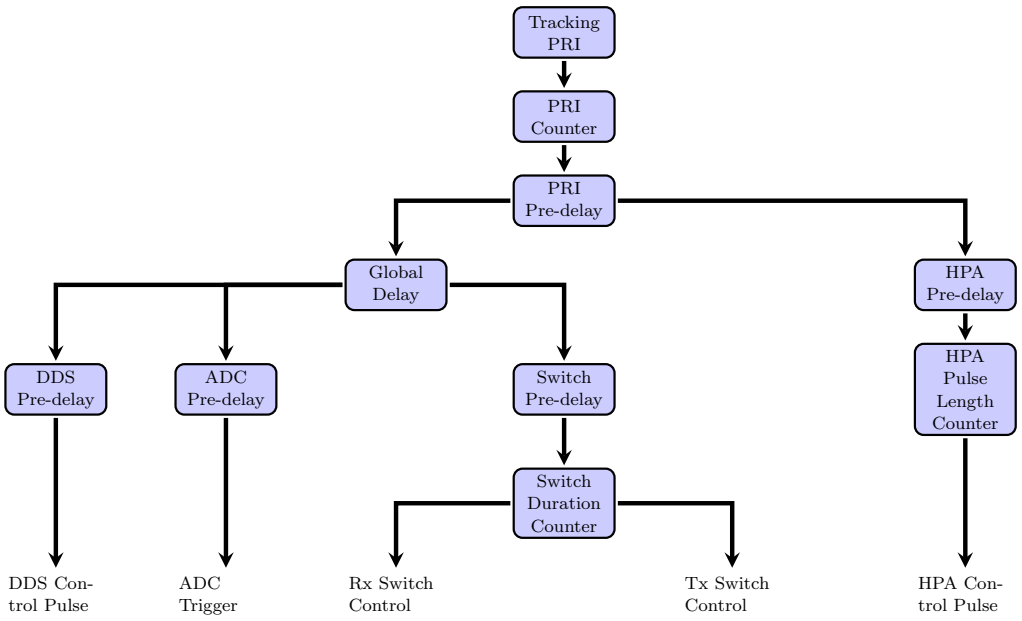

Figure 3.6: Block diagram of the timer core in the FPGA

Since the required input power for both amplifiers is much less than the original output power of the node. It was necessary to reduce the low power output. Furthermore, the original low power amplifier (Minicircuits ZRL-2400LN) is rated to 2.4 GHz, which causes the gain to drop at higher frequencies. The amplifier was replaced by Minicircuits ZX60-2534M amplifier which has a gain of 32.8 dB at 2.5 GHz, the input to the amplifier was attenuated by 20 dB which gives an output power of around 10 dBm, taking out the switch and cable losses, as illustrated in Fig. 3.4. The effect on the linearity of the chirp is discussed in Section 3.3.1.7. The addition, of the 20 dB attenuator was because it was not possible to find a more suitable amplifier with a high input power rating and a lower gain at the required frequency.

3.2.2 Instantaneous Dynamic Range

The amplitude of the radar returns can vary widely depending on the target range and RCS. The effective number of bits of the capture card is 13 bits. When the capture card is set to 1 V_{p-p} the quantisation noise level is -74.28 dBm, hence, the maximum instantaneous dynamic range is 78.27 dB. When the ADC is terminated the measured noise power $P_{nADC} = -62.8$ dBm, which around 11.5 dB higher than the

theoretical value. However, the receiver noise in the original system level was about -34.5 dBm, and the receiver would saturate at 7 dBm. Hence the maximum achievable dynamic range was 41.5 dB.

To increase the dynamic range the noise should be reduced without saturating the baseband amplifier or the capture card. This could be achieved by reducing the noise figure (NF) of the receiver or reducing the total gain of the receiver[6]. As long as the NF was not increased, reducing the gain of the receiver will not affect single pulse detection as detection is a function of SNR not the received power only.

Replacing the current mixer with an image rejection mixer would have reduced the noise power by 3 dB; however, this would be difficult since the zero IF was used. Another option to reject the image could have been the use of an identical mixer with the reference shifted by $90°$. However, this option would have required replicating the baseband part of the receiver chain and recording the I and Q channels separately and would have been susceptible to amplitude and phase imbalance between the channels. Reducing the gain of the LNA was not an option as this would have increased the noise figure. It would have been possible to reduce the gain while having a negligible effect on the NF by attenuating the output of the receiver just before the input of the capture card. For example installing a 20 dB attenuator before the input of the capture card would have reduced the receiver gain to about 37 dB. However, this would have shifted the dynamic range downwards, as can be seen in Fig. 3.7. This can be explained by the premature saturation of the baseband amplifier, which is explored in more details in Section 3.2.2.1.

To be able to reclaim the instantaneous dynamic the baseband amplifier must be prevented from saturating. Alternatively, the 20 dB could be split into two 10 dB attenuators; one installed before the capture card and the other before the baseband amplifier, the result is shown in Fig. 3.7. This would increase the NF by around 1.9 dB. Thus the maximum reduction in gain was approximately 21 dB. The approach used in this work was to replace the baseband amplifier with one which has lower gain and higher input power capabilities. This approach is discussed in the next section.

3.2.2.1 Baseband Amplifier Issues

The baseband amplification stage consisted of two amplifiers [124, page 210], a video amplifier (Analog Devices AD605) followed by a wideband op-amp (Texas Instruments THS4304). The aim was that the combined gain of these two stages should be 35 dB. However, from measurements the gain was closer to 39 dB. Furthermore, upon examining the datasheet of AD605 video amplifier it was found that it was rated to a maximum frequency of 40 MHz. The gain of the baseband amplifier was measured in the laboratory using a calibrated vector network analyser, and it can be seen that the gain drops from 38 dB

[6]The gain of the LNA must not be reduced as this will increase the NF.

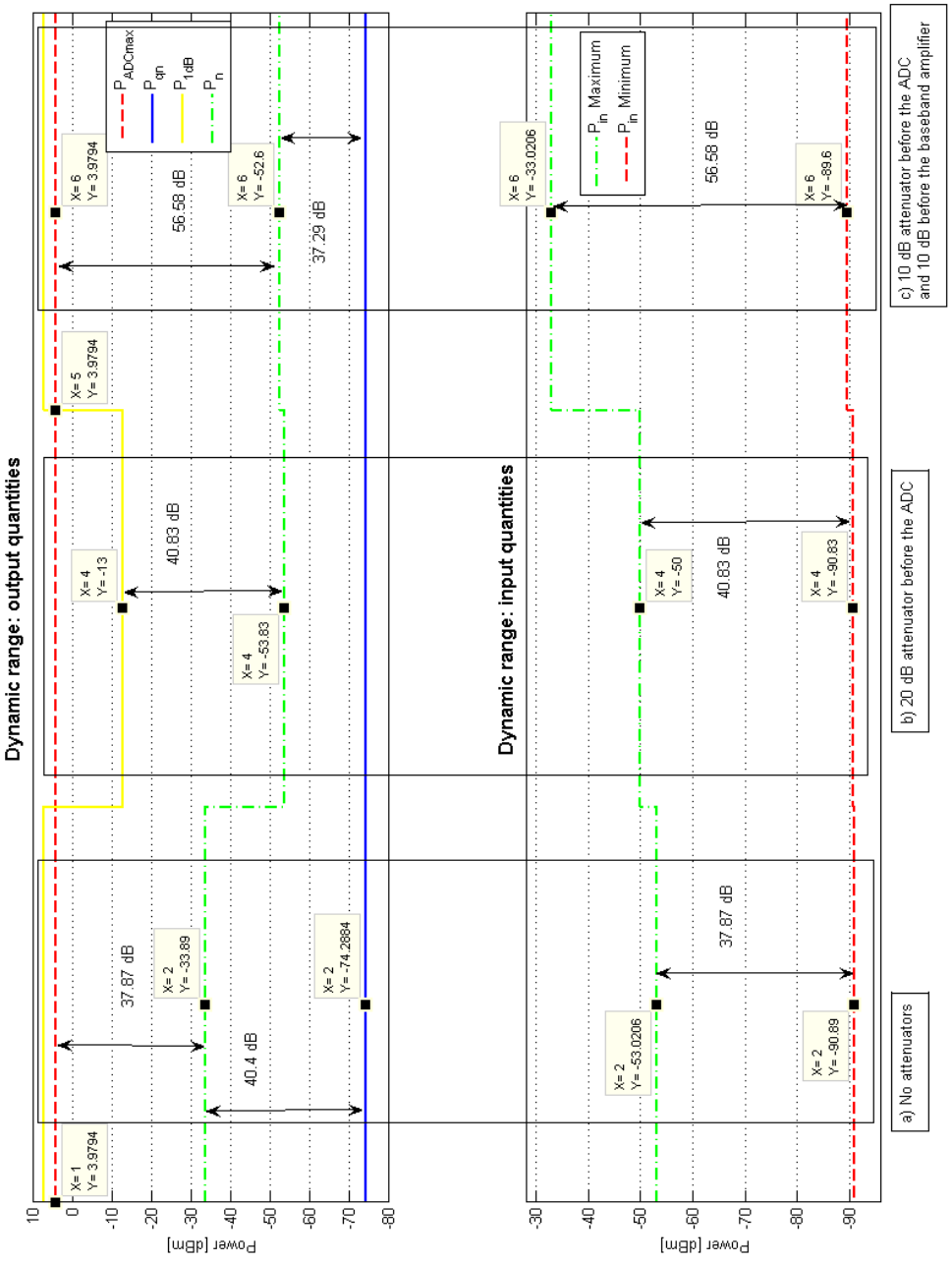

Figure 3.7: Effect of attenuators on the dynamic range of the receiver, using different attenuators

at $f = 30$ MHz by to 35.4 dB at $f = 50$ MHz. Furthermore, the 1 dB compression point at $f = 30$ MHz was -26 dBm when referred to the input of the amplifier or 7.9 dBm when referred to the output as shown in Fig. 3.8.

To solve both problems (dynamic range and linearity of the received signal), the baseband amplification stage was replaced by Minicircuits ZFL-500. All three amplifiers were characterised in the laboratory using a vector network analyser. The gain was measured up to 60 MHz, Fig. 3.9. The mean gain of amplifiers 1 and 3 was found to be around 22.7 dB and that of amplifier 2 was around (22.5 dB). The gain variation was ± 0.5 dB. In addition the compression characteristics of the amplifiers were measured. For amplifiers 1 and 3 the 1 dB compression point was 5.27 dB and 5 dB for amplifier 2. The improvement in dynamic range is almost 16 dB, when the capture card is set to $1\,V_{p-p}$ or lower voltage levels. At higher voltage settings the improvement is 13.5 dB due to the drop in the receiver 1 dB compression point. The gain and compression properties of the receivers are discussed in Section 3.3.1.4.

3.2.2.2 Out-of-Band Interference

Since the LNAs have a very broad bandwidth, the inter-modulation products of out-of-band signals could end up within the band of the radar. The source of such signals could be local radio stations. To reduce the effect of out-of-band signals a low loss band pass filter (L-Com BPF2400) was installed. The nominal loss of the filter is 0.25 dB. In addition, since the bandpass filter has a pass band 2398 MHz to 2498 MHz, this will reduce the effect of the lower sideband breakthrough.

3.2.3 Increasing the baseline

In the original NetRAD design, the reference clock signal and synchronisation pulses were transmitted from the master node (node 1) to the other nodes. Data communication between the nodes was achieved via wired Ethernet. Mainly due to logistical issues the maximum inter-node separation was set to 50 m and the maximum achievable baseline was on the order of 100 m. In this section only changes related to the hardware are discussed, software modifications are discussed in Section 3.2.4. To remove all cables 5 GHz microwave links were used for data communication and GPS disciplined oscillators (GPSDOs) were used to provide a coherent clock reference and to synchronise the nodes in time. A functional block diagram of the synchronisation and data communication is shown in Fig. 3.10.

Several options are available to synchronise the carrier frequency of the nodes, [125]. The original system used cables which limited the maximum baselines. In the new system GPSDO were used. The integration of the GPSDO was a major achievement as it removed the baseline limitations which allowed NetRAD to be used at arbitrary bistatic and multistatic geometries. In this implementation the GPSDO was not used just to provide a coherent carrier but also to synchronise the nodes in time. Integrating the GPSDOs with NetRAD was a major undertaking not the least because of the geographical separation between UCL where NetRAD is being developed and University of Cape Town where the GPSDOs were

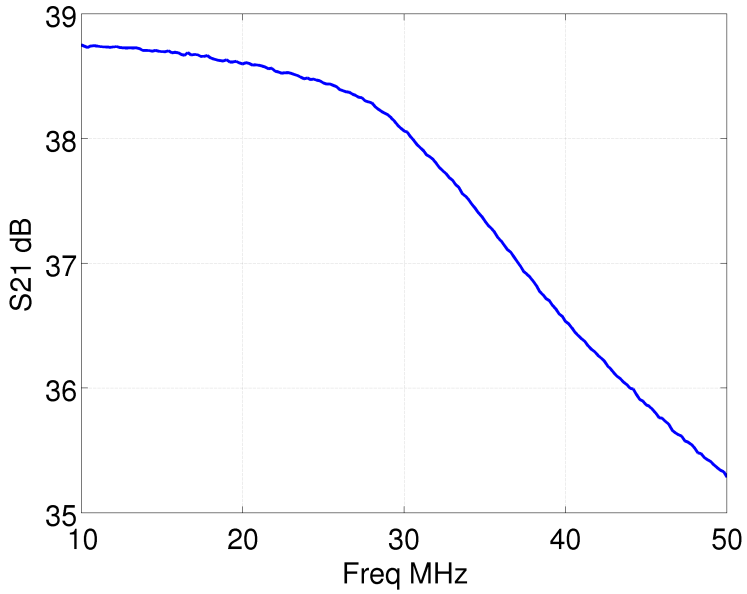

(a) Effect of frequency on baseband amplifier gain

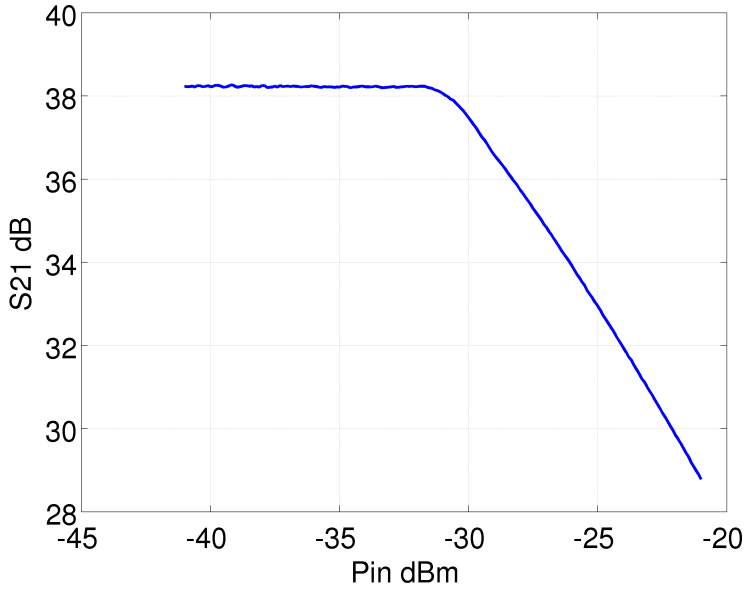

(b) Effect of increasing input power on baseband amplifier gain

Figure 3.8: Original baseband amplifier characteristics.

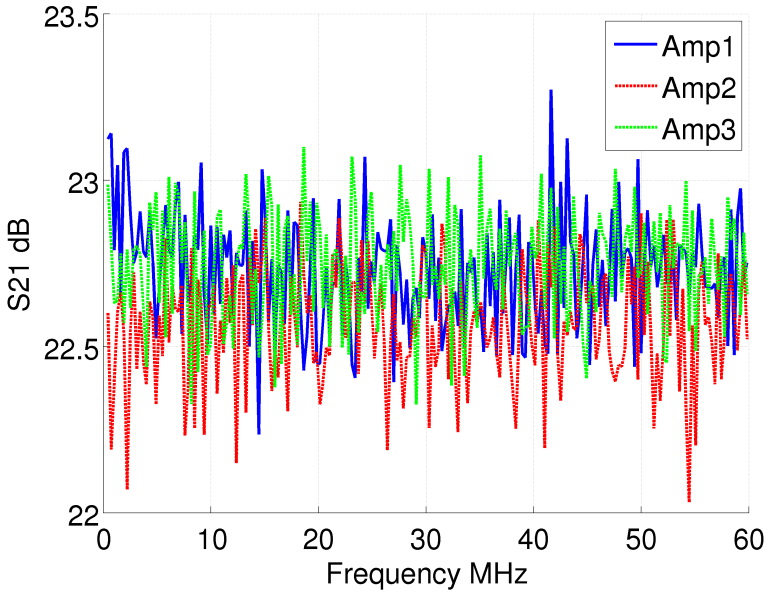

(a) Baseband amplifier gain vs. frequency.

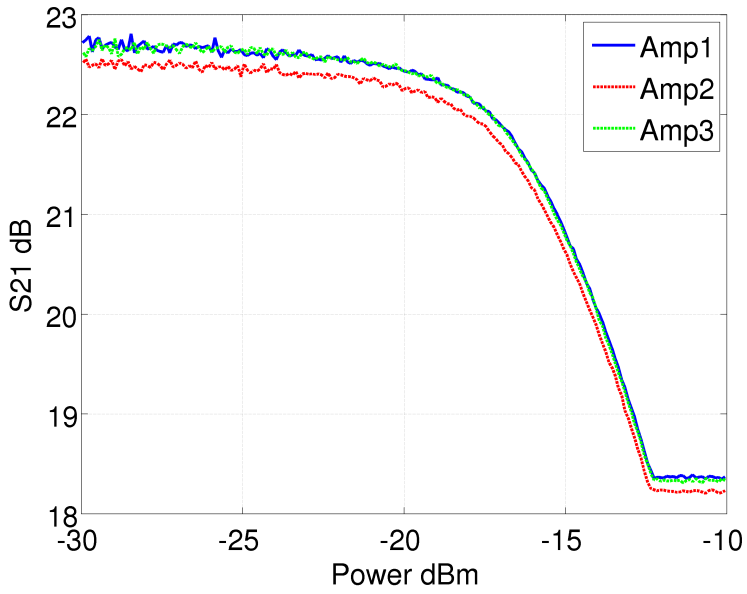

(b) Effect of increasing input power on baseband amplifier gain

Figure 3.9: Baseband amplifier characteristics.

being developed. To overcome this problem two visits from UCT to UCL were made to test the inter-operability of the two systems. Many firmware and software rewrites were necessary during these visit as it is impossible to completely test the system without physically connecting the GPSDOs to the nodes.

According to [125], the oscillator stability is given by:

$$\delta f = \frac{\Delta\phi}{2\pi f T_{int}} \tag{3.1}$$

where $\Delta\phi$ is the phase stability over the integration time (T_{int}). For bistatic radars $\Delta\phi$ can be relaxed to $\pi/2$ rad [125], to be able to get good coherent data $\Delta\phi = 10°$, $T_{int} = 10$ s and $f = 2.4$ GHz were assumed; the required frequency stability is 1 156e-12 which is well within the capabilities of temperature controlled oscillators. However, the free oscillators could not be used as they would not have been able to provide the necessary time reference. Hence it was necessary to use the GPSDOs to provide the required time reference for the start of the experiment.

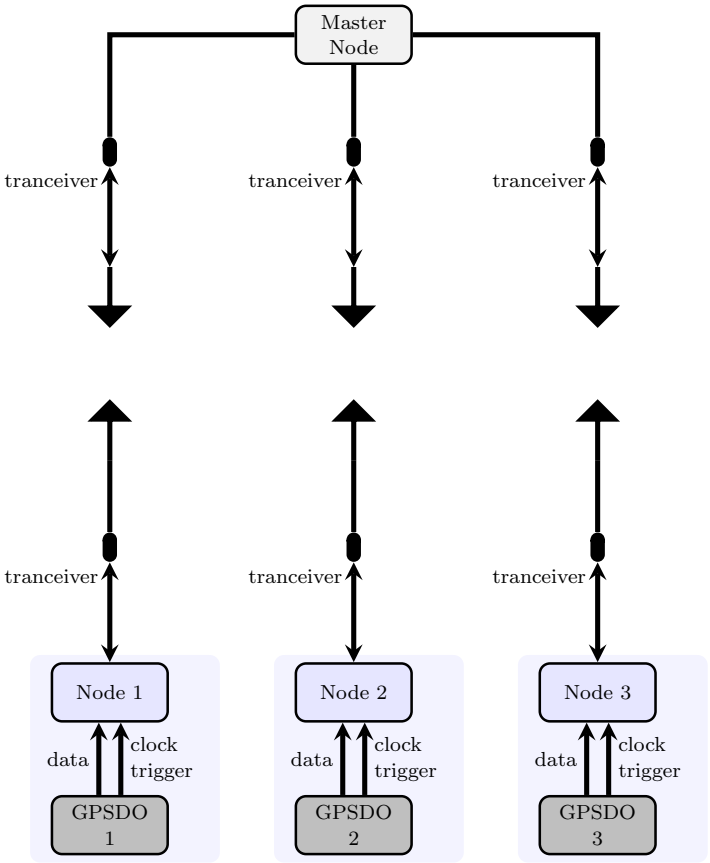

Figure 3.10: Communication and synchronisation in the current version of NetRAD.

3.2.3.1 Integrating the GPSDOs

The GPSDOs were developed at the University of Cape Town (UCT). A more detailed account of the architecture of the GPSDOs can be found at [126]. The integration and testing of the complete system, NetRAD + GPSDO, was carried out mainly by the author and J.S. Sandenbergh from UCT. Any work that was not carried out by the author will be clearly highlighted. Only a brief description of the GPSDO units will be presented in this section, parts of this section were taken from [126, 127].

A GPSDO provides a suitable means to synchronise the carrier in NetRAD. GPS time is traceable to that of a Rubidium atomic source. However, the long-term stable GPS time mark exhibits a large amount of short term phase jitter. This phase jitter can be reduced by phase-locking to a stable oscillator. In this design, Fig. 3.11, the 1 Hz GPS signal is locked to a 10 MHz ultra low phase noise ovenised oscillator (OCXO)[7]. Analogue multiplication is used to produce the 100 MHz for the radar. The phase error is then fed into a 2nd order infinite repose (IIR) filter that drives a DAC which controls the 10 MHz OCXO.

As can be seen in Fig. 3.11, the GPSDO communicates with the host PC using two serial ports, one for the GPSDO and the other for the GPS. The GPSDO is fully controlled from the GUI in NetRAD. An alarm clock style trigger was implemented. The user would enter the time for the start of the next experiment. Then, relying on the carrier being precisely synchronized to GPS, a trigger pulse is generated. This pulse is sent to NetRAD using LVDS causing the radar to start.

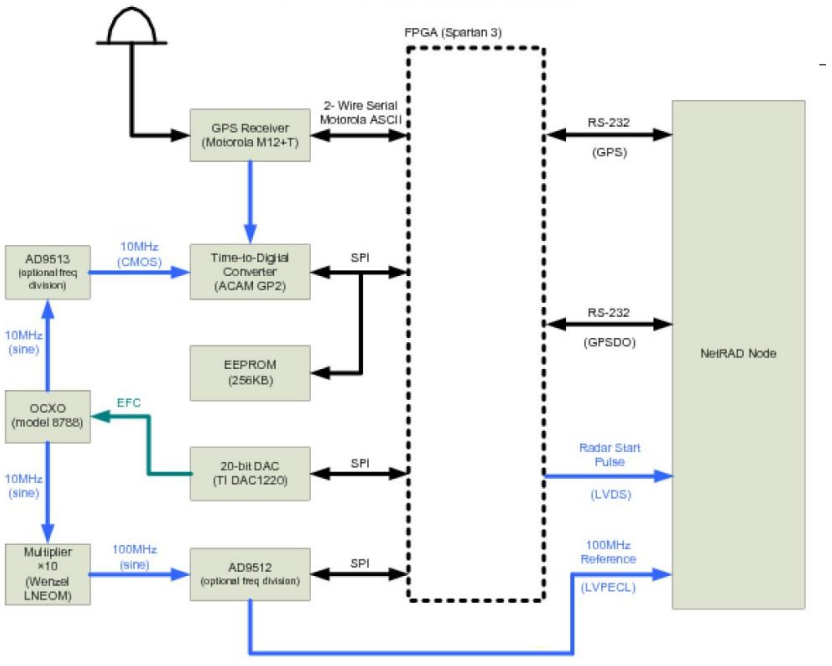

Figure 3.11: A functional block diagram of UCT GPSDO, block diagram courtesy of J.S. Sandenberg.

[7] Oscilloquartz 8788 OCXO was used

3.2.3.2 Wireless Network

The data network was mainly used for sending commands to the nodes and remote desktop access between the three nodes, thus the bit rate was relatively small. The main criteria for selecting the wireless network were the ease of integration with the current system and that it would not cause interference. The wired Ethernet network was replaced by pairs of 5 GHz WiFi links (Fig. 3.10). Standard 2.4 GHz WiFi links cannot be used because they would cause in-band interference. Ubiquiti networks 'bullet5' were used. Figure 3.12 shows a typical deployment. A bullet was connected to the Ethernet port of the host PC using an RJ-45 cable, the same cable is used to power the bullet using power over Ethernet. The bullet modulated and transmitted the data as an 802.11a data packets. The carrier frequency can be set 5.475 GHz to 5.825 GHz. In addition both the bandwidth and the bit rate can be changed. The maximum average transmitted power is about 20 dBm.

In the field experiments each slave node – master node pair made up a single network. The RF output of the bullets was connected to 20 dBi flat patch antennas (L-Com HG5158-23P). The bullets were powered using power over Ethernet (PoE). The power was provided from the nodes, or using AC-DC adapters when available.

Figure 3.12: A bullet connected to a flat- plate antenna, also visible in the photo is the GPS antenna. The red UTP cable was used to for both data and power. This photo was taken during the elevation separation experiments, the antenna was pointing downward towards the bistatic node.

3.2.4 Software Modification

The NetRAD system can be fully controlled by using bespoke user interface (UI) which was written in Microsoft C#. All the user controllable radar parameters are entered via this user interface, see Fig. 3.13. The UI controls both the FPGA and the capture card. The original NetRAD code was written by Doughty

[121]. It was extremely difficult to find bugs in the code since it is multi-threaded. Thus standard debugging tool provided with Microsoft Visual Studio cannot detection these bugs and some of the bugs are difficult to reproduce. Several bug fixed and modifications were made to this code by the author, these modification can be summarised as follows:

- The ability to store the current configuration as XML files which could be loaded when needed.
- The capability to selectively export pulses and samples.
- A tool to report the average power in any sequential combination of pulses and samples.
- The ability to check for saturated pulses and samples.
- The facility to adjust the dc-offset via the software was added.
- Added the required interface in the software to control the GPSDO and log the output messages of the GPSDO and the GPS units.
- Experimental versions of the software were written to support experimental triggering paradigms such as triggering NetRAD using network time protocol (NTP) and using the voltage level at the input of ADC. The latter was integrated in the main software.

In the original NetRAD system, a client-server architecture was used. Node 1 was arbitrarily set as the server (master) node, while the other two nodes were the slave nodes. After starting up the NetRAD software the slave nodes try to connect to the sever node. When the connection succeeded a tab corresponding to that particular slave node was created on the server node interface. It was populated with the default parameters. Any subsequent modifications to these parameters could be only performed from the server node.

In the new design the same client server paradigm was still used. However, it was desired to be able to control all the nodes remotely thus the master node could be any windows based PC with access to the NetRAD network, a screen shoot of the master node user interface is shown in Fig. 3.14. A separate interface was created for the master node and the slave nodes. Sections of the data communication code for the master and slave was implement by G. Inggs at UCT, most of the underlying code relating to the control of the hardware itself was taken from the current UCL code. Upon testing and using the code in the laboratory and in field trials several bugs were fixed.

Furthermore, it was desired to control the GPSDO and the GPS from the same program. The original code was written by Gordon Inggs at UCT. However, since the code could only be tested with both the node and GPSDO fully or partially operational, this part of the code could not be tested properly at UCT. The code was almost completely rewritten by the author.

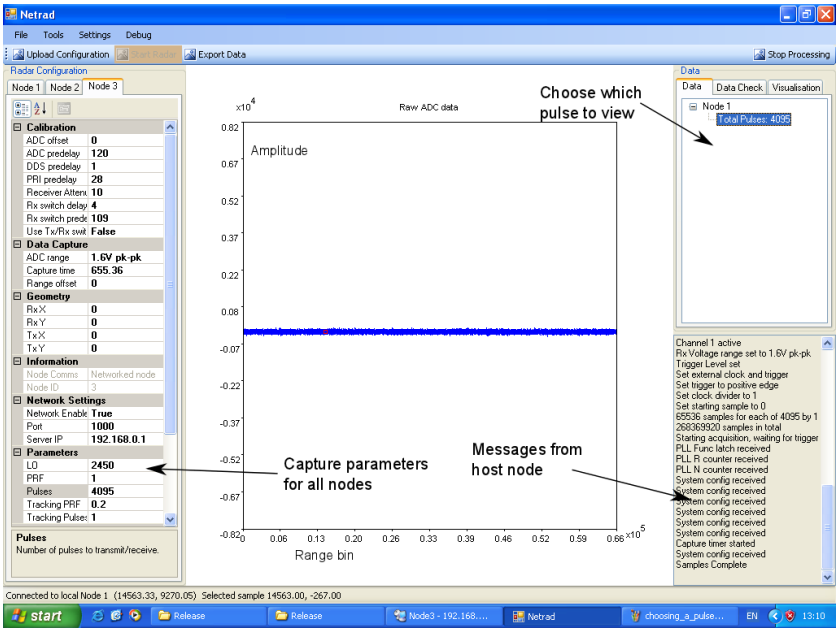

(a) Viewing a noise capture

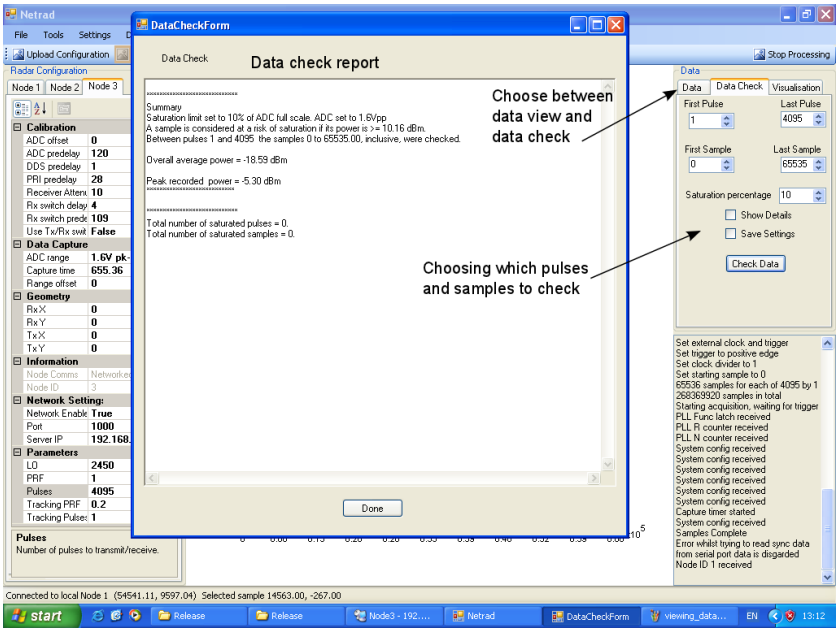

(b) Data integrity report

Figure 3.13: Original user interface

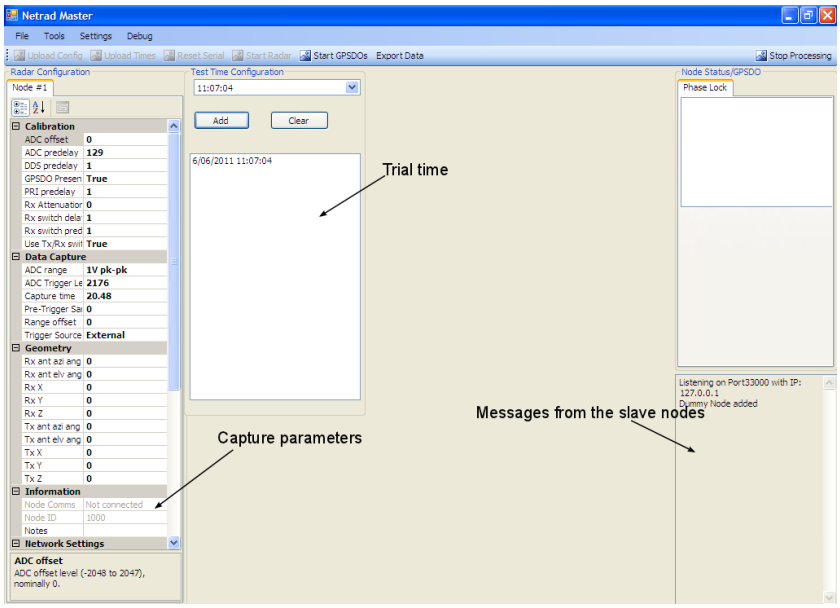

Figure 3.14: New user interface for the master node.

3.2.5 Antennas and Antenna alignment

Although the original antennas provided sufficient gain (24 dBi) and beamwidth ($10° \times 10°$), they were not very rigid, the sub-reflector was prone to breaking and the mesh making up the parabolic reflector was easily deformed during transportation, which made them unsuitable for repeated field trials. Other options were therefore explored. Eventually Poynting K-GRID-003-05 grid antennas were identified as suitable for field testing of the system. A gain of around 24 dBi and 3 dB beamwidth of around $10°$ provided enough power to be able to measure returns at monostatic ranges on the order of 3 km while maintaining a cross range resolution on the order of 100 m to 200 m. A much higher gain antenna would have been too bulky to handle and would have a much smaller cross range resolution which could change the clutter statistics. On the other hand, a smaller antenna would have a lower gain which would have reduced the maximum range.

The mounting brackets supplied with the antennas were modified so that it could be attached to the azimuth positioner, by means of a beam made from angle aluminium, with suitable counterweigth, to allow for smooth azimuth rotation. The azimuth positioner (Newport M-RS65) is fitted with a scale measured in two degree intervals and a vernier measured in $0.2°$. A close up of the azimuth scale is shown close up in Fig. 3.16. An isotropic view of the antenna mounts is shown in Fig. 3.15. In addition each antenna mount was fitted with an optical telescope (Hawke KH3005). The mounting arrangement is shown in Fig. 3.17. The half-moon slot limits the elevation positioning to about $25°$ in elevation and depression. The telescopes were fixed in position via screws. The screws are loosened during calibration, the alignment of the optical and electromagnetic boresights is discussed in Section 3.3.1.2. The elevation angle was measured using an electronic inclinometer (DigiPas DL 80G) which is specified to have an

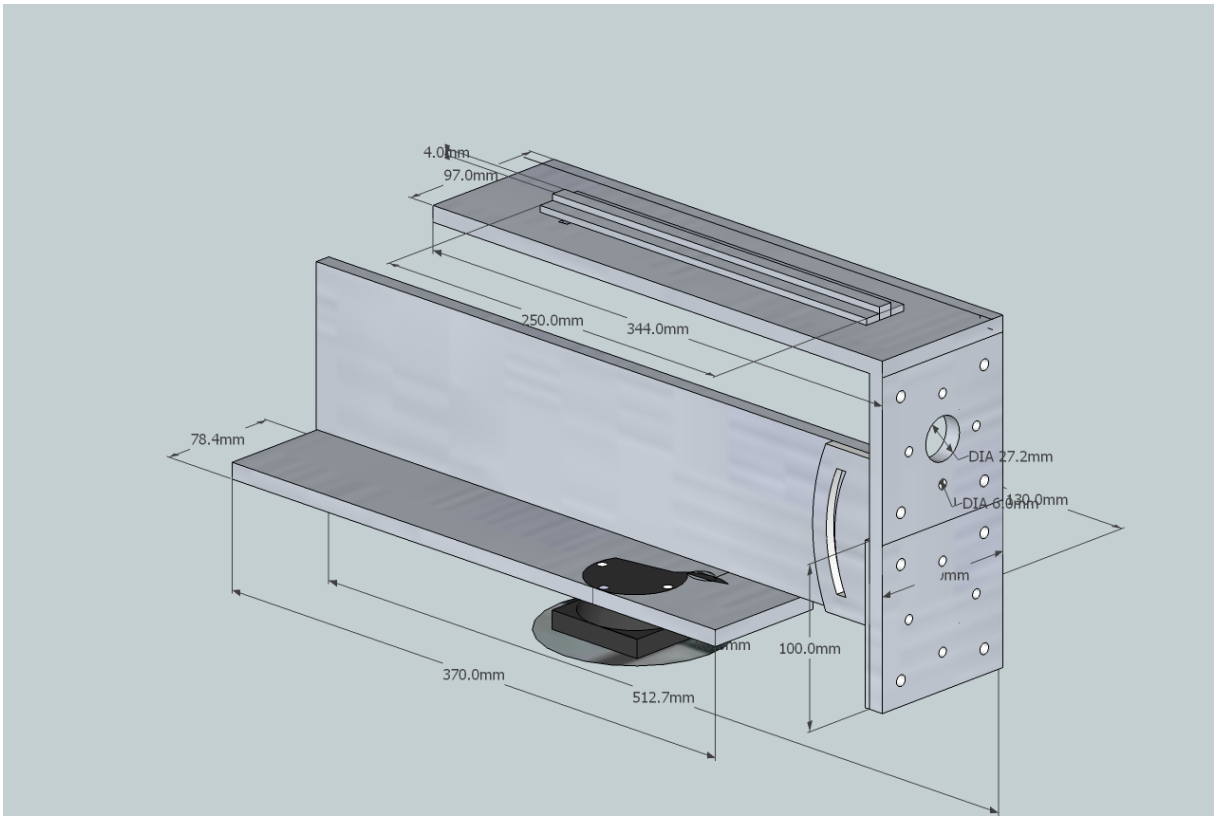

Figure 3.15: Isotropic view of an antenna mount.

Figure 3.16: Close up of the azimuth rotation stage, showing the scale and the vernier.

Figure 3.17: Antenna positioner on top of pedestal. In the picture the antenna was set to vertical polarisation. The electronic inclinometer is placed on base of the L-bracket, when used to measure the elevation angle it is placed next to the optical telescope. The telescope is secured on the upper L-bracket. The azimuth positioner with its scale is between the tripod and the L-bracket. To the left is the counterweight, and to the right, the elevation setting clamp (a knurled knob, acting through a half-moon shaped slot) on the right, are four bolts that hold the antennas/telescope bracket. Unbolting here and swinging the dish and the probe by $90°$ changes the polarisation to the other orthogonal polarisation. Note also the counter weight.

accuracy of $0.1°$. When aligning the antenna in elevation the inclinometer is placed next to the telescope. The polarisation can be changed by swinging the antenna by $90°$, as described in the caption of Fig. 3.17.

3.3 Radar Calibration and Testing

Radar calibration allows the systematic errors in the radar measurements to be determined. Since some of the main components in NetRAD had been changed it was necessary to recalibrate the system and verify the assumed improvements and characterise the system. Furthermore, it was essential at this stage to check the performance of the complete integrated system (NetRAD+GPSDO) and the operation of the microwave links. In this section calibration performed at UCL are discussed. Some of calibration tests were repeated particularly those related to aligning the telescopes and the antennas, and the transmitter and receiver subsystems were repeated at UCT, and these results are discussed in Section 4.2.5.2. Radars can be calibrated by:

- System Calibration: Measuring the transfer function of the transmitter and receiver under controlled conditions.

- Absolute Calibration: Measuring the received power scattered from a target with a known RCS in a controlled environment. In this method the received power can be related to directly to the target

RCS.

3.3.1 System Testing and Calibration

To fully characterise the system it is necessary to make sure that each constituent part operates as expected. Prior to characterising the system itself, the operation and characteristics of the accessories used in the calibration and testing were checked. During this stage of the development the transmitters, receivers and antennas were calibrated under controlled conditions, and the transmitted signal was measured and analysed. The effect of the receiver non-linearity was also investigated.

3.3.1.1 Antenna Calibration

As mentioned in Section 3.2.5 the original antennas were not robust enough for field work. Several options were considered for upgrading these. After some investigation the antennas are supplied by Poynting, South Africa (model K-GD-03-08), were selected. The performance specifications for these antennas are available from the manufacture's webiste[8], it is worth noting that the gain has been revised in the current datasheet as discussed in the next paragraph.

The antennas were tested in the UCL near field anechoic chamber. To be able to measure the gain of the antennas reliably it is necessary to first characterise the chamber. This was achieved by measuring the gain of a calibrated wideband horn antenna (ETS-Lindgren model 3115 S/N 00094766). The reference calibration data was provided by Queen Mary University. The measurement was repeated twice on two different days with the difference being around 0.3 dB, see Table 3.3 for more details.

In total five antennas were characterised, one for each receiver, one for the transmitter and a spare antenna. Because of the size and weight of the antennas special attachment had to be made to attach the antennas correctly to the pedestal in the near field chamber. One antenna was completely disassembled and then its radiation pattern and gain were remeasured. All antennas had similar gain and radiation pattern as can be seen in Fig. 3.18 and Table 3.4. The average gain of the antennas was 23.76 dBi; whereas the maximum gain quoted in the original datasheet is 27 dBi, the gain has been revised in the new data sheet to 23.5 dBi–25 dBi for frequencies between 2.3 GHz–2.9 GHz which agrees with the measurement results. The E-field and H-field 3 dB beamwidths were $11°$ and $9°$ respectively, which is consistent with the datasheet. The measured results are more plausible. The gain of an aperture is given by [128]:

$$G_{ap} = \frac{4\pi A\eta}{\lambda^2}$$

where A is the aperture area and η is the aperture efficiency. The antennas are $0.7\,\text{m} \times 0.9\,\text{m}$, hence assuming ideal aperture and a frequency of 2.42 GHz $G_{ap} = 27.12$ dBi. However, practical antennas have lower gain due to several loss factors such as spillover loss and illumination efficiency. Furthermore,

[8] `http://www.poyntingdirect.co.za/UserFiles/File/K-GD-03-08_BROC%20V5.0.pdf` last accessed 07/06/11.

since the reflector is mesh grid rather than a solid dish there will be small losses due to surface leakage [128]. A good approximation for practical antennas can be found in [129]:

$$G_{ap} = \frac{30000}{\theta_{3dB}\phi_{3dB}}$$

where θ_{3dB} and ϕ_{3dB} are the 3 dB elevation and azimuth beamwidths in degrees. For these antennas the computed gain is 24.8 dB.

Freq GHz	Ref gain dBi	Meas. #1 dBi	Meas. #2 dBi	ΔG_1dB	ΔG_2dB
2	7.87	8.96	8.9	1.09	1.03
2.05	7.45	8.55	8.4	1.1	0.96
2.1	7.69	8.82	8.8	1.13	1.11
2.15	8.34	9.44	9.5	1.1	1.16
2.2	8.78	10.04	9.9	1.26	1.12
2.25	9.28	10.41	10.4	1.13	1.12
2.3	9.73	10.61	10.5	0.88	0.77
2.35	10	10.74	10.6	0.74	0.6
2.4	10.14	10.85	10.7	0.71	0.56
2.45	10.18	10.83	10.6	0.65	0.42
2.5	10.17	10.93	10.7	0.76	0.53
2.55	10.35	10.99	10.8	0.64	0.45
2.6	9.94	10.94	10.9	0.99	0.96

Table 3.3: Calibration of UCL near field chamber

Node #	Gain dBi		E Bandwidth degree		H Bandwidth degree	
	Mean	Variation	Mean	Variation	Mean	Variation
1	23.7	0	11	0.2	9.1	0.2
1 repeat	23.78	0.1	11.35	0.1	8.85	0.3
2	23.77	0.1	11.27	0.1	8.92	0.2
3	23.8	0	11.3	0.2	8.87	0.3
Spare	23.77	0.1	11.23	0.1	9.07	0.3
Transmitter	23.75	0.2	11.2	0	9	0.2
Average values	23.76	0.10	11.23	0.35	8.97	0.25

Table 3.4: Measured gain and 3 dB beamwidths of NetRAD antennas. The gain and beamwidth were measured 2.4 GHz to 2.45 GHz every 0.1 GHz. Mean and variation are calculated across the measurement band.

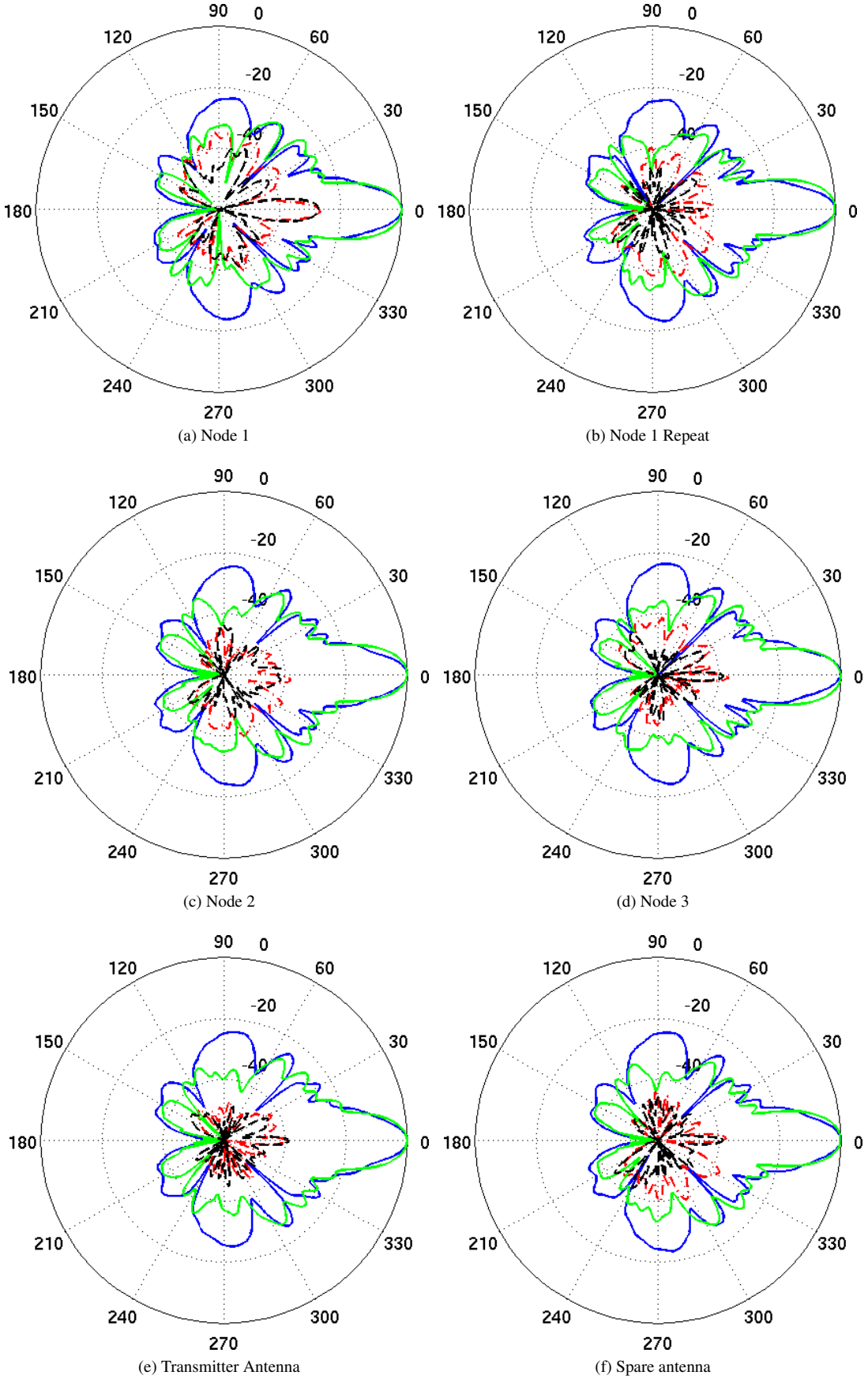

(a) Node 1

(b) Node 1 Repeat

(c) Node 2

(d) Node 3

(e) Transmitter Antenna

(f) Spare antenna

Figure 3.18: Measured normalised radiation pattern of NetRAD antennas at 2.42 GHz (Co-polarised E-field: solid green line, Co-polarised H-field: solid blue line, Cross-polarised E-field: dashed black line, Cross-polarised H-field: dashed red line).

3.3.1.2 Boresight Alignment

As discussed in Section 3.2.5 optical telescopes were mounted on the antenna mounts to aid in aligning the antennas. To be able to use the optical telescope to align the antennas the optical boresight was aligned with the electromagnetic boresight by placing a broad beam source in the far field of the antenna in clear view of the antenna and then finding the -10 dB points on either side of the peak and noting down the angles the angle that corresponds to the centre of the beam is equal to mean value of these two angles. The following procedure was used:

1. The calibration sight was surveyed for electromagnetic interference and suitable frequency in the 2.4 GHz to 2.45 GHz was chosen.
2. The broad band source was a 30° beamwidth antenna placed at the 11th floor of the Engineering building at UCL. The antenna under test (AUT) was placed on the roof an adjacent building with a clear line of sight from the AUT. The distance between the two sites was around 170 m.
3. Prior to starting the measurements the AUT area was surveyed for RF interference. The source frequency was set to 2.42 GHz, as it is at the centre of the band and was clear of interference. A bandpass filter was used to reduce the effect of out-of-band interference.
4. The output of the AUT was connected to a spectrum network analyser centred around the test frequency.
5. The antenna was rotated in azimuth and the peak power was noted.
6. The antenna was then rotated in the anti-clockwise direction until the power was 10 dB below the peak, the corresponding angle was read of the rotation stage.
7. The antenna was rotated in the clockwise direction and (6) was repeated.
8. The antenna was fixed in azimuth.
9. Steps 6 to 8 were repeated to find the peak in the elevation plane; except that the antenna was moved upwards and downwards.
10. The screws holding the telescope to the mount were now loosened and the cross-hair was aligned with the small antenna in the Roberts Building.
11. The telescope was fixed in place. The telescope, antenna and mounting brackets are marked as belonging to a particular node.
12. The alignment was checked by pointing the AUT towards the source antenna, the power level was checked to confirm that the peak was found. It was then rotated to check that the offset angles were equal to those obtained in the previous steps; the same power levels were recorded in all cases.

13. The same procedure is repeated for all antennas.

It should be noted that after sequentially transporting the nodes to Peacehaven[9] for field trials, the alignment in the azimuth plane was checked, and the error was found to be around $\pm 0.5^{\circ}$. Because of the height of the antennas alignment in the elevation plane could not be completely checked. These results showed that the mounting was robust enough to withstand the transportation of the system between locations without affecting the calibration.

3.3.1.3 Transmitter Calibration

The transmitter subsystem was described in Section 3.2.1. To calibrate the high power amplifiers it is necessary to use a carefully calibrated input source. Since the amplifiers response to the transmitted chirp is more important than the response at discrete frequencies, the transmitting node was used as an input. However, its output must be

An average power meter was used to measure the output power. Thus to increase the accuracy of the measurement the duty cycle was increased, such that the measured power is at least 20 dB above the noise floor of the power meter. It was found that the node 3 output power was not a function of the pulse length but was affected by pulse bandwidth. Increasing the bandwidth from 20 MHz to 45 MHz caused a drop in the measured power of around 0.78 dB. This is to be expected since the DDS is operating close to Nyquist. For all practical experiments and further calibrations a bandwidth of 45 MHz was used unless specified otherwise. Furthermore, the effects of out of band signals was removed by using a DC block and a bandpass filter identical to that used in the receiver. The results are summarised in Table 3.5. The peak power in the pulse was computed by using:

$$P_{pulse} = P_{meas} - 10\log_{10}(\tau * PRF) \tag{3.2}$$

where P_{pulse} is the average power in the transmitted pulse, P_{meas} is the measured power using the power meter, τ is the pulse length and PRF is the pulse repetition frequency.

BW, MHz	PL, µs	PRF, kHz	Measured mean power	Mean power in pulse
20	1	20	-3.73	13.26
20	2	20	-.73	13.25
20	5	20	3.25	13.25
45	1	20	-4.49	12.50
45	2	20	-1.52	12.46
45	5	20	2.45	12.45

Table 3.5: Summary of the measurement of node 3 low power output, where BW bandwidth, PL is the pulse length and PRF is the pulse repetition frequency. The measured values are corrected for filter and dc-block losses.

[9]Peacehaven is test site owned by Thales UK on the South Cost of England which was made available to UCL.

The setup used in calibrating the HPAs is shown in Fig. 3.19. Prior to calibrating the high power amplifiers the output power from node 3 was measured prior to starting the experiment and the end of the calibration the repeatability of the measurement was $0.2\,\text{dB}$.

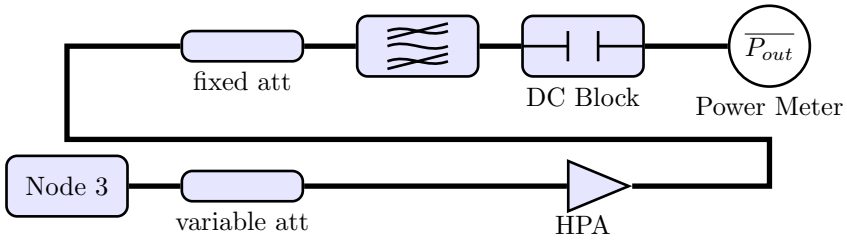

Figure 3.19: Block diagram illustrating the method used to determine $1\,\text{dB}$ compression point and the output power of the HPA.

The output power of the node was held at 100% and the input power to the HPA was varied by using a calibrated stepped attenuator. The measurements were repeated at UCT and reproduced within $\pm 0.14\,\text{dB}$, and these results are discussed in Section 4.2.5.2. The gain calibration for the main HPA is shown in Fig. 3.20. From Table 3.5 the output power of node 3 is $12.47\,\text{dBm}$, and from Fig. 3.20 it is convenient to operate the HPA when the input power is around $-1\,\text{dBm}$. Taking into account that the cable connecting the node to the HPA has a loss of $2\,\text{dB}$ adding attenuation of $12\,\text{dB}$ will reduce the input power at the input of the HPA to $-1.5\,\text{dBm}$, hence the output power is $57.1\,\text{dBm}$. As can be seen from the Fig. 3.20 the output power is fairly insensitive in this region and a variation of $\pm 2\,\text{dB}$ will only cause a change less than $\mp 0.5\,\text{dB}$. Similar plots were produced for the secondary amplifier. It was found that attenuating the input by output of node 3 $4\,\text{dB}$ to $2\,\text{dB}$ gives an output power $52.72\,\text{dBm}$ to $52.73\,\text{dBm}$. The cable connecting the transmitting node the HPA provides the required $2\,\text{dB}$ attention. Thus no extra attenuators are required to operate the $200\,\text{W}$ amplifier.

3.3.1.4 Receiver Gain and Compression Properties

The receiver system block diagram is shown in Fig. 3.5. All three nodes were characterised. The radar was set to transmit from node 3 in the low power mode. A stepped attenuator was used to vary input power to the node, a DC block was used at the output of the transmitter. A bandpass filter was placed at the input of the node. A block diagram of the measurement setup is shown in Fig. 3.21 The output power of the node was measured using NetRAD, with ADC set to $1\,\text{V}_{\text{p–p}}$ and the power meter. NetRAD always had a lower reading and the maximum error was $-0.5\,\text{dB}$, (Table 3.6.

In addition, in order to find the $1\,\text{dB}$ compression point of the receiver the input power was varied using the attenuator and the output of the receiver was measured using the power meter. In all cases the receiver $1\,\text{dB}$ compression point corresponded to ADC values larger than $1\,\text{V}_{\text{p–p}}$, Figs. 3.22 to 3.24. It is interesting to note that the gain as reported in Table 3.6 is the same as that shown in these plots.

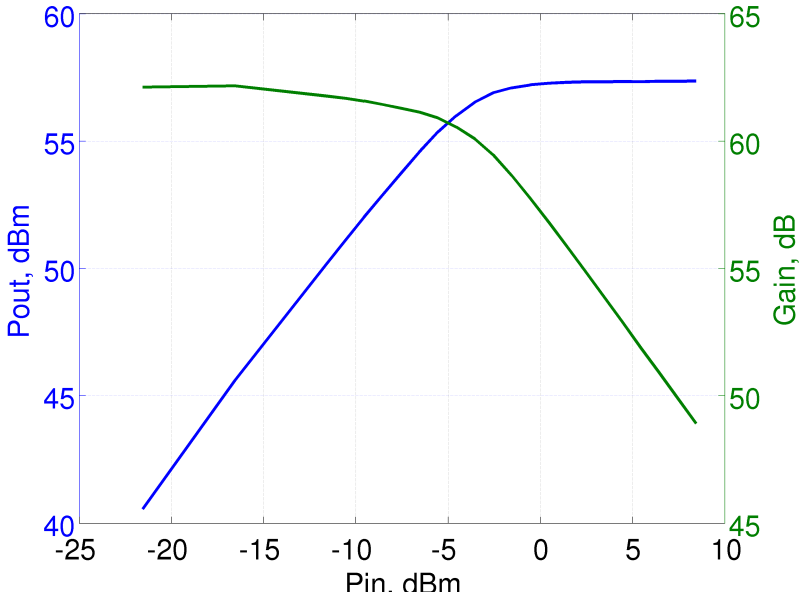

Figure 3.20: Main HPA gain and out power as a function of input power.

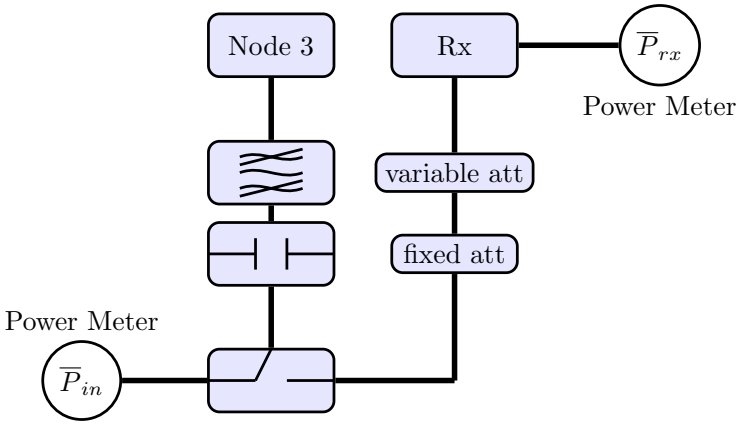

Figure 3.21: A block diagram of the setup used to measure the receiver gain and 1 dB compression point.

Node	Pin	Pout[PM], dBm	Pout[NetRAD], dBm	Difference, dB	Gain dB
1	-40.55	1.44	0.98	-0.46	41.99
2	-40.51	0.54	0.38	-0.16	41.05
3	-40.58	0.7	0.91	-0.06	41.55

Table 3.6: Comparison of the power measured by NetRAD and a calibrated power meter and the receiver gain as measured by the power meter around Pin=-40.5 dBm and pulse bandwidth of 45 MHz

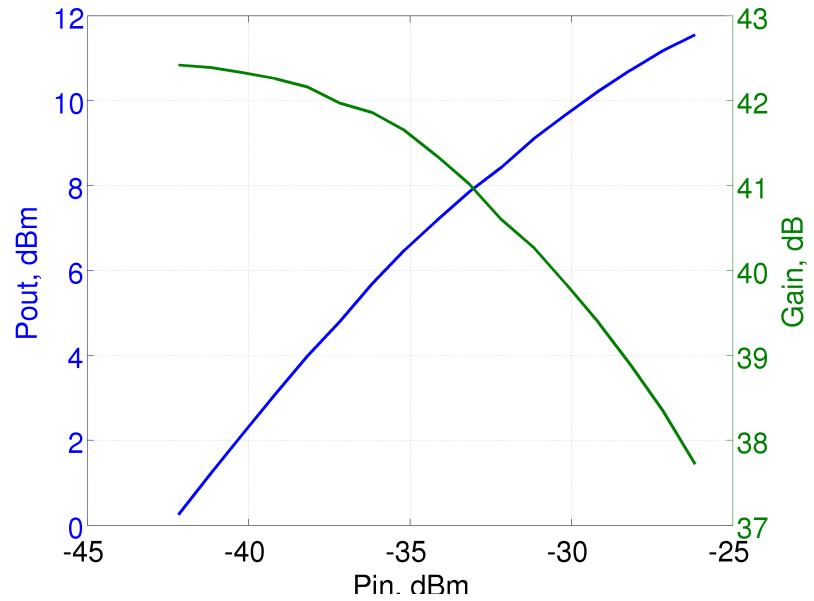

Figure 3.22: Node 1 output power and gain as a function of the input power.

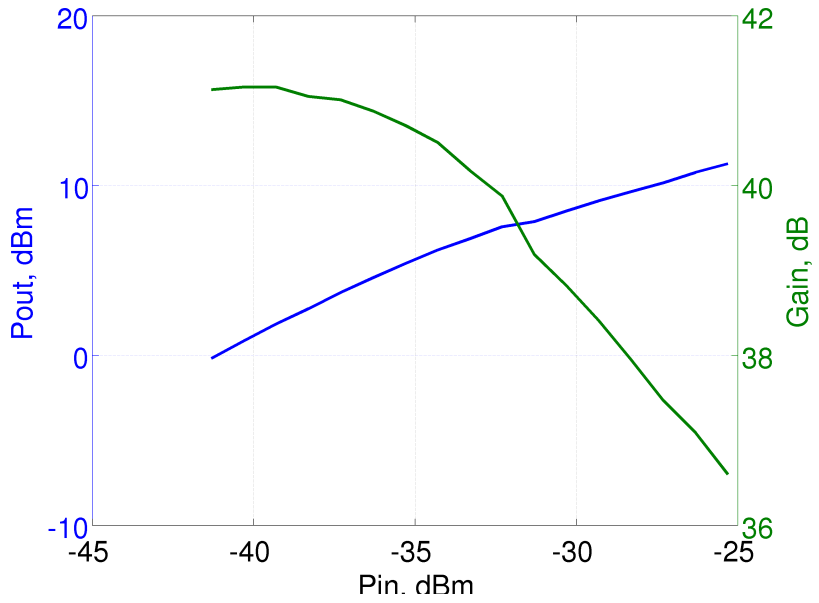

Figure 3.23: Node 2 output power and gain as a function of the input power.

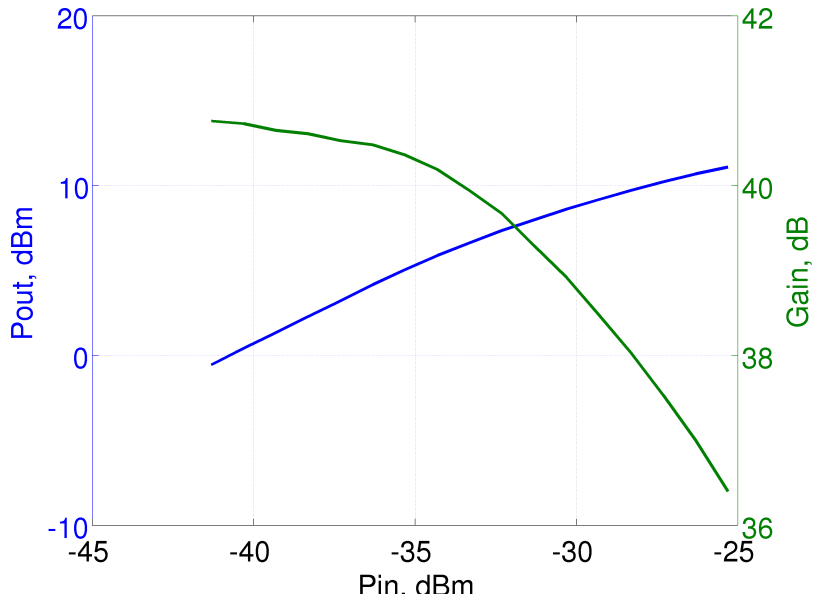

Figure 3.24: Node 3 output power and gain as a function of the input power.

3.3.1.5 Receiver Noise Measurement

Having accurately determined the gain of the nodes. The noise figure of the receiver can now be computed. Since the receiver uses zero IF and the image is not rejected the noise power will be higher than expected. The effects of low frequency noise and the noise power in the lower sideband are included in the noise figure (NF). The results are summarised in Table 3.7. The doubling in the power is due to the use of the decimated Hilbert transform doubled power [130]. It is interesting to note that the noise figure before filtering is significantly higher than that of the original system. This is because the current baseband amplifier did not block the low frequency interference[10].

To reduce the effect of the low frequency noise, the lower and upper 5 MHz were filtered out. This did not have a great effect on the received signal as the transmitted pulse bandwidth is 45 MHz. The spectrum of the raw receiver noise and after Hilbert transformation bandpass filtering is shown in Fig. 3.25, the interference is around 20 dBm in node 1 and 10 dBm in node 3. A summary of the effect of the filtering on all the nodes is presented in Table 3.7.

It can be easily shown that the dynamic range of the radar has increased to around 55 dB when the data is filtered and the capture card set to $1\ V_{p-p}$ compared to only 38.5 dB at the same setting.

3.3.1.6 Effect of the Receiver Switch

As discussed in Section 3.2.1 it was necessary to install a switch in the receiver path to protect the monostatic receiver. The loss due to the switch and the required connectors and cables was around 2.33 dB. In addition to reducing the overall gain of the monostatic node, the switching process introduced transient

[10]This feature allowed the use a small IF frequency to characterise the performance of the GPSDO clocks using dual mixer time delay technique [131].

Node #	Raw ADC data, dBm	Hilbert Transformed, dBm	Bandpass filtered, dBm	NF (raw data), dB	NF (filtered), dB
1	−46.8911	−43.893	−48.3545	8.1044	4.6101
2	−47.3331	−44.3821	−48.9111	8.6024	4.9935
3	−49.606	−46.6195	−48.5585	5.8295	4.8461

Table 3.7: Noise power in NetRAD noise, the use of the decimated Hilbert transform increased the noise power by dB. Removing the first and last MHz improved the performance.

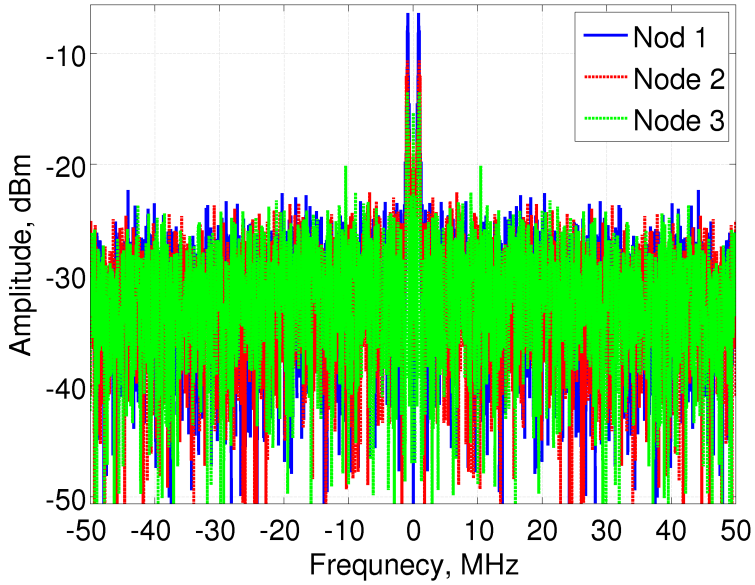

(a) Raw ADC noise.

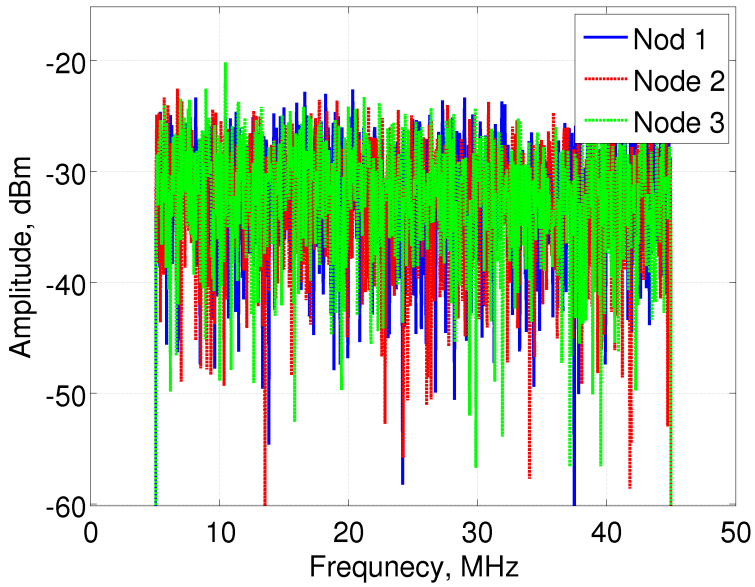

(b) After decimated Hilbert transformation and bandpass filtering filtering.

Figure 3.25: Noise spectrum of NetRAD receivers.

just after the switch changes state. This effect could influence the effective noise level particularly at close ranges. The effect was present regardless of the pulse length used. As can be seen in Fig. 3.26a, the noise level only returns to the normal noise level at around bin 450. Furthermore, this transient was not decorrelated by coherent integration as can be seen in Fig. 3.26b in which 1000 pulses were coherently summed. However, removing the first and last 5 MHz eliminated the problem, when both a single pulse was used and after coherently integrating 1000 pulses as can be seen in Fig. 3.26. This effect was not inherent in the radar as it cannot be seen when the switch was not used, Fig. 3.27.

3.3.1.7 Pulse Fidelity

Due to various effects in the transmitter and receiver chains the generated pulse deviates from the ideal chirp. The aforementioned modifications improved the linearity of the chirp as can be seen in Fig. 3.28. The effect of the various modifications at different pulse lengths is shown in Table 3.8. It is clear that replacing the low power transmit amplifier and the baseband amplifier greatly improved the linearity of the received chirp. This was characterised by measuring the mean to peak ratio of the received chirp. It can be seen from Table 3.8 that replacing the baseband amplifier and the transmit amplifier improved the performance of the system by around 4 dB. Introducing the bandpass filter had little effect on the linearity of the received chirp. Rather than trying to generate a filter to improve the characteristics the received chirp and use an ideal chirp in the matched filter, it was decided to use a copy of the actual chirp for performing the matched filter. A repository of reference pulses have been recorded in the laboratory for all three nodes.

Furthermore, the fidelity of the transmitted signal was evaluated by examining the spectrogram of the transmitted chirp. An example of the spectrogram of a 45 MHz chirp is shown in Fig. 3.29, the duration of the chirp was 5 µs. The chirp was recorded by node 3, the signal was taken from the output of 450 W amplifier. Also clear in the image is a second harmonic component which is 30 dB below the main chirp. Similar results were obtained without the HPA.

Pulse Length	Original System	With new BBA[a]	With new BBA[a] and LTXA[b]	With new BBA,[a] TXA[b] and BPF
1 ms	−9.29 dB	−6.2 dB	−4.63 dB	−4.75 dB
2 ms	−8.78 dB	−6.77 dB	−4.84 dB	−4.92 dB
5 ms	−9.29 dB	−7.3 dB	−5.25 dB	−5.56 dB
10 ms	−9.76 dB	−7.53 dB	−5.5 dB	−5.56 dB

Table 3.8: Comparison between the mean to peak ratios different configurations of the original and the improved NetRAD system.

[a] Baseband amplifier [b] Low power transmit amplifier

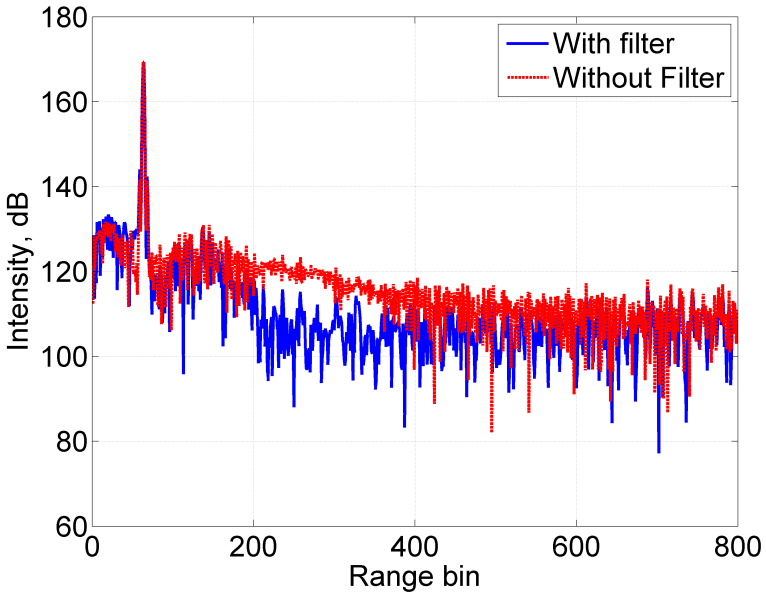

(a) Using a single pulse with the switch active

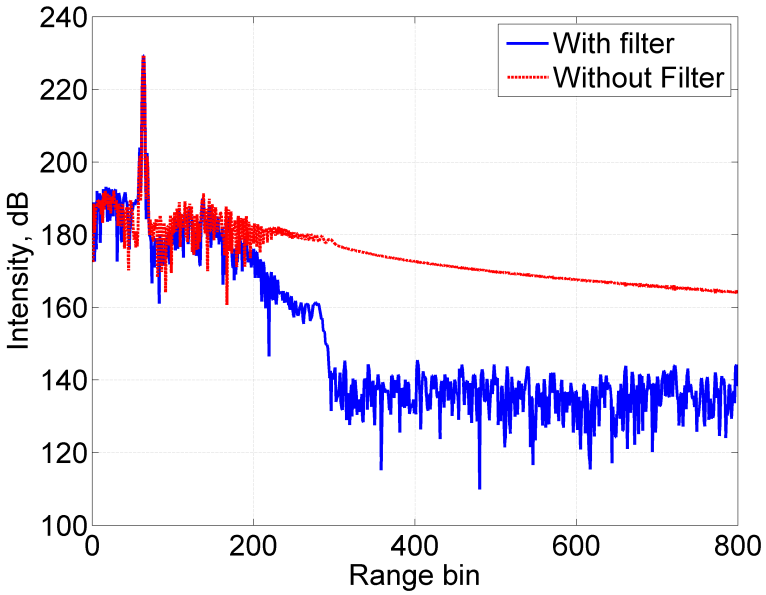

(b) After coherently integrating 1000 pulses with the switch active

Figure 3.26: Effect of removing the first and last 5 MHz on the switch transient. The pulse length was 4 ms and the bandwidth was 45 MHz.

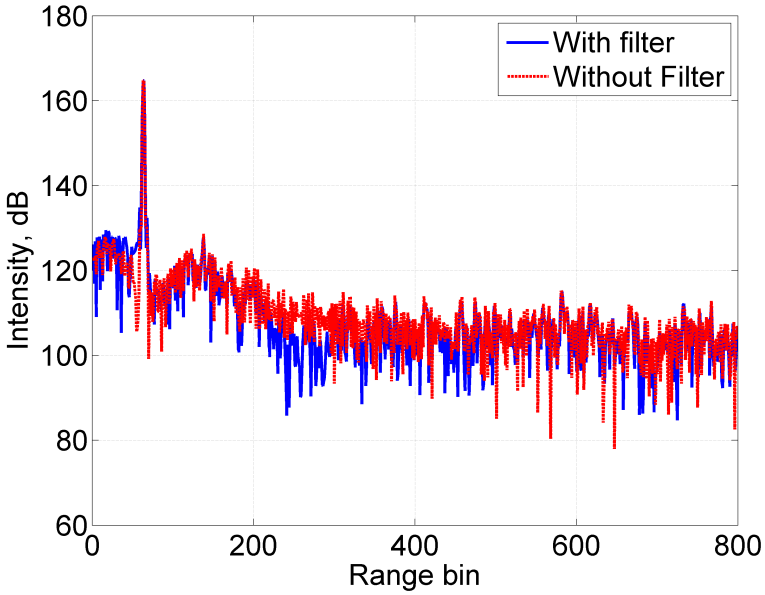

Figure 3.27: Amplitude of received signal in the passive node after match filtering and coherent integration of 1000 pulses. The pulse length was 4 ms and the bandwidth was 45 MHz.

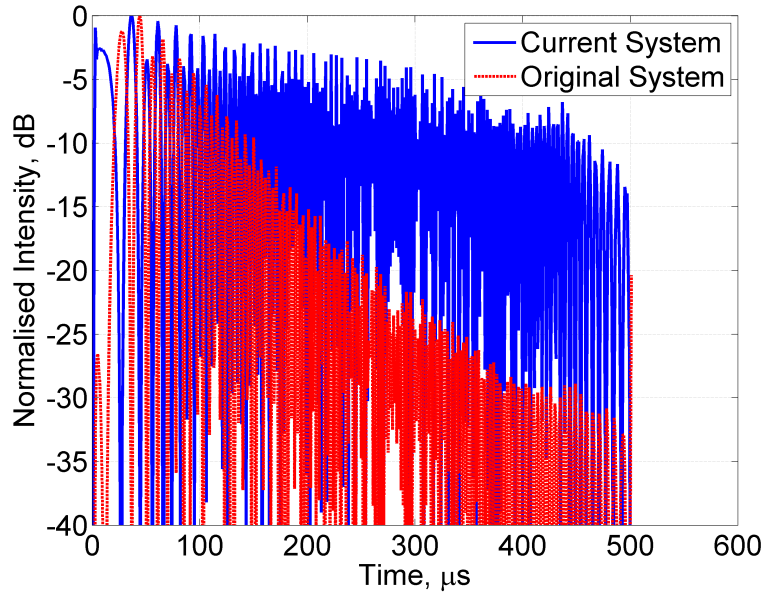

Figure 3.28: Comparison of the normalised intensity of a 5 μs chirp with a bandwidth of 45 MHz in the original and current system.

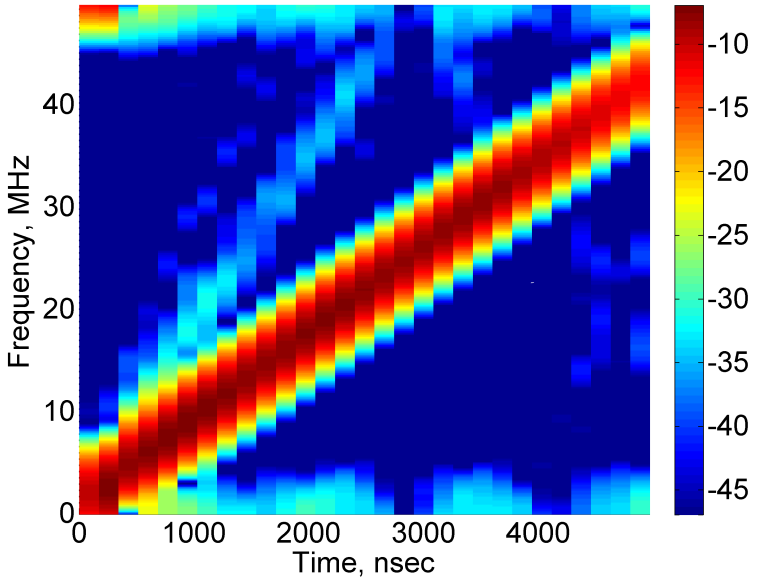

Figure 3.29: Spectrogram of 45 MHz 5 µs linear chirp. Colour scale in dB.

3.3.1.8 Transmitter and receiver stability

Repetitive measurements of the transmitter and the receiver have shown that the system is stable. However, the manner in which the power changes during a typical transmission and during an experiment have not been discussed. To test the stability of output was connected to a three way splitter and then connected to all three receivers. Initially the low power system with the nodes were tested. These results were analysed and the stability of the system was confirmed. Then the high power amplifiers were connected to the output of node three and the stability of the complete system was evaluated. The normalised standard deviation was used to measure the stability of the system. The stability was not found to be a function of the pulse length or the PRF. Example results are shown in Table 3.9.

Node #	Low Power	High Power
1	0.0307	0.0090
2	0.0162	0.0161
3	0.0057	0.0051

Table 3.9: NetRAD receiver gain and transmitted power stability. The normalised standard deviation was used as a measure of NetRAD stability. 130 000 samples were recorded of 5 µs pulses with 45 MHz bandwidth at 1 kHz PRF

3.3.2 Verification

Due to the lack of a fully controlled environment, the response of the system, including the antennas, could not be measured accurately. The system performance was therefore assessed at the UCL open field test site. The main issues with the site are:

1. The presence of land clutter from the surrounding trees, hedges and houses.

2. The ground is not completely flat which would affect the multipath calculations.

A sketch of the geometry used for validation is shown in Fig. 3.30. A short-circuited calibrated dual ridge horn antenna (Satimo model SH800 serial number 188) was used as reference target. To avoid saturating the receivers the output of the HPA was attenuated by 30 dB. A summary of the experimental parameters is shown in Table 3.10. The RCS of a short-circuited antenna of gain G can be approximated by [132]:

$$\sigma = \frac{\lambda^2 G^2}{4\pi} \tag{3.3}$$

Since the gain of the horn antenna is 9.36 dBi, $\sigma = -10.91$ dB m^2. The output of the antenna was short-circuited the loss of the short circuit was taken to be 0.5 dB. The angle between the line-of-sight from nodes 2 and 3, and the boresight of reference antenna was $18.4°$ which means that the effect gain of the horn antenna is reduced by 1 dB. Given the above information and the measured radar parameters provided in the previous sections the received power due to the horn antenna can be estimated. In the experiment 5 separate measurements each consisting of 1024 pulses were processed. The average received power from all 5 measurements is shown in Table 3.11. From these results it is clear that the multipath cannot be ignored. To account for multipath the antenna height was taken to be approximately 1.5 m and the distance to the reference antenna 150 m, as shown in Fig. 3.31 the two-way-propagation gain is approximately 5.57 dB. Furthermore, since the wavelength is of the order of 12 cm small changes in the relative antenna height can have significant effect on the multipath gain as demonstrated in Fig. 3.31. A change of the relative height by ± 0.3 m changes the multipath gain from just more than 2 dB to around 8 dB. Errors in the distance to the reference antenna had a smaller effect on the multipath gain. Hence, these measurements verified that the received power is within the expected limits.

Property	Value	Property	Value
Short circuit loss	1	Reference antenna Gain	9.36
Range to target	150	PRF	1
Polarisation	HH	Pulse length	0.4
Short circuit losses	0.5	Number of Pulses	1024

Table 3.10: Capture parameters for validation test.

3.3.3 Effect of the Clocks

In this section analysis of the effect of the GPSDOs on NetRAD will be discussed, detailed analysis of the GPSDOs themselves will not be carried out as it is outside the scope of this thesis. Some of the preliminary stability analysis of the GPSDO clocks can be found in [131]. The GPSDO clocks were integrated in two stages. During the first stage the clocks were not locked to GPS, however; two GPS

Figure 3.30: A sketch of the geometry used for testing NetRAD at UCL sports ground.

Node #	Calculated Power, dBm		Measured Power, dBm	Error, dB	
	Without multipath	With Multipath		Without multipath	With multipath
1	-6.69	-4.18	-9.75	-3.06	2.52
2	-6.68	-6.17	-7.74	-1.06	0.51
3	-10.98	-7.095	-13.52	-2.54	3.04

Table 3.11: Comparison of calculated and measured from a 9.36 dBi horn antenna 150 m from all the nodes, multipath gain was taken to be 5.57 dB.

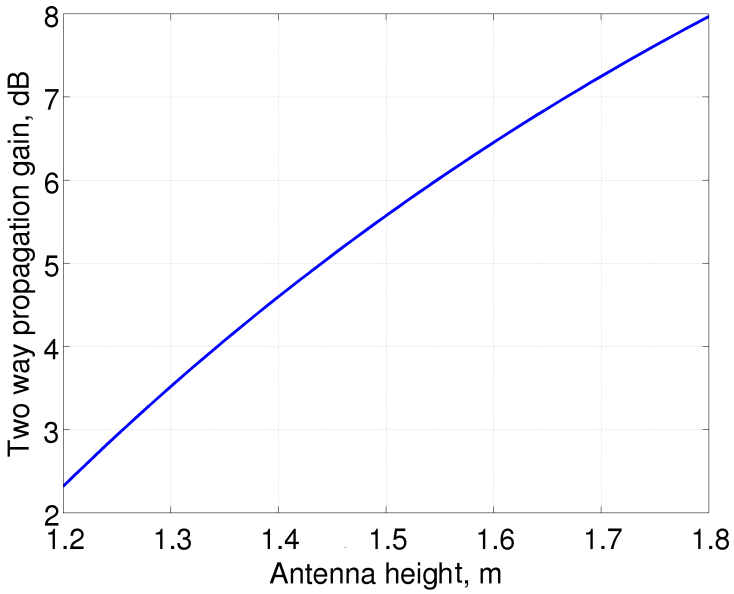

Figure 3.31: Effect of changes in the relative height of the antennas and the target on multipath gain, the separation was assumed to be fixed at 150 m.

disciplined Rb clocks were made available by Fraunhofer Institute for High Frequency Physics and Radar (FHR) for these experiment. In the next stage the GPSDOs were locked to GPS and were fully integrated into the system.

3.3.3.1 Stage I Testing

The first stage was carried out between November – December 2009. In this stage the clocks were used as highly stable oscillators. Several experiments were carried out in both the field and the laboratory. One of the main aims of this exercise was to check the compatibility of the clocks with NetRAD and study the effects of the frequency drift on the radar operation. Several measurements using both CW and pulsed signals were carried out, in both the laboratory and controlled field environment. In all experiments Node 1 was using NetRAD oscillator while the other nodes were either using UCT unlocked GPSDOs (which are in this case merely highly stable oscillators) or Rb oscillators[11]. The experimental set-up is shown in Fig. 3.32. For brevity only result from field experiments using UCT GPSDOs will be discussed in this section.

Node 1 was used as the transmitter in all cases and was positioned in the centre of the baseline, the distance to the bistatic nodes was 48 m. A metallic cylinder was placed 92 m away Fig. 3.33. The radar parameters are shown in Table 3.12. The range intensity plot for node 1 is shown in Fig. 3.34 it is clear from the plot that the target is fixed in range. However, in Figs. 3.35 and 3.36 related to nodes 2 and 3 respectively the fixed cylinder seems to be moving quite fast and disappears from the 10.24 µs capture window after around 0.7 s. By measuring the movement of the peak the difference in period between

[11] Not all the experiments were carried out with the Rb oscillators locked to GPS.

NetRAD oscillator and UCT GPSDOs can be calculated. Since the target is advancing the GPSDOs have a shorter period (higher frequency), the results are shown in Table 3.13. The difference between the OCXO is only 1 Hz which confirms the stability of the oscillators in the GPSDO clocks. The shift in the oscillator frequency will also cause distortion in the Doppler spectrum, this effect will be explored in the next section.

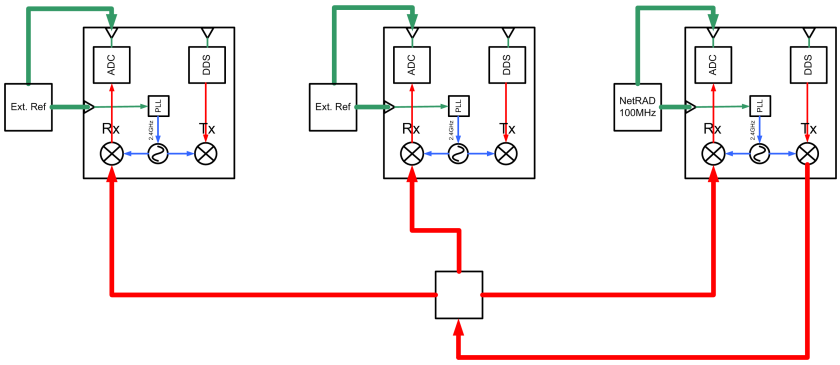

Figure 3.32: Block diagram of stage I GPSDO-NetRAD integration experimental set-up, diagram courtesy of J.S. Sandenbergh

Parameter	value	Parameter	Value
Pulse length	0.4 µs	Number of pulses	10 000
Bandwidth	45 MHz	PRF	1 kHz

Table 3.12: Radar parameters used in field measurements during stage I of NetRAD-GPSDO integration tests

	Difference in Period	Difference in Clock Frequency
Node 2	0.1242 ps	1.242 kHz
Node 3	0.1243 ps	1.243 kHz

Table 3.13: Period and clock frequency offsets in Nodes 2 and 3 when using UCT GPSDOs with reference to NetRAD oscillator in Node 1.

3.3.3.2 Stage II Testing

In July and August 2010, laboratory and field trials were carried out to test the interoperability between NetRAD and the locked GPSDOs. In addition, some measurements were made to characterise the operation of the GPSDO clocks. Only two GPSDOs were operational at that time. The field measurements were conducted both at the UCL test site and at a Thales UK test site at Peacehaven on the South Coast of England. An example of the Peacehaven results will be discussed below.

In this experiment node 3 was use as the transmitter while node 2 was the bistatic receiver. Both nodes were clocked using the GPSDOs, the baseline was 96 m. Both nodes were pointed towards some adjacent cliffs; the cliffs were around 6 km from the both clocks had almost the same frequency there

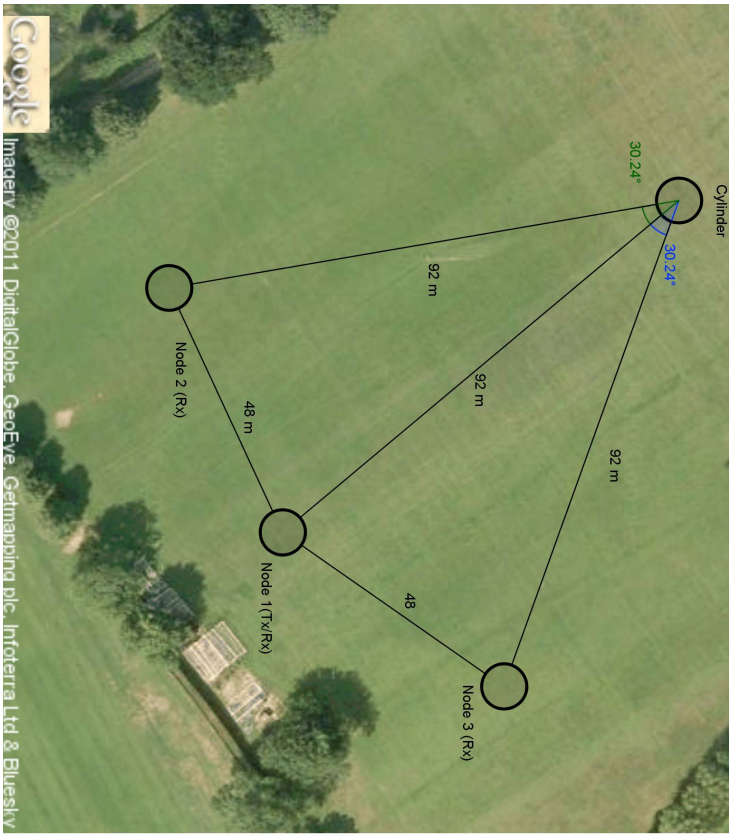

Figure 3.33: Experiment layout for field measurements during stage I of NetRAD-GPSDO integration tests. Node 1 was using NetRAD oscillator, Nodes 2 and 3 were using the GPSDOs

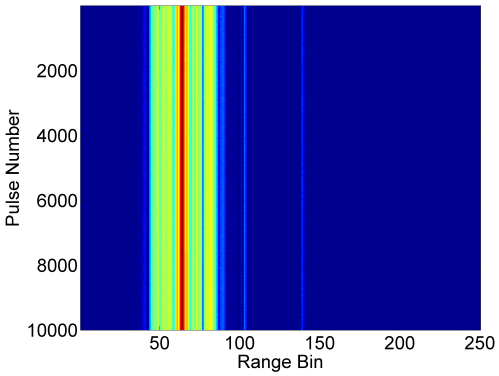

Figure 3.34: Returns for the fixed target as recorded by node 1.

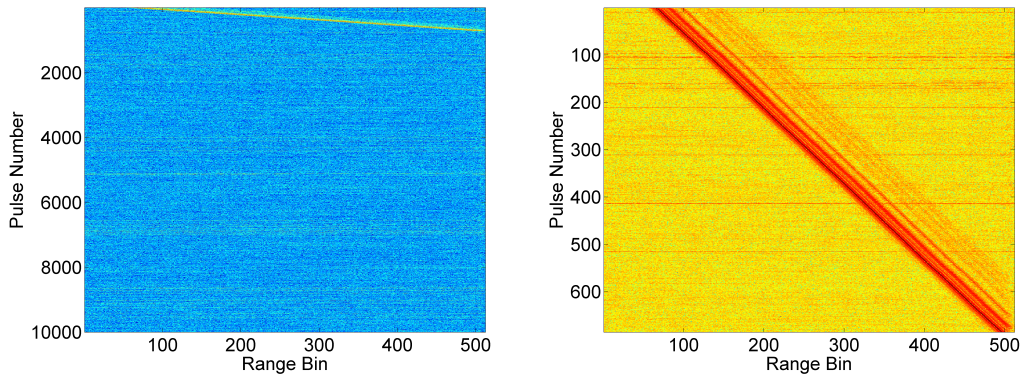

(a) The complete 10 s capture

(b) Only the pulses where the target was present

Figure 3.35: Returns for the fixed target as recorded by node 2, note how the fixed targets appears to be moving. Note how the target (orange line to the top of (a)) moves quickly outside the 10.24 µs capture window.

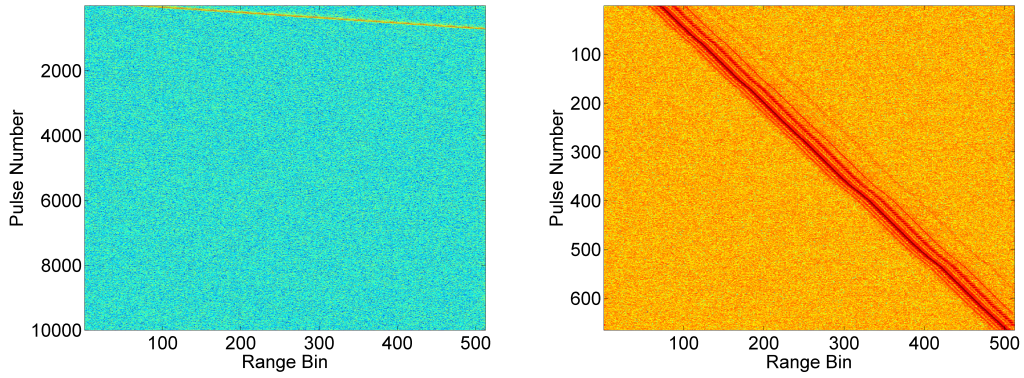

(a) The complete 10 s capture

(b) Only the pulses where the target was present

Figure 3.36: Returns for the fixed target as recorded by node 3, note how the fixed targets appears to be moving. Note how the target (orange line to the top of (a)) moves quickly outside the 10.24 µs capture window.

was no range drift. However, the small frequency difference caused the phase from fixed targets to drift. The behaviour was different depending on whether or not the GPSDO was locked to the GPS signal. When the clocks where in free running mode the phase vs. time plot was a straight line (Fig. 3.38). By fitting a straight line the frequency offsets computed from the sidelobe breakthrough and the cliff return were 0.0658 Hz and 0.0631 Hz respectively. On the other hand when the clocks are locked to the GPS the loop steers the phase of the oscillator trying to lock it to GPS thus the relationship is different from that of a straight line as can be seen in Fig. 3.39. These effects influence the Doppler spectrum of the received signal. This phase drift and the method used to reduce its effect are discussed in Chapter 4 and [127]. In both cases the plots have the same shape except for a fixed phase shift due to the changes in the path length. This indicates that the frequency difference can be considered to be constant within the same capture time, in all field trials the capture time is on the order of tens of microseconds considerably shorter than the PRI. This is important to be able to correct for the phase drifts using the returns from the sidelobe breakthrough. This concept is explored further in Section 4.3.1.

Figure 3.37: Trial location at Peacehaven showing nodes layout and the cliff used to check the oscillators. The cliff can be seen towards the left side of the picture, node 3, is the one with the two antennas, one for the transmitter and the other for the receiver.

Parameter	value	Parameter	Value
Pulse length	$0.4\,\mu$s	Number of pulses	30 000
Bandwidth	45 MHz	PRF	1 kHz

Table 3.14: Radar parameters used in field measurements during stage II of NetRAD-GPSDO integration tests

3.4 Summary

In this chapter the main aspects of the hardware and software development have been reviewed. The original NetRAD system has been substantially upgraded and a novel system has been developed which is capable of simultaneously transiting from all nodes in low power mode or transmitting a single node in high power mode and receiving on all three nodes simultaneously. The system is capable of operating

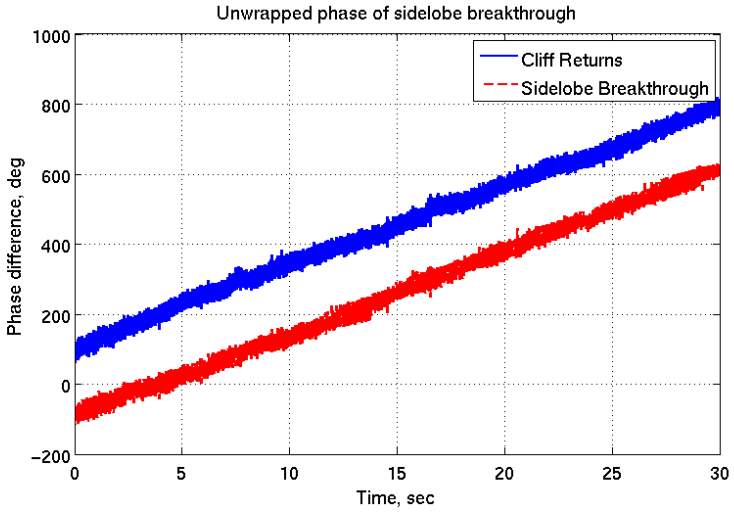

Figure 3.38: Phase of the sidelobe breakthrough and the returns from the cliff, both GPSDOs were in free run mode.

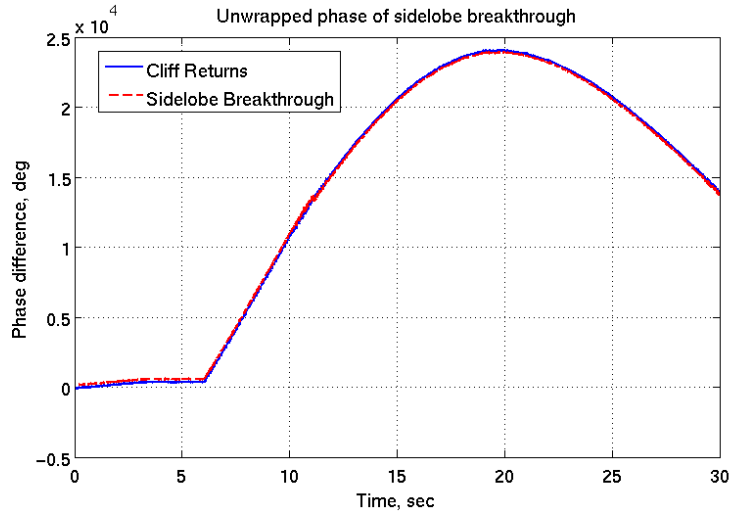

Figure 3.39: Phase of the sidelobe breakthrough and the returns from the cliff, both GPSDOs were locked to GPS.

without hard wiring between the nodes allowing a wide range of baselines and bistatic or multistatic geometries. A thorough calibration and performance evaluation has been carried out. The characteristics of NetRAD receivers are provided in Table 3.15, a summary of the properties of the high power transmitter are provided in Table 3.16.

Property	Node 1	Node 2	Node 3
Receiver gain[a]	41.99 dB	41.05 dB	41.55 dB
Noise Figure[b]	4.61 dB	4.99 dB	4.84 dB
Antenna gain	23.746 dB	23.746 dB	23.746 dB
Beamwidth E x H	$11.23° \times 8.97°$	$11.23° \times 8.97°$	$11.23° \times 8.97°$
Losses	2 dB	2 dB	4.3 dB
1 dB compression point	6.48 dBm	6.487 dBm	7.36 dBm
Max. num. of recorded samples	256 MiS	256 MiS	256 MiS

Table 3.15: Summary of the characteristics of NetRAD receiver nodes.

[a] Excluding losses mentioned in this table
[b] Measured in the laboratory excludes cables and antenna effects; it includes the effect of post processing on the noise.

Property	Value
Transmit power	57.71 dBm
Loss	2 dB
Transmitted waveforms	linear chirp, continuous wave
Pulse length	0.4 ms to 20 ms
Maximum effective bandwidth	45 MHz

Table 3.16: Summary of the characteristics of NetRAD high power transmitter.

By comparing the UCL measurements and those performed at UCT Section 4.2.5.2, the maximum combined error due to the change in receiver gain and HPA output power was 0.58 dB. The mean error in the antenna measurements was 0.3 dB. Thus the combined error is slightly less than 1 dB. Another 1 dB should be included to account for alignment and connections error, hence the total error in the system is 2 dB.

The single pulse noise limited monostatic range of the system has been increased from 208 m, to 2008 m. This was achieved by introducing a 450 W pulsed HPA, a 200 W HPA is used as a backup amplifier and replacing the baseband amplifier to improve the receiver linearity and dynamic range. A BPF was installed to reduce the effect of out-of-band interference. A system for filtering the recorded data in post-processing has been developed to improve the noise figure and remove the effect of the receiver switch transients.

In addition UCT GPSDO clocks have been fully integrated into NetRAD enabling the nodes to be

synchronised in both time and frequency without cables. Wireless communication links replaced the existing wired data network. Baseline separation of the order of 5 km has been achieved in field trials. The maximum node separation has been found to be limited by the communication links SNR.

The user interface code has been completely rewritten to support operating the radar from any PC running 32-bit a Microsoft Windows operating system with access to the NetRAD network. The GPSDO clocks are fully controllable from the same user interface. The user interface is also capable of logging the internal registers of the GPSDO.

This redesign and development has resulted in a powerful and flexible tool for collection of coherent sea clutter and target data, at different monostatic, bistatic and multistatic geometries. Use of this system for field data collection and subsequent analysis is presented in the following chapters of this thesis.

Chapter 4

Data Collection and Pre-Processing

4.1 Introduction

Having discussed the hardware development in the previous chapter, this chapter will discuss the trials planning and execution and main the aspects of the pre-processing applied to the data. The chapter starts with a description of the trials carried out in the UK and South Africa, including both technical and logistical issues. This is followed by an outline of the processing carried out on the data.

4.2 Data Collection

Several data sets have been collected in both the UK and South Africa. It was decided that the bulk of the data collection would be conducted around Cape Town South Africa, mainly due to the more favourable environmental conditions and the logistical support available in South Africa. Several field trials were initially performed in the UK mainly to test the operation of the radar. In addition, several laboratory experiments were conducted, some of which were described in the previous chapter. Several hundred Gigabytes of unique sea clutter and target data were collected.

4.2.1 Site Selection

These trials were limited to fixed land based measurements of sea clutter and marine targets and their signature. By fixed it is meant that the nodes were not mobile while a measurement was being taken. The main draw backs of such a setup are:

1. There is less flexibility in choosing the coverage area after the nodes have been setup.
2. There is a possibility that the data could be affected by land clutter from the backlobe and side-lobes, this issue addressed in Section 4.4.
3. Given the power constraints, the chosen site has to be as close as possible to the sea.

The main advantages of fixed-land based measurement are as follows:

1. The experiments are easier to set up.

2. The Doppler spectrum is not corrupted by platform motion.

3. There are fewer logistical and regulatory constraints.

4. The vehicles are just needed to transport the equipment and thus need not be modified to support radar experiments which greatly reduces the cost of the experiment.

The exact nature of the site will depend on the required measurements; for low grazing angles the site should ideally be located as close as possible to the sea. The site should be raised from the sea surface to protect the antennas from breaking waves. While for high grazing angle measurements both the height of the site and the horizontal distance to the sea are important, the site should be as high as possible to be able to achieve high depression angles at far ranges. An ideal site would be a high cliff with a shear drop very close to the sea. Even at medium grazing angles choosing a proper site for can be difficult. The minimum clearance given the maximum depression angle θ_{dep} and cliff height h is given by:

$$d_{min} = \frac{h}{\tan\left(\theta_{dep}\right)} \tag{4.1}$$

For example if it is desired to measure the sea clutter returns between 10° to 20° and a cliff height of $200\,\mathrm{m}$ the minimum required clearance is $549\,\mathrm{m}$.

Depending on the desired bistatic geometry and the experiment, there could be more constraints. For example, if the purpose of the experiment is to measure the effect of changing the azimuth angle on sea clutter, it is desired that the difference in height between the nodes is negligible at the ranges of interest. On the other hand, if the aim was to study sea clutter using in-plane geometry, then it is necessary to consider the height of both the monostatic and bistatic nodes and the ability to align them such that the nodes and the interception point all lay in the same vertical plane.

Furthermore, logistical and regulatory constraints influence the site selection such as access, facilities, personal safety and the ability to transmit at the desired frequency and power. In addition, the effect of in-band interference must be taken into consideration when choosing a site.

4.2.2 Radar Parameter Selection

Radar parameters selection is dependent on the geometry, required range and the environmental conditions. Given the available maximum power, range ambiguity will not be a problem. In these trials the PRF was set to $1\,\mathrm{kHz}$, this gives a maximum unambiguous Doppler frequency of $\pm 500\,\mathrm{Hz}$, which translates to an unambiguous speed of about $30\,\mathrm{m\,s^{-1}}$ (approximately $58\,\mathrm{kn}$) which corresponds to sea state 8 on the Douglas scale[1]. Under such conditions it would be impossible to operate the radar; thus for the purpose of clutter measurements the radar is Doppler unambiguous. Using such a PRF it was

[1] Douglas Sea scale is a scale which relates the sea 'state' in terms of the significant wave height [42].

possible to gather $130\,\mathrm{s}$ of data per recording. At this PRF the clutter samples are not decorrelated from pulse to pulse. The same PRF was also used for target data.

Although the HPAs have a maximum duty cycle of $10\,\%$ including the fall and rise time, the actual limit was the eclipsing and nearby clutter. The pulse length used was determined depending on the minimum and maximum range requirements.

4.2.3 Antenna Alignment

For bistatic geometry antenna alignment is clearly an important issue. Since the electromagnetic boresight of the antennas and the optical boresight of the telescopes have been aligned an object that is aligned with the cross-hair of the telescope will be at the peak of the antenna pattern. The antennas could therefore be pointed to a fiducial marker and then rotated as required. The point on the sea surface at which the mainlobes of the transmitter and the bistatic receiver intersect is defined as the intersection point. Existing landmarks or buoys cannot be used as references to align the antennas, unless their exact or relative coordinates are known, which was not usually the case. Hence markers having predetermined locations, such as the antennas, were used as fiducial markers. When two nodes are used or all three nodes make a straight line, the marker was positioned on the extended baseline or the antennas were used a reference for each other. After some experimentation the following procedure was developed to align the antennas:

1. To ease the calculations the azimuth rotation stage was set to 0° for the passive nodes and 180° for the monostatic node. When this was not the case the initial recorded values were taken into account when aligning the antennas.

2. Prior to mounting the antenna on a tripod, it was fixed in placed and levelled. The antenna was then rotated until it was pointing towards the transmitter if it was a bistatic node antenna, and vice versa. Finally, the antennas were locked in position.

3. For clutter measurements an intersection point was chosen, from which the angles for the monostatic and bistatic nodes were calculated. The antennas were then pointed to the required point using the azimuth rotation stages and an inclinometer.

4. If the aim was to align with a target then the antennas were rotated until the target was aligned with the telescope cross-hair, the angles were then noted for reference.

Although the azimuth rotation stages have a scaling of 0.2° during field trials specially during the strong winds the error is likely to be around $\pm 0.5^\circ$. Regarding the elevation angle tightening the antenna was found to change the elevation angle slightly, hence the error is also estimated to be $\pm 0.5^\circ$.

When the baseline was relatively short, such as at the UK trials site, the error in the GPS location measurement could not be ignored and an optical survey total station (Pentax R-125) was used to

determine the location of the antennas, in both range and angle.

4.2.4 UK Trials

The main aims of the UK trials were to test the new modifications to the radar system, particularly those that cannot be tested in the laboratory, such as the isolation between the transmitter and the monostatic and bistatic nodes and the stability of the antenna mounts. These trials were also used to gather preliminary data to test and calibrate the system. These trials were carried out at two locations, a UCL open test site and a coastal test site. This test site is near Peacehaven cliffs ($50°47'1.6''$ N, $0°1'36.5''$ E), on UK South Coast; the site is owned by Thales Aerospace UK. The maximum achievable base line was of the order of 100 m at both locations. This section will be concerned with the description of the sea clutter and marine target measurements of the final system which were carried at Peacehaven during the summer of 2010.

4.2.4.1 Surface Truth

The importance of surface truth in sea clutter measurements cannot be underestimated. Unfortunately, the surface truth could not be easily measured directly by UCL during the measurements. Historical data provided by Weather Underground for nearby weather stations were downloaded after the trials. Weather buoys operated by the UK Meteorological Office were used to obtain the surface truth. The nearest buoy to the trial site at Peacehaven was the Greenwich Light Vessel, which was used as the primary reference for wave-height, and wind speed and direction data. The data was compared with that measured by Sandettie Light Vessel to check for consistency between the two measurements. If the measurement recorded by both stations was of the same magnitude this indicated that the weather is consistent in that area. The sea state and swell direction were estimated using visual observations during the trial.

To measure the node separation an optical total station was used as described in Section 4.2.3. GPS could not be used because the error in GPS measurement was significant compared to the baseline length. However, the GPS coordinates were used to approximate the bearing of the baseline with respect to true north. Estimating the antennas height with respect to mean sea level proved to be a more difficult undertaking. There is a fixed difference between the GPS height measurement and the actual height with respect to mean sea level which is dependent on the location. This error is due to the Geodetic system use by used by the GPS (WSG84) which assumes that Earth is a perfect ellipsoid, which is not the case. For Peacehaven the error was around $45\,\text{m}^2$. In addition, the GPS height measurements can have around ± 15 m residual error. This error can be significant if the height of the antennas is small and the range is short. To get an estimate of the height of the antennas the antenna height was varied until the nulls from the measurements were almost aligned with those from the simulation. This method did not take into account the effects of super-reflectivity and errors in the measurement of the depression angle. Given

[2]The following site can be used to convert from WSG84 Geodetic or ETRS89 Geodetic to the national grid `http://gps.ordnancesurvey.co.uk/etrs89geo_natgrid.asp`

the range of the measurement super-reflectivity should not be a problem and the error in measuring the depression was less than $\pm 0.5°$. Hence the dominant error was due to the GPS measurements.

4.2.4.2 Logistical Challenges

The equipment had to be transported from UCL to the trial site. Since the trial dates had to be set at least one week before the start of the trial, the weather conditions were not always favourable on the day of the trial. In the latter stages of the testing program the trials were typically scheduled for 3 to 7 days.

To transport the equipment from UCL to the trial site, three vehicles were used, one of which was a medium sized van[3]. Care was taken when packing the vehicles such that the equipment was not damaged during transportation and the calibration of the telescopes was not affected. The vehicles were also used to house the nodes during the trials, which provided weather protection for the equipment and team members. The medium sized van was also used as a control centre, and would also host node 1.

Although, the radar operated in the ISM band, the effective isotropic radiated power (EIRP) was much higher than that allowed for exempt operation set by the Office of Communications (Ofcom). A special non-operational licence was obtained. The licence limited the operation to the power levels and locations mentioned in the licence.

The wireless microwave links operated as a wireless access system (WAS) operating in the $5470\,\text{MHz}$ to $5725\,\text{MHz}$ band. However, the output power of the bullets was reduced such that the EIRP was less than $1\,\text{W}$ to comply with the UK interface requirement [133]. This was adequate for the short baselines used in the UK trials but would have posed problems if the baseline was much longer.

4.2.4.3 Trials Using Wired NetRAD

The NetRAD system was tested in stages for new modifications, when possible these tests were carried out in the field. Initially, the trigger and clock distribution was achieved by using cables. The wireless links were used for data communication. Of particular interest in this section are the measurements carried out between 09-June-2010 and 10-June-2010. During these experiments the sea was relatively calm. The main aims of these experiments were:

1. To test the complete system, including the antenna pedestals and alignment technique but not the GPSDOs.

2. To establish the system performance using the wired system and use this as a reference to compare the results when using the GPSDOs.

3. To train the core team members in setting up the nodes.

4. To test the new software interface.

[3] It had a capacity of around $5\,\text{m}^3$.

5. Evaluate the performance of the wireless links.

6. Test different proposed methods to deploy the system.

4.2.4.4 Trials Using Wireless NetRAD

After testing the new NetRAD+GPSDO setup in the laboratory setup, the wireless system was tested at the UCL open field and Peacehaven test sites. The aim of these trials was:

1. Test the inter-operability between NetRAD and the GPSDOs.

2. Validate the calibration of NetRAD.

3. Check the suitably of the NetRAD wireless system to measure simultaneous monostatic and bistatic sea clutter and target data.

4. Train core team members on the operation and setting up NetRAD.

The first two items in the above list were discussed in Section 3.3. To enhance the training, the same core team used in the June 2010 trials was used during these trials. The main operational effect of using the GPSDO was the increase in the phase offset between the nodes and that the starting time of the experiments could differ by tens of nanoseconds between different experiments. Both these effects are discussed in Section 4.3.

During these trials there was moderate southern to south westerly wind on most days with the sea state around 1 to 2. A schematic of the set-up is shown in Fig. 4.1. The bistatic angle was changed by rotating the antennas by a predetermined angle off the baseline and range gating. Because of the short baseline the maximum achievable bistatic angle was limited, for example at a monostatic range of 500 m the bistatic angle was about $10°$. Data was gathered for both VV and HH polarisations. Besides being used to check the operation of the radar, data from this experiment has been used to study the effect of small bistatic angles on the spikiness of the amplitude statistics of monostatic and bistatic sea clutter [134] and the statistical properties of the spectrum of bistatic and monostatic sea clutter [135].

4.2.5 NetRAD Trials in South Africa

After analysing the data gathered during the UK trials it was decided to conduct a major data collection campaign in the Cape Town area of the Republic of South Africa. In addition to the nodes, the antennas, the data links, the RF accessories and cables, and non-RF accessories such as the telescopes, inclinometers and the battery chargers were also shipped. The trial dates were chosen such that they would coincide with radar trials that were being conducted by the South African Council of Scientific and Industrial Research (CSIR). CSIR, UCT and UCL worked closely together to coordinate the trials.

Figure 4.1: Schematic of the setup for the trials in Peacehaven, other angles off the baseline were used as well.

The equipment was shipped on a 12 month ATA Carnet to allow trials to be carried out over a reasonably long period[4].

South Africa and Cape Town offered many advantages as compared to conducting the trials in the UK. The main ones are:

1. The coastline in the Cape Town area offers many diverse environments from high cliffs suitable for high grazing angle measurements and beaches which are suitable for low grazing angle out-of-plane trials.

2. It is much easier to obtain permission to transmit at different locations, whereas in the UK if a new location is needed a new application has to be made.

3. More targets of opportunity are available and it is easier to coordinate cooperative targets.

4. The trials were coordinated with CSIR radar trials in the same area which allowed access to CSIR cooperative targets and surface truth data.

5. UCT provided logistical support in terms of administration, local knowledge, storage area, test equipment and laboratory facilities.

6. UCT staff were heavily involved in the trials specially after UCL team left and in the trials conducted in 2011.

For these trials four vehicles were used. A small car, two single cabin pick-up trucks with canopy and a medium sized van. Since only two nodes were used in these trials, each node was assigned to a

[4]Two sets of trials were carried out in April and June 2011. The first concentrated on small marine targets and their signature while the latter concentrated on sea clutter. Both trials were lead by UCT.

(a) Monostatic node housed in a pickup (b) The medium van was used as an operating station

Figure 4.2: Photos of the setup used in the trials carried out in Cape Town.

pick-up, most of the spares were kept in the van. During the trials, the nodes were setup in the back of the pickup trucks, the van was used as an office and the small car to move people and equipment, when needed, between the two sites, photos of the setup are shown in Fig. 4.2.

The main UCL led trial was planned for three weeks. The first week was set for sea clutter measurements, the second week was intended for target measurement in cooperation CSIR when possible. The last week was reserved for further trials on both sea clutter and target measurements. Prior to starting the trials around a week was allocated for operational check and calibration of NetRAD, the GPSDOs and the communication links. In addition, the electromagnetic and optical boresights of the antennas and the telescopes were realigned. The schedule of the trials is summarised in Table 4.1. This work will concentrate on the low grazing angle out-of-plane measurement conducted during the first week of the trials.

The first trial was carried out on 04-Oct-2010 at Table Mountain National Park; however, due to excessive interference the trial was cancelled after the nodes have been setup and connected. In the wake of that incident, all other sites were checked for interference.

Date	Activity	Notes
28-Sep-2010 – 1-Oct-2010	NetRAD testing and calibration, and final logistical preparation	Author arrived on 28-Sep,
4-Oct-2010 – 10-Oct-2010	Sea Clutter trials	Remaining UCL team arrived on 1-Oct
11-Oct-2010 – 15-Oct-2010	Target measurement	UCL team departs on 15-Oct
16-Oct-2010 – 22-Oct-2010	Complementary target and clutter measurements	Trials carried out by UCT team.

Table 4.1: Schedule of the trials in RSA

4.2.5.1 Surface Truth

In addition to using the weather reports from www.wundcerground.com, UCL and UCT had access to wave data from Cape Point Buoy and wind data from Roman Rock for most days during the trials[5]. The node location and baseline length were measured using the GPS in the GPSDO clocks. The approximate antenna heights were determined as in Section 4.2.4.1.

4.2.5.2 Operational Test and Calibration

Prior to starting the trials the operation of NetRAD was checked, the antennas were reassembled and the optical telescopes boresight was realigned with the electromagnetic boresight of the antennas. A similar procedure to that described in Section 3.3.1.2 was used.

In addition, to check the operation of the system a closed loop test was performed. All three nodes and the main HPA were tested. The output of the HPA was attenuated and connected to a three-way splitter, followed by attenuators, the setup is shown in Fig. 4.3. Data was recorded for several pulse lengths all at a bandwidth of 45 MHz. The recorded data was also used to extract the reference signals used for match-filtering the experimental data.

The HPA output and the gain of the nodes were measured using a procedure and setup similar to that described in Section 3.3.1.4. The results are summarised in table Table 4.2. The HPA output power was measured to be 57.57 dBm compared to 57.71 dBm when measured at UCL. The average error between the receiver gain measurements was approximately 0.3 dB and the average error gain in the output power measurement was 0.14 dB. These measurements confirmed that the receiver gain and output power of the amplifier were stable.

Node #	Gain (UCT), dBm	Gain (UCL), dBm	Error, dB
1	41.55	41.99	0.44
2	41.23	41.05	-0.14
3	41.83	41.55	-0.28

Table 4.2: Comparison between NetRAD receivers gain at UCT and UCL.

4.2.5.3 Sea Clutter Measurements

In this section a brief summary of the sea clutter measurements carried out during these trials are presented. The main aim was to gather coherent simultaneous bistatic and monostatic sea clutter data at various geometries under different weather conditions. Three out-of-plane and two in-plane clutter measurements were carried out as described below. A summary of the location data and trials is presented in Table 4.3.

In-Plane measurements were conducted in Table Mountain National Park. An aerial photograph of the trials site is shown in Fig. 4.4, and a nautical chart of the Cape Point area is shown in Fig. 4.5. Two

[5]The data was supplied by the CSIR, Stellenbosch, which was collected on behalf of the Transnet National Port Authority (TNPA)

Date	Bistatic Node			Monosstaic Node			Horizontal separation, m	Vertical separation, m	Baseline, m	Trial summary
	Latitude, °	Longitude, °	Height, m	Latitude, °	Longitude, °	Height, m				
5- Oct- 2010	-34.343442	18.461090	65	-34.340187	18.458848	71.84	416.40	6.84	416.46	Out-of-plane, low grazing calm sea
6- Oct- 2010	-34.347105	18.465415	60.08	-34.346208	18.467187	133.14	190.80	73.06	204.31	In-plane,
7- Oct- 2010	-34.347045	18.465352	63.43	-34.346248	18.467268	133.06	197.00	69.63	208.94	calm sea
10- Oct- 2010	-34.189073	18.366482	65.4	-34.176775	18.353305	79.57	1827.00	14.17	1827.05	Out-of-plane, low grazing rough sea
11- Oct- 2010	-34.173820	18.427922	42.38	-34.197250	18.436578	47.31	2724.00	2.72	2724	
12- Oct- 2010	-34.173842	18.427900	59.8	-34.200855	18.448248	147.95	3539.00	88.15	3540.1	
13- Oct- 2010	-34.157742	18.434212	57.69	-34.186393	18.436393	44.94	3192.00	12.75	3192.03	Target data
14- Oct- 2010	-34.157765	18.434240	51.67	-34.200780	18.448103	165.74	4950.00	114.07	4951.31	
15- Oct- 2010	-34.157765	18.434240	51.67	-34.200780	18.448103	165.74	4950.00	114.07	4951.31	

Table 4.3: Summary of location and trial data

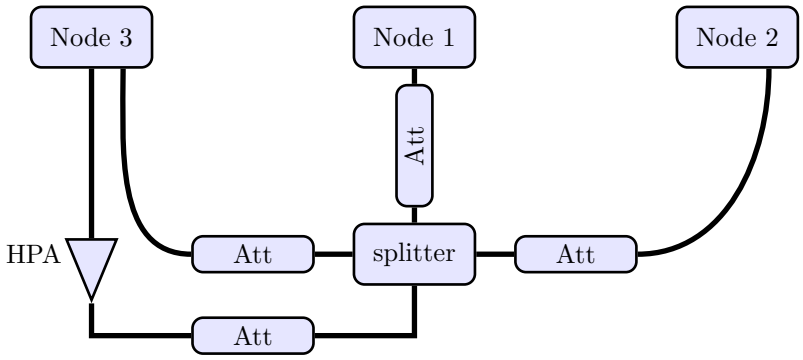

Figure 4.3: Block diagram of the setup used in testing NetRAD at UCT.

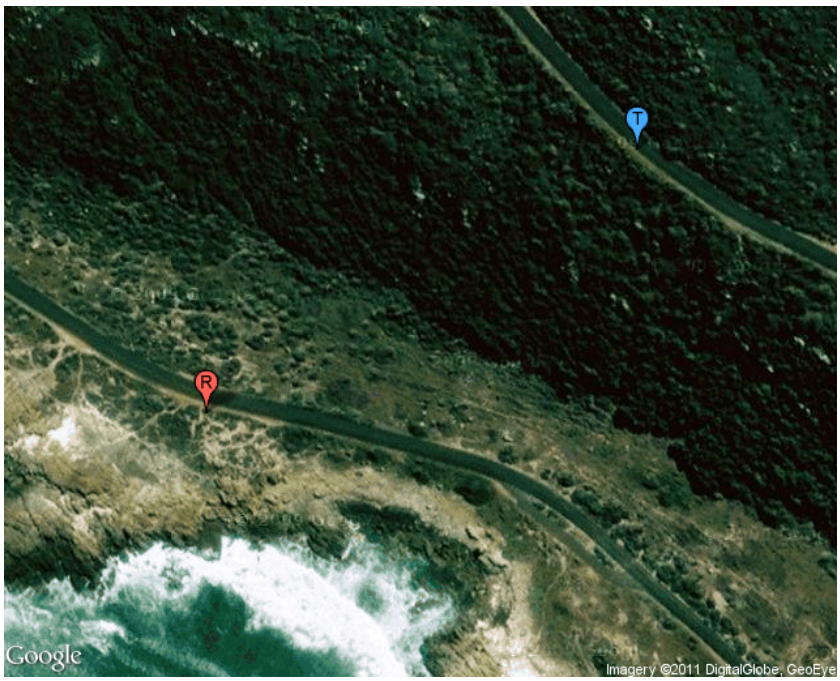

Figure 4.4: A bird's eye view of the location used for in-plane measurements; T and R mark the locations of the monostatic and bistatic nodes respectively.

sets of trials were carried out on the 6 and 7-Oct-2010. Only two nodes were used in this experiment, the monostatic node was placed on the upper access road and the bistatic node was placed on the lower access road. The vertical separation between the nodes was around 70 m, while the average horizontal separation was approximately 190 m. The bistatic angle was changed by changing the tilt angle of the transmitter, while the tilt angle of the bistatic node remained at 0°. More information on the location data for both days is provided in Table 4.3. On both days the weather was relatively calm.

Out-of-Plane measurements were conducted in Table Mountain National Park and to the north of Scarborough[6]. In both experiments the tilt angle of the antennas was kept constant, and the bistatic angle was changed by rotating the antennas in azimuth. In all cases the range from the intersection point to the transmitter was equal to that of the intersection point to the receiver. A sketch of the geometry is shown

[6]Scarborough is a conservation village on the west side of the Cape Peninsula.

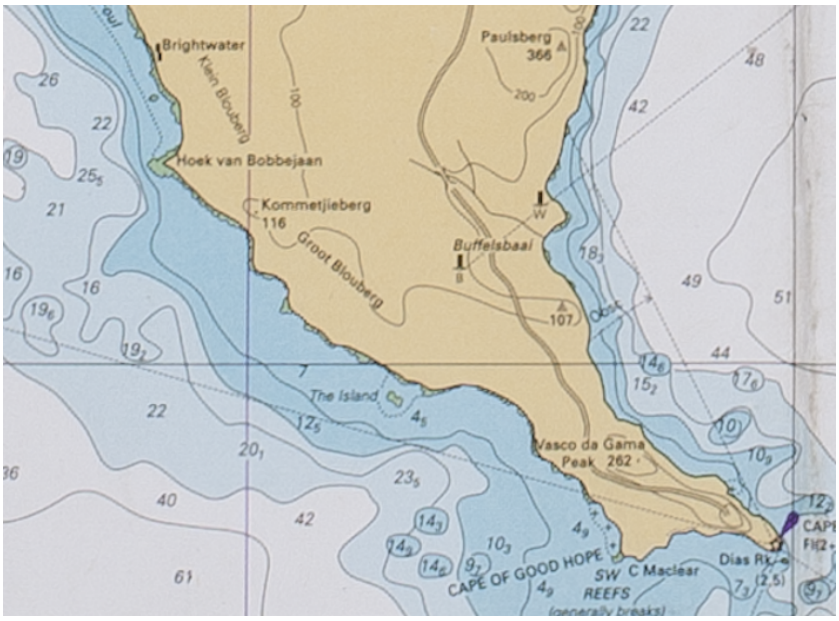

Figure 4.5: Nautical chart of Cape Point. Data has been reproduced with the permission of the Hydrographer, SA Navy.

in Fig. 4.6.

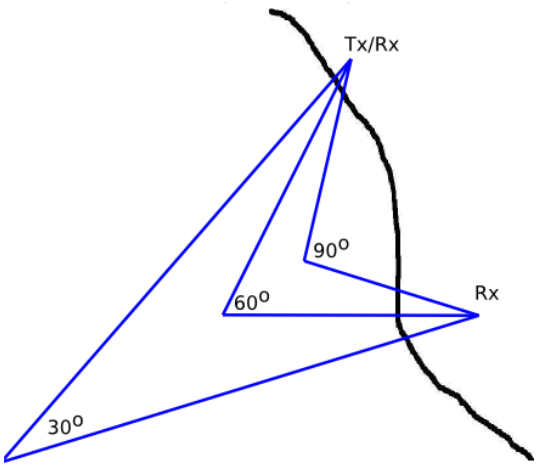

Figure 4.6: A sketch for the geometry used for out-of-plane measurements.

The Cape Point measurements were carried out on 05-Oct-2010. The nodes were placed just off the lower access road in the same area where the receiver was located in the in-plane measurements. An aerial view of the area is shown in Fig. 4.7. A nautical chart of the Cape Town area is shown in Fig. 4.5. Only two nodes were used in this experiment. The vertical separation between the nodes was negligible compared to the baseline and ranges used in this experiment. The baseline length was approximately 416 m; more details on the location are provided in Table 4.3. During these trials a longer baseline was tried; however; the lack of line-of-sight between the locations made it difficult to align the nodes and the communication links did not have a high enough SNR to operate.

Both back- and forward-scattering geometries were studied at both HH and VV polarisation. A

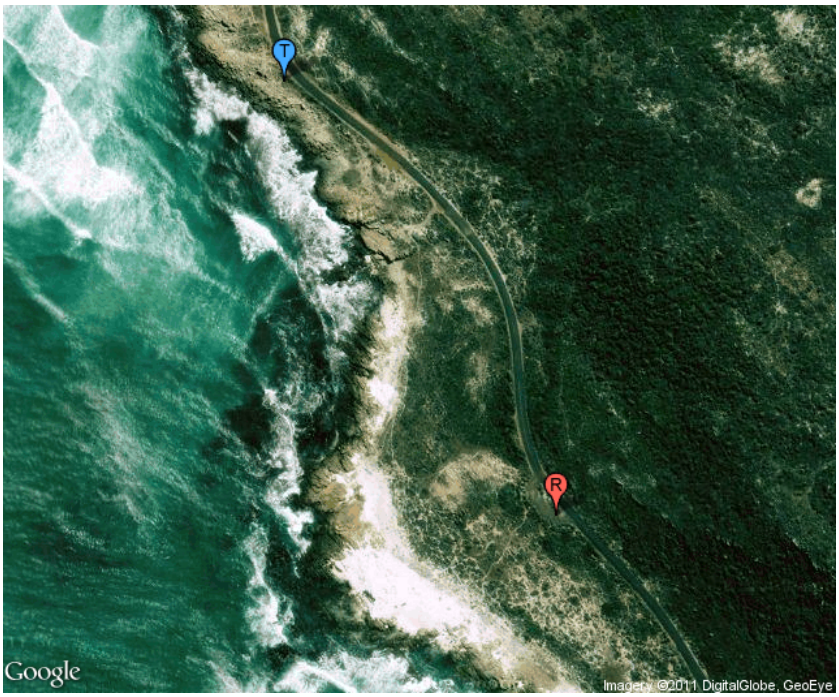

Figure 4.7: A bird's eye view of the location used for out-plane measurements at Cape Point; T and R denote the positions of the monostatic and bistatic nodes respectively.

cross-polar measurement was also recorded. The bistatic angle was changed by rotating the antennas in azimuth. In all cases the bistatic triangle was an isosceles triangle. The transmit and receive antennas tilt angle was held constant at $-3°$. The wind was calm and the sea was approximately sea state 2. The data gathered on this day is analysed in more detail in Chapters 5 and 6.

The second data set was collected on 10-Oct-2010. The nodes were placed just off a coastal road north of Scarborough, a aerial view of the area is shown in Fig. 4.8, a nautical chart of the area is shown in Fig. 4.9. Two nodes were used in this experiment. The vertical separation between the nodes was negligible compared to the baseline and ranges used in this experiment. The baseline length was approximately $1.8\,$km, more details on the location are provided in Table 4.3. Both back- and forward-scattering geometries were studied at both HH and VV polarisation. The bistatic angle was changed by rotating the antennas in azimuth. In all cases the bistatic triangle was an isosceles triangle. The transmit and receive antennas tilt angle was held constant at $-1°$. The wind was very strong with strong precipitation at times and the sea was approximately sea state 4 – 5. The data gathered on this day is analysed in more detail in Chapters 5 and 6.

4.2.5.4 Target Measurements

In addition to the clutter measurements, measurements were also carried out on various marine targets. Both cooperative target and target of opportunity data were collected. Various locations around Simon's Town were used for the trials. Since this is an urban environment there was strong in-band interference. This data set is not an integral part of this thesis, although the author was also involved in the analysis

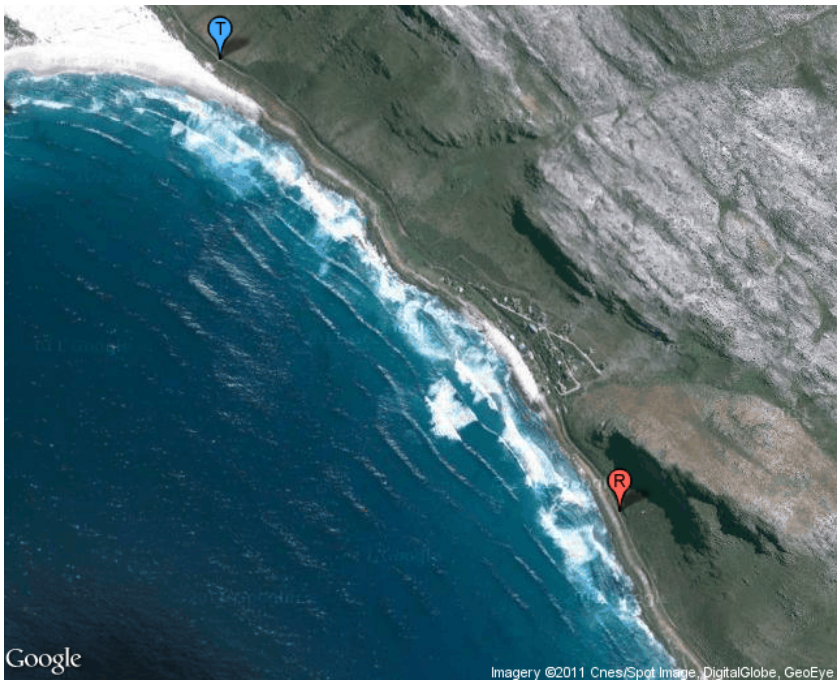

Figure 4.8: A bird's eye view of the location used for out-plane measurements north of Scarborough; T and R denote the locations of the monostatic and bistatic nodes respectively.

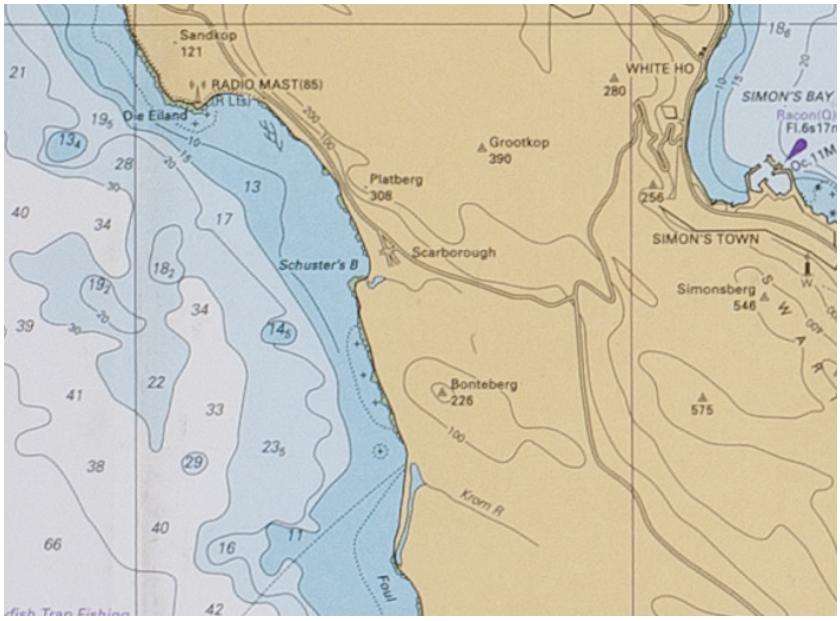

Figure 4.9: Nautical chart of the area around Scarborough. Data has been reproduced with the permission of the Hydrographer, SA Navy.

of this target data. In particular, statistical analysis of the spectrum of coherent bistatic and monostatic sea clutter and the micro-Doppler properties of the target data were analysed. In some of the cooperative target experiments the target movement was restricted such that it remained within the antenna footprint. These presented some of the more interesting data sets such as rigid inflatable hull boats making circles or spirals. In other experiments the targets were moving outside of the bistatic coverage area and the target was tracked manually. In both these methods it is difficult to estimate the error due to antenna pattern loss. However, since the antennas have a beamwidth of around $11^\circ \times 9^\circ$, the error would be around 2 dB provided that the target was successfully tracked. Failing to track the target would result in a sudden drop in the SNR.

4.3 Pre-processing NetRAD Data

NetRAD data was exported from the capture card to the local hard drive in each node as 16 bits unsigned integers. When the data was exported an m-file was also exported which contained the capture parameters such as the number of pulses, capture duration, pulse length, ..., etc. The data was read as an unsigned array A_{uint16}, the signed data was recovered by

$$A_{int16} = A_{uint16} - 2^{n-1} \tag{4.2}$$

where n is the number of bits in the ADC, for NetRAD $n = 14$. The number of pulses m and the number of samples n were determined from the m-file. The array was converted to a matrix of size $m \times n$. The complex data was recovered by using Hilbert transform[7]. A laboratory recorded copy of the transmitted chirp signal was used to perform the matched filter. The data was weighted by a Hamming window and filtered to remove the low frequency interference and reduce the noise figure, this was discussed in Section 3.3.1.5.

To reduce the sidelobe levels the reference signal is weighted by a Hamming window. In addition, depending on the environment and the required processing interference reduction and phase correction are applied. For data recorded using the GPSDO the relative start recording time between the nodes can vary slightly from capture to capture but not from pulse to pulse if the clocks are stable. As discussed in Section 3.3.1.5 the first and last 5 MHz were removed to improve the SNR and reduce the effects of switch transients in the monostatic node.

4.3.1 Phase Correction

As discussed in Section 3.3.3, since two independent oscillators are used they tend to drift. Thus there will be a finite difference in frequency between the two clocks. When the clocks are locked to GPS their relative phase might not be linear. If the difference is large this could lead to range migration as

[7] In this work the decimated Hilbert transform as described in [130].

shown in Section 3.3.3.1. However, if the difference is small then this would result in tramlines in the Doppler spectrum and images in the spectrum if the target has a non-zero radial velocity, as discussed in Section 3.3.3.2. Furthermore, if the clocks are locked to the GPS the frequency drift can become non-linear, as shown in Fig. 3.39. In this section the method used to discuss the phase correction will be discussed in more detail.

The phase and amplitude of the echoes returned from a stationary target are fixed, provided that the multipath is constant, since the phase is dependent only on the wavelength and the path length each copy of the signal takes. In bistatic radar, the sidelobe breakthrough could satisfy these conditions. Thus any variation in the phase of the sidelobe breakthrough or stationary target return ϕ_k^{fixed} are due to the oscillator instability (relative instability in the bistatic case). To correct for this a fixed phase reference ϕ^{ref} was chosen for this fixed return, such as the phase of the return from the first pulse or $0°$. Any deviation from this fixed phase was considered to be the phase error for that particular pulse and was applied to the returns from the pulse.

$$\phi_k^e = \phi^{ref} - \phi_k^{fixed} \tag{4.3}$$

$$x_{k,l}^c = \exp\left(j\phi_k^e\right) x_{k,l} \tag{4.4}$$

where

$$\mathbf{X} = \begin{bmatrix} x_{1,1} & x_{1,2} & \cdots & x_{1,m-1} & x_{1,m} \\ x_{2,1} & x_{2,2} & \cdots & x_{1,m-1} & x_{2,m} \\ \vdots & \vdots & \ddots & \vdots & \vdots \\ x_{n-1,1} & x_{n-1,2} & \cdots & x_{n-1,m-1} & x_{n-1,m} \\ x_{n,1} & x_{n,2} & \cdots & x_{n,m-1} & x_{n,m} \end{bmatrix}$$

is the data before correction and

$$\mathbf{X^c} = \begin{bmatrix} x_{1,1}^c & x_{1,2}^c & \cdots & x_{1,m-1}^c & x_{1,m}^c \\ x_{2,1}^c & x_{2,2}^c & \cdots & x_{1,m-1}^c & x_{2,m}^c \\ \vdots & \vdots & \ddots & \vdots & \vdots \\ x_{n-1,1}^c & x_{n-1,2}^c & \cdots & x_{n-1,m-1}^c & x_{n-1,m}^c \\ x_{n,1}^c & x_{n,2}^c & \cdots & x_{n,m-1}^c & x_{n,m}^c \end{bmatrix}$$

is the phase corrected data, and k and l are the pulse and range bin indices respectively.

Using this method it is assumed that the oscillator frequency is constant during the capture period. For the data captured using NetRAD this is the case when the capture time is small, as show in Figs. 3.38 and 3.39.

To demonstrate the effectiveness of this method the Doppler spectrum of a large ship will be compared before and after the phase correction. The data was collected on 14-Oct-2010, the baseline was approximately 4951 m and the transmitted pulse length was 4 µs. The bandwidth was set to 45 MHz. As discussed above the data was filtered to remove low frequency interference and a Hamming window was used. The root mean square (rms) phase error was 101.68°. The Doppler spectrum was generated using 8192 pulses, for two-way range of 5448 m. By comparing Fig. 4.10a and Fig. 4.10b it can be clearly seen that the images in the Doppler spectrum has been eliminated and that the noise floor is much lower.

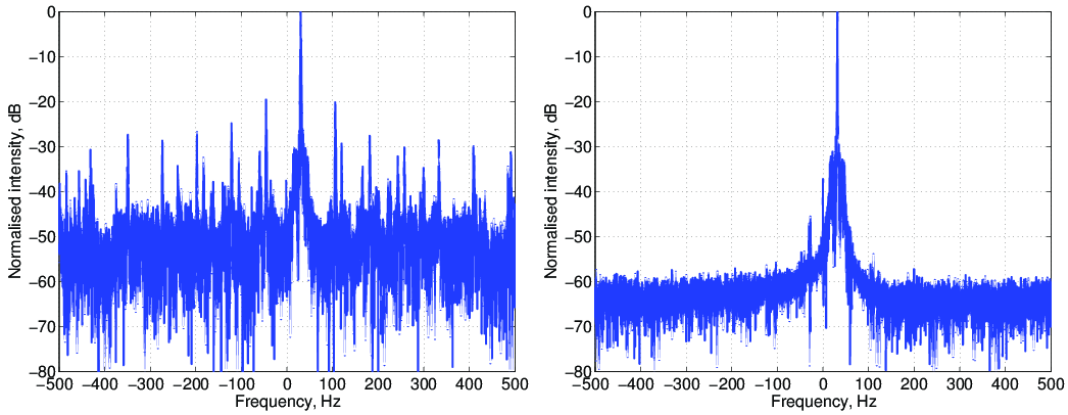

(a) Without phase correction

(b) With phase correction

Figure 4.10: The effect of phase correction of the bistatic Doppler spectrum. 8192 samples were used to generated the Doppler spectrum in both cases.

4.3.2 Interference Reduction

Since NetRAD operates in the ISM band, in-band interference represents a real problem particularly in urban areas. Since the sea clutter measurements were generally carried in remote locations interference was not a significant problem at most sites. The low grazing angle clutter data collected at Cape Point on 05-Oct-2010 was however, affected by interference. The interference seems to be due to the communication link between the lighthouses in the area. When the interference level was substantially higher than the noise floor the interference manifested itself as straight lines across the range time intensity (RTI) plot with constant amplitude, as shown in Fig. 4.11. In this image there is clear interference around pulse number 70 000 However, upon close examination other interfering pulses are found. Figure 4.12 shows the power return from three pulses a clean pulse (number 500), pulse number 7125 corrupted by moderate power interference and pulse number 69 033 which was corrupted by high power interference.

Since the background noise was Gaussian, the intensity was an exponential process. Large excursions were indicative of the presence of interference. The pulses that had these excursions were assumed to be corrupted by interference and were removed from the data. Since the noise is random, excursions can also be due to variation in the instantaneous noise power, and these bins cannot be used to estimate

the receiver background noise level. To reduce the probability of mistaken noise variation for interference, at least 20 range bins were averaged. Since thermal noise decorrelates from pulse to pulse the average noise power drops much faster than spikes due to interference. However, other bins could be used to estimate the noise level. To illustrate the effectiveness of this method, normalised intensity of the noise was plotted before (Fig. 4.13a) and after interference removal (Fig. 4.13b). The corrupted pulses were found using bins 840 to 900, and bins 810 to 830 were used to compute the normalised moments, only 404 out of 130 000 recorded pulses were removed. It is clear from Fig. 4.13b that the noise is Gaussian as the normalised moments are almost equal to theoretical values of $n!$.

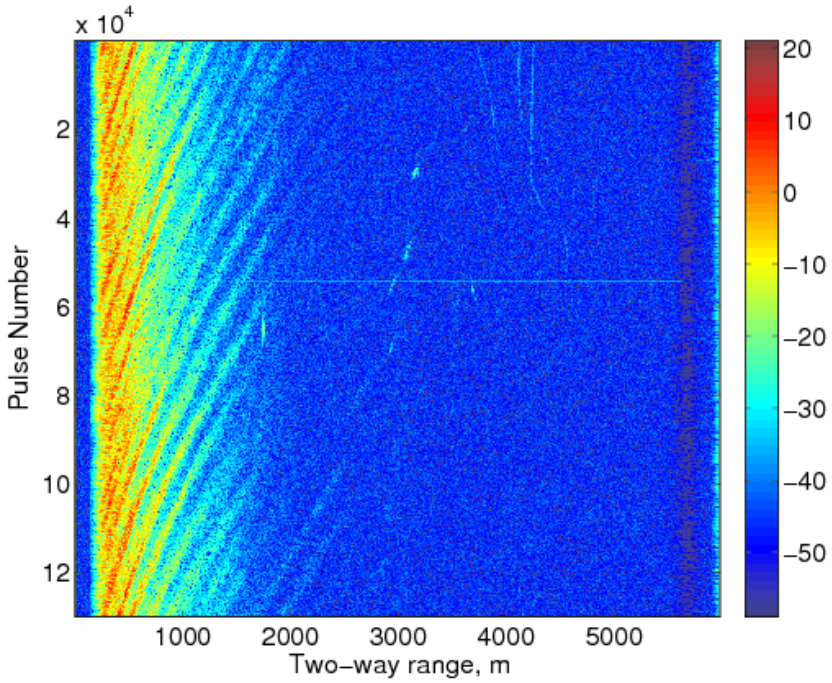

Figure 4.11: RTI image of monostatic sea clutter gathered on 05-Oct-2010 at Cape Point. When the interference is much higher than the noise level interference can be seen as bright horizontal lines in the image, around pulse number 5500. In this case the interference level was not much higher than the noise level. Colour scale in dB.

4.3.3 Radar Start Time Correction

When using the wired system the relative radar start times were accurately known, since they were simply due to propagation delay in the different electronic components and the synchronisation and clock cables connecting nodes 2 and 3 to node 1. However, when using the GPSDO there could be a small difference between the triggering of the two GPSDOs. Relying on the carrier being precisely synchronised to GPS, a start trigger was generated. The carrier edge corresponding closest to the GPS time mark was used as this trigger. This jitter was usually around ± 10 ns [127]. In all cases the transmitting node was taken as the reference. Since the baseline was fixed and known, by subtracting the measured range from the

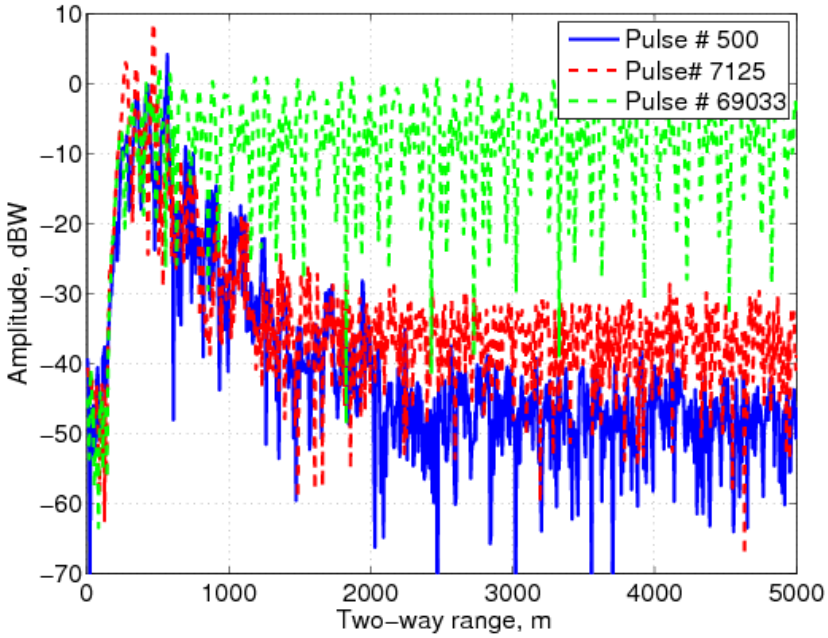

Figure 4.12: Comparison between the power levels between two corrupted and a clean pulse. Note how the interference can vary greatly.

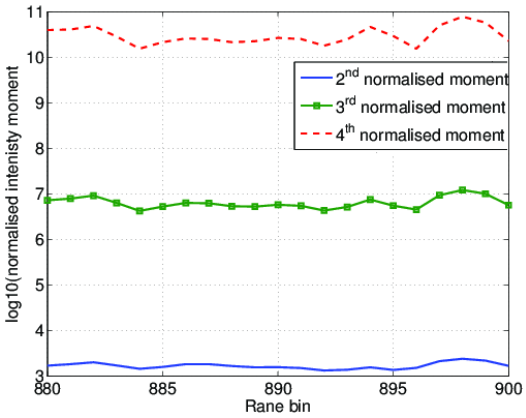

(a) Before removing interference

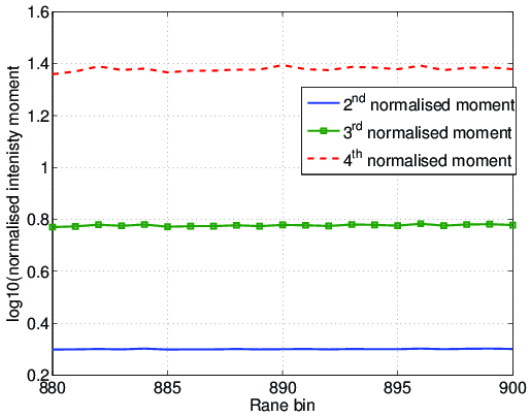

(b) After removing interference

Figure 4.13: Comparison of the normalised intensity of noise before and after removing interference.

assumed range the offset due to the GPSDO and the electronics (64 bins[8]) were accurately determined. Figure 4.14, shows the sidelobe breakthrough before and after range correction. From the figure the shift in range was 390 m or 65 range bins, which is one range bin more than the fix delay.

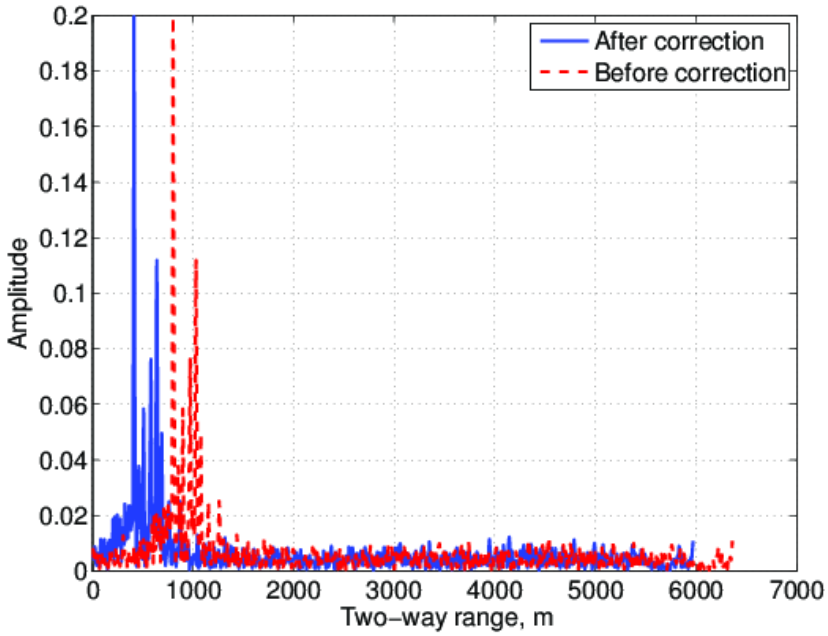

Figure 4.14: Range profile of the received power in the bistatic node, the baseline was 416 m, the correction was 65 bins inclusive of the fixed DDS delay of 64 bins.

4.4 Effect of Land Clutter

As the measurements are made with land based radar, land clutter my also affect the data. Two types of land clutter are of concern here, range extended land clutter, and range limited clutter. As the radar antennas were pointing towards the sea, the land was usually in the backlobe of the antennas. The exact amplitude of the returns is difficult to predict as it depends on the geometry and the surrounding environment. The effect of small targets such as vehicles is negligible at the ranges of interest. However, stationary objects in the sidelobe or in the mainlobe, such as cliff sides or marine markers will be detected by the radar.

The effect of extended land clutter was studied by simulating the returns from in front of and behind the antenna. In this simulation the transmitter and receiver were assumed to be on the x-axis of the coordinate system. The positive y-axis was in front of the antenna and the negative y-axis was behind the antenna. Both sides were assumed to have the same reflectivity. The actual measured antenna radiation pattern was used in the simulation. The ratio of the simulated received power from in front of the antenna and the back of the antenna are shown in Fig. 4.15.

As far as the bistatic node is concerned, the node locations and antenna directions were based on

[8]To improve accuracy this produce was performed after matched filtering.

those of the data gathered on 05-Oct-2010. The baseline was 416 m and the bistatic angle was $60°$, hence the two-way range was 832 m. The ratio was maximised close to the intersection point of the antennas. This is to be expected as away from the intersection point the returns are due to the overlap between the sidelobes or a mainlobe and a sidelobe. However, in the monostatic case, the ratio was almost constant except for the variation due to the change in the elevation angle. In the zone of interest the ratios ranged from 40 dB to 70 dB. Because of the high cliffs close to the shore line at trial locations, the effect of range extended land clutter was limited to the nearby returns. To further suppress land clutter, the zero Doppler is removed.

On the other hand there could be a large structure such as a cliff or a lighthouse, that has a considerably high RCS which could contaminate the returns in a few range bins. Such features were seen as straight vertical lines in the RTI and have zero Doppler. They were used to further check the phase correction or as markers. However, these bins were then not used for sea clutter data analysis.

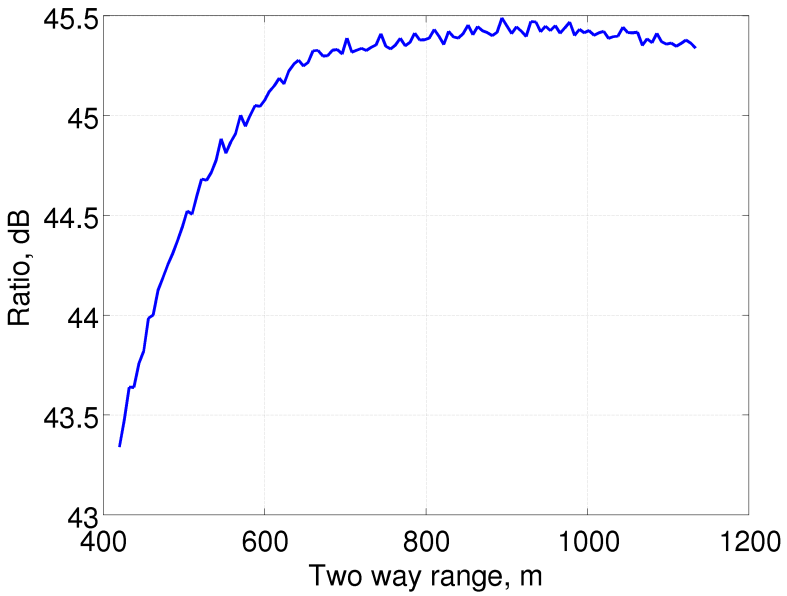

Figure 4.15: Ratio of the power returns from in-front of the antenna (sea) and the back (extended land clutter) for a monostatic radar, assuming $\sigma^\circ = 0\,\text{dB}\,\text{m}^2/\text{m}^2$.

Another effect which is more difficult to eliminate is land clutter in the mainlobe. This effect was noticed on the data gathered on 21-Oct-2010. Since the distance between the node locations and the shoreline was relatively long, most of the data was affected by land clutter. Figure 4.17 shows a sketch of the geometry at $\beta = 90°$, note how close the intersection point is to the land, even at smaller bistatic angles the effect of land clutter was still present. By examining the average returned intensity, shown in Fig. 4.18, there is a sudden increase in the power as the the echoes were returned from the land in front of the antenna. As the antenna beam starts to clear the land, the power starts to drop.

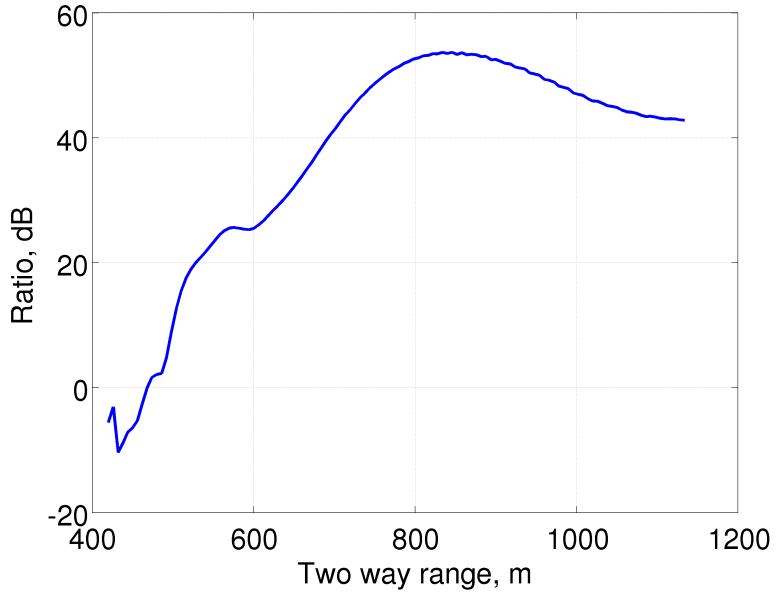

Figure 4.16: Ratio of the power returns from in-front of the antenna (sea) and the back (extended land clutter), assuming $\sigma^\circ = 0\,\text{dB}\,\text{m}^2/\text{m}^2$. The bistatic triangle was equilateral with each side equal to $416\,\text{m}$

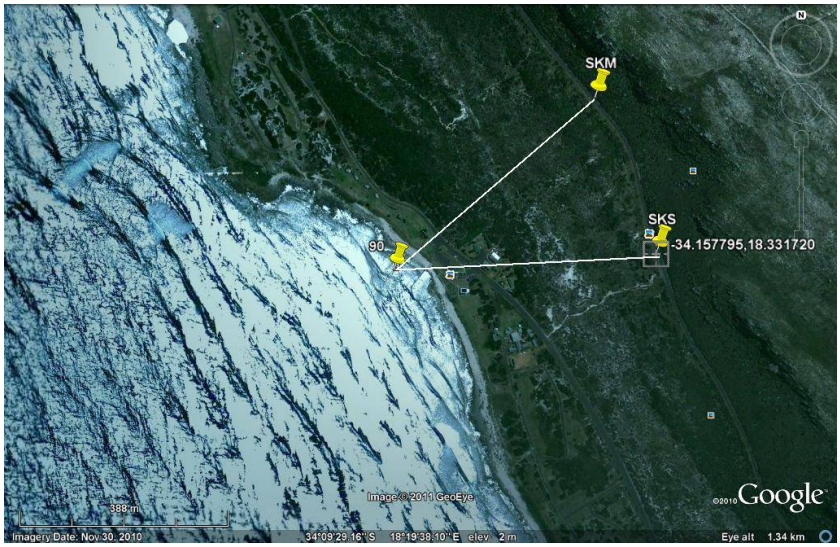

Figure 4.17: A Google earth picture showing how close the intersection point was to land at $\beta = 90°$.

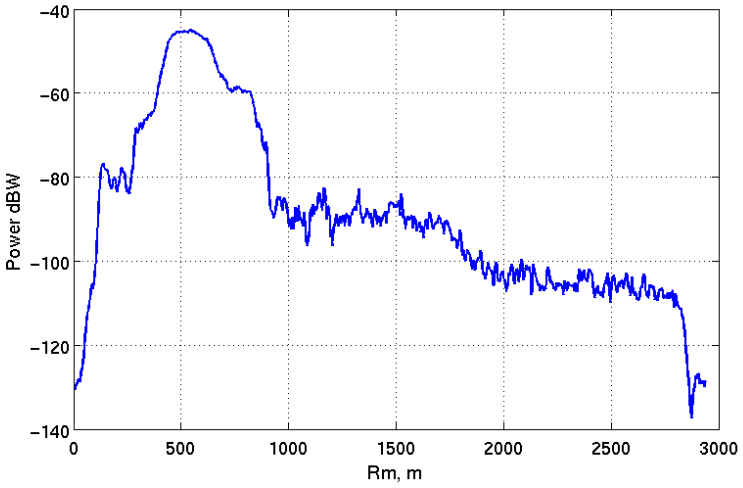

Figure 4.18: Average power recorded by the monostatic node, note the sudden increase in power around 500m and the sudden drop around 700 m

4.5 Summary

In this section a summary of the field trials in the UK and South Africa has been given. The chapter discussed both the technical and logistical issues. The variety of the environment and the availability of cooperative, non-cooperative maritime targets, the link with UCT and the cooperation with CSIR were the major reasons for conducting the main trials in South Africa.

An overview of the pre-processing preformed on the raw data has been presented. It was also shown that the effect of range extended land clutter is negligible because of the combined effects of the directivity of the antennas, the environment and the processing carried out.

The effect of in-band interference was also discussed. A simple yet effective method to eliminate the effect of interference was demonstrated.

The techniques to deal with the complications introduced by using the GPSDO were discussed. It has been shown that the effect of the phase drift has been almost completely removed and that the small uncertainty in the triggering system can be completely removed provided.

Some of the substantial logistical issues involved in planning and organising major radar trials in both the UK and South Africa have been briefly discussed. A general description of the data and surface truth has been given. Some of the measurements were taken at shallow depths, they are of great practical and theoretical interest as there are a few measurements reported on littoral water.

The following two chapters will concentrate on the average normalised reflectivity and statistical analysis of the amplitude of bistatic and monostatic sea clutter.

Chapter 5

Analysis and Modelling of Average Reflectivity

5.1 Introduction

In this chapter some of the data gathered during the trials in the Cape Town area in October 2010 is analysed. A description of the data processing and pre-processing was presented in the previous chapter. In this chapter, the variation of the bistatic angle across the resolution cell is studied. Next the method used to estimate σ° is described. The next section focuses on the analysis of the average reflectivity of out-of-plane bistatic and monostatic sea clutter data under different environmental conditions and geometries. The following section discusses a novel model to describe σ° for both in-plane and out-of-plane geometries. Finally the main findings and conclusions are discussed.

5.2 Effect of Beamwidth on Bistatic Angle

The antenna beamwidth of around 10° was chosen such that the clutter cell area at the measurement ranges is comparable to that of operational radars. However, this meant that the bistatic angle could vary across the clutter patch. A solution to this problem was not found in the published literature, thus this issue had to be studied in some detail.

Returns to a radar at a specific range cell can come from all directions. When using directive antennas the radiation pattern modulates the magnitude of the returned power. For surface clutter, the cross-range is usually used as a limit to the radar resolution in azimuth. Since the sea is a distributed target consisting of many scatterers, the bistatic angle subtended by the individual scatterers in the same isorange will change from $\beta = 0^\circ$ on the extended baseline to β_{max} when the bistatic angle bisector is perpendicular to the baseline i.e. the bistatic triangle is an isosceles triangle. Since the beam is finite, the bistatic angle will vary within the cross range resolution.

To assess the effect of beamwidth on the bistatic angle it was assumed that the range resolution at the zone of interest was negligible compared to distance to both the transmitter and receiver. To find the worst case scenario and simplify the calculations the gain was assumed to be constant across the one-way 3 dB beamwidth and negligible elsewhere. The four intersection points between the transmitter and

receiver beams and the isorange were found. These points were used as vertices for the bistatic triangle formed by the scatterer at that point and the transmitter receiver pair. A schematic diagram of such a geometry is shown in Fig. 5.1. The bistatic angle with the largest deviation from that at the centre of the beam was considered to be the upper limit for the variation in bistatic angle across the range cell. At this point the power drop with respect to the centre of the patch is at least 6 dB due to the antenna pattern.

$$\Delta\beta_i = |\beta_\circ - \beta_i| \quad \text{where} \quad i = 1, 2, 3, 4 \tag{5.1}$$

$$\Delta\beta = \max\left(\Delta\beta_1, \Delta\beta_2, \Delta\beta_3, \Delta\beta_4\right) \tag{5.2}$$

where $\beta_\circ$ is the bistatic angle at centre of the clutter patch, β_1 to β_4 are the bistatic angles subtended by the line of sight from the transmitter and receiver to the intersection points between the antennas 3 dB points and the isorange contour. An example result for a bistatic configuration with beamwidths of $10°$ and a baseline of 400 m is shown in Fig. 5.2. It is worth noting that as the intersection point approaches the baseline, one side of the beamwidth can cross to the other half ellipse thus increasing the variation in the bistatic angle. More details are provided in Appendix C.

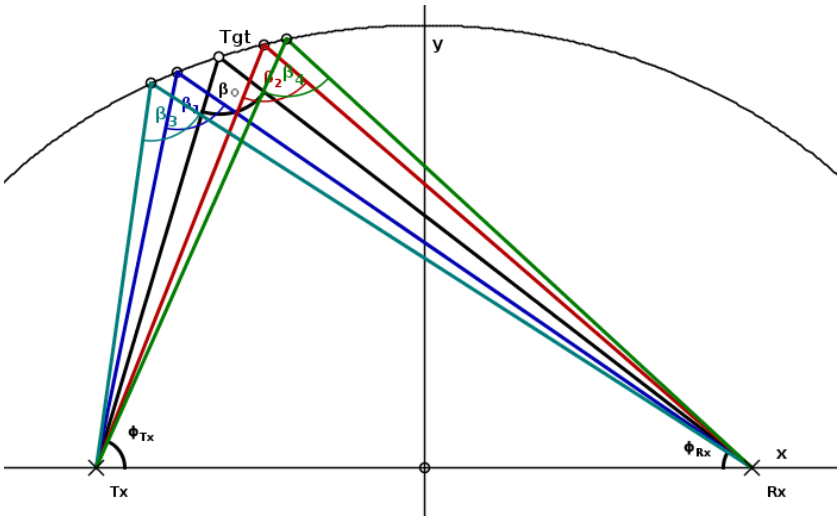

Figure 5.1: A sketch showing the variation of the bistatic angle across in a clutter cell, the dimensions are exaggerated for clarity.

5.3 Calculating the Normalised Reflectivity

As discussed in Section 2.1.4, there is no general closed form solution for the clutter cell area in the bistatic geometry. This being said, there is not a need to calculate the clutter cell area if the received power can be calculated. The required equations were developed in Section 2.1.4, but are repeated here for clarity.

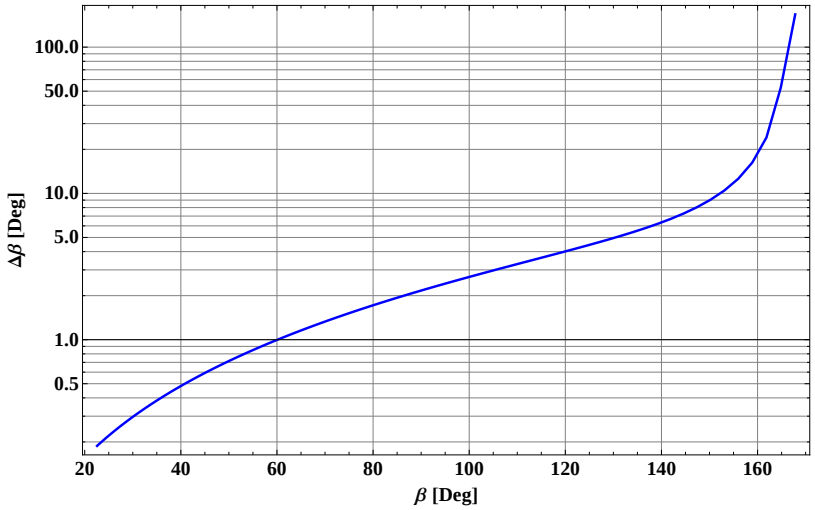

Figure 5.2: Variation of bistatic angle across the clutter cell as a function of the bistatic angle, the baseline was $400\,\mathrm{m}$ the bistatic triangle was an isosceles triangle. Note the large error as when $\beta > 144°$.

The received power P_R is given by:

$$P_R = K_A \sigma_B^{\circ} I \tag{5.3}$$

where

$$K_A = \frac{P_T G_{T\circ} G_{R\circ} G_{rx} \lambda^2 K_{mf}}{(4\pi)^3 L_T L_R L_P} \tag{5.4}$$

and

$$I = \int_x \int_y \frac{f_T^2(\phi_T, \theta_T) f_R^2(\phi_R, \theta_R)}{R_T^2 R_R^2} \, dxdy \tag{5.5}$$

where:

P_T: is the transmitted power, in Watts.

P_R: is the received power, in Watts.

G: is the antenna gain, in natural units.

G_{rx}: is the receiver chain gain.

λ: the wavelength, in metres.

L:is the system losses > 1, in natural units.

K_{mf}: is the matched filter gain.

L_p: processing loss, in natural units > 1.

$f(\phi, \theta)$: is the antenna propagation pattern factor as a function of the azimuth angle ϕ and elevation angle θ.

$_T$ and $_R$ denote transmitter and receiver related quantities respectively.

The integral I can be approximated by:

$$\hat{I} \approx \begin{cases} \sum_i \sum_j \frac{f_T^2(\phi_{Tij},\theta_{Tij}) f_R^2(\phi_{Rij}\theta_{Rij})}{R_{Tij}^2 R_{Rij}^2} \Delta x_i \Delta y_j & \text{if } |R_{Tij} + R_{Rij} - R_\circ| \leq \tau c \\ 0 & \text{if } |R_{Tij} + R_{Rij} - R_\circ| > \tau c \end{cases} \tag{5.6}$$

Estimating the backscatter coefficient σ° from the measured data is a three step process:

1. Evaluating Eq. (5.6). This is straightforward since the geometry is determined by knowing the antenna depression and azimuth angles of the transmit and receive antennas, the location of the transmit and receive antennas and the radiation pattern of the antennas.

2. Calculating K_A. All the radar parameters have been accurately measured.

3. P_R is estimated by averaging the received power from a single range bin over slow time.

Thus all the parameters in Eq. (5.3) are known system parameters except for σ_B°, which can be approximated by:

$$\hat{\sigma_B^\circ} \approx \frac{\hat{P_R}}{K_A \hat{I}} \tag{5.7}$$

To check the validity of the code, the clutter cell area was calculate and compared with the monostatic and bistatic approximations. The total received clutter power is given by:

$$P_R = \frac{K_A \sigma_B^\circ f_T^2(\theta_\circ, \phi_\circ) f_R^2(\theta_\circ, \phi_\circ) A_c}{R_{R\circ}^2 R_{T\circ}^2} \tag{5.8}$$

while the power received due to the scatterer at the centre of the clutter patch $P_{R\circ}$ is given by:

$$P_{R\circ} = \frac{K_A \sigma_B^\circ f_T^2(\theta_\circ, \phi_\circ) f_R^2(\theta_\circ, \phi_\circ) \Delta A}{R_{R\circ}^2 R_{T\circ}^2} \tag{5.9}$$

Thus the clutter cell area is given by:

$$A_c = \frac{P_R}{P_{R\circ}} \Delta A \tag{5.10}$$

The results from the above equation were compared with those obtained by using a closed form equation for the monostatic radar

$$A_{cM} \approxeq 0.7527 \phi_{3dB} R_{M\circ} \Delta R_M \tag{5.11}$$

As can be seen from Fig. 5.3a, the two estimates are almost the same. To compare the bistatic measurements, the monostatic clutter cell area was divided by $\cos^2(\beta/2)$, as suggested in [22], and the results are plotted in Fig. 5.3b. In the bistatic case the baseline was 416 m. The error between the two estimates was reduced as the range was increased (the bistatic angle was decreased). As can be seen from the plot

the magnitude of the ripple was reduced by reducing Δx and Δy from $1\,\mathrm{m}^2$ to $0.2\,\mathrm{m}^2$. Such errors have negligible effect on the final results as the clutter area greater than $100\,\mathrm{m}$.

5.4 Reflectivity of Monostatic and Bistatic Sea Clutter

In this section σ° of both monostatic and bisector sea clutter are analysed. This analysis is based on data was gathered on 05 and 10-Oct-2010 between 14:00 and 18:00. Only out-of-plane data will be discussed in this section. In both cases the grazing angles were small, it can be seen from Eq. (2.32) that the bistatic angle was almost equal to the difference between the azimuth angles of the transmit and receive antennas.

5.4.1 Low Sea State Data

This data set was gathered at Cape Point on 05-Oct-2010. A subset of this analysis was reported in [136]. Because of the transmitted power limitations the maximum attempted monostatic range was $1600\,\mathrm{m}$, which corresponds to a bistatic angle of 15°. Thus the data collection area may be classed as littoral. A nautical chart of the area is shown in Fig. 4.5. Examples of the antenna coverage pattern for the monostatic and bistatic nodes are shown in Figs. 5.4a and 5.4b, the blue line in the image represents the isorange contour. The colour intensity in the plot is proportional to the power at the receiver due to a $1\,\mathrm{m} \times 1\,\mathrm{m}$ scatterer. It is clear from the plot that most of the power is directed towards the sea. Examples of the monostatic and bistatic RTI are shown in Fig. 5.5, it is interesting to note how the clutter returns in the bistatic case were limited by the beams intersection. Both nodes were looking down wind and up swell; a sketch of the geometry is shown in Fig. 5.6. The wave data was based on the Cape Point station around $20\,\mathrm{km}$ to the north, this data indicated that the waves were coming from a southerly direction however, because of the waves close proximity to the shore the wind was coming towards the coast line almost normal to the bistatic bisector; the reported wave height was around $1.3\,\mathrm{m}$. The wind data was obtained from the historical reading of the Cape Point weather station and compared by the average historical readings of three weather stations in the Cape Point area, the wind speed was around $3.1\,\mathrm{m\,s}^{-1}$ and the wind direction was south-southwest. From visual observation and the wave height and wind speed the sea was between sea states 1 and 2. A summary of the surface truth is provided in Table 5.1, from the wind speed and wave height the sea state was around 2. The summary of the radar geometries is provided in Table 5.2, it is clear that the clutter cell area increased as the range increased. The difference between the bistatic and monostatic clutter cell areas was almost inversely proportional to $\cos^2(\beta/2)$. In addition, since the azimuth beam was wider at horizontal polarisation, 11° compared to 9° at vertical polarisation the clutter cell area was larger when using horizontal polarisation, the cross-polarised clutter cell area was closer to that of vertical polarisation since the clutter cell area is limited by the smallest cross-range.

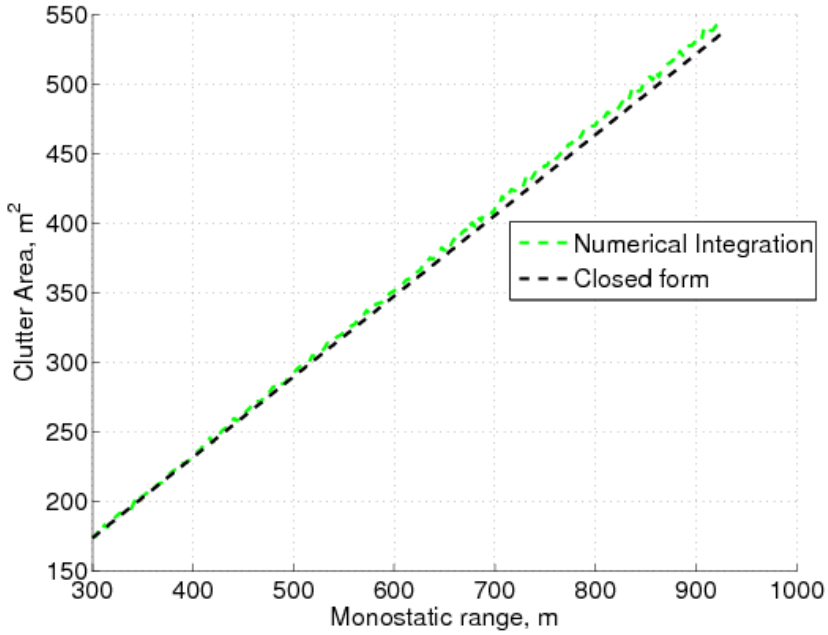

(a) Monostatic clutter cell area

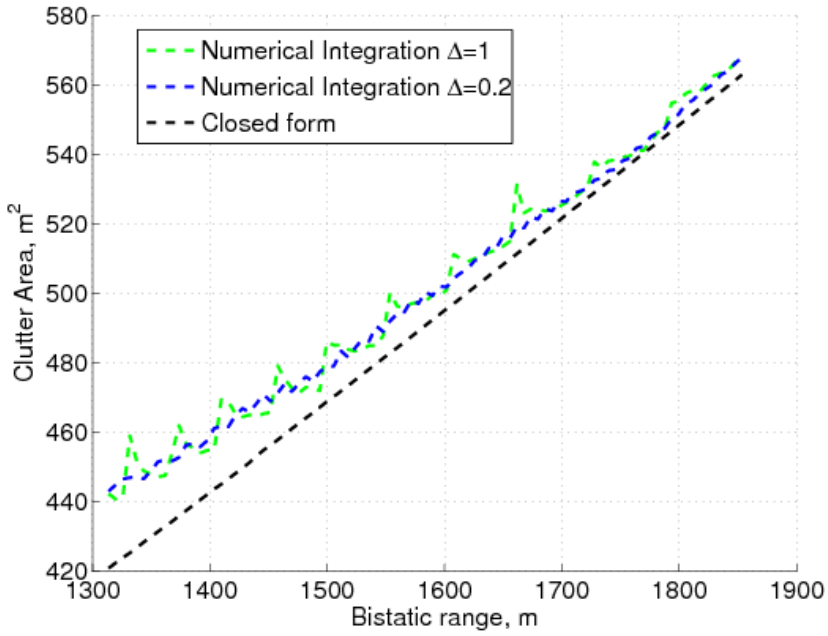

(b) Bistatic clutter cell area

Figure 5.3: Comparison of approximate closed form methods and numerical methods for estimating the monostatic and the bistatic clutter cell area. The simulation was performed using the measured antenna patterns in vertical polarisation. In the bistatic case the baseline was 416 m. Colour scale in dB.

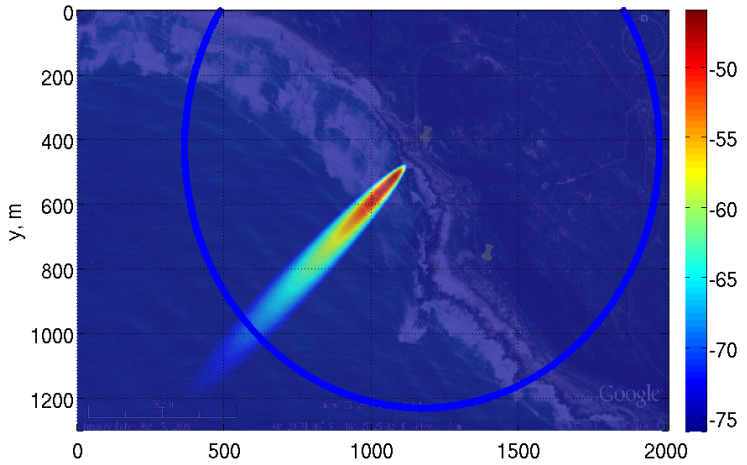

(a) Monostatic node

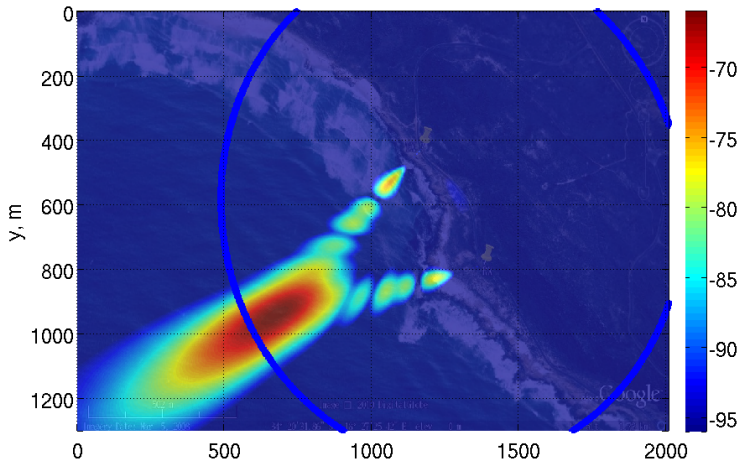

(b) Bistatic node, $\beta = 30°$

Figure 5.4: Antenna coverage pattern for monostatic and bistatic nodes superimposed on an aerial image of the trial site at Cape Point. The equivalent monostatic range was 805 m corresponding to a bistatic angle of 30°. The antennas of both nodes were vertically polarised. Colour scale in dB.

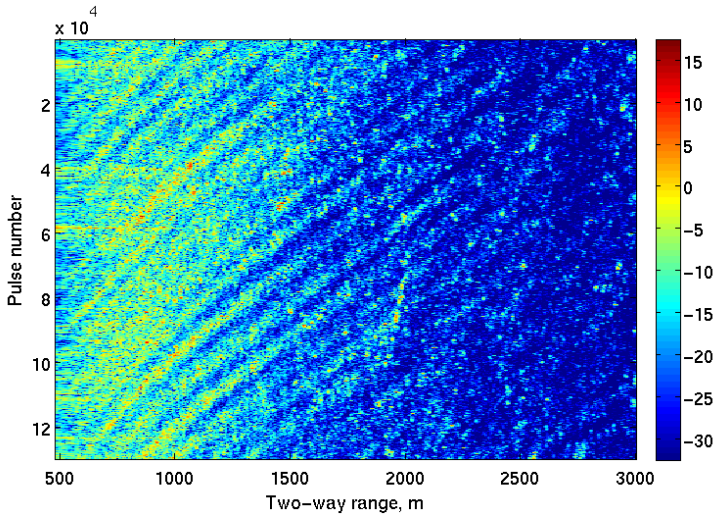

(a) Monostatic geometry

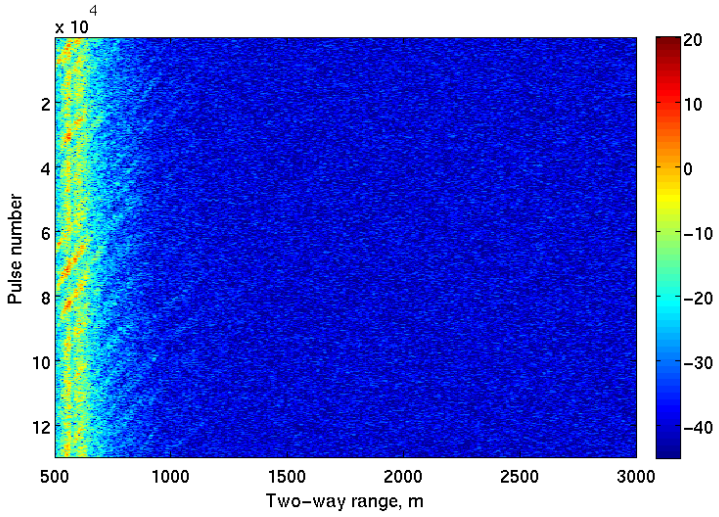

(b) Bistatic geometry, $\beta = 90°$

Figure 5.5: RTI of simultaneously recorded vertically polarised monostatic and bistatic sea clutter, recorded at 15:09 on 05-Oct-2010, note how the clutter returns are limited to the intersection area in the bistatic case, the colour bar represents the received power in dBm. Colour scale in dBm

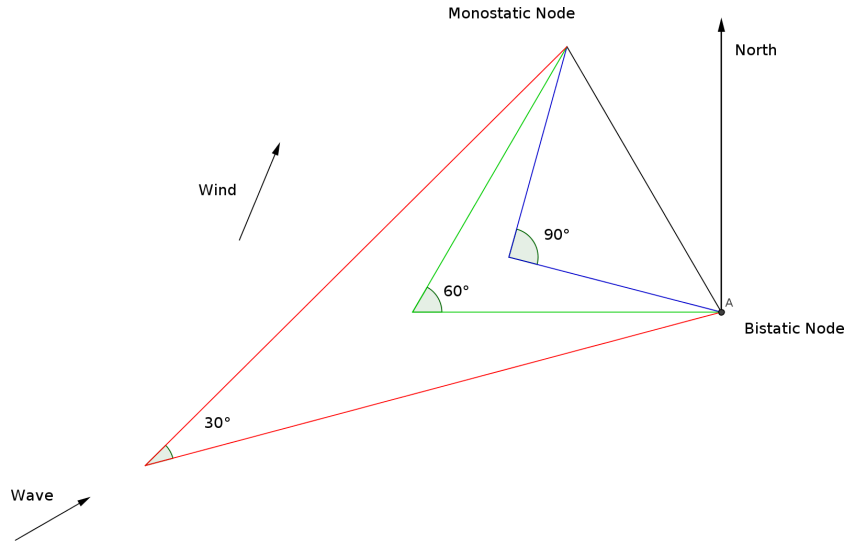

Figure 5.6: A sketch of the geometry used on 05-Oct-2010, showing the wind and wave directions.

Based on these measurements the CNR and σ° were calculated and these results are summarised in Table 5.3. As expected both σ°_M and σ°_B decreased with increasing range (decreasing depression angle θ). σ°_B and σ°_M are plotted in Fig. 5.7. The difference between σ°_M and σ°_M increased as the bistatic angle increased up to $\beta = 90°$. The reported measurements were taken at the range bin closest to the intersection point, except for those at the vicinity of $\beta = 90°$ which were taken at the value that gave the minimum σ°_B, which could be off by around $1°$. The σ°_B was almost identical to σ°_M up to bistatic angles of $60°$. However, there was a very sharp drop close to $\beta = 90°$ as can be seen at both polarisations. Although the repeat measurement at 16:08 resulted in an increase in σ° by about 7 dB, ratio of the bistatic to monostatic σ° changed by less than a dB. Such changes are not uncommon in sea clutter measurements. The ratio of σ°_B to σ°_M was larger in horizontal polarisation, -16 dB compared to -10 dB in vertical polarisation. As far the cross-polarised measurements are concerned, σ°_B was more than σ°_M around $\beta = 90°$, by around 5 dB. Similar results have been reported for smooth sand [137]. However, this is the first time such results have been reported for sea clutter.

The measured normalised radar cross section values were also compared with those predicted by theoretical models. The GIT model [1] [59, 138] was used for the co-polar σ°_M, while Long's model [31] was used for σ°_{MHV}; the results are summarised in Fig. 5.10. The results were in good agreement except for that when at a depression angle of $0.72°$. This could be because that the angle is smaller than the critical angle, hence, the drop in σ°_M is volatile.

Since the clutter cell area also increases with increasing bistatic angle, a reduction in the normalised radar cross section that is smaller than the increase in the clutter cell area will not reduce the clutter power. However, it is clear from Table 5.3 that the CNR is smaller for the bistatic node. This is also

[1] The GIT is discussed in more details in Appendix B

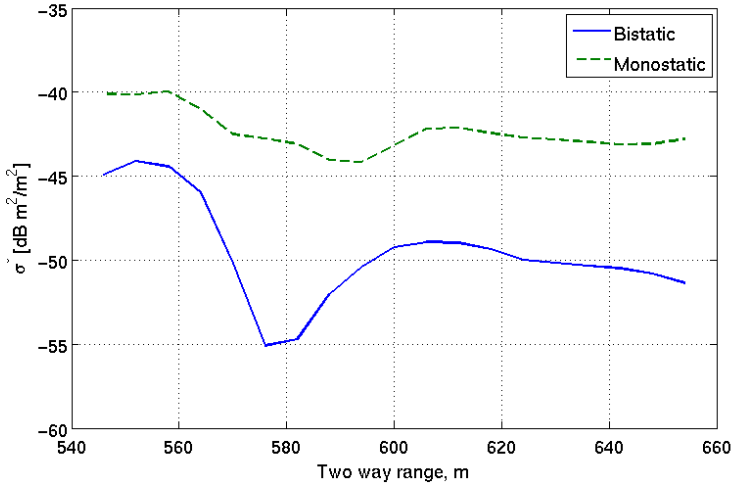

Figure 5.7: Bistatic and monostatic normalised reflectivity data gathered at 15:09 on 05-Oct-2010 , $\beta = 90°$ corresponds to a two-way range of 590 m.

Time	Wind speed, m s^{-1}	Wind Direction, degree	Period, s	Wave direction, degree	$H_{1/3}$, m
14:46	3.23	South-southwest	10.55	To coast	1.3
14:55	3.23	South-southwest	10	To coast	1.32
15:09	3.23	South-southwest	10	To shore	1.32
15:53	3.43	South-southwest	9	To coast	1.28
16:08	3.35	South-southwest	9	To coast	1.28
16:26	3.37	South-southwest	8.3	To coast	1.33
17:16	3.6	South-southwest	8.65	To coast	1.36
17:30	3.23	South-southwest	9	To coast	1.39
17:41	3.23	South-southwest	8.65	To coast	1.39

Table 5.1: Sea and wind conditions for the trial conducted on 05-Oct-2010, the wind direction was measured with respect to true north.

reflected in Fig. 5.9 where it is clear that $\sigma_B < \sigma_M$ except when $\beta = 30°$, the pseudo-monstatic case. The ratio was larger for horizontal polarisation, as compared to the ratio of vertically polarised clutter. The cross-polarised component was larger in the bistatic configuration at $\beta = 90°$ by almost 7 dB an increase of around 2 dB from normalised ratio.

5.4.2 High Sea State Data

This data set was gathered on 21-Oct-2010, the nodes were placed off a coastal road to the north of Scarborough on the Cape Peninsula. The separation between the two nodes was 1827 m. An aerial view and a nautical chart of the area are shown in Figs. 4.8 and 4.9. A plot of the antenna coverage superimposed on an aerial image of the Scarborough area is shown in Figs. 5.11a and 5.11b, it is clear from the image that most of the power is directed towards the sea. The blue curve represents the isorange. Examples of the monostatic and bistatic RTI are shown in Fig. 5.12, the bistatic clutter was also limited

β, degree	Polarisation	R_T, m	θ, degree	A_{cB}, m^2	A_{cM}, m^2
15	VV	1596	0.72	965	942
30	VV	805	1.42	510	475
60	VV	418	2.75	330	250
90	VV	296	3.88	378	181
90	HV	296	3.88	410	190
15	HH	1596	0.72	1168	1138
30	HH	805	1.42	610	573
90	HH	296	3.88	463	228

Table 5.2: Summary of the geometries used on 05-Oct-2010.

Time	β	Polarisation	Bistatic		Monostatic	
			CNR_B, dB	σ°_B, dB m^2/m^2	CNR_M, dB	σ°_M ,dB m^2/m^2
14:46	30°	VV	10.5	-59	8	-59
14:55	60°	VV	27	-47.9	26	-47.1
15:09	90°	VV	25	-55	33	-44.5
15:53	15°	VV	-7	–	-12	–
16:08	90°	VV	32	-47.8	39	-37.6
16:26	90°	HV	26	-55	16	-59.8
17:16	90°	HH	18	-61	31	-44.8
17:30	30°	HH	-15	–	-5	–
17:41	15°	HH	-10	–	-4	–

Table 5.3: Summary of the normalised reflectivity and CNR for data collected on 05-Oct-2010.

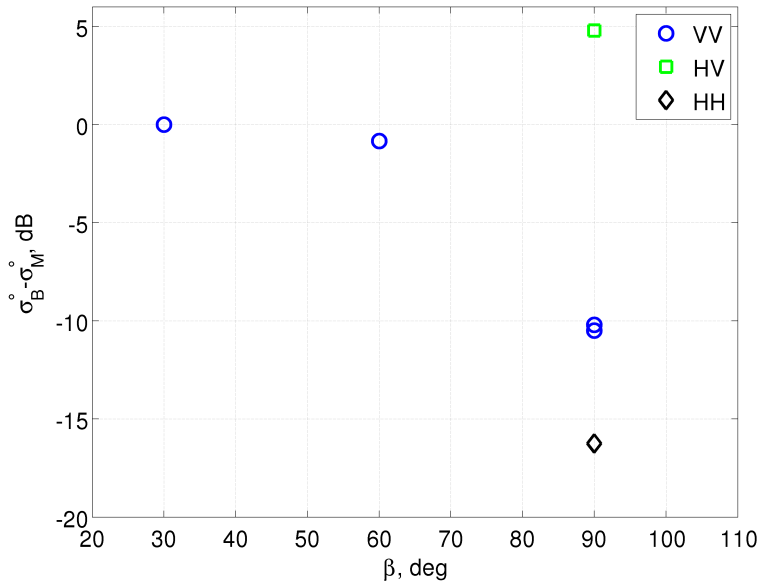

Figure 5.8: The ratio of σ°_B to σ°_M as a function of the bistatic angle, for a low sea state. Data gathered on 05-Oct-2010.

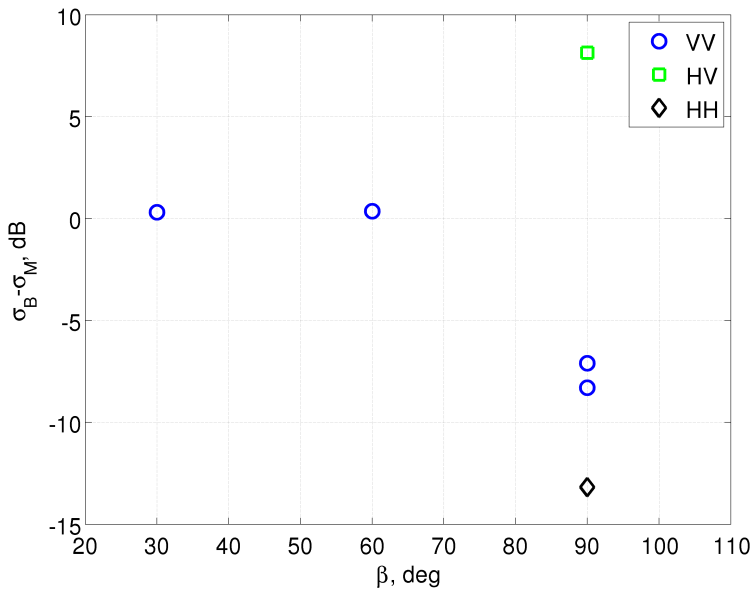

Figure 5.9: The ratio of σ_B to σ_M as a function of the bistatic angle for a low sea state. Data gathered on 05-Oct-2010.

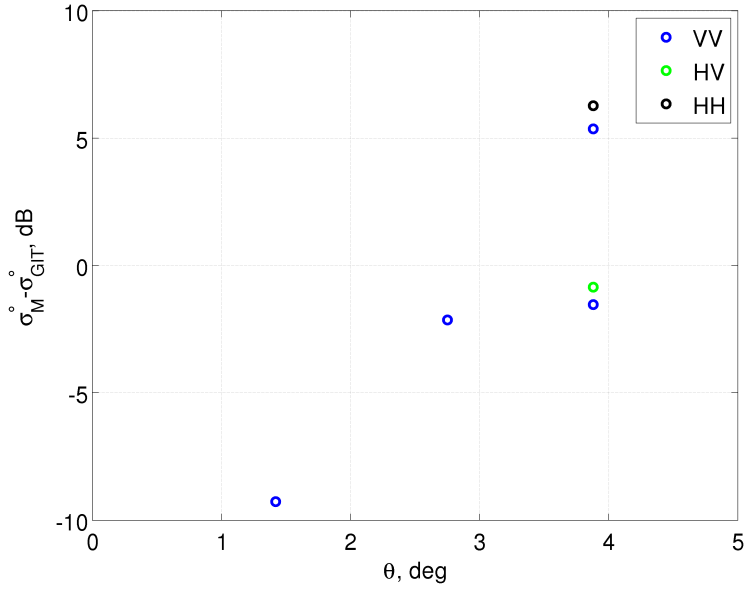

Figure 5.10: Comparison between the σ° as predicted by theoretical models σ°_{GIT} and as computed from the data collected on 05-Oct-2010 ($NRCSM$ as a function of the depression angle. The GIT model was used to predict the co-polar normalised cross-section and Long's model for the cross-polar.

by the overlap between the transmit and receive antenna beams.

A summary of the ground truth is presented in Table 5.4. As can be seen from Table 5.4 the wind speed increased during the trial from around $10.18\,\mathrm{m\,s^{-1}}$ to $12.3\,\mathrm{m\,s^{-1}}$, similarly the significant wave height $H_{1/3}$ increased from $3.28\,\mathrm{m}$ to $4.2\,\mathrm{m}$. Both nodes were looking across wind with the waves travelling towards the receiver, it should be noted that the wave direction will change from that in Table 5.4 as it is approaching the shore. A sketch of the experiment setup showing the wind and wave directions is shown in Fig. 5.13. The wave data was based on the Cape Point station around $6.8\,\mathrm{km}$ to the west. The wind data was obtained by averaging the historical readings of two weather stations in the Cape Town area. Given the close proximity of the wave buoy the wave data would be more accurate at this location compared to Cape Point. Nevertheless, the actual values might change as the waves approach the shore, i.e. at closer ranges and larger bistatic angles. Furthermore, the wind speed and the significant wave height corresponds to sea states 5; during the trial the sea state was estimated visually to be between sea states 4 and 5. There was intermittent heavy rain during this trial.

The summary of the radar geometry is given in Table 5.5. As in the Cape Point data the ratio of the monostatic clutter cell area to the bistatic one is proportional to $\cos^2(\beta/2)$. For the data analysed in this section the depression angle θ varied slightly between $0.63°$ and $1.08°$ corresponding to one way ranges between $1827\,\mathrm{m}$ at a bistatic angle of $60°$ and $1055\,\mathrm{m}$ at $\beta = 120°$.

Based on these measurements the CNR and σ° were calculated and the results are summarised in Table 5.6. A comparison between the measured σ°_M and those predicted by the GIT model is shown in Fig. 5.16. The GIT predicted that the horizontally polarised σ°_M would drop from $-45\,\mathrm{dB}$ to $-42\,\mathrm{dB}$, the vertically polarised σ°_M was estimated to be between $-44\,\mathrm{dB}$ and $-39\,\mathrm{dB}$, as the depression angle was changed form $0.63°$ to $1°$. Although discrepancies might seem large, they are either due the critical angle effect, and small variations in the grazing angle could result in large changes in σ°. As expected both σ°_M and σ°_B decreased with increasing range, decreasing depression angle θ. On the other hand, σ°_B, remained almost unaffected by the change in the depression angle and bistatic angle. Both monostatic and bistatic σ°_M were much higher at vertical polarisation. In addition, the ratio of the σ°_B to σ°_M had a minimum around $90°$, as shown in Fig. 5.14.

It is interesting to note although σ°_M was larger than σ°_B by around $12\,\mathrm{dB}$ at $\beta = 120°$ at vertical polarisation the radar cross section was only larger by around $4\,\mathrm{dB}$; the same was true for horizontal polarisations were σ°_M was larger than σ°_B by around $10\,\mathrm{dB}$ but the radar cross section was larger by $3\,\mathrm{dB}$ only. This was due to the increase in the clutter cell area. The ratio of the bistatic to monostatic radar cross section is shown in Fig. 5.15. In all cases the ratio was smaller in horizontally polarised clutter.

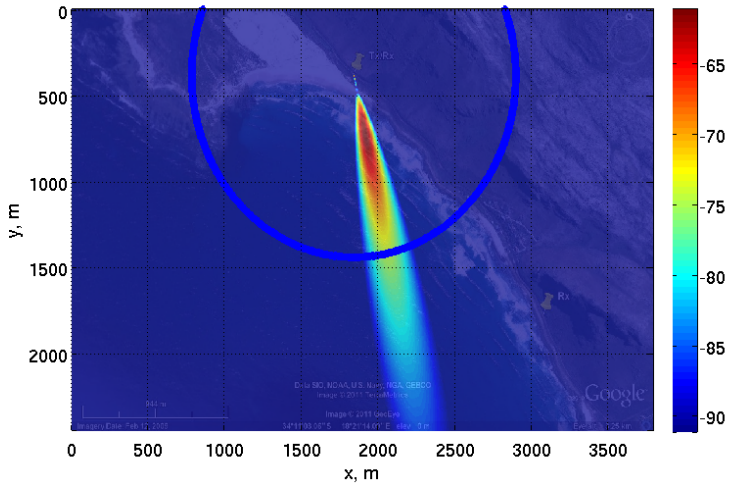

(a) Monostatic node

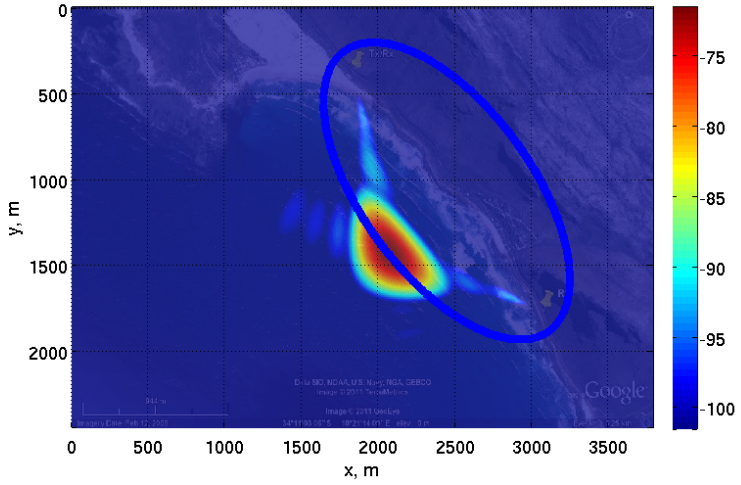

(b) Bistatic node, $\beta = 120°$

Figure 5.11: Antenna coverage pattern for monostatic and bistatic nodes superimposed on an aerial image of the trial site at Scarborough. The equivalent monostatic range was 1055 m corresponding to a bistatic angle of $120°$. The antennas of both nodes were vertically polarised. Colour Scale in dB.

Time	Wind speed, meter/s	Wind Direction, degree	Period, second	Wave direction	$H_{1/3}$, meter
12:20	10.18	North	7.1	289	3.28
12:33	10.15	North	7.1	289	3.28
12:44	10.37	North	7.7	279.5	3.48
12:53	10.8	North	8.3	270	3.67
15:51	11.55	North	8.3	283	3.89
16:03	11.55	North	8.3	283	3.89
16:17	12.3	North	8.65	276	4.02

Table 5.4: Sea and wind conditions for the trial conducted on 10-Oct-2010

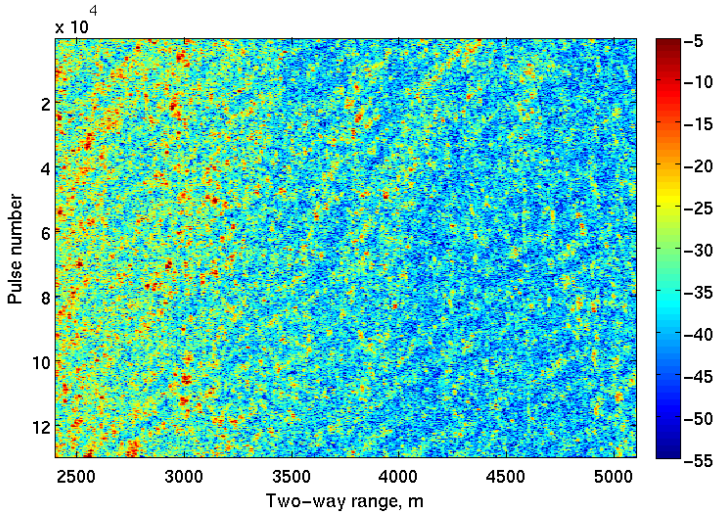

(a) Monostatic geometry

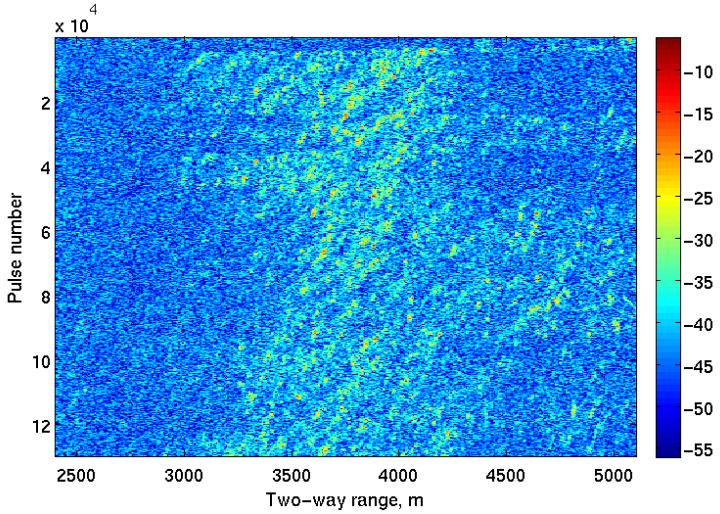

(b) Bistatic geometry, $\beta = 90°$

Figure 5.12: RTI of simultaneously recorded horizontally polarised monostatic bistatic sea clutter recorded at 12:53 on 10-Oct-2010, note how the clutter returns are limited to the intersection area in the bistatic case. Colour scale in dBm

β, degree	Polarisation	R_T, meter	θ , degree	A_{cB} , m^2	A_{cM} , m^2
60	HH	1827	0.63	1462	1936
90	HH	1292	0.89	1025	2021
120	HH	1055	1.09	835	3322
60	VV	1827	0.63	1199	1588
90	VV	1292	0.89	841	1641
120	VV	1055	1.09	685	2671

Table 5.5: Summary of the geometries used for the data recorded on 10-Oct-2010.

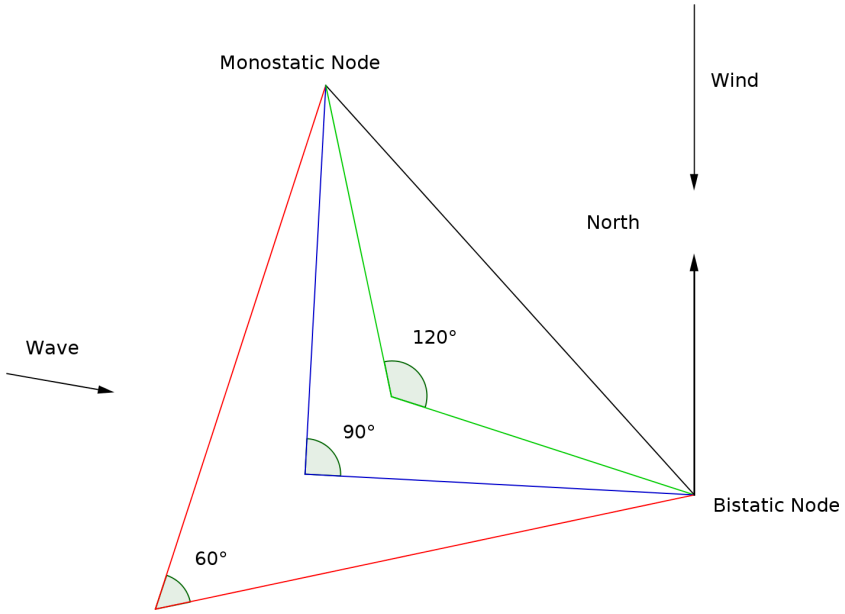

Figure 5.13: A sketch of the geometry used on 10-Oct-2010 showing the wind and wave direction.

Time	β, degree	Polarisation	Bistatic		Monostatic	
			CNR	σ°, dB m^2/m^2	CNR, dB	σ°, dB m^2/m^2
12:20	60	HH	7	-58.1	9	-51.2
12:33	60	HH	7	-58.2	10.5	-49.5
12:44	90	HH	12.5	-57.1	18.5	-44.3
12:53	120	HH	15	-58.9	16.2	-49.8
15:51	60	VV	13.5	-51.6	20.5	-38.4
16:03	90	VV	17	-52.6	24	-38.6
16:17	120	VV	23.6	-51	25.6	-38.8

Table 5.6: Summary of the normalised reflectivity and CNR for data collected on 10-Oct-2010.

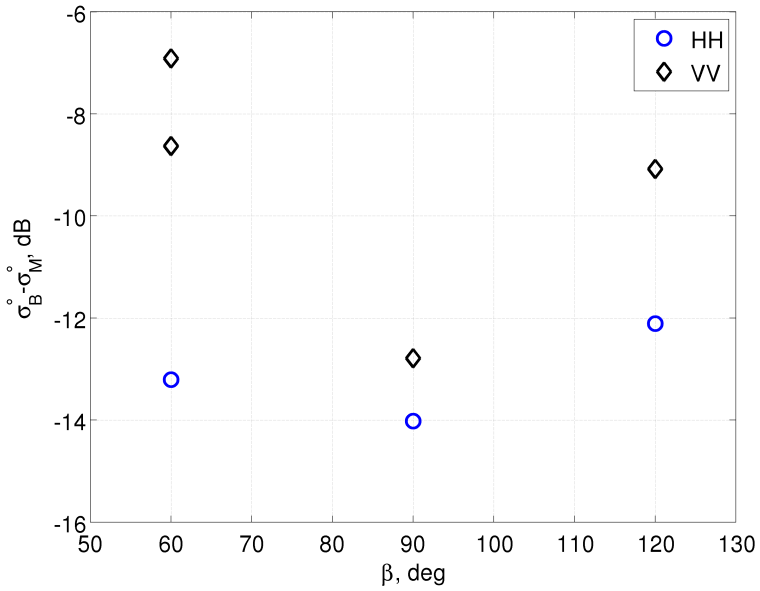

Figure 5.14: The ratio of σ_B° to σ_M° as a function of the bistatic angle, the data was recorded on 10-Oct-2010.

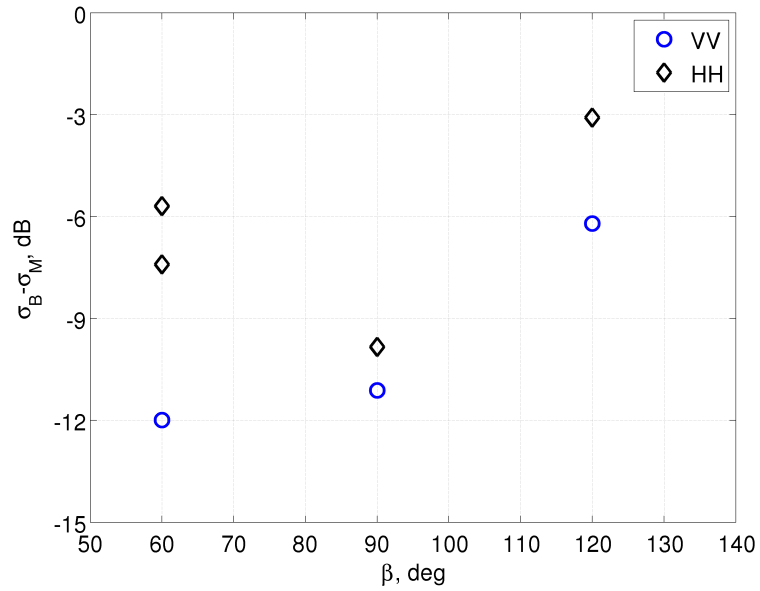

Figure 5.15: The ratio of σ_B to σ_M as a function of the bistatic angle, the data was recorded on 10-Oct-2010.

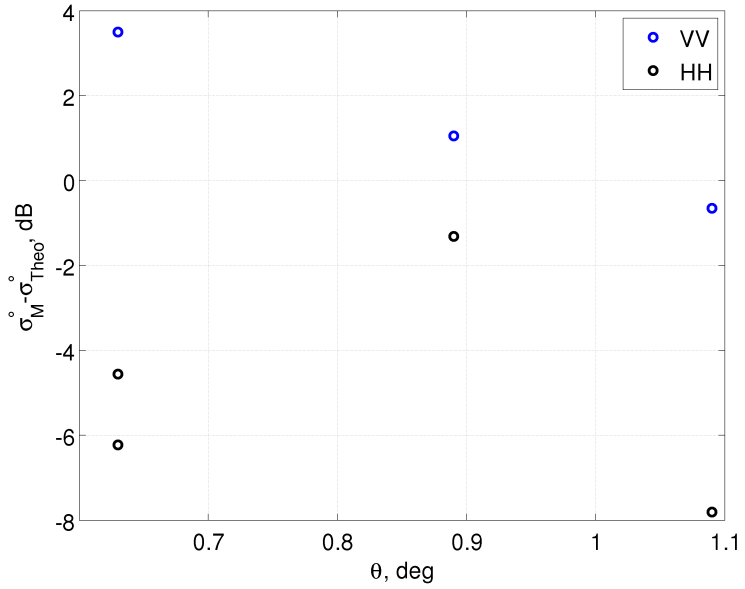

Figure 5.16: Comparison between the σ° as predicted by the GIT (σ°_{GIT}) model and that from the data collected on 10-Oct-2010 ($NRCSM$).

5.5 Empirical Modelling of Bistatic Sea Clutter

In this section an analysis of published radar bistatic clutter data and those described in the previous sections are used to test a new empirical model for the average σ°_{B}, of bistatic sea clutter, [106]. More insight has been gained into the model and the predicted behaviour of bistatic clutter, thus the fits generated in this work are different from these reported in [106]. The model is applicable to backscattering rather than forward scattering geometries and concentrates on low grazing angles. Following Barton's approach to land clutter [120], in-plane geometries are modelled as the geometric mean of the monostatic clutter from the transmitter and receiver positions. For out-of-plane clutter this method is extended to include the effects of changing the look angle the different scattering environment. Both UCL out-of-plane data and published data were fitted to the model. Ideally, simultaneous polarimetric monostatic and bistatic measurements of sea clutter should be used to as inputs to the models. Due to the lack of such data, empirical models were used to fill the gaps, it was found that the GIT was the most suited model for use with co-polarised data. For the cross-polarised terms the only model found in literature was Long's model which has its limitations in frequency and wind speed. If other models exist which better describe a particular data set or environmental conditions they can be used without much change to the model.

5.5.1 Modelling In-Plane Sea Clutter

Early in-plane sea clutter experiments by Pidgeon [108] and Domville [109, 110], and more recently by Kochanski et. al [111], have shown that the smaller of the transmitter and receiver grazing angles tends

to dominate the resulting $NRCSB$. Willis [25] analysed Domville's data using Barton's model [120] for bistatic land clutter, which is of the form:

$$\sigma_B^\circ = \gamma \sqrt{\sin(\theta_1)\sin(\theta_2)} \tag{5.12}$$

where γ is the so-called 'constant Gamma coefficient'.

Equation (5.12) is the geometric mean of the, σ_M° (derived using the constant gamma clutter model) that would be obtained by radars positioned at the transmitter and the receiver. This may be improved by using a more accurate description of monostatic clutter, such as the Georgia Institute of Technology (GIT) model[2], which is described in Appendix B. For the in-plane backscattering case the normalised bistatic radar cross section σ_B° is given by:

$$\sigma_B^\circ = \sqrt{\sigma_M^\circ(\theta_1)\,\sigma_M^\circ(\theta_2)} \tag{5.13}$$

where $\sigma_M^\circ(\theta_1)$ and $\sigma_M^\circ(\theta_2)$ are the co-polarised normalised radar cross sections from the monostatic transmitter and the bistatic receiver positions respectively in $\mathrm{m}^2/\mathrm{m}^2$.

In general, it is difficult to compare models with individual sets of experimental data because of the inaccuracies inherent in measuring and reporting the surface truth in most sea clutter measurements. Specific environmental conditions, such as ducting and undeveloped seas, can result in significant discrepancies. Furthermore, most bistatic measurements have not reported simultaneous monostatic results.

Despite these limitations, in order to check that no additional terms are required in Eq. (5.13), it was compared with Willis's overall analysis of the Domville's data. In both models the wind speed was set to 20 kn (about $10\,\mathrm{m\,s^{-1}}$), the transmitter grazing angle was set to 1°, and a fully developed sea was assumed. Willis used $\gamma = 20$ dB for vertically polarised σ_B°. For the GIT model the radar was assumed to be looking crosswind[3]. Figure 5.17 shows a good agreement between the models, with just a small difference, which increased slightly as the receiver grazing angle was increased. At $\theta_2 = 10^\circ$ the model estimate was higher than Willis's by 2.5 dB, which is within the overall data variability. Contour plots for Eq. (5.13) have also been generated and compared with Domville's plots for horizontal and vertical polarisations at a wind speed of 20 kn; the same parameters were used as stated above except for θ_2 which was variable. Figures 5.18a and 5.18b show the results for horizontal and vertical polarisation respectively. Domville's original plots are reproduced in Fig. 2.5. The model did not predict the extremely small σ_B° reported by Domville when one of the grazing angles was small and the other was much larger[4]. However, at other angles the models were within close agreement, for example at

[2]Other σ_M° models, or measurements of σ_M° from both locations can be used.
[3]In the GIT model the σ_M° returned for cross wind conditions is between that of the upwind and downwind conditions.
[4]This might be because the GIT model over estimated σ_M° at small angles, this was the case with UCL data.

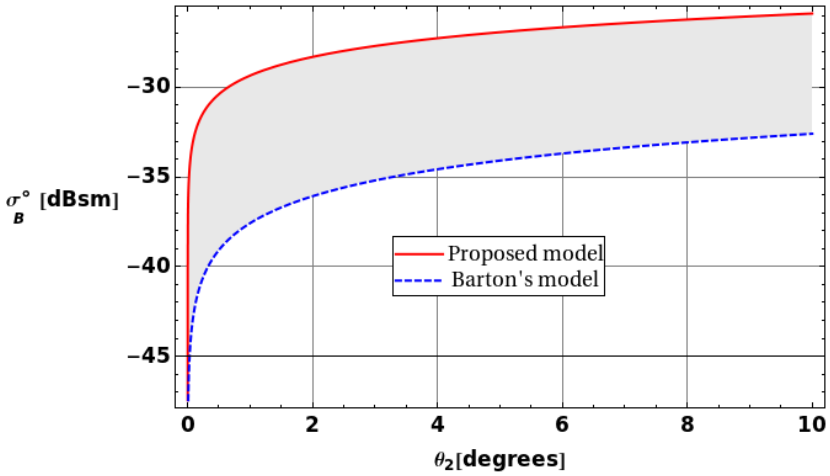

Figure 5.17: Proposed model vs. Willis's fit for V-pol and 20 kn wind speed

$\theta_1 = 10°$ and $\theta_2 = 8°$ the difference between the model predictions and Domville's measurements was less than 0.5 dB, and at $\theta_1 = 20°$ and $\theta_2 = 20°$ the model overestimates the σ_B° by around 1 dB. The differences were within those usually found in clutter measurements, despite the use of the GIT model at angles up to 30°. Furthermore, the general shape, spacing between contours and the differences between horizontally and vertically polarised data were consistent with those reported by Domville. In addition, the model fits the data best in the monostatic case which indicate that the GIT model as used provided a good fit up to 30°. This model provided a better fit than that proposed by Willis.

5.5.2 Out-of-Plane Bistatic Sea Clutter Model

In order to extend the new model to out-of-plane scattering, firstly the effect of different transmitter and receiver azimuth angles must be taken into account in the terms in Eq. (5.13). The monostatic normalised radar cross section of the sea surface depends on both the depression angle and the look angle. Their effects on σ_M° from the transmitter and the equivalent σ_M° from receiver positions can be calculated using a model that takes into account the antenna look angle with respect to the sea such as the GIT model.

In addition to the above effects. Measured out-of-plane bistatic data [137] and theoretical analysis of bistatic clutter [103] has shown that the co-polarised clutter normalised radar cross section decreases with increasing scattering angle. In addition, the cross-polar component increased with decreasing frequency up to a scattering angle of around 90°. In this model, it was assumed that the contributions are due to the co-polarised clutter as in the in-plane model and a cross-polar term that increases with increasing scattering angle until it reaches the peak at around 90°. Weighted sinusoidal multipliers were used to control the contribution of the co- and cross-polarised components. For the co-polar contribution $|\cos\phi|^m$ was proposed, where m is adjusted to match the data, the function will have a maximum of 1 for in-plane geometries. As the contribution of the cross-polar component is zero at $\phi = 0°$ and

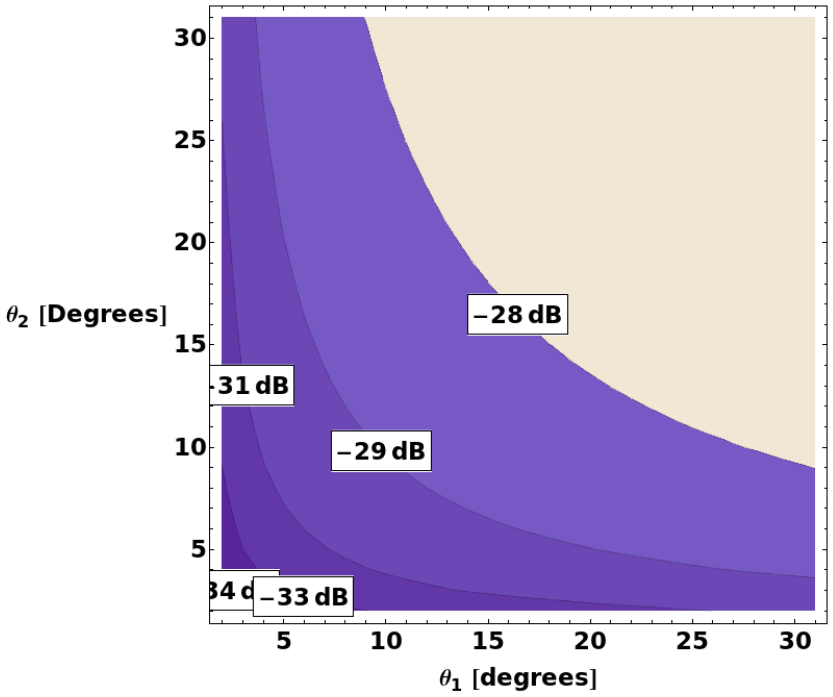

(a) Vertical polarisation

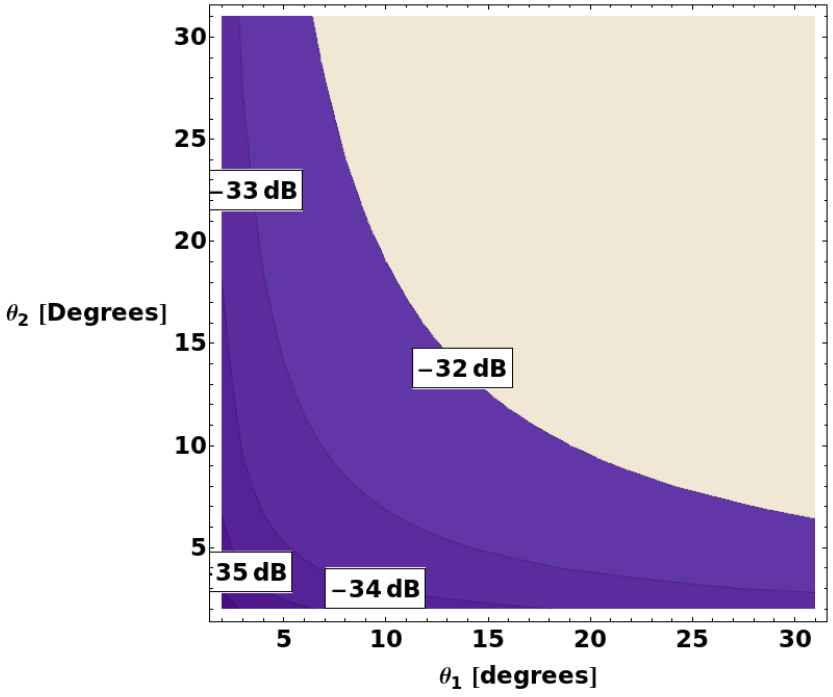

(b) Horizontal polarisation

Figure 5.18: Simulation of in-plane σ_B° for a fully developed wind speed 20 kn, using the proposed empirical model, (a)vertical Polarisation and (b) horizontal polarisation.

maximum at $90°$, $k|\sin\phi|^n$ was used as a multiplying function is chosen, with n and k adjusted to fit the data. For the monostatic cross-polar component, Long's model [31] was used:

$$\sigma^{\circ}_{Mx}\,(\text{dB}) = 29.8\log\left(0.5144 v_w\right) + 6\cos\left(\phi_w\right) - 84.7 - 10\log_{10}\left(\frac{f_{ref}}{f}\right) \tag{5.14}$$

where ϕ_w is the angle between the radar line of sight and the wind, v_w is the wind speed, σ°_{Mx} is the cross-polar normalised radar cross-section, f is the radar operating frequency and f_{ref} is Long's reference frequency of $6.3\,\text{GHz}$. The last term in this equation takes into account the change in the cross-polarised component with the frequency, Long suggested a λ^{-1} dependency, since his reference measurements were made at $6.3\,\text{GHz}$ it was used as the reference frequency. Thus, assuming that the two contributions add incoherently, the overall model is given by:

$$\begin{aligned}\sigma^{\circ}_{B} =& 10\log_{10}\left(\sqrt{\sigma^{\circ}_{M}\left(\theta_1,0\right)\sigma^{\circ}_{M}\left(\theta_1,\phi\right)}|\cos\left(\phi\right)|^m + \right. \\ & \left.\sqrt{k^2\sigma^{\circ}_{Mx}\left(\theta_1,0\right)\sigma^{\circ}_{Mx}\left(\theta_1,\phi\right)}|\sin\left(\phi\right)|^n\right),\ \forall k,m,n \geq 0\end{aligned} \tag{5.15}$$

Different combinations of parameters are used to find the best fits to data. The $\cos$-term is the dominant term when the difference in azimuth angles is small and thus it controls how fast σ°_{B} decreases at small bistatic angles, the larger the exponent m the faster it drops. The $\sin$-term is dominant at angles close to $90°$, n and k control the magnitude of σ°_{B}, the larger k the higher σ°_{B} particularly at large bistatic angles. Increasing n delays the contribution of the cross-polar component with respect to the scattering angle.

To validate the model it would be best to use measurements in which simultaneous measurements of both the monostatic and bistatic NRCS are reported. Ewell and Zehner [112, 113] measured the σ°_{B} and the σ°_{M} simultaneously. However, only their ratio was reported.

Their measurements were taken over three days. The transmitter had a fixed bearing of either $90°$ or $150°$, the bearing of the receiver and range delay were adjusted to modify the bistatic angle. The sea was easterly to south easterly, with occasional local frontal activity with associated rain. On 3 and 4 August the significant wave height was between $1.2\,\text{m}$ to $1.8\,\text{m}$ and the wind speed was approximately $8.7\,\text{m}\,\text{s}^{-1}$, approximately sea state 4. On 5 August, the sea was calmer with estimated significant wave height of $0.9\,\text{m}$, sea state 2, the wind speed was reported to be $6.9\,\text{m}\,\text{s}^{-1}$ which corresponds to sea state 3, this indicates that the sea was not fully developed. The wind direction was assumed to be that of the sea and having a bearing of $100°$. Figure 5.19 shows the diagram of the resulting bistatic geometry. Because the grazing angles are very small, the bistatic angle β is approximately equal to the difference in scattering angle between the transmitter and the bistatic receiver $\Delta\phi$.

A total of six measurements were reported, four with the transmitter looking upwind, and two with transmitter looking crosswind. In most cases the ratio of the normalised bistatic to the normalised

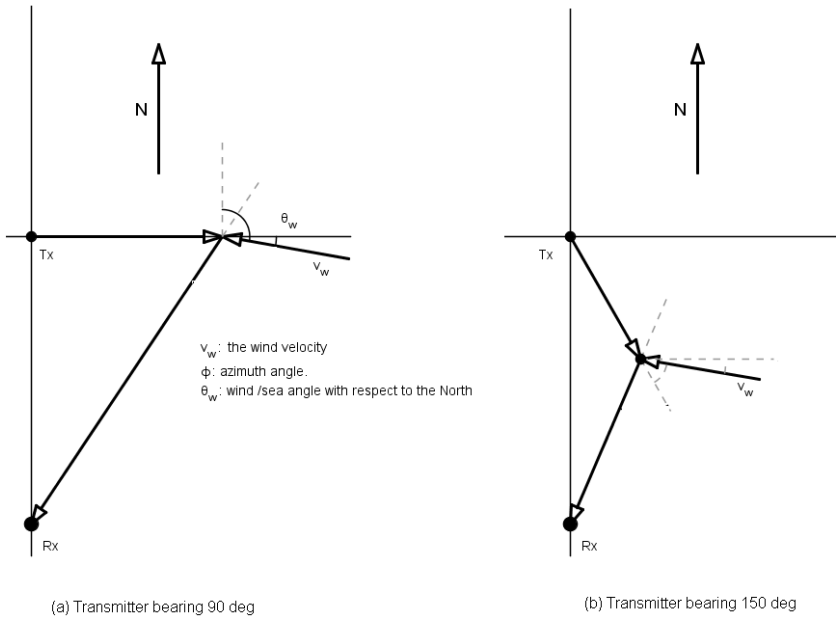

Figure 5.19: Plan view of the bistatic geometry showing the sea and radar bearings, for data reported by Ewell and Zehner.

monostatic radar cross section ($\Delta\sigma^\circ$) decreased with increasing bistatic angle, the maximum drop was at a bistatic angle of about 60°. The slope of the curve dropped as the azimuth angle was increased. This is attributed to the increase in the contribution of the cross-polarised component. The fit parameters are shown in Table 5.7. The fits and plots presented below are different from those reported in [106], a better understanding of bistatic sea clutter gained by analysing and collecting UCL data helped improve the fits. In particular, it is likely that the minima would be around $\beta = 90^\circ$.

Figures 5.20 and 5.22 show plots of the model vs. the reported data. When the measured points followed the expected trend of decreasing σ_B° with increasing bistatic angle, the fits were very good. At the higher sea state Fig. 5.20 the decrease in σ_B° occurred at smaller bistatic angles, and a larger maximum difference as well. This trend was also noticed in UCL data, the opposite was true for the lower sea state, Figs. 5.21 and 5.22. The individual cases are discussed below in more detail.

In Fig. 5.20, the transmitter was looking into the sea and the sea was approximately at sea state 4. The model provided a good fit with a maximum error was $1.84\,$dB for the points which followed the expected trend. The data point at 35° deviated from the trend in both the vertical and horizontal polarisation plots. In both cases when the data confirmed to the trend the maximum error was on the order of $2\,$dB.

Figures 5.21 and 5.22 are for data taken on 5 August, for which the sea was calm. In Fig. 5.21 the transmitter was looking into the sea. Both vertically and horizontally polarised returns good fits with the maximum error in the vertically polarised case around $2.3\,$dB, for the horizontally polarised data the

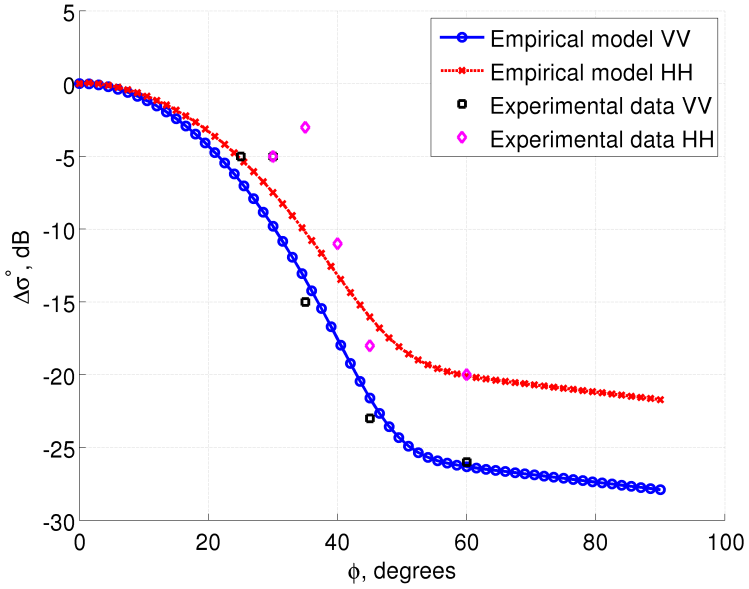

Figure 5.20: Comparison between the measured data, from Ewell and Zehner, source [112, 113], and the proposed empirical model state 4, transmitter looking into the wind.

error was less than 1 dB.

Figure 5.22 represents the crosswind condition at sea state 2. As can be seen, the vertically polarised data represented a good fit, except at the data point at $\phi = 30°$ which had an error of around 3 dB, the error at the other points was less than 1 dB. As for the horizontal data, there were two points at $\phi = 20°$, with very different $\Delta\sigma°$, 11 dB and 7.5 dB. Furthermore, the latter value was equal to that of the data point at $\phi = 30°$. For fitting and comparison purposes the point at (20°,11 dB) was not used, and the fit line was made to pass approximately between the two other points such that the error was almost equal. The maximum error in the points which conformed to trend was around 0.2 dB, corresponding to the last two points, at the other points it was around 2 dB.

Generally speaking the model has been a better fit for vertically polarised data, this could be due to two main reasons:

1. The underlying models such as the GIT are more accurate when applied to vertically polarised sea clutter.

2. The scattering mechanisms are more complex at horizontal polarisation and thus may require additional terms in the model.

5.5.2.1 Fitting to UCL Data

To further validate the model, the model was fitted to UCL data gathered in Oct-2010. Since $\sigma°_M$ was recorded simultaneously it was not necessary to use a model to predict the monostatic normalised radar

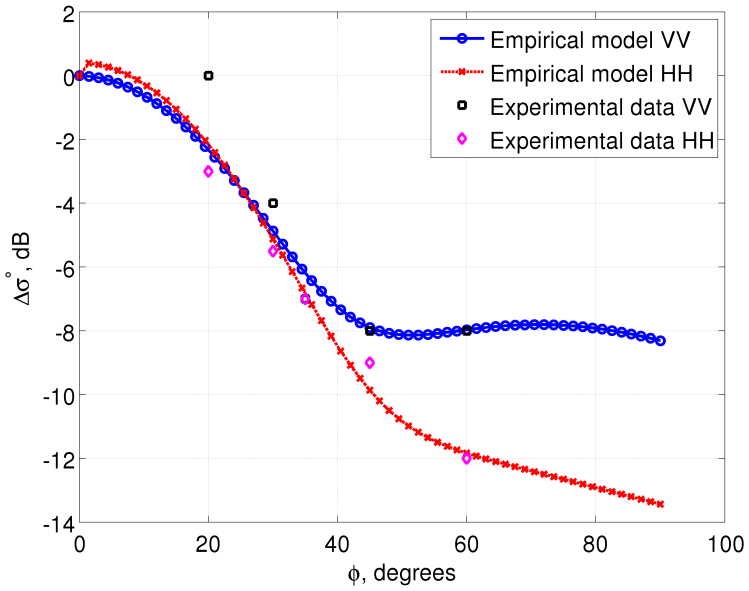

Figure 5.21: Comparison between the measured data from Ewell and Zehner, source [112, 113], and the proposed empirical model on state 2, transmitter looking into the wind.

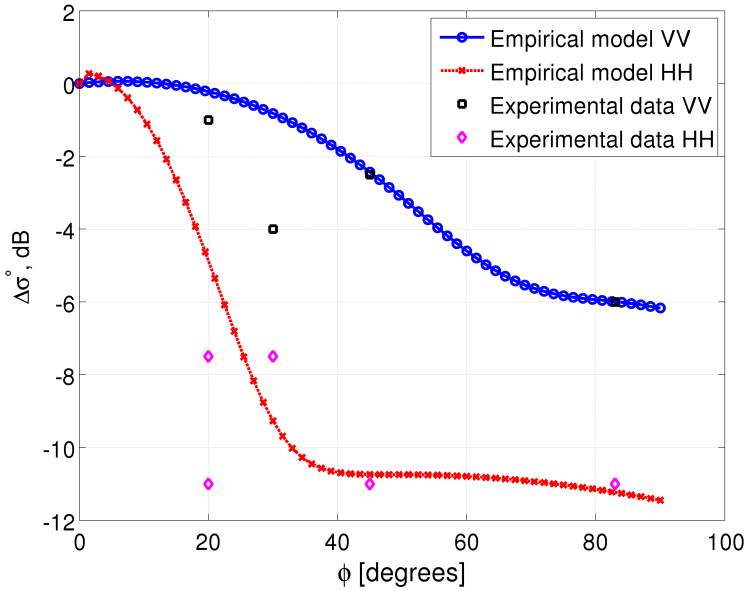

Figure 5.22: Comparison between the measured data from Ewell and Zehner, source [112, 113], and the proposed empirical model on state 2, transmitter looking crosswind.

Sea State	Look angle	Polarisation	m	n	k
4	Into wind	VV	15.4	0	0.02
4	Into wind	HH	12	0	0.0846
2	Into wind	VV	9	2	1.1
2	Into wind	HH	10	0	0.3
2	Cross wind	VV	2	10	0.95
2	Cross wind	HH	23.5	0	0.25

Table 5.7: Fit parameters for Ewell and Zehner data, source [112, 113].

cross section. However, it was still necessary to estimate σ°_M as would have been recorded by a monostatic radar at the bistatic receiver location. Since the difference in height between the two sites was negligible compared to the range, the main factor affecting the average σ°_M as seen by a monostatic radar at the bistatic node location (σ°_{M2}) was the look angle with respect to the wind and sea. Sea clutter models such as the GIT model do not include the effect of the swell. Thus only factor that was changing was the upwind-downwind factor A_u, Eq. (B.6). The GIT model is discussed in Appendix B. Hence, the average monostatic clutter as would have been seen by a monostatic radar at the location of the bistatic node is given by:

$$\sigma^\circ_{M2} = \sigma^\circ_M - 10\log_{10}\left(\exp 0.2\left(\cos\left(\phi_{w1}\right) - \cos\left(\phi_{w2}\right)\right)\right) \tag{5.16}$$

where ϕ_{w1} and ϕ_{w2} are the look angles with respect to the direction of the wind for monostatic and bistatic node respectively. Using the above equation it was found that the difference was less 0.5 dB.

The only remaining measurement needed was the cross-polar component. A single cross-polar measurement was recorded at 16:26. As can be seen from Fig. 5.10 that the difference was around -2 dB. The variation in the cross-polar component due to the change in the look direction with respect to wind was also less 0.5 dB.

Since there was little difference between the σ°_M and σ°_B up to $\beta = 30°$, the in-plane model was initially used, and the contribution of the cross-polarised component was ignored. The model estimate $\sigma^\circ_B = (-59.25, -47.25 \text{ and } -44.75)$ dB m^2/m^2 for $\beta = (30°, 60° \text{ and } 90°)$, which greatly overestimated σ°_B at $\beta = 90°$. Using the out-of-plane model Eq. (5.15) with $k = 3$, $m = 0$ and $n = 14$ resulted in $\sigma^\circ_B = (-59.2, -47.2 \text{ and } -55.0)$ dB m^2/m^2 increasing n beyond this had little effect on the overall result, higher values of k only had a significant effect on the value at $\beta = 90°$. By comparing the fitted results with the measurement Table 5.3, it can be seen this is a very good fit for the data with a maximum difference of less than 0.5 dB.

To fit the data gathered on 10-Oct-2010 the same procedure described above can be used; however, since the cross-polarised cross section was not measured, Long's model must be used. When using Long's model, the cross-polarised normalised section was around -40 dB m^2/m^2, which is too high. This might be because the wind speed (10.18 m s^{-1} to 12.3 m s^{-1}) was higher than that specified for the model, 16 kn or 8.2 m. Due to the lack of a reliable method to estimate the cross-polarised component it was difficult to use this data set to validate the model.

5.6 Summary and Conclusions

It was shown in the first section of this chapter that although the antenna beamwidths are on the order of $10°$, the variation of the bistatic angle across the clutter patch was negligible. In the subsequent sections the method used to calculate the normalised radar cross section was validated by estimating the clutter

cell area and comparing the results with known approximations from literature.

In this chapter, the analysis of a unique set of data has been presented. Not only is the bistatic data unique, some of the monostatic data is also unique because it was recorded within littoral waters. Monostatic and bistatic data were recorded simultaneously in these experiments to enable a comparison of the bistatic and monostatic sea clutter properties. Two data sets were analysed at horizontal and vertical polarisation and a cross-polarised measurement covering bistatic angles between $30°$ to $120°$. One data set was recorded during a relatively calm day, sea state 2, while the other was recorded on a very rough day, the sea state was estimated to be around 5 with some frontal activities.

In both measurements it was found that the ratio of σ°_B to σ°_M was a minimum around a bistatic angle of $90°$. It should be noted that in these measurements the depression angle was small, thus the bistatic angle is almost equal the difference in the azimuth angle of approximately $90°$. Since such phenomenon was not reported in in-plane measurements it is expected that the cause of the drop is the change in the azimuth angle not the bistatic angle. There was little variation in the ratio in low sea state for vertically polarised clutter up to $\beta = 60°$. However, at $\beta \approx 90°$ the ratio was around -10 dB. The ratio was higher for horizontally polarised clutter around -16 dB. All other data sets recorded in horizontal polarisation had a negative CNR and thus this is the only valid measurement for σ°_{HH} in both geometries. Cross-polarised clutter had a larger normalised radar cross section at $\beta = 90°$.

Similar trends were found in the high sea state data set; however, the drop in σ°_B at $\beta = 60°$ was substantially higher than that in the low sea state. Subsequently, the difference between this value and that at $\beta = 90°$ was just around 4 dB in vertical polarisation, σ°_B increased by around 3 dB when $\beta = 120°$. The variation in horizontal polarisation was less pronounced, but the minimum was at $\beta = 90°$. Nevertheless σ°_B was less than simultaneously measured σ°_M by at least 12 dB.

The apparent difference in the behaviour between the horizontal and vertical polarisations at different sea states can be understood by noting that σ°_{MHV} has a magnitude similar to that of σ°_{MHH} during spiking events [41] which are both more pronounced and more likely to occur in rough seas, which means that the contribution of the cross-polarised component is substantial when compared to that in σ°_{MVV}, thus increasing the magnitude of σ°_{BHH} and reducing its ratio to σ°_{MHH}. Such spiking events are less likely to happen at vertical polarisation or at low sea states thus the ratios were greater at these conditions.

Similar trends were observed in the Ewell and Zehner data [112, 113], the drop in σ°_B was more pronounced in rough sea conditions and in under such condition it was more pronounced at vertical polarisations. For low sea states the drop had a larger magnitude at horizontal polarisations, however the difference between σ°_{BH} and σ°_{BV} was smaller in UCL data but the trends were similar.

A new model to describe bistatic sea clutter has been developed. It is an extension of Barton's bistatic clutter model. However, it takes into account the radar look angle and grazing angle when

estimating the clutter. In the in-plane geometry it successfully described Domville's data [109, 110]. For the out-of-plane geometries it models into account the effect of the cross-polarised component and the difference in the scattering environment. Both UCL data and Ewell and Zehner data were fitted successfully.

In the next chapter studies on statistical properties of bistatic and monostatic sea clutter and their correlation properties will be reported. Since there is no data available in the open literature, only UCL data was used for this analysis.

Chapter 6

Analysis of Monostatic and Bistatic Sea Clutter Amplitude Statistics

6.1 Introduction

In this chapter the amplitude properties of the monostatic and bistatic sea clutter are analysed. The data recorded in South Africa on 05-Oct-2010 and 10-Oct-2010 was used. The validity of the compound model for sea clutter is tested by means of studying the autocorrelation function of the speckle, intensity and the texture. This was followed by studying the statistical properties of the clutter by fitting the intensity to five different distributions. The spikiness of the clutter was studied by analysing the time histories and the parameters of the KA distribution. Finally, the average properties of the clutter are combined with the results of the statistical analysis to study the effect of the bistatic geometry on the performance of the radar.

6.2 Correlation Properties and the Compound Model

According to the compound model for sea clutter, the clutter is assumed to be a Gaussian mixture with texture τ which modulates the speckle. According to this model the complex envelope of the sea returns is given by:

$$x(i) = \sqrt{\tau(i)}s(i) \tag{6.1}$$

The compound K-distribution assumes that the texture ($\tau(i)$) is a gamma random variable and the speckle ($s(i)$) is a stationary complex Gaussian process. The intensity of the clutter is given by:

$$z(i) = |x(i)|^2 = \tau s(i)s^*(i) \tag{6.2}$$

where * denotes the complex conjugate. Since the texture and the speckle are assumed to be uncorrelated the autocorrelation function (ACF) of the clutter is given by [82, 139]:

$$\begin{aligned} R_X(m) &= R_{\sqrt{\tau}}(m) R_s(m) \\ R_X(m) &= E\left[\sqrt{\tau(i)}\sqrt{\tau(i+m)}\right] E\left[\left(x_I(i) + jx_Q(i)\right)\left(s_I(i+m) - js_Q(i+m)\right)\right] \end{aligned} \tag{6.3}$$

Assuming the speckle is stationary

$$R_X(m) = 2R_{\sqrt{\tau}}(m)\left(R_{S_I}(m) + jR_{S_I S_Q}(m)\right) \tag{6.4}$$

The clutter autocorrelation function can be estimated by:

$$\hat{R}_X(m) = \frac{1}{N_s}\sum_{i=1}^{N_s - m}\sqrt{\tau(i)\tau(i+m)}s(i)s^*(i+m) \tag{6.5}$$

where N_s is the number of samples. If N_s is chosen such that it is long enough that the speckle would decorrelate and short enough such that texture is constant the autocorrelation function can be used to estimate the texture. Then

$$\hat{\tau_j} = \hat{R}_X(0) = \frac{i=j}{N_s + j - 1}\sum_{i=1}^{N_s} z\left(i\right) \tag{6.6}$$

Since there is a significant difference between the decorrelation times of the speckle and the texture there could is a large number of window sizes which can be used. The chosen window size should be large enough to decorrelate the clutter but small enough such that the texture is not decorrelated. In this thesis $N_s = 256$ was used[1]; however, other values were tested and the upper bound was found to be $N_s \approx 1024$. Using smaller values but larger than the speckle decorrelation time did not have significant effect on the results. Thus the texture can be estimated by the average of the intensity over a window of size N_s. The real and imaginary parts of the clutter decorrelation function are given by:

$$\hat{R}_{S_I}(m) = \frac{1}{2\hat{\tau}_k}\Re\left(\hat{R}_X(m)\right) \tag{6.7}$$

$$\hat{R}_{S_Q}(m) = \frac{1}{2\hat{\tau}_k}\Im\left(\hat{R}_X(m)\right) \tag{6.8}$$

Since the number of samples is much greater than N_s the above was repeated across the total number of samples with 50% overlap. Similarly for the intensity the autocorrelation function is given by:

$$R_z(m) \approx 4R_\tau(m) \tag{6.9}$$

[1] Each array of the data consisted of 130 000 samples recorded at a PRF of 1 kHz.

which is estimated using

$$\hat{R}_\tau(l) = \frac{1}{N_\tau} \sum_{k=1}^{N_\tau - l} \hat{\tau}_k \hat{\tau}_{k+l} \tag{6.10}$$

6.2.1 Low Sea State Data

This data set was recorded on 05-Oct-2010. Monostatic and bistatic sea clutter were recorded simultaneously. The surface truth and geometry data were provided in Section 5.4.1 Tables 5.1 and 5.2, the sea state around 2. The speckle autocorrelation function was computed using Eq. (6.3), the results are plotted in Figs. 6.1 and 6.2. In monostatic and bistatic sea clutter data the decorrelation time was around 30 ms and 50 ms respectively. The main differences between the two autocorrelation functions were that the magnitude of the imaginary part was smaller in bistatic clutter and that the monostatic autocorrelation function seems to drop faster but oscillates before it reaches the steady state. Figure 6.1 shows the autocorrelation function for vertically polarised bistatic and monostatic clutter. For horizontally polarised clutter the initial drop was much faster than vertical clutter but the decorrelation time was similar as shown in Fig. 6.2.

In addition, the autocorrelation of the texture was studied. The texture decorrelation times of vertically polarised monostatic and bistatic sea clutter were very similar. They were of the order of 6 s, example results are shown in Fig. 6.3. According to Eq. (6.10), the ACF of the intensity is a scaled version of the texture ACF. By comparing Fig. 6.4 and Fig. 6.3, it was clear that both ACFs have similar decorrelation times. In horizontally polarised clutter, the decorrelation time was much smaller particularly for the monostatic node as can be seen in Fig. 6.5. Unlike vertically polarised sea clutter, the bistatic and monostatic ACFs were more different, the decorrelation time in the monostatic case was much smaller around 2 s compared to 3 s. The monostatic and bistatic ACF had similar decorrelation times but the amplitude of the peaks but not their times were different. The same behaviour was observed in the ACF of the texture. By examining Fig. 6.7 it can be seen that ACF of the texture of cross-polarised monostatic and bistatic sea clutter decorrelation times were almost the same and was similar to that of vertically polarised clutter. However, the general shape of the ACFs was different from that of vertically polarised sea clutter. Like the other two cases the intensity ACF was similar to the texture AFC. By comparing the trends in the ACF of simultaneously recorded bistatic and monostatic sea clutter it is clear that they were correlated. The periodic nature of the sea surface can be seen in the intensity and texture plots for both monostatic and bistatic geometries and all polarisations.

The decorrelation times of the speckle ACF and the decorrelation times of the texture and intensity ACFs confirmed the compound model was applicable to both monostatic and bistatic sea clutter data in this data set. The texture was also fitted to the gamma distribution, in some cases the fit looked good visually as shown in Fig. 6.9, but it failed the Anderson-Darling test [140].

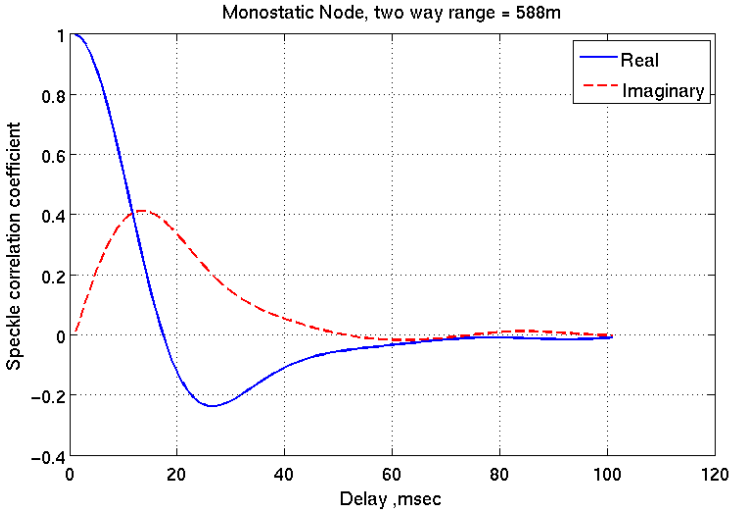

(a) Monostatic

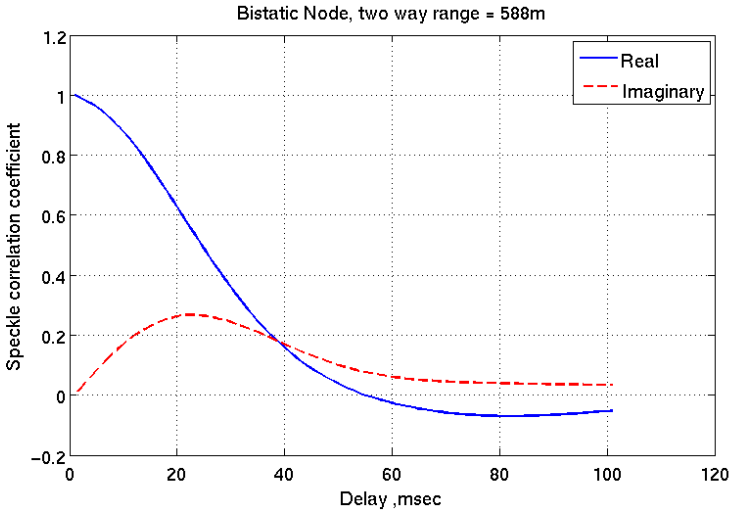

(b) Bistatic, $\beta = 90°$

Figure 6.1: Autocorrelation function of the speckle of simultaneously collected vertically polarised monostatic and bistatic sea clutter recorded at 16:08 on 05-Oct-2010.

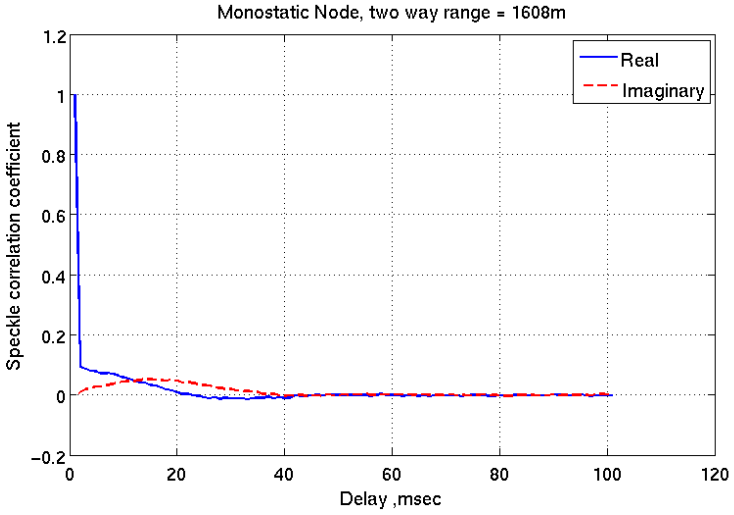

(a) Monostatic

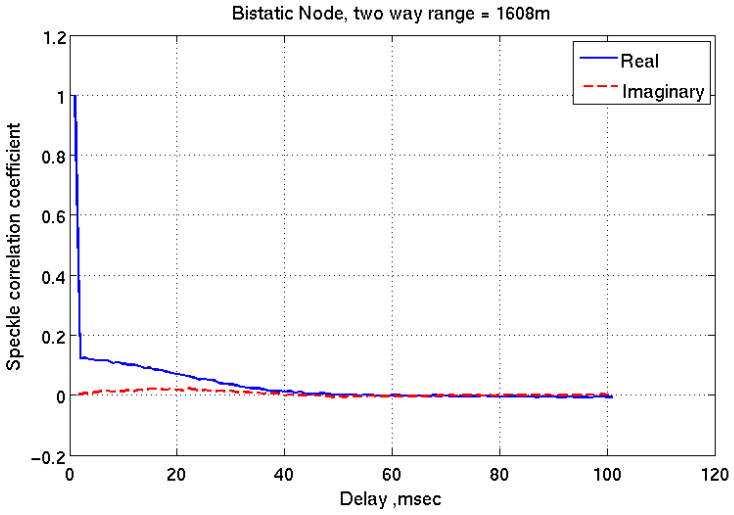

(b) Bistatic, $\beta = 90°$

Figure 6.2: Autocorrelation function of the speckle of simultaneously collected horizontally polarised monostatic and bistatic sea clutter, data recorded at 17:16 on 05-Oct-2010.

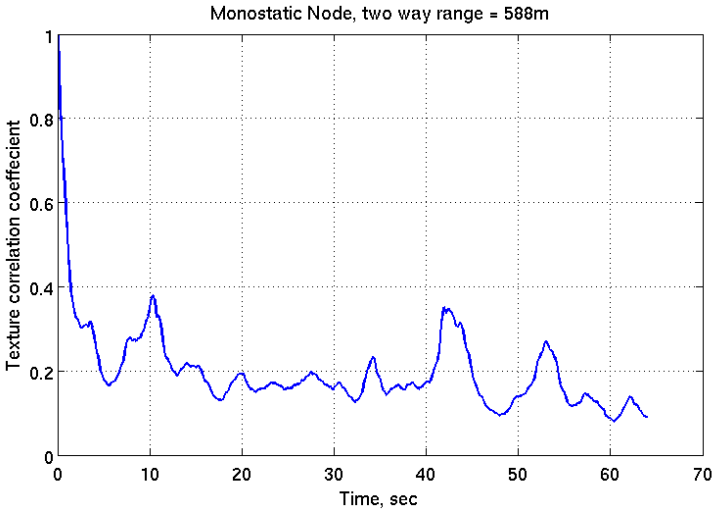

(a) Monostatic

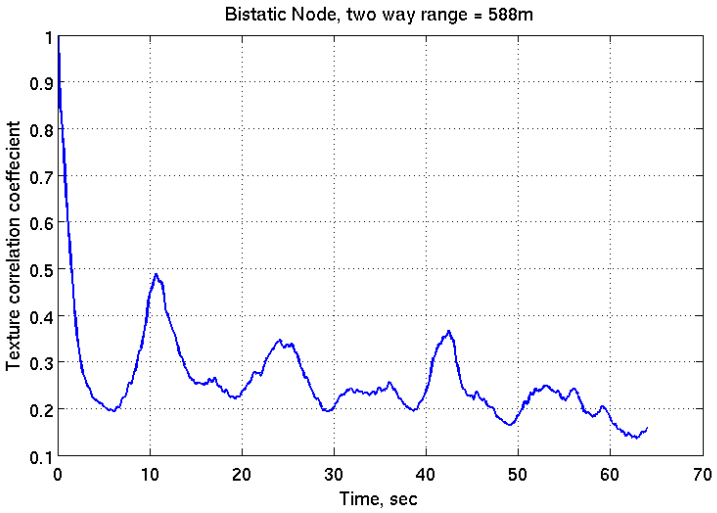

(b) Bistatic, $\beta = 90°$

Figure 6.3: Autocorrelation function of the texture of simultaneously collected vertically polarised monostatic and bistatic sea clutter, data recorded at 15:09 on 05-Oct-2010.

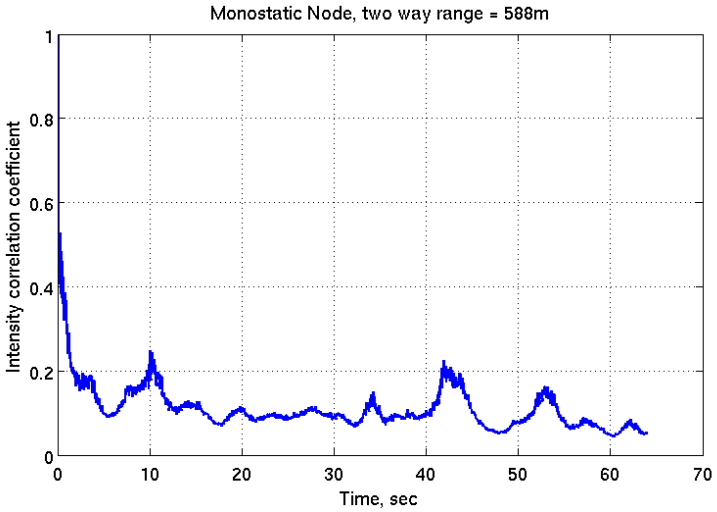

(a) Monostatic

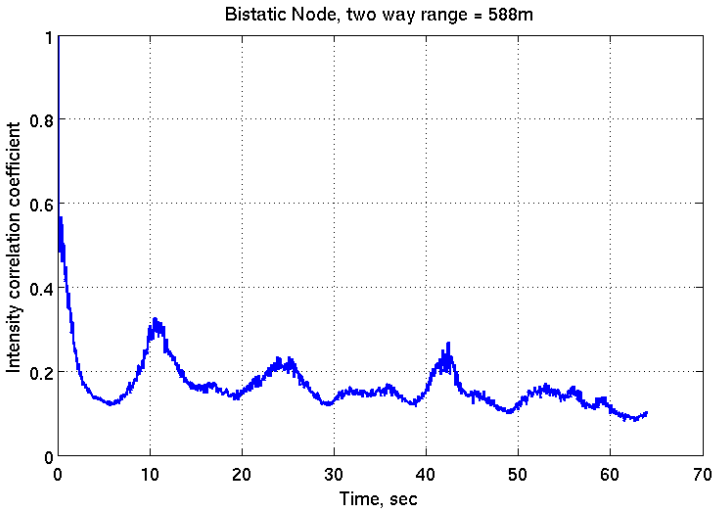

(b) Bistatic, $\beta = 90°$

Figure 6.4: Autocorrelation function of the intensity of simultaneously collected vertically polarised monostatic and bistatic sea clutter, data recorded at 15:09 on 05-Oct-2010.

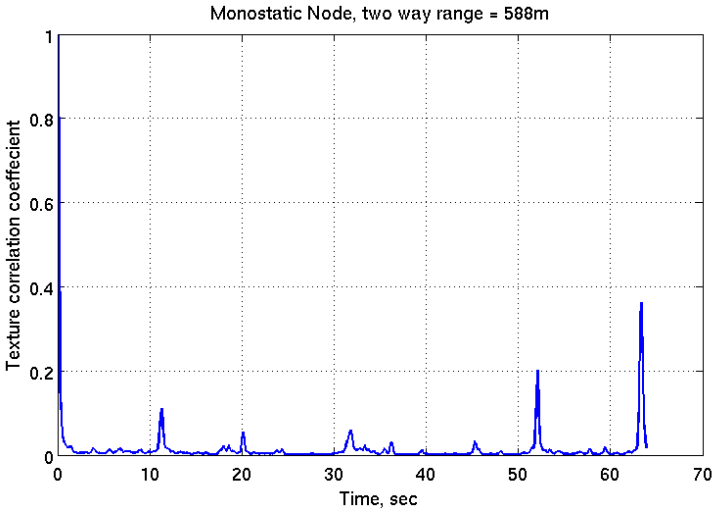

(a) Monostatic

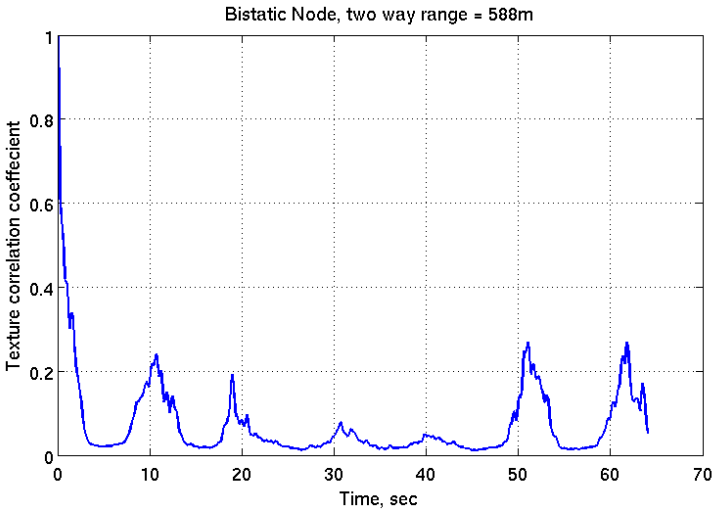

(b) Bistatic, $\beta = 90°$

Figure 6.5: Autocorrelation function of the texture of simultaneously collected horizontally polarised monostatic and bistatic sea clutter, data recorded at 17:16 on 05-Oct-2010.

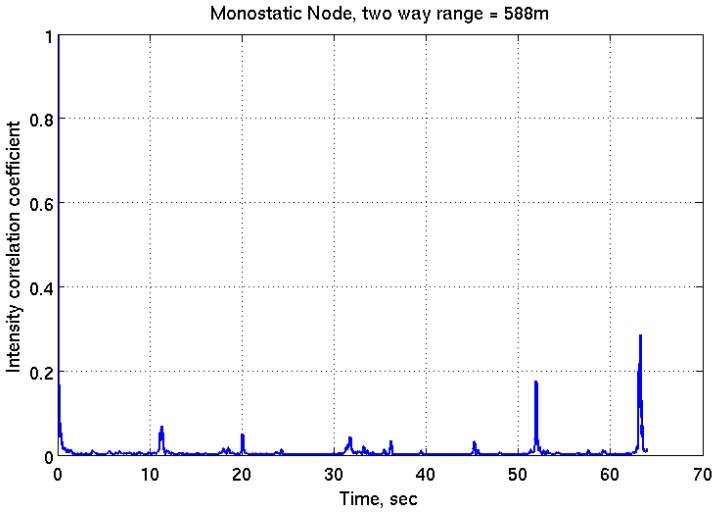

(a) Monostatic

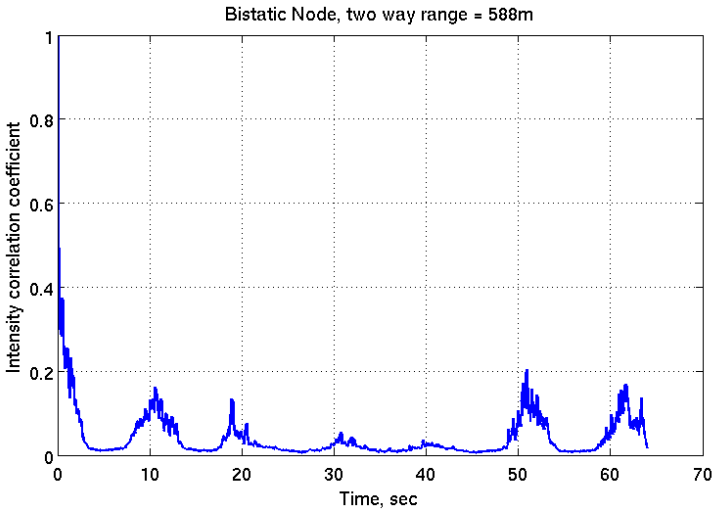

(b) Bistatic, $\beta = 90°$

Figure 6.6: Autocorrelation function of the intensity of simultaneously collected horizontally polarised monostatic and bistatic sea clutter, data recorded at 17:16 on 05-Oct-2010.

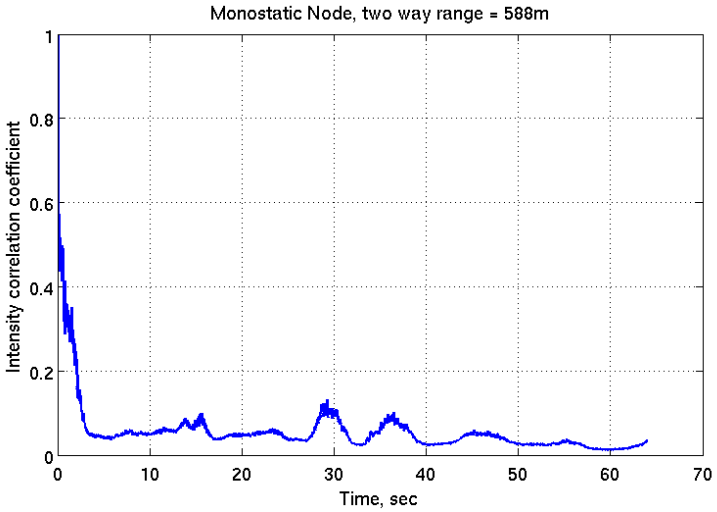

(a) Monostatic

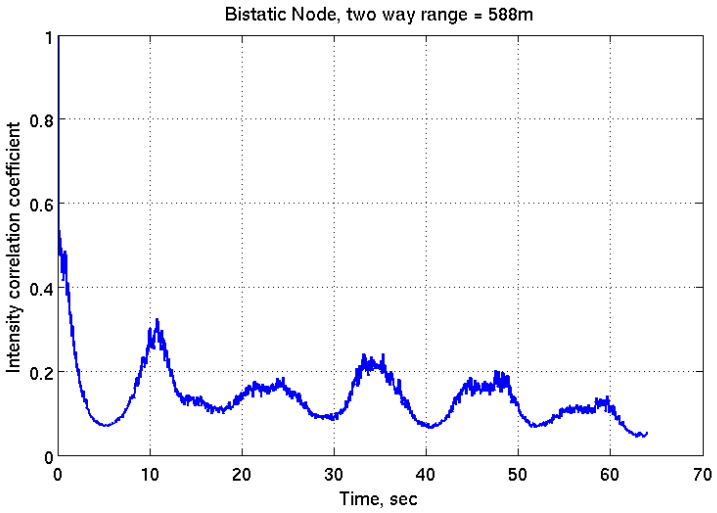

(b) Bistatic, $\beta = 90°$

Figure 6.7: Autocorrelation function of the intensity of simultaneously collected cross-polarised monostatic and bistatic sea clutter, data recorded at 16:26 on 05-Oct-2010.

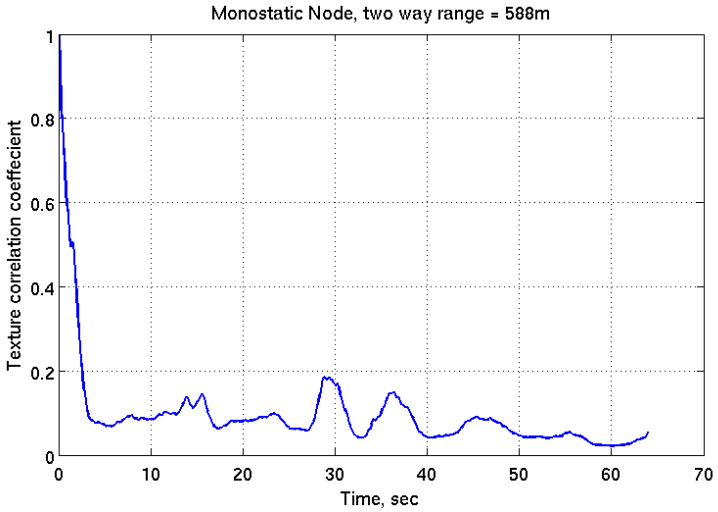

(a) Monostatic

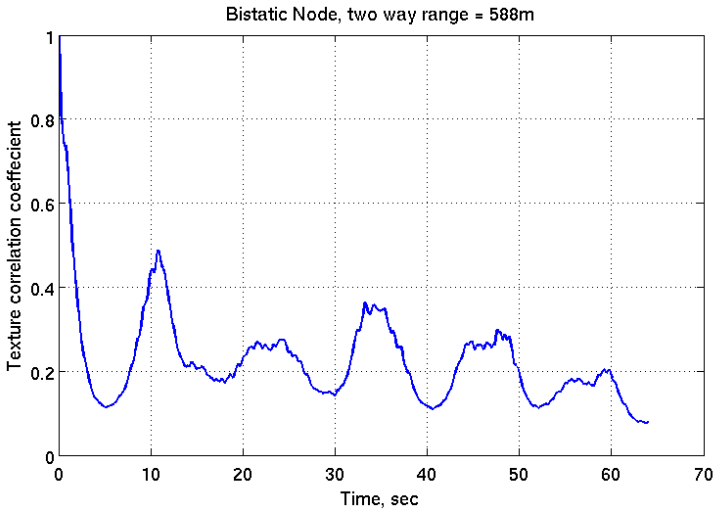

(b) Bistatic, $\beta = 90°$

Figure 6.8: Autocorrelation function of the texture of simultaneously collected cross-polarised monostatic and bistatic sea clutter, data recorded at 16:26 on 05-Oct-2010.

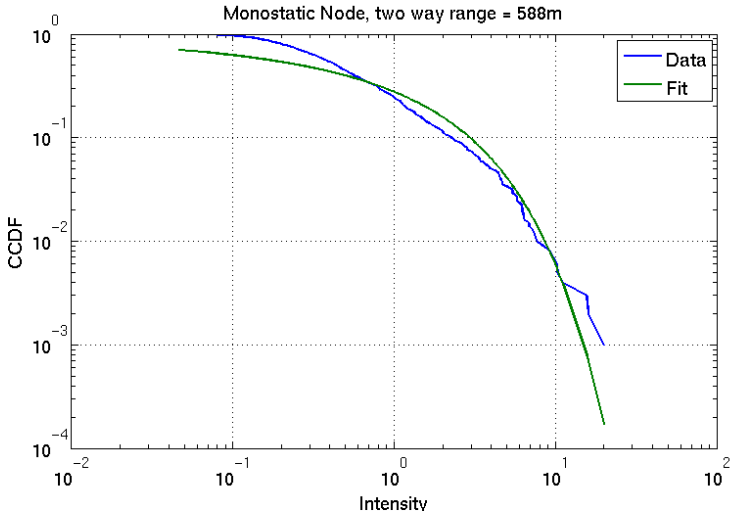

(a) Monostatic

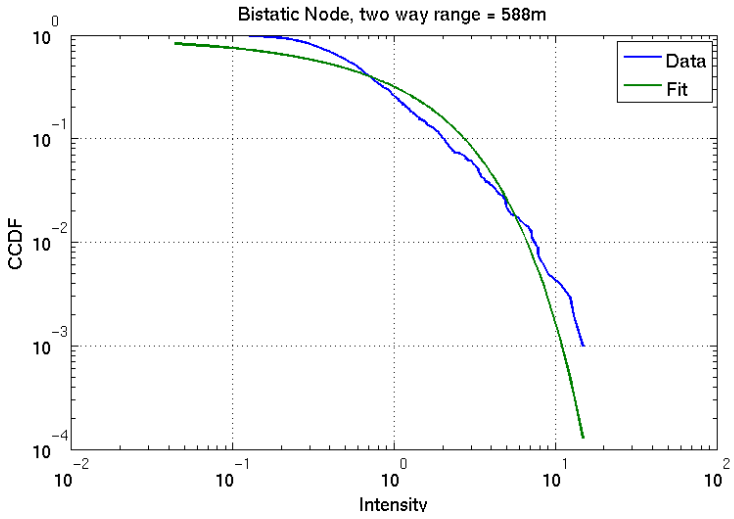

(b) Bistatic, $\beta = 90°$

Figure 6.9: Fit of the texture to the gamma distribution, data was recorded at 15:09 on 05-Oct-2010

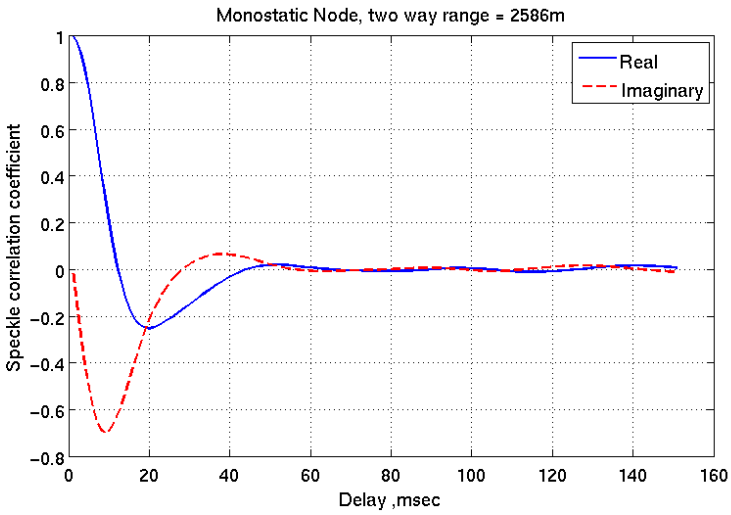

(a) Monostatic

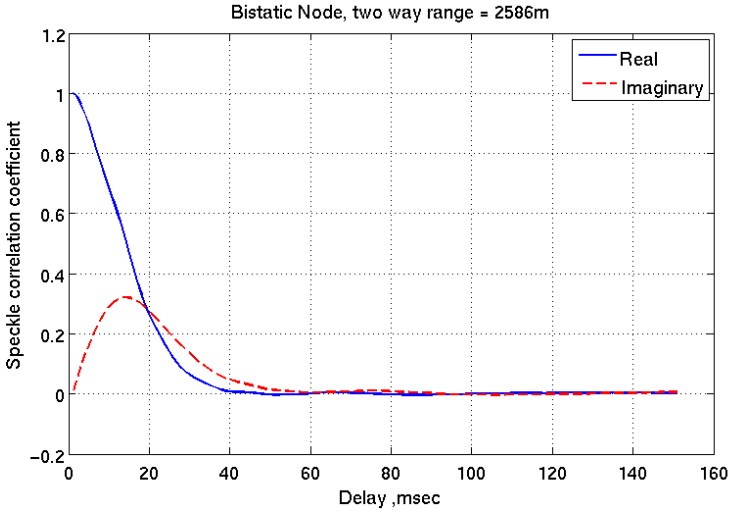

(b) Bistatic, $\beta = 90°$

Figure 6.10: Speckle autocorrelation function of simultaneously collected horizontally polarised monostatic and bistatic clutter gathered at 12:53 on 10-Oct-2010.

6.2.2 High Sea State Data

This data set was recorded on 10-Oct-2010; the surface truth and geometry were described in Section 5.4.2 Tables 5.4 and 5.5, the sea state was around 4 – 5. The ACF of the speckle of simultaneously recorded monostatic and bistatic sea clutter had a correlation time between 40 ms and 60 ms. However, there were clear differences in the shape of ACF of the speckle of bistatic and monostatic data. The shape of the ACF of bistatic clutter resembled that of the response of an over-damped system, whereas that of simultaneously recorded monostatic clutter was slightly under-damped. The imaginary parts were different as well, that of the monostatic clutter had a larger amplitude. Example plots are provided in Fig. 6.10 for horizontally polarised clutter and vertically polarised clutter in Fig. 6.11. This is the same behaviour observed in the low sea state data in the previous section.

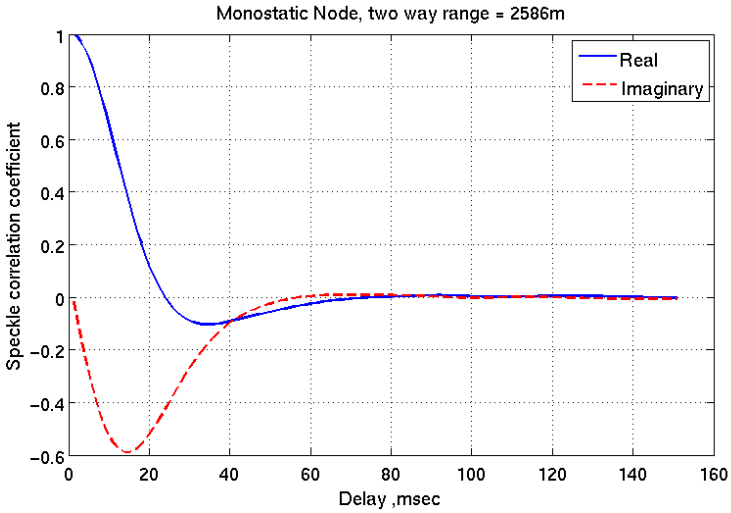

(a) Monostatic

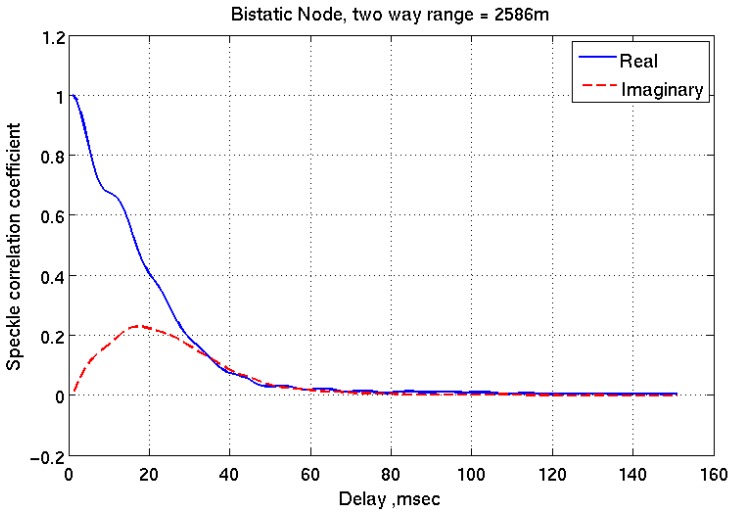

(b) Bistatic, $\beta = 90°$

Figure 6.11: Speckle autocorrelation function of simultaneously collected vertically polarised monostatic and bistatic clutter gathered at 16:03 on 10-Oct-2010.

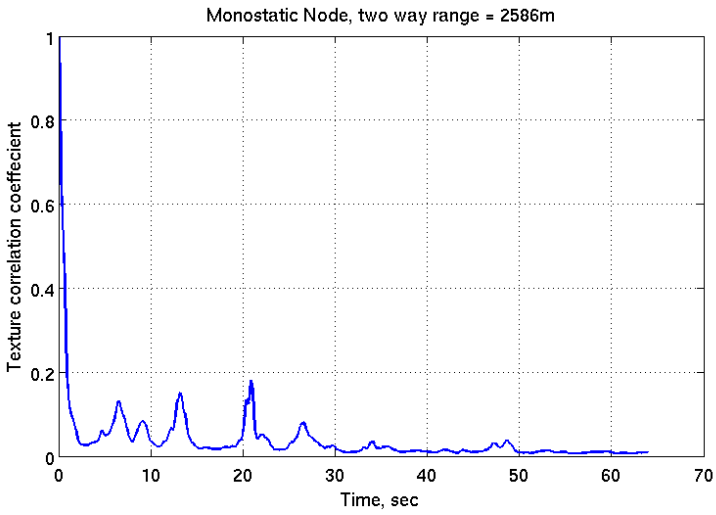

(a) Monostatic

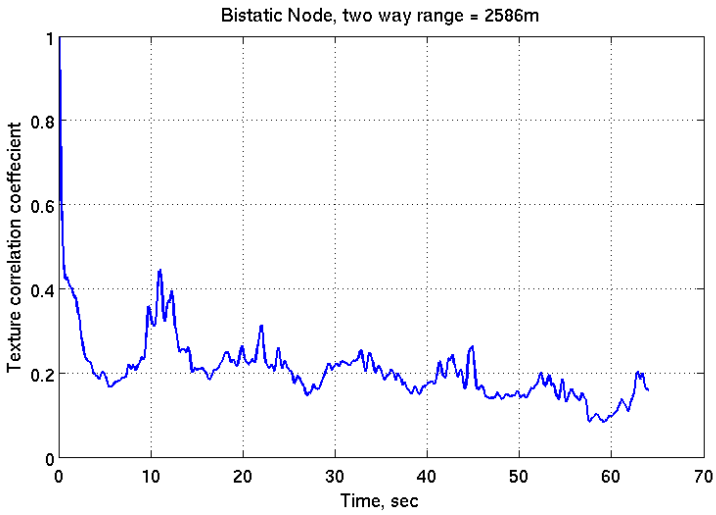

(b) Bistatic, $\beta = 90°$

Figure 6.12: Autocorrelation function of the texture of simultaneously recorded horizontally polarised monostatic and bistatic gathered at 12:44 on 10-Oct-2010.

By comparing the ACF of the texture Figs. 6.12 and 6.13 and that of the intensity Figs. 6.14 and 6.15, it is clear that they were very similar and that the compound model is still valid. However by comparing vertically polarised clutter ACF with horizontally polarised clutter, it can be seen that vertically polarised clutter had longer decorrelation times between $5\,\mathrm{s}$ and $8\,\mathrm{s}$, compared to only a few seconds for horizontally polarised sea clutter. The decorrelation times were similar for different ranges and bistatic angles. By comparing the trends in the ACF of simultaneously recorded bistatic and monostatic sea clutter it is clear that they were correlated. The texture was also fitted to the gamma distribution, in some cases the fit looked good visually as shown in Fig. 6.16, but it failed the Anderson-Darling test [140]. The cyclic nature of the sea surface can be seen in the intensity and texture plots for both monostatic and bistatic geometries and all polarisations

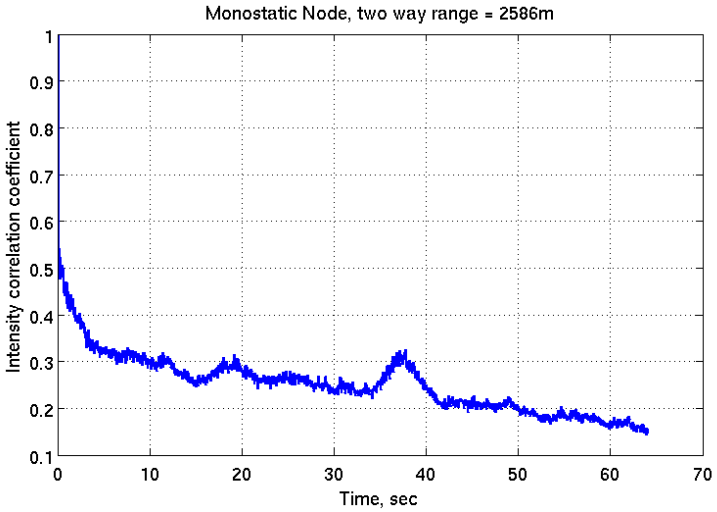

(a) Monostatic

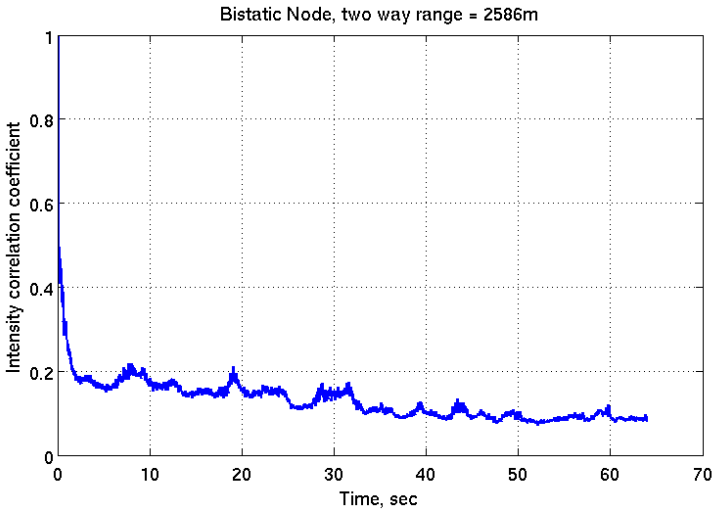

(b) Bistatic, $\beta = 90°$

Figure 6.13: Autocorrelation function of the texture of simultaneously recorded horizontally polarised monostatic and bistatic gathered at 16:03 on 10-Oct-2010

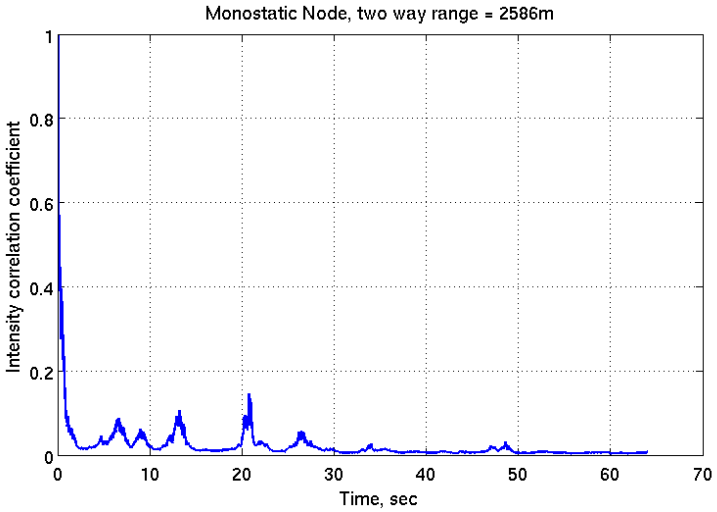

(a) Monostatic

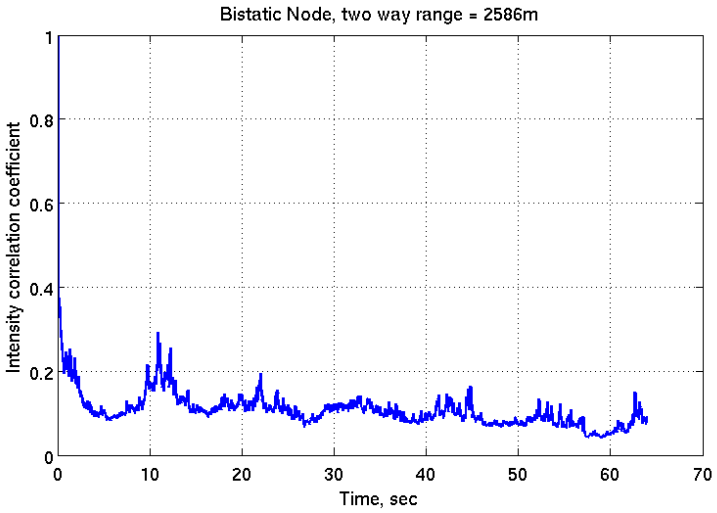

(b) Bistatic, $\beta = 90°$

Figure 6.14: Autocorrelation function of the intensity of simultaneously recorded horizontally polarised monostatic and bistatic gathered at 12:44 on 10-Oct-2010.

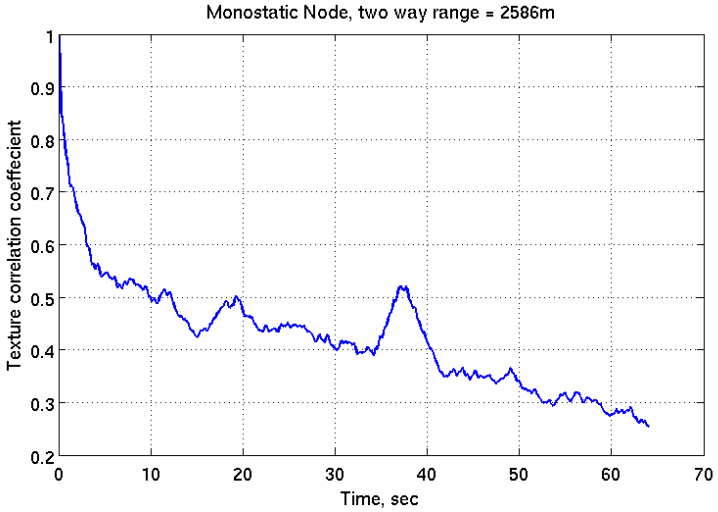

(a) Monostatic

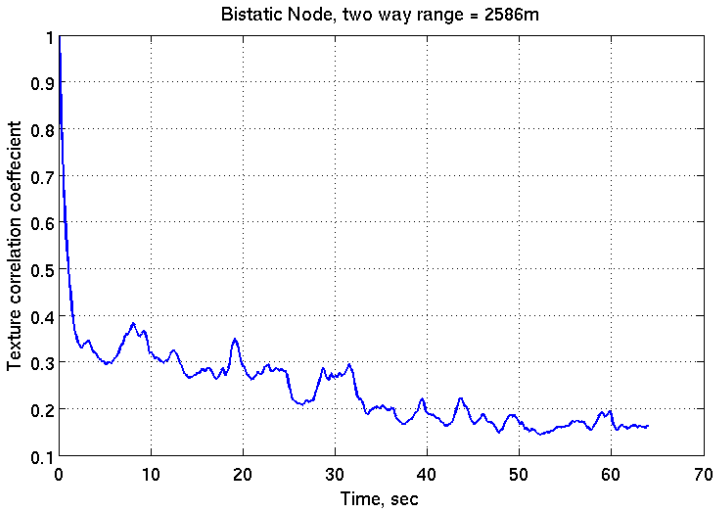

(b) Bistatic, $\beta = 90°$

Figure 6.15: Autocorrelation function of the intensity of simultaneously recorded vertically polarised monostatic and bistatic gathered at 16:03 on 10-Oct-2010.

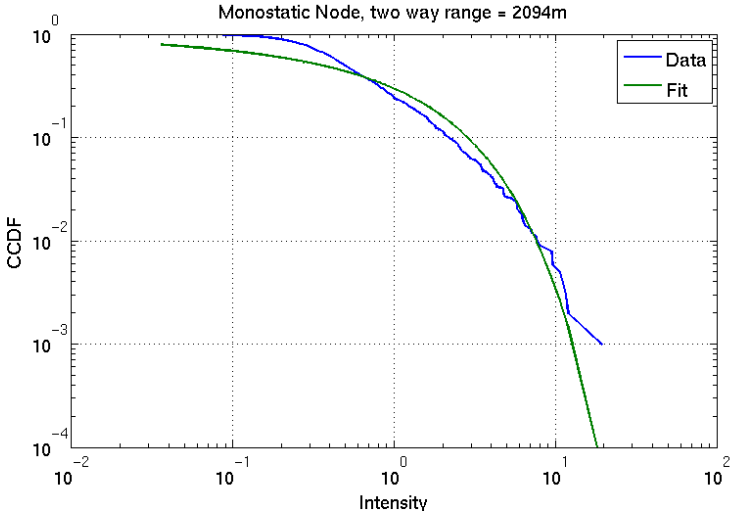

(a) Monostatic

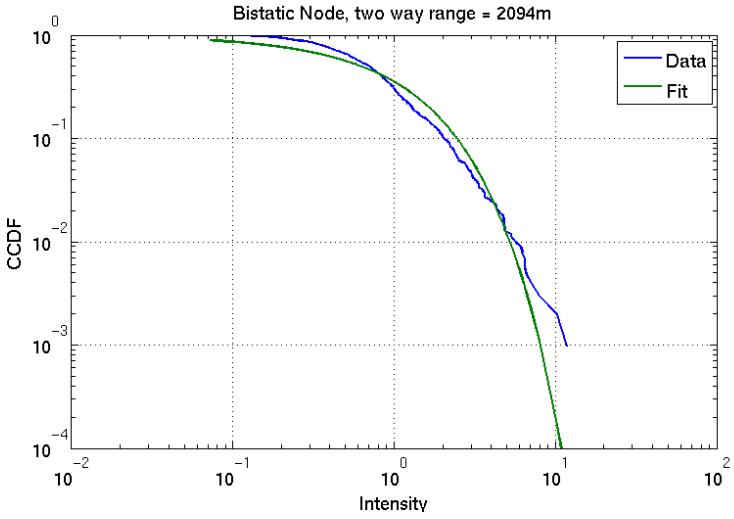

(b) Bistatic, $\beta = 60°$

Figure 6.16: Fit of the texture to the gamma distribution, data was recorded at 12:53 on 10-Oct-2010.

6.3 Analysis of the Amplitude Statistics

As discussed in Section 2.2.5 several statistical distributions have been proposed to model the fluctuation in the amplitude of monostatic sea clutter. In this section, the log-normal, Weibull, K plus thermal noise, KA and Pareto distributions were used to model simultaneously recorded monostatic and bistatic sea clutter. Prior to the discussing the fit results a brief review of each distribution is presented. The intensity of the recorded data was used, only the compound K distribution and its variants have different forms for the intensity and amplitude models. The intensity was chosen because the limiting case of sea clutter is a complex Gaussian random process whose intensity is described by the exponential distribution which is a special case of all the distribution under test except the log-normal, whereas the amplitude is described by the Rayleigh distribution which is only a special case of the Weibull distribution and compound K family of distributions, but not the Pareto and log-normal distributions.

The distribution parameters were computed from the recorded data. Although maximum likelihood estimators (MLEs) can be more efficient, the method of moments (MoM) (also known as moment matching) was used since there is no maximum likelihood estimator available for the K+thermal noise or the KA distributions. Furthermore, there is enough data points such that the performance of the MoM is comparable with fits found using MLE. This assumption was checked by comparing the fit results from both methods on numerically generated noise of a known distribution and the trial data. The n^{th} moment is given by:

$$m_n = \frac{1}{N_t} \sum_{i}^{N_t} z(i)^n \tag{6.11}$$

For the data sets analysed in this thesis N_t was in the order of $130\,000$, sampled every 1 ms. The only exception is the KA distribution fit in which order only part of the data was used to estimate the shape and scale parameters for the Bragg scattered components in the returns as discussed below.

Log-normal distribution The Pdf of the log-normal distribution is given by [141]:

$$p(z) = \frac{1}{z\sqrt{2\pi\sigma^2}} \exp\left(-\frac{(\ln(z) - \mu)}{2\sigma^2}\right), \qquad z \geq 0 \tag{6.12}$$

where σ is the shape parameter, and $\exp(\mu)$ is the scale parameter. The raw moments of the order n are given by:

$$m_n = \exp\left(n\mu + \frac{n^2\sigma^2}{2}\right) \tag{6.13}$$

thus the first and second moments are given by:

$$m_1 = \exp\left(\mu + \frac{\sigma^2}{2}\right) \tag{6.14}$$

$$m_2 = \exp\left(2\mu + 2\sigma^2\right) \tag{6.15}$$

The second normalised moment is a function of σ only and is given by:

$$N_2 = \frac{m_2}{m_1^2} \exp\left(\sigma^2\right) \tag{6.16}$$

this equation is solved for $\hat{\sigma}$, which is then substituted in Eq. (6.15) to find $\hat{\mu}$.

Weibull Distribution The Pdf of the Weibull distribution is given by [142]:

$$P(z) = \frac{cz^{c-1}}{a^c} \exp\left(-\left({}^{z}/_{a}\right)^c\right), \qquad z \geq 0 \tag{6.17}$$

where a is the scale parameter and c is the shape parameter. It can be seen that by setting $c = 1$ the Pdf reduces to that of the exponential distribution which is the limiting case for sea clutter intensity. The raw moments are given by:

$$m_n = a^n \Gamma\left(\frac{n+c}{c}\right) \tag{6.18}$$

The first and second moments are given by:

$$m_1 = a\gamma\left(\frac{1+c}{c}\right) \tag{6.19}$$

$$m_2 = a^2\gamma\left(\frac{2+c}{c}\right) \tag{6.20}$$

The second normalised moment is a function of c only and is given by:

$$N_2 = \frac{m_2}{m_1^2} = \frac{\Gamma\left(\frac{2+c}{c}\right)}{\Gamma^2\left(\frac{1+c}{c}\right)} \tag{6.21}$$

Equation (6.21) equation was solved using Newton-Raphson method, then the estimated shape parameter $\hat{c}$ is substituted in Eq. (6.20) to find $\hat{a}$.

K+Thermal Noise Distribution The K+thermal noise distribution was proposed by Watts [86]. When used to model the intensity it is given by[2]:

$$p(z) = \left(\frac{\nu}{\sigma_B}\right)^{\nu} \frac{1}{\Gamma(\nu)} \int_0^{\infty} x^{\nu-1} \frac{\exp\left(-\frac{x\nu}{\sigma_B}\right)}{x+p_n} \exp\left(\frac{-z}{x+p_n}\right) dx, \qquad z \geq 0 \tag{6.22}$$

where p_n is the receiver thermal noise power, x is the local mean intensity, ν is the shape parameter and σ_B is the mean clutter power. The scale parameter b is given by $b = \frac{nu}{\sigma_B}$. Since the noise power is a

[2]Radar works Matlab toolbox by G. Davidson was used generate the K+thermal noise cdf which can be found at http://www.radarfactory.com/software.htm, accessed 20-Sep-2011

measured quantity two equations are needed to find the distribution parameters:

$$\hat{\sigma_B} = m_1 - p_n \tag{6.23}$$

$$\hat{\nu} = \frac{2\left(m_1^2 - 2m_1 p_n + p_n^2\right)}{m_2 - 2m_1^2} \tag{6.24}$$

KA Distribution The KA distribution is a modification of the compound K distribution to include the effects of spiking events by modelling them as discrete scatterers whose number is Poisson distributed $P_m(m)$ with average $\overline{N} << 1$. The KA distribution is given by [48, 88]:

$$\begin{aligned} p(z|x) &= \sum_{m=0}^{\infty} \frac{1}{x + p_n + m\sigma_{sp}} \exp\left(\frac{-z}{x + p_n + m\sigma_{sp}}\right) P_m(m), \quad 0 \le z \\ p_c(x) &= \frac{x^{\nu_{BW}-1}}{\Gamma(\nu_{BW})} \left(\frac{\nu_{BW}}{\sigma_{BW}}\right)^{\nu_{BW}} \exp\left(\frac{-\nu_{BW} x}{\sigma_{BW}}\right), \qquad 0 \le x \\ P(z) &= \int_0^{\infty} P(z|x) P_c(x)\, dx \end{aligned} \tag{6.25}$$

x: is the local mean power of the Bragg and whitecap scattering.

z: is the intensity of the received signal.

σ_{BW}: is the mean Bragg and whitecap intensity, it given by $\sigma_{BW} = \nu_{BW}/b$.

m: is the number of spikes in a range cell

ν_{BW}: is the shape parameter for Bragg and whitecap scattering.

σ_{SP}: is the mean burst spike intensity.

p_n: is the receiver noise power.

Since the average number of spikes is assumed to be very small $\bar{N} \ll 1$, $p_m(m)$ is given by:

$$\begin{aligned} p_m(0) &= 1 - \bar{N} \\ p_m(1) &= \bar{N} \\ p_m(m \ge 2) &= 0 \end{aligned} \tag{6.26}$$

The mean intensity of the received signal is given by:

$$m_1 = \sigma_{BW} + \bar{N}\sigma_{SP} + p_n \tag{6.27}$$

Expanding the summation yields:

$$\begin{aligned} p(z) = \int_0^{\infty} \Bigg[&(1 - \overline{N}) \frac{1}{x + p_n} \exp\left(\frac{-z}{x + p_n}\right) \\ &+ \overline{N} \frac{1}{x + p_n + \sigma_{SP}} \exp\left(\frac{-z}{x + p_n + \sigma_{SP}}\right) \Bigg] P_c(x)\, dx, \;\; z \ge 0 \end{aligned} \tag{6.28}$$

the first term is just the K+thermal noise Pdf weighted by $(1-\overline{N})$, while the second term also has the same form as the K+thermal noise Pdf but weighted by $\overline{N}$ and the interference level increased by σ_{SP}.

To find the distribution parameters a procedure similar to that described in [48, 88], $\overline{N}$ was set to 0.01. In addition, at high exceedance (false alarm rates) the effect of spikes is small thus the clutter can be described using the K+thermal noise model. Hence, ν_{BW} and σ_{BW} were found by moment matching. By varying this threshold (Th) the contribution of the specular spikes and Bragg scattering components is varied under the following constraint:

$$\sigma_{sp} = \frac{m_1 - \sigma_{BW} - pn}{N} \tag{6.29}$$

In this work the optimum values are found using a Fibonacci search algorithm [143].

Generalised Pareto Distribution The Pdf of the generalised Pareto distribution is given by [78]:

$$p(z) \begin{cases} \frac{1}{\lambda}\left(1-k\frac{z}{\lambda}\right)^{\frac{1}{k}-1} & \text{when } k \neq 0 \\ \frac{1}{\lambda}\exp(\frac{-z}{\lambda}) & \text{when } k = 0 \end{cases} \tag{6.30}$$

where λ is the scale parameter and k is the shape parameter. When $k > 0$ the domain of z is $0 \leq z \leq \frac{k}{\lambda}$ and $0 \leq z \leq \infty$. The exponential distribution is a special case of the generalised Pareto distribution with $k = 0$. For sea clutter applications k is defined between $-0.5 \leq k \leq 0$. The n$^{\text{th}}$ moment is defined provided that $kn > -1$ and are given by:

$$\frac{\left(-\frac{\lambda}{k}\right)^n \Gamma(1+n)\Gamma\left(-\frac{1+kn}{k}\right)}{\Gamma\left(-\frac{1}{k}\right)} \tag{6.31}$$

The first two moments are given by:

$$m_1 = \frac{\lambda}{k+\lambda} \tag{6.32}$$

$$m_2 = \frac{2\lambda^2}{1+3k+2k^2} \tag{6.33}$$

the second normalised moment is a function of λ only and is given by:

$$N_2 = 1 + \frac{1}{1+2k} \tag{6.34}$$

hence $\hat{k}$ is given by:

$$\hat{k} = \frac{(2-N_2)}{(2(N_2-1))} \tag{6.35}$$

and $\hat{\lambda}$ can be found by substituting in Eq. (6.33).

Since many distributions are being compared a common metric had to be used to assess the goodness of the fit. Use of parametric statistical techniques is not suitable as they are not defined for all the distributions being compared. The only option is to use non-parametric techniques. In most engineering applications and especially in radar there is greater interest in the goodness of the fit in the tail region. The Kolmogorov–Smirnov (K-S) test is not suitable since an equal weight is placed on all points in the distribution. The Anderson-Darling test places more weight on the tail of the distribution [140]; however, the test results cannot be used to accept or reject the distributions since the critical values are distribution specific and they are not defined for all the distributions under test. The sum or mean of the square error between the theoretical complimentary cumulative distribution function (ccdf) and the empirical ccdf cannot be used as it it is more sensitive to the difference in values of empirical ccdf and the theoretical ccdf. The mean square error in the log domain was used to measure the goodness of fit as it is sensitive to the change in the ratio:

$$\Delta e = \frac{1}{N_s} \sum_{i=1}^{N_s} \left(10 \log_{10}\left(w_t(i)\right) - 10 \log_{10}\left(w_e(i)\right)\right)^2 \tag{6.36}$$

where $w_e(i)$ and $w_t(i)$ are the empirical and theoretical values of the Pfa (or ccdf) respectively, and N_s is the number of samples being used. Rather than reporting the fit results and error for the intersection range bins, the values reported here were averaged over the three bins which are closest to the intersection point.

To check the algorithms and the performance of the radar and the algorithm used to remove the interference Section 4.3.2. The five distributions were used to fit data collected at 15:53 on 05-Oct-2010. Due to the power limitations this data was just background noise. The shape parameters for the KA and the K+thermal noise, Weibull and Pareto were, $\nu = 246$, $c = 0.995$ and $k = -0.005$, while the skewness and kurtosis were 2.01 and 5.98 respectively, for the monostatic node. For the bistatic node the shape parameters were $\nu = 54$, $c = 0.981$ and $k = -0.019$ and the skewness and kurtosis were 2.18 and 7.68 respectively. The skewness and kurtosis of the exponential distribution are equal to 2 and 6 respectively. The fit errors in all those distributions were less than 1. It is clear that these distribution approached the special case of the exponential distribution. Nevertheless, the fit error was around 4 when using the log-normal distribution since the exponential distribution is not a special case of the log-normal distribution. The plot of the fit is shown in Fig. 6.17.

Most of the clutter data was also fitted to the KA and K+thermal noise ignoring the effect of the noise. There was little improvement particularly in the KA distribution, as σ_{SP} was higher to compensate for the effect of noise. This is to be expected since the CNR was relatively high in all the data sets as shown in Tables 5.3 and 5.6.

The reported fit errors and distribution parameters were averaged over three range bins around the

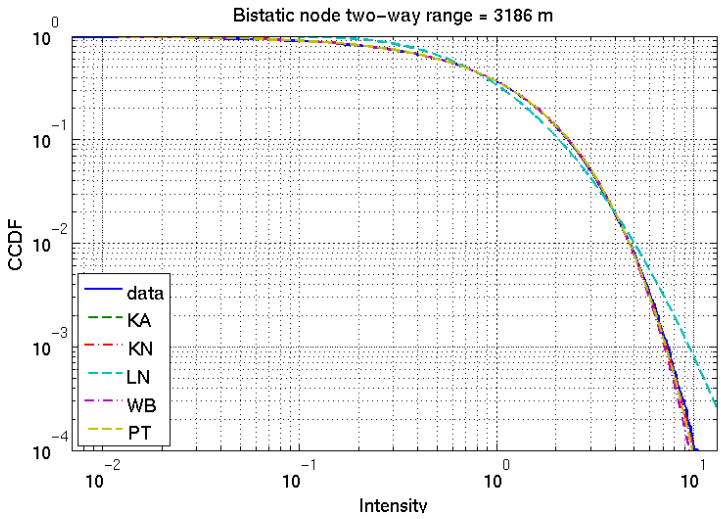

(a) Monostatic

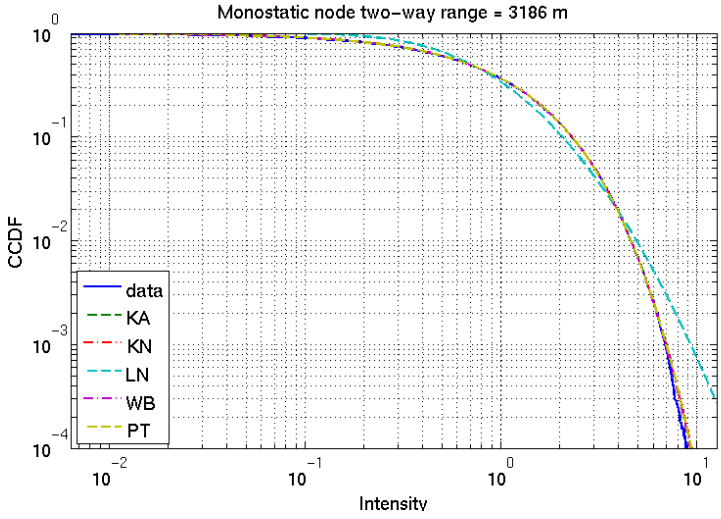

(b) Bistatic

Figure 6.17: Plot of ccdf of the data and theoretical fits, for data recorded on 15:53 on 05-Oct-2010 the two way range range was 3186 m at that range the received signal was well below the noise floor.

intersection point.

6.3.1 Low Sea State Data Fit Results

The intensity of the sea clutter data recorded on 05-Oct-2010, approximately sea state 2, was fitted to the log-normal, Weibull, Pareto, K+thermal noise and KA distribution. A summary of the fit error for the five different distributions is shown in Table 6.1. In this table LN, WB, PT, KN and KA stand for the log-normal, Weibull, Pareto, K+thermal noise and KA distribution respectively. The average error is denoted by $\overline{\Delta e}$. In all almost all cases the KA had the smallest error and was by far the best fit at both linear polarisations and for both bistatic and monostatic configurations. For vertically polarised monostatic sea clutter the second best distribution was K+thermal noise, followed by the log-normal distribution. For bistatic clutter the KA provided the best fit, the other distributions had fit errors of the same order with

time	R_T, m	Polarisation	LN	WB	PT	KN	KA
14:46	1610	VV	5.6567	35.4263	4.5023	4.0070	0.4647
14:55	832	VV	8.5583	4.7110	14.7273	4.1000	2.7737
15:09	590	VV	2.2077	7.2867	10.0863	10.1027	1.1937
16:08	590	VV	4.5827	5.1467	16.9630	9.7233	2.7560
$\overline{\Delta e}_{MV}$			5.4742	15.8080	9.7720	6.0699	1.4773
16:26	590	HV	20.0350	857.4377	31.4663	8.5443	5.6193
17:16	590	HH	16.5390	532.4830	137.9017	4.2053	4.2053

(a) Monostatic

time	R_T, m	Polarisation	LN	WB	PT	KN	KA
14:46	30°	VV	27.6980	6.3137	16.2393	8.1693	6.9133
14:55	60°	VV	6.2387	37.8767	17.4570	14.0337	2.5040
15:09	90°	VV	6.2143	7.5397	6.8753	6.1980	3.2800
16:08	90°	VV	10.8273	5.6690	12.5783	5.1930	3.9760
$\overline{\Delta e}_{BV}$			13.3837	17.2433	13.5239	9.4670	4.2324
16:26	90°	HV	3.4923	5.9363	4.9173	6.2040	1.6600
17:16	90°	HH	14.1085	74.9585	105.9675	3.5140	3.5140

(b) Bistatic

Table 6.1: Summary of fit errors for the bistatic and monostatic sea clutter data gathered on 05-Oct-2010.

the K+thermal noise providing a slightly better fit than the rest and the Weibull distribution provided the worst fit. For cross-polarised sea clutter data the KA proved to be the best distribution to model the data for both geometries. However, for the horizontally polarised data the KA algorithm defaulted to the K+thermal noise distribution and this was the best fit compared to the other distribution, i.e. the fit could not be improved by varying the percentage of contributions of σ_{SP} and σ_{BW} while keeping $\overline{N} = 0.01$. Example plots of vertically polarised clutter is shown in Figs. 6.18 and 6.19 and for horizontally polarised clutter in Fig. 6.20. As can be seen from Fig. 6.20 all the distributions were not able to fit the data. Figure 6.21 shows the fit results for the cross-polarised clutter, this particular plot is interesting because it shows how the KA distribution was able to follow the behaviour across the complete range of values while the other distributions either provided a bad fit or followed only part of the ccdf.

The fit parameters for the five different distributions are summarised in Tables 6.2 to 6.6. In the compound K family of distributions the shape parameter is used as a measure of the spikiness, the larger it is the less spiky the clutter is, the distribution of the clutter approaches that of an exponential distribution. It was noted that when the fits were reasonable, as ν increased, the shape parameter of the Weibull distribution approached 1 and that of the generalised Pareto distribution approached 0. That is, all of these distributions were approaching the limiting case of Gaussian clutter. The exponential distribution is not a special case of the log-normal distribution, hence it tended to over estimate the tail of the distribution when the clutter was not very spiky. The KA distribution uses two different parameters to describe the spikiness of the clutter, the shape parameter ν_{BW}, and $\rho = {}^{\sigma_{SP}}/_{\sigma_{BW}}$. In all cases the

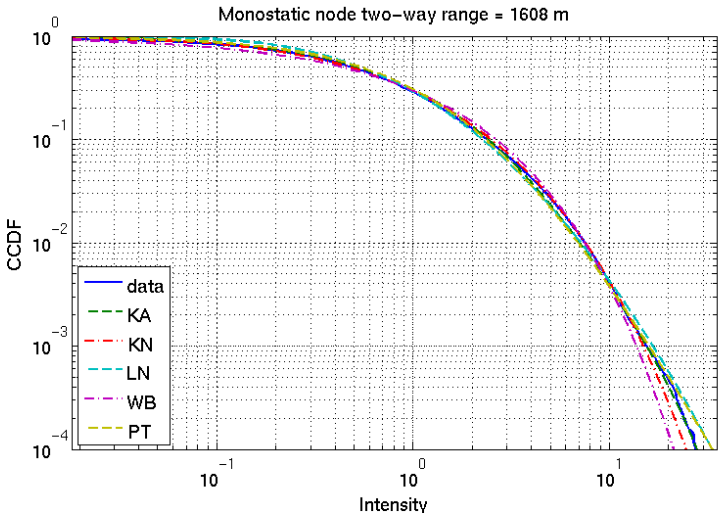

(a) Monostatic

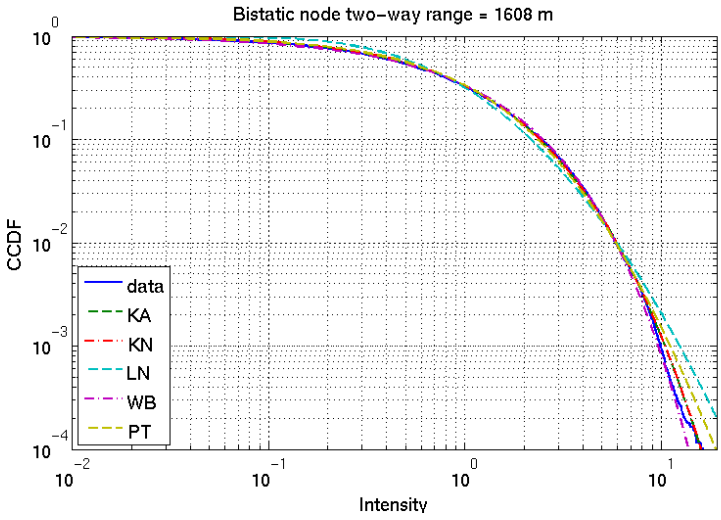

(b) Bistatic

Figure 6.18: Plot of ccdf of the data and theoretical fits, for data recorded on 14:46 on 05-Oct-2010. the antennas were vertically polarised, the two-way range was 1608 m and $\beta = 30°$.

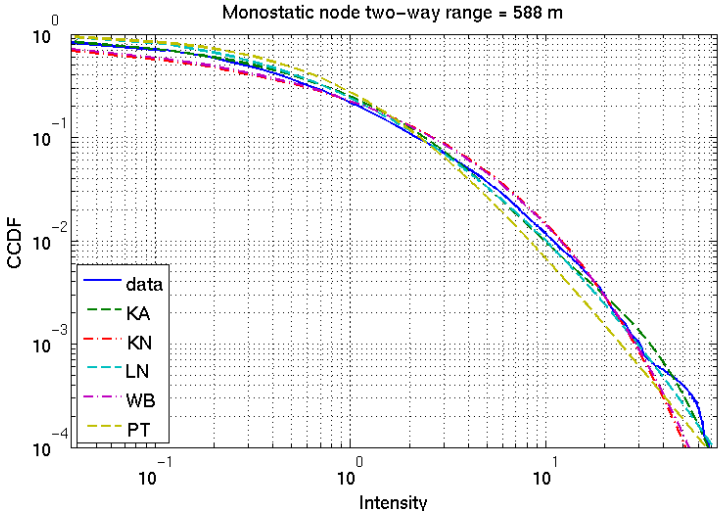

(a) Monostatic

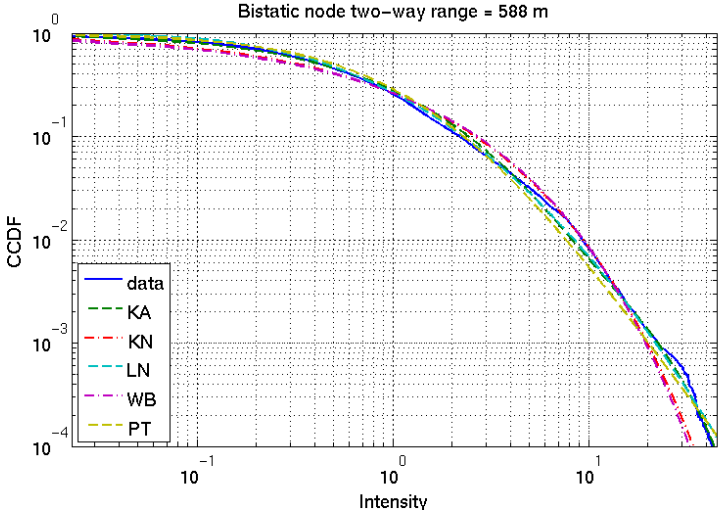

(b) Bistatic

Figure 6.19: Plot of ccdf of the data and theoretical fits, for data recorded on 15:09 on 05-Oct-2010. the antennas were vertically polarised, the two-way range was $588\,\mathrm{m}$ and $\beta = 90°$.

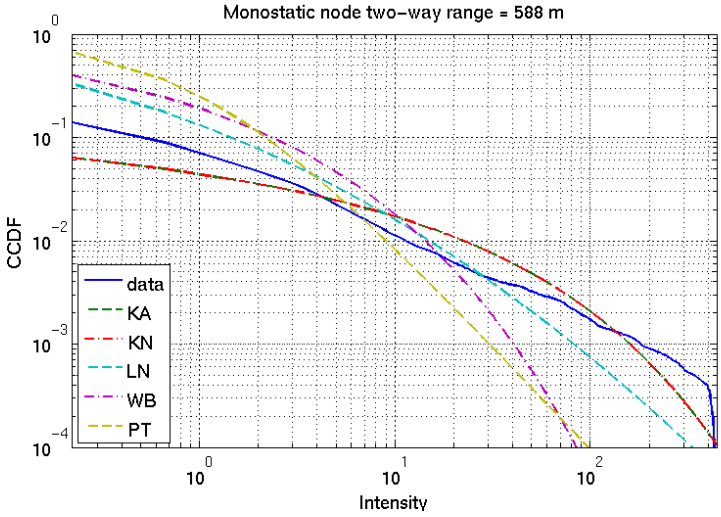

(a) Monostatic

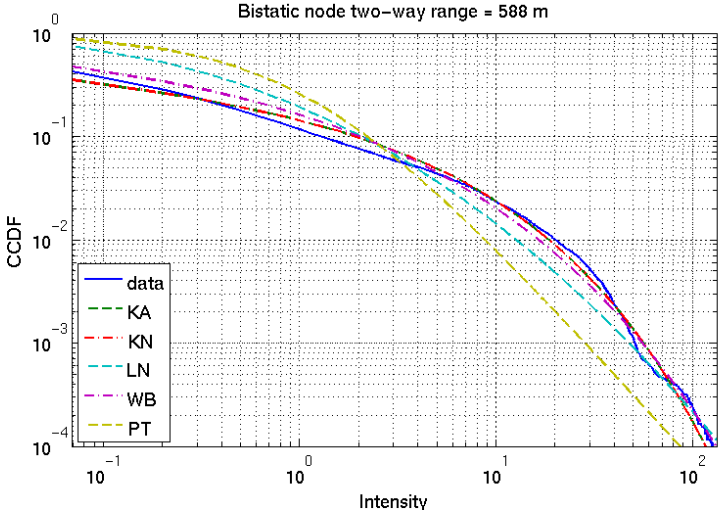

(b) Bistatic

Figure 6.20: Plot of ccdf of the data and theoretical fits, for data recorded on 17:16 on 05-Oct-2010. the antennas were horizontally polarised, the two-way range was $588\,\mathrm{m}$ and $\beta = 90°$.

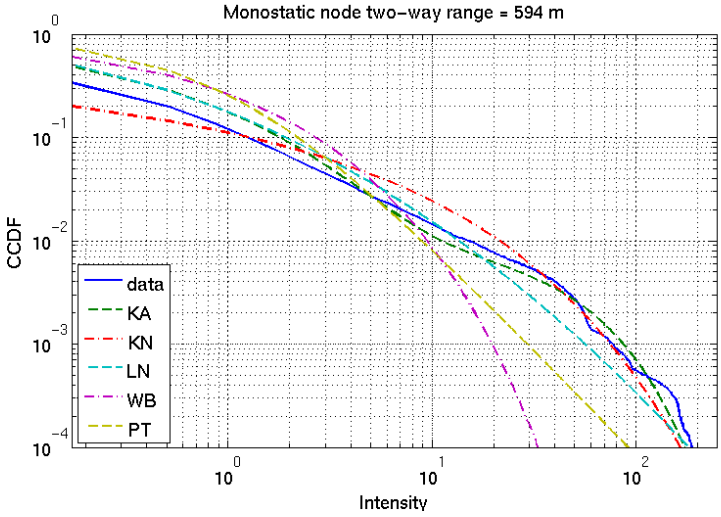

(a) Monostatic

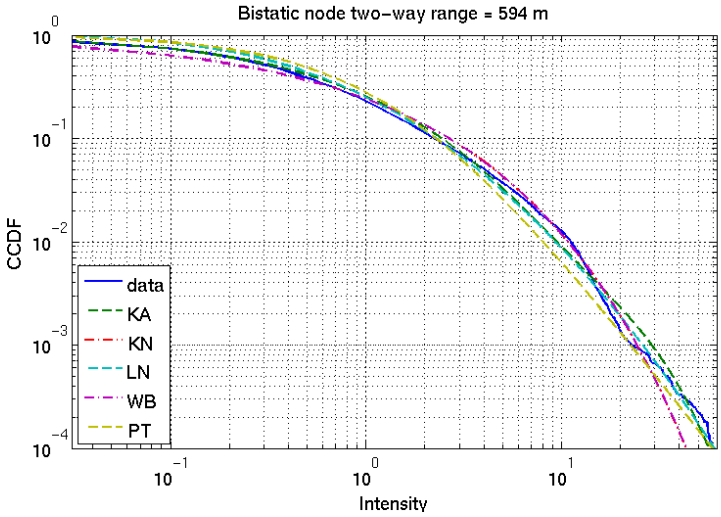

(b) Bistatic

Figure 6.21: Plot of ccdf of the data and theoretical fits, for data recorded on 16:26 on 05-Oct-2010. the antennas were the transmitting antenna was horizontally polarised, while both receiving antennas were vertically polarised. the two-way range was $588\,\mathrm{m}$ and $\beta = 90°$.

time	Monostatic				Bistatic			
	$\overline{\sigma}$	stdev(σ)	$\overline{\mu}$	stdev(μ)	$\overline{\sigma}$	stdev(σ)	$\overline{\mu}$	stdev(μ)
14:46	-0.5923	0.1779	0.8580	0.0026	-1.8533	2.3787	0.9730	0.0178
14:55	-1.1140	0.0000	0.9980	0.0000	-1.0933	0.1718	1.4753	0.1190
15:09	-1.0603	0.1090	0.9990	0.0000	-0.7623	0.0199	1.2347	0.0161
16:08	-1.2443	0.0240	1.0000	0.0000	-0.9810	0.0380	1.4007	0.0270
16:26	-1.4783	0.0580	0.9780	0.0026	-0.2780	1.0275	1.3633	0.0391
17:16	-2.1347	0.0316	0.9987	0.0006	-1.9390	0.6095	1.9565	0.3118

Table 6.2: Fit parameters for the log-normal distribution, data was collected on 05-Oct-2010. The upper part of the table is for vertically polarised clutter, the bottom row is for cross-polar clutter while the row before the last is for horizontally polarised clutter. See text for symbols.

time	Monostatic				Bistatic			
	$\overline{c}$	stdev(c)	$\overline{a}$	stdev(a)	$\overline{c}$	stdev(c)	$\overline{a}$	stdev(a)
14:46	0.6830	0.0248	0.7707	0.0278	0.8037	0.0210	0.8850	0.0168
14:55	0.4263	0.0475	0.3547	0.0976	0.4333	0.0577	0.3677	0.1155
15:09	0.4417	0.0440	0.3857	0.0892	0.5663	0.0115	0.6123	0.0178
16:08	0.3870	0.0125	0.2743	0.0255	0.4663	0.0140	0.4357	0.0275
16:26	0.3733	0.1816	0.2857	0.2927	0.4863	0.0214	0.4747	0.0409
17:16	0.3650	0.0554	0.2327	0.1070	0.3905	0.0827	0.2825	0.1690

Table 6.3: Fit parameters for the Weibull distribution, data was collected on 05-Oct-2010. The upper part of the table is for vertically polarised clutter, the bottom row is for cross-polar clutter while the row before the last is for horizontally polarised clutter. See text for symbols.

shape parameter $\nu_{BW} \geq \nu$, this is understandable since the K+thermal noise was used to modelled all of the data including the tail extremities. These points were not used when computing the ν_{BW}, the effect of these points was included when computing the overall KA distribution.

In this data set when the error was in single digits the bistatic clutter was less spiky than the monostatic clutter. A subset of this data has been published [136]. The reported fits were based on a single range bin rather than an average. In addition, the data was fitted to the K+thermal noise distribution by using a Fibonacci optimisation algorithm. While in this work the data was fitted using MoM and averaged over three range bins, which caused small differences in the reported results.

6.3.2 High Sea State Fit Results

The data was recorded on 10-Oct-2010, approximately sea state 4 – 5; as in the previous section it was fitted to the log-normal, Weibull, Pareto, K+thermal and KA distributions. The KA provided the best fit in almost all of the cases under test after averaging around the intersection point, as can be seen in Table 6.7. For horizontally polarised monostatic sea clutter the second best fit was provided by the log-normal distribution. K+thermal noise distribution was better than than the Pareto distribution, while the Weibull failed to fit the data. As for bistatic sea clutter the error was of the same order, however, the

time	Monostatic				Bistatic			
	$\overline{k}$	stdev(k)	$\overline{\lambda}$	stdev(λ)	$\overline{k}$	stdev(k)	$\overline{\lambda}$	stdev(λ)
14:46	-0.2793	0.0189	0.7207	0.0189	-0.1823	0.0183	0.8177	0.0183
14:55	-0.4367	0.0214	0.5633	0.0214	-0.4330	0.0286	0.5670	0.0286
15:09	-0.4293	0.0203	0.5690	0.0231	-0.3610	0.0070	0.6390	0.0070
16:08	-0.4543	0.0047	0.5457	0.0047	-0.4180	0.0075	0.5820	0.0075
16:26	-0.4703	0.0135	0.5297	0.0135	-0.4073	0.0112	0.5927	0.0112
17:16	-0.4907	0.0076	0.5093	0.0076	-0.4850	0.0156	0.5150	0.0156

Table 6.4: Fit parameters for the generalised Pareto distribution, data was collected on 05-Oct-2010. The upper part of the table is for vertically polarised clutter, the bottom row is for cross-polar clutter while the row before the last is for horizontally polarised clutter. See text for symbols.

time	Monostatic				Bistatic			
	$\overline{\nu}$	stdev(ν)	$\overline{\sigma}_{BW}$	stdev (σ_{BW})	$\overline{\nu}$	stdev(ν)	$\overline{\sigma}_{BW}$	stdev (σ_{BW})
14:46	1.1737	0.1779	0.8580	0.0026	2.9910	0.4444	0.9223	0.0006
14:55	0.2927	0.1070	0.9980	0.0000	0.3170	0.1585	0.9993	0.0006
15:09	0.3313	0.1090	0.9990	0.0000	0.7717	0.0533	0.9993	0.0006
16:08	0.2000	0.0240	1.0000	0.0000	0.3927	0.0416	1.0000	0.0000
16:26	0.1223	0.0580	0.9780	0.0026	0.4547	0.0675	0.9970	0.0000
17:16	0.0370	0.0316	0.9987	0.0006	0.0615	0.0615	0.9885	0.0049

Table 6.5: Fit parameters for the K+thermal noise distribution, data was collected on 05-Oct-2010. The upper part of the table is for vertically polarised clutter, the bottom row is for cross-polar clutter while the row before the last is for horizontally polarised clutter. See text for symbols.

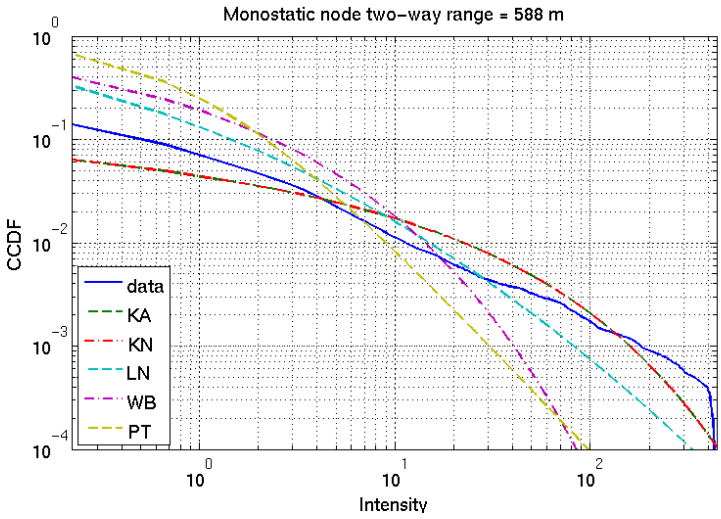

(a) Monostatic

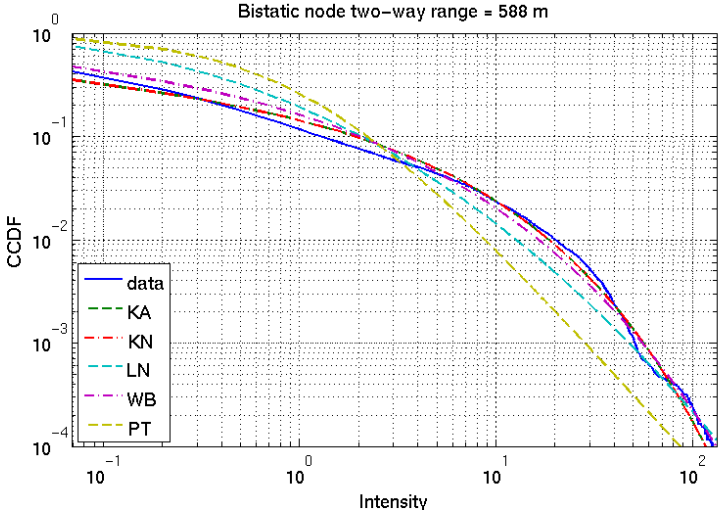

(b) Bistatic

Figure 6.22: Plot of ccdf of the data and theoretical fits, for cross-polarised monostatic and bistatic sea clutter recorded at 17:16 on 05-Oct-2010. the monostatic range was 588 m and a bistatic angle of 90°.

Time	$\overline{\nu}$	stdev (ν)	$\overline{\sigma}_{BW}$	stdev (σ_{BW})	$\overline{\sigma}_{SP}$	stdev(σ_{SP})	Th	stdev(Th)
14:46	1.8990	0.3741	0.8113	0.0025	4.6683	0.3905	0.0033	0.0001
14:55	0.4133	0.0575	0.8927	0.0667	10.5307	6.7341	0.0032	0.0014
15:09	0.7620	0.1707	0.8503	0.0379	14.8873	3.7950	0.0053	0.0004
16:08	0.4457	0.0826	0.8160	0.0459	18.3877	4.6198	0.0059	0.0029
16:26	0.4420	0.0771	0.7410	0.1128	23.6930	11.5794	0.0046	0.0014
17:16	0.0370	0.0316	0.9987	0.0006	0	N/A	N/A	N/A

(a) KA monostatic

Time	$\overline{\nu}$	stdev (ν)	$\overline{\sigma}_{BW}$	stdev (σ_{BW})	$\overline{\sigma}_{SP}$	stdev(σ_{SP})	Th	stdev(Th)
14:46	3.6957	0.4183	0.9060	0.0053	1.6557	0.5010	0.0014	0.0004
14:55	1.0063	0.0576	0.8320	0.0592	16.7163	5.9399	0.0064	0.0024
15:09	1.1357	0.2156	0.9427	0.0257	5.6467	2.4874	0.0029	0.0013
16:08	0.5247	0.0250	0.9280	0.0199	7.1783	2.0221	0.0025	0.0006
16:26	0.7887	0.1302	0.8960	0.0144	10.1377	1.4348	0.0036	0.0002
17:16	0.0615	0.0615	0.9885	0.0049	0	N/A	N/A	N/A

(b) KA bistatic

Table 6.6: Fit parameters for the KA distribution, data was collected on 05-Oct-2010. The upper part of the table is for vertically polarised clutter, the bottom row is for cross-polar clutter while the row before the last is for horizontally polarised clutter. See text for symbols.

log-normal K+thermal noise and Pareto distributions had similar performance. Nevertheless, the Weibull distribution was not a good fit for this data set.

Generally, the errors were smaller for vertically polarised sea clutter. For the monostatic case KA provided the best fit followed by the generalised Pareto distribution, the Weibull provided the worst fit but the error was much smaller than that of the horizontally polarised clutter. As for the low sea state case, the KA provided the best fit. The performance of the K+thermal noise and the Weibull was very similar. The log-normal and the Pareto provided the worst fit and their fit errors were of the same order.

As in the low sea state results, when the fits were not too bad, all the distributions followed a similar trend with regards to spikiness. However, contrary to the results in the previous section, the bistatic clutter was not less spiky than the monostatic clutter. A summary of the results is presented in Tables 6.8 to 6.12.

6.3.3 Sea Clutter Spikiness

Since the KA distribution provided the best fit it was subsequently used to study the spikiness of the data. Furthermore, using the KA distribution the cause of the spikiness can be traced to either the modulation by the texture (due to Bragg scattering) or to burst scattering. An empirical model for the shape parameter

time	R_T, m	Polarisation	LN	WB	PT	KN	KA
12:20	1827	HH	8.6220	636.9283	29.5250	3.5323	2.5850
12:33	1827	HH	6.8597	680.9087	21.8313	7.6273	1.2043
12:44	1292	HH	9.3587	1,737.6250	70.6587	5.3573	2.1420
12:53	1055	HH	6.6223	92.9293	6.1467	82.1807	6.6993
$\bar{\Delta e}_{MH}$			7.8657	787.0978	32.0404	24.6744	3.1577
15:51	1827	VV	1.0960	19.6780	1.9337	15.1660	1.3653
16:03	1292	VV	7.1750	20.0417	5.6053	11.0003	1.9743
16:17	1055	VV	10.2543	19.9007	2.8217	3.8260	1.6020
$\bar{\Delta e}_{MV}$			6.1751	19.8734	3.4536	9.9974	1.6472

(a) Monostatic

time	β, degree	Polarisation	LN	WB	PT	KN	KA
12:20	30°	HH	7.042	2,370.4563	42.9217	5.0700	3.2823
12:33	30°	HH	10.6787	1,583.7900	48.1573	11.0767	3.3490
12:44	90°	HH	5.6730	3.6513	12.6617	6.5003	0.9000
12:53	120°	HH	7.4203	13.0023	7.3117	8.2213	3.4180
$\bar{\Delta e}_{BH}$			7.7035	992.7250	27.7631	7.7171	2.7373
15:51	30°	VV	8.2617	4.1137	10.1860	4.2947	2.6843
16:03	90°	VV	9.944	3.8063	9.6017	2.4777	1.1443
16:17	120°	VV	17.1603	4.4377	12.0513	2.8540	2.4687
$\bar{\Delta e}_{BV}$			11.7887	4.1192	10.6130	3.2088	2.0991

(b) Bistatic

Table 6.7: Summary of fit errors for the bistatic and monostatic sea clutter data gathered on 10-Oct-2010. See text for symbols.

time	Monostatic				Bistatic			
	$\overline{\sigma}$	stdev(σ)	$\overline{\mu}$	stdev(μ)	$\overline{\sigma}$	stdev(σ)	$\overline{\mu}$	stdev(μ)
12:20	1.6503	0.1840	-1.3733	0.3123	1.7693	0.0718	-1.5667	0.1266
12:33	1.5363	0.1885	-1.1917	0.2993	1.6833	0.2456	-1.4370	0.4298
12:44	1.8840	0.0225	-1.7743	0.0419	1.4790	0.1044	-1.0977	0.1577
12:53	1.3277	0.0231	-0.8817	0.0309	1.1443	0.0712	-0.6567	0.0823
15:51	1.2907	0.0535	-0.8340	0.0698	1.3257	0.0880	-0.8810	0.1198
16:03	1.0973	0.0834	-0.6043	0.0929	1.2020	0.0187	-0.7223	0.0222
16:17	0.9417	0.0029	-0.4443	0.0021	1.0333	0.0140	-0.1870	0.6123

Table 6.8: Fit parameters for log-normal distribution, the upper part of each table is for horizontal polarisation and the bottom half is for vertical polarisation. See text for symbols.

time	Monostatic				Bistatic			
	$\overline{c}$	stdev(c)	$\overline{a}$	stdev(a)	$\overline{c}$	stdev(c)	$\overline{a}$	stdev(a)
12:20	0.4513	0.0897	0.3723	0.1270	0.4337	0.2727	0.4350	0.3770
12:33	0.5010	0.0836	0.4927	0.1468	0.4600	0.1025	0.4127	0.1907
12:44	0.5373	0.0105	0.5657	0.0180	0.4307	0.0459	0.3633	0.0935
12:53	0.5063	0.0134	0.5113	0.0248	0.6360	0.0577	0.7100	0.0769
15:51	0.5300	0.0332	0.5520	0.0580	0.5100	0.0496	0.5153	0.0924
16:03	0.6787	0.0736	0.7600	0.0881	0.5890	0.0131	0.6483	0.0201
16:17	0.8400	0.0030	0.9123	0.0015	0.7367	0.0150	0.8267	0.0140

Table 6.9: Fit parameters for Weibull distribution data collected on 10-Oct-2010. The upper part of table is for horizontal polarisation and the bottom half is for vertical polarisation. See text for symbols.

time	Monostatic				Bistatic			
	$\overline{k}$	stdev(k)	$\overline{\lambda}$	stdev(λ)	$\overline{k}$	stdev(k)	$\overline{\lambda}$	stdev(λ)
12:20	-0.4607	0.0208	0.5393	0.0208	-0.4767	0.0068	0.5233	0.0068
12:33	-0.4420	0.0297	0.5580	0.0297	-0.4620	0.0236	0.5380	0.0236
12:44	-0.4853	0.0012	0.5147	0.0012	-0.4347	0.0203	0.5673	0.0169
12:53	-0.3963	0.0076	0.6037	0.0076	-0.3123	0.0399	0.6877	0.0399
15:51	-0.3823	0.0196	0.6177	0.0196	-0.3933	0.0275	0.6067	0.0275
16:03	-0.2810	0.0541	0.7190	0.0541	-0.3453	0.0091	0.6547	0.0091
16:17	-0.1507	0.0025	0.8493	0.0025	-0.2380	0.0115	0.7620	0.0115

Table 6.10: Fit parameters for generalised Pareto distribution. The data was collected on 10-Oct-2010. The upper part of each table is for horizontal polarisation and the bottom half is for vertical polarisation. See text for symbols.

time	Monostatic				Bistatic			
	$\overline{\nu}$	stdev(ν)	$\overline{\sigma}_{BW}$	stdev (σ_{BW})	$\overline{\nu}$	stdev(ν)	$\overline{\sigma}_{BW}$	stdev (σ_{BW})
12:20	0.1370	0.0721	0.8990	0.0234	0.0700	0.0183	0.8463	0.0150
12:33	0.1760	0.1261	0.9403	0.0161	0.1613	0.0170	0.8180	0.0128
12:44	0.0603	0.0067	0.9917	0.0072	0.2813	0.0858	0.9683	0.0275
12:53	0.4937	0.0448	0.9707	0.0015	1.1813	0.3888	0.9770	0.0000
15:51	0.6107	0.1308	0.9930	0.0010	0.5027	0.1573	0.9550	0.0010
16:03	1.6430	0.6773	0.9987	0.0023	0.8553	0.0964	0.9933	0.0115
16:17	4.6167	0.1046	0.9980	0.0017	2.1940	0.2032	0.9957	0.0006

Table 6.11: Fit parameters for K+thermal noise distribution. The data was collected on 10-Oct-2010. The upper part of each table is for horizontal polarisation and the bottom half is for vertical polarisation. See text for symbols.

Time	$\overline{\nu}$	stdev (ν)	$\overline{\sigma}_{BW}$	stdev (σ_{BW})	$\overline{\sigma}_{SP}$	stdev(σ_{SP})	Th	stdev(Th)
12:20	0.2967	0.0603	0.6797	0.1019	21.9253	12.4939	5.02E-003	1.76E-003
12:33	0.6057	0.0546	0.7050	0.0814	23.5173	9.5992	7.26E-003	1.97E-003
12:44	0.4247	0.0575	0.5940	0.0202	39.2885	1.3343	8.89E-003	8.67E-004
12:53	1.9213	0.8283	0.8413	0.0159	9.6143	4.3647	7.06E-003	2.44E-003
15:51	1.1850	0.1591	0.8963	0.0172	9.6480	1.7918	4.82E-003	4.32E-004
16:03	2.3457	0.3445	0.9577	0.0308	4.1140	3.2434	2.53E-003	1.78E-003
16:17	7.1680	1.1305	0.9757	0.0059	2.1370	0.5964	1.93E-003	6.20E-004

(a) KA monostatic

Time	$\overline{\nu}$	stdev (ν)	$\overline{\sigma}_{BW}$	stdev (σ_{BW})	$\overline{\sigma}_{SP}$	stdev(σ_{SP})	Th	stdev(Th)
12:20	0.3167	0.0708	0.5377	0.0499	30.8717	6.1248	8.12E-003	2.12E-003
12:33	0.5627	0.2320	0.6417	0.0362	17.5933	2.4688	6.01E-003	2.64E-003
12:44	0.6270	0.1239	0.8233	0.0430	14.5060	6.9749	5.22E-003	2.48E-003
12:53	1.8847	0.1072	0.9260	0.0340	5.0873	3.4005	2.78E-003	1.64E-003
15:51	0.8280	0.0910	0.8690	0.0392	8.5853	3.9480	3.48E-003	1.13E-003
16:03	1.2493	0.0261	0.9373	0.0230	5.6033	1.4356	3.04E-003	7.74E-004
16:17	2.7817	0.3782	0.9157	0.1080	2.0037	0.4635	1.40E-003	3.61E-004

(b) KA bistatic

Table 6.12: Fit parameters for KA distribution data collected on 10-Oct-2010. The upper part of table is for horizontal polarisation and the bottom half is for vertical polarisation. See text for symbols.

of the compound K distribution was proposed in [60] based on I-band (9 GHz) measurements:

$$\log_{10}(\nu) = \frac{2}{3}\log_{10}(\psi) + \frac{5}{8}\log_{10}(A_c) - k_{pol} - \frac{1}{3}\cos(2\theta_{SW}) \tag{6.37}$$

where:

ψ: is the grazing angle in degrees.

θ_{SW}: is the aspect angle with respect with the swell.Aspect angle with respect with the swell

k_{pol}: depends on the polarisation and is 1.39 for vertical polarisation and 2.09 for horizontal polarisation.

A_c: is the clutter cell area.

6.3.3.1 Low Sea State Data Set

This data set was recorded on 05-Oct-2010 and the sea state was estimated to be around 2. The surface truth and geometry data was provided in Section 5.4.1; a sketch of the geometry is repeated in Fig. 6.23. Because of the limited range in this data set, the wave direction was taken to be approaching the coast line. The baseline was almost parallel to the coast line. Therefore, $2\theta_{SW}$ was assumed to be equal to β. The expected shape parameter was calculated using using Eq. (6.37), and the results for the monostatic node are plotted in Fig. 6.24. Since the look angles of both nodes were symmetric with respect to the swell direction chaining the bistatic angle will have similar effect on both nodes and a monostatic node

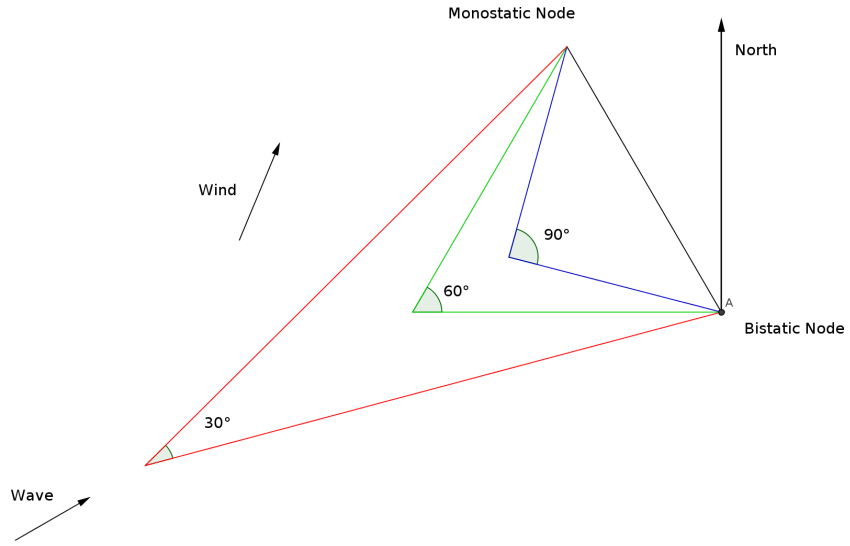

Figure 6.23: A sketch of the geometry used on 05-Oct-2010, showing the wind and wave directions.

located at the position of the bistatic node was expected to to have the same shape parameter as the monostatic node. Only the shape parameter value at a monostatic range of $804\,\mathrm{m}$ was close to the the value computed from the gathered data, cf. Table 6.6. Contrary to the model predictions the calculated shape parameter decreased as the range was reduced. This was due to the increased probability of breaking waves as the waves approach the shore. This was particularly true for horizontally polarised and cross-polarised measurements.

To further study the origin of the spikes example time histories were analysed. The time history of a range bin of the data gathered at 14:46 is shown in Fig. 6.25, and it can be seen from the plot that the spikes have a larger intensity in the monostatic plot, the spikes that look noise like and have a long duration and hence are due to whitecap scattering. Furthermore, since there were no clear specular spikes which are related to burst scattering, it is expected that σ_{SP} would be small, this was the case in this data set cf. Table 6.6. The time history of a range bin of the data gathered at 15:09 is shown in Fig. 6.26. The monostatic range was $294\,\mathrm{m}$ and it is clear that the spike intensity to the average intensity has increased. However, the intensity was much higher in the monostatic data. This change was reflected by the unexpected decrease in the shape parameter, as compared to the data gathered at a monostatic range of range of $804\,\mathrm{m}$. All the distributions were not able to fit the horizontally polarised monostatic sea clutter and the bistatic was not an especially good fit, cf. Table 6.1. The time histories for a range bin of this data is shown in Fig. 6.27. As for the monostatic there was a very large spike at around second 75, and a smaller one around second 10. These spikes are not due to interference as they lasted only for a fraction of a second. The spike at second 75 can also be seen in the bistatic time history but its amplitude is much weaker around 140.

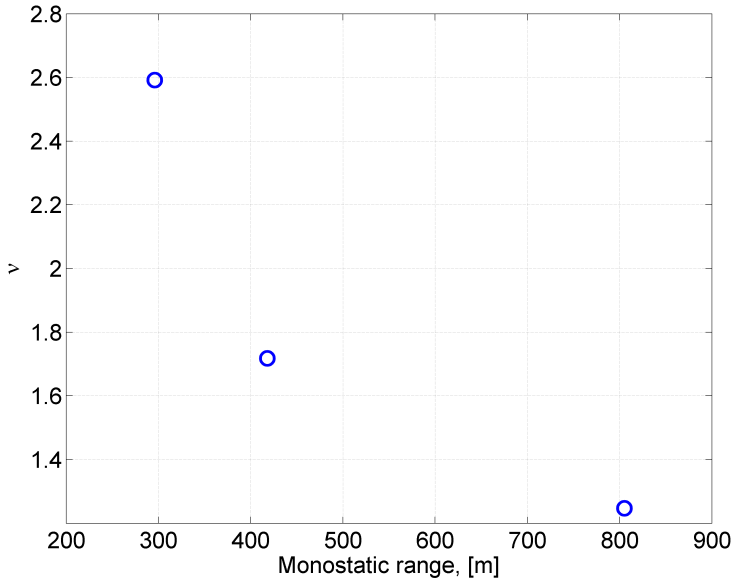

Figure 6.24: Theoretical K distribution shape parameter vs the monostatic range for the vertically polarised monostatic sea clutter data gathered on 05-Oct-2010.

6.3.3.2 High Sea State Data

Unlike the low sea state data the shape parameter was not higher for bistatic sea clutter when compared with simultaneously recorded monostatic sea clutter. The high sea state data was recorded on 10-Oct-2010 and the sea state was estimated to be between 4 and 5. As can be seen in Fig. 6.28 the monostatic node was looking across the swell while the bistatic node was looking into the swell. It is worth noting that the measured data was spikier than that predicted by Eq. (6.37) and the change in value of the shape parameter in the measured data was higher than that predicted by the empirical formula as shown in Fig. 6.29a. The lack of repeated measurements made it difficult to determine the statistical significance of the difference between the bistatic and monostatic measurements especially since the differences were not large. Using Eq. (6.37) the shape parameter of a monostatic node located at the position of the bistatic node can be computed. From Fig. 6.29b it can be seen that this hypothetical node would have had a shape parameter approximately 40% of that of the monostatic node. It can be seen in Table 6.12 that the ratio was around 1 for the horizontal polarisation, while using Eq. (6.37) gives a ratio of around 0.4. The ratio in vertical polarisation was similar to that predicted by Eq. (6.37). By comparing σ_{SP} in Table 6.12, it is clear that the contribution of the specular spikes to the total clutter power was smaller in horizontally polarised bistatic sea clutter. While the ratio was comparable in vertically polarised clutter. This indicates that the bistatic geometry reduced the effect of burst spikes but not of those due to Bragg scattering and the modulation of the waves.

In the single repeated measurement there was significant change in both ν_{BW} and σ_{SP} in both the bistatic and monostatic horizontally polarised clutter. For the data collected at 12:20 the bistatic

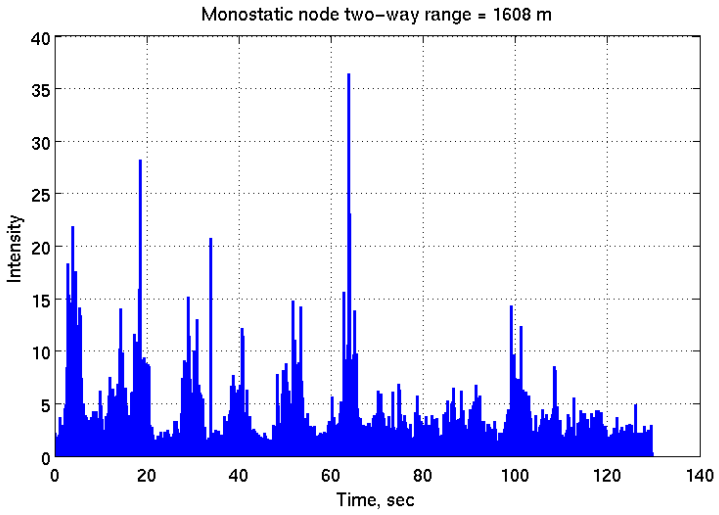

(a) Monostatic

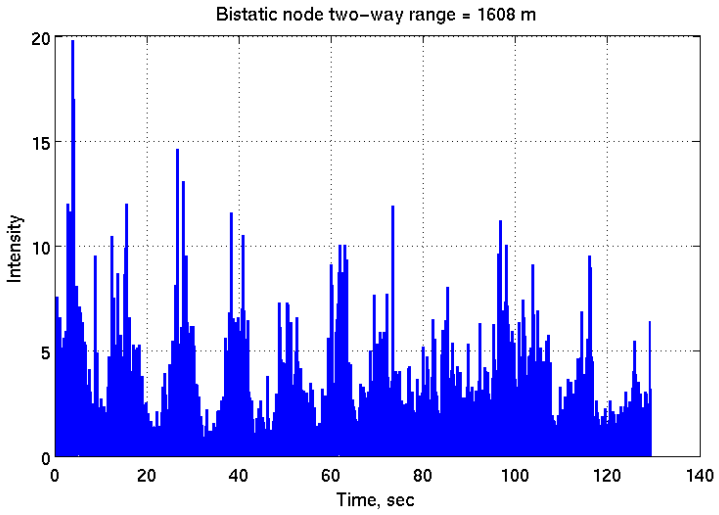

(b) Bistatic, $\beta = 30°$

Figure 6.25: Time history of vertically polarised monostatic and bistatic clutter gathered at 14:46 on 05-Oct-2010.

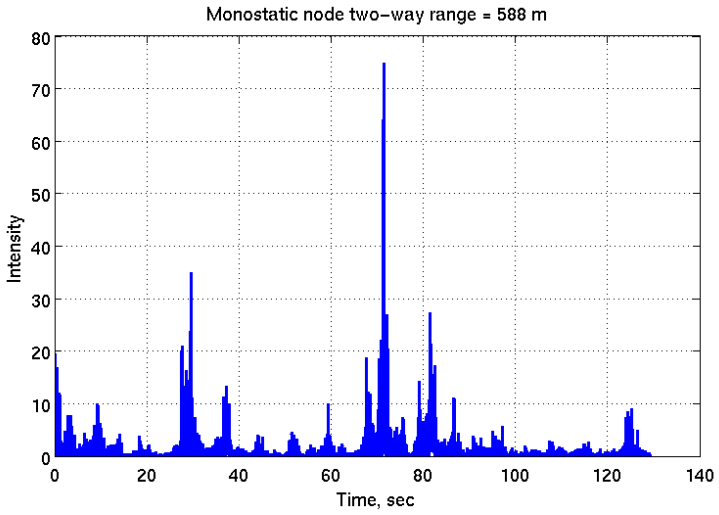

(a) Monostatic

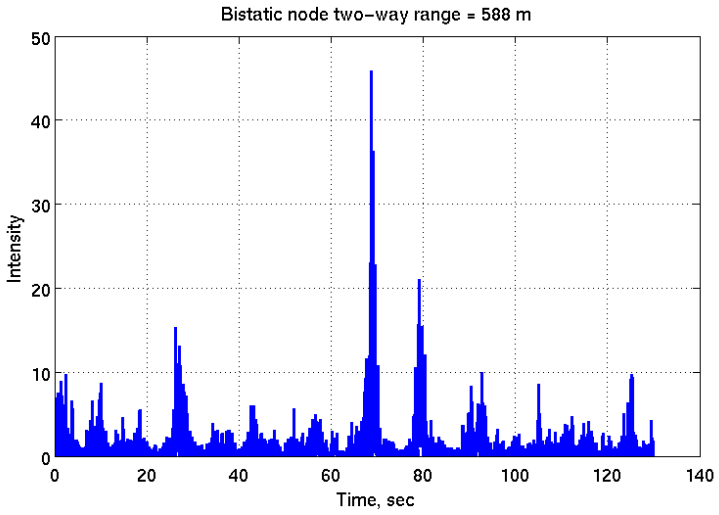

(b) Bistatic, $\beta = 90°$

Figure 6.26: Time history of vertically polarised monostatic and bistatic clutter gathered at 15:09 on 05-Oct-2010.

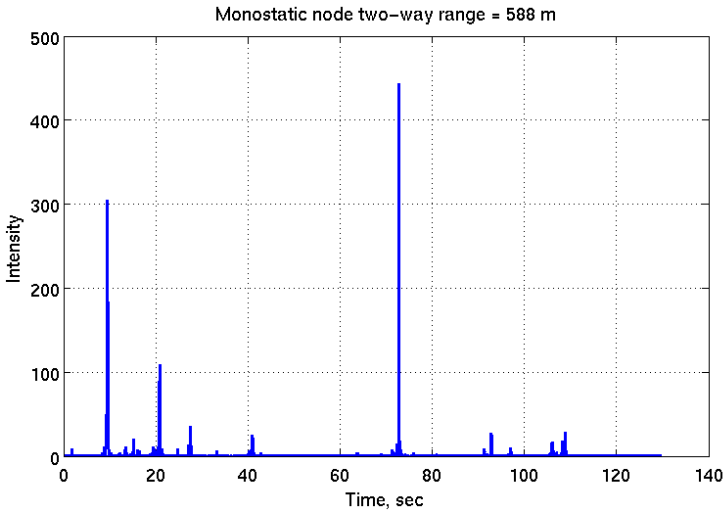

(a) Monostatic

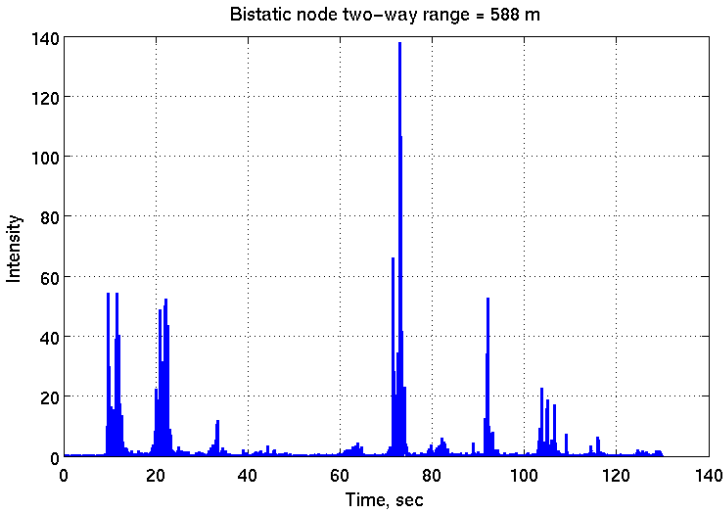

(b) Bistatic, $\beta = 90°$

Figure 6.27: Time history of horizontally polarised monostatic and bistatic clutter gathered at 17:16 on 05-Oct-2010.

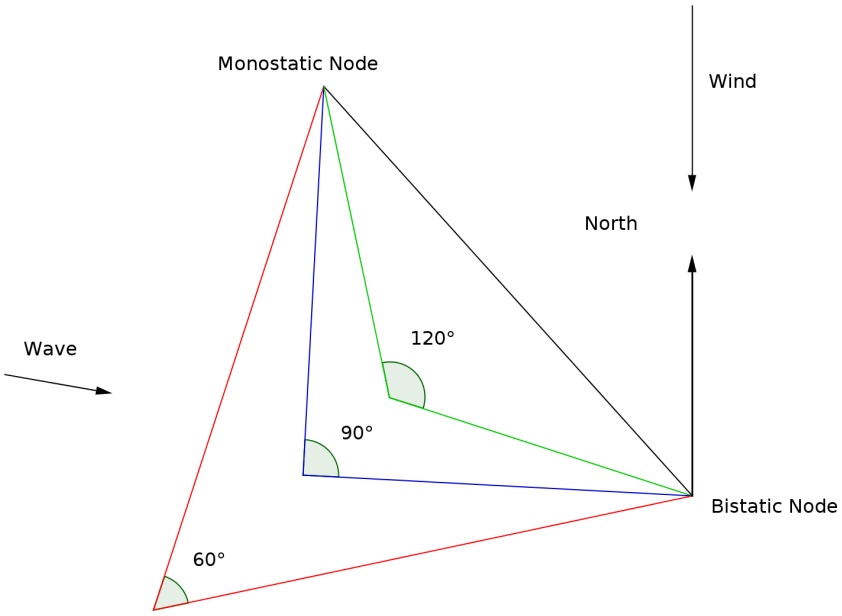

Figure 6.28: A sketch of the geometry used on 10-Oct-2010.

clutter was spikier and there was a large spike at around second 70. This explains the very high ratio of σ_{SP}/σ_{BW}. Most of the spikes appeared in both time histories but their amplitude was different. On the other hand, the data gathered at 12:33 had more spikes but had smaller magnitude particularly in the bistatic case. It is also worth noting that the σ_{SP}/σ_{BW} in the bistatic case was much smaller compared to the previous data set.

6.3.4 Preliminary Radar Performance Analysis

To assess the difference in radar performance between the bistatic and monostatic nodes, the probability of detection (Pd) was plotted vs. the signal to interference ratio (SIR), which is defined as the sum of the clutter and the receiver noise. Particularly at low Pfa the achievable Pd is greatly influenced by the tails of the distribution. Hence the spikier the clutter the lower the Pd for a given SIR. Another factor that will affect the performance is the clutter power, the lower the clutter power the less target power is required to achieve a certain SIR. A probability of false alarm (Pfa) of 1×10^{-4} was chosen for these calculations to simulate a realistic radar Pfa. Choosing a lower Pfa would have meant that the available number of samples to estimate the Pfa were too small to provide a reasonable estimate.

6.3.4.1 Background

Generally the presence of a target return will increase the output power of the radar receiver. In threshold detection a target is detected if the received signal exceeds a threshold V_T . However, since the the noise and clutter are stochastic processes the increase could be due to the random variation in the background

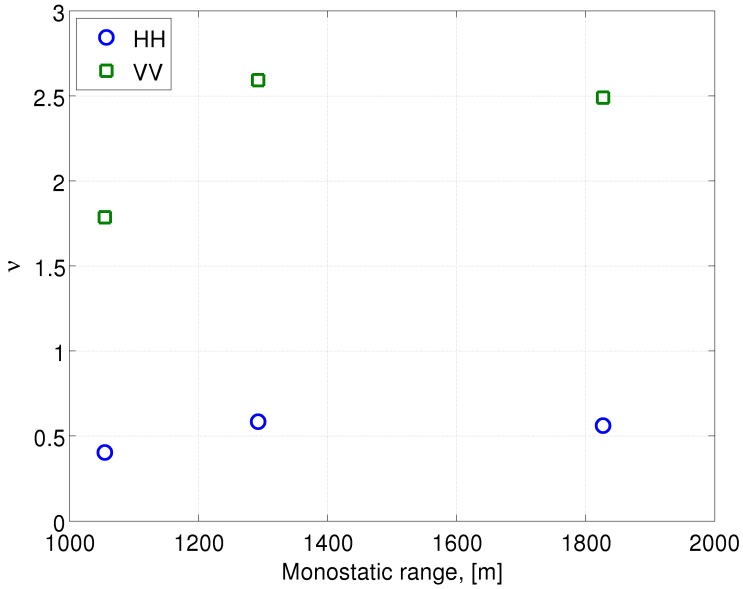

(a) Monostatic

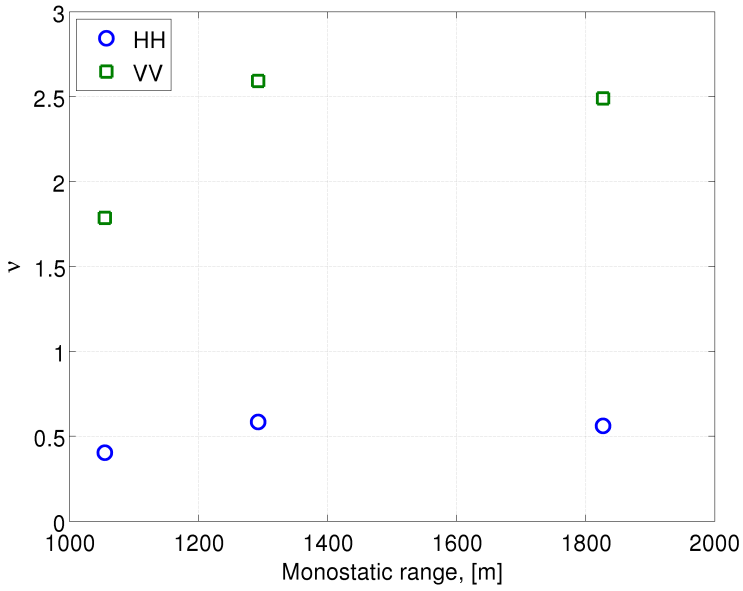

(b) Monostatic at bistatic node location

Figure 6.29: Expected K distribution shape parameter for the monostatic node and a monostatic node located at the bistatic node position, using the parameters and geometry of the data gathered on 10-Oct-2010.

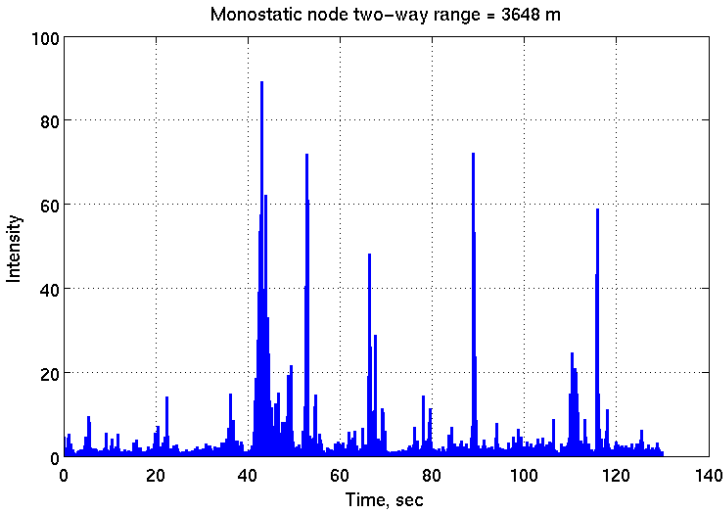

(a) Monostatic

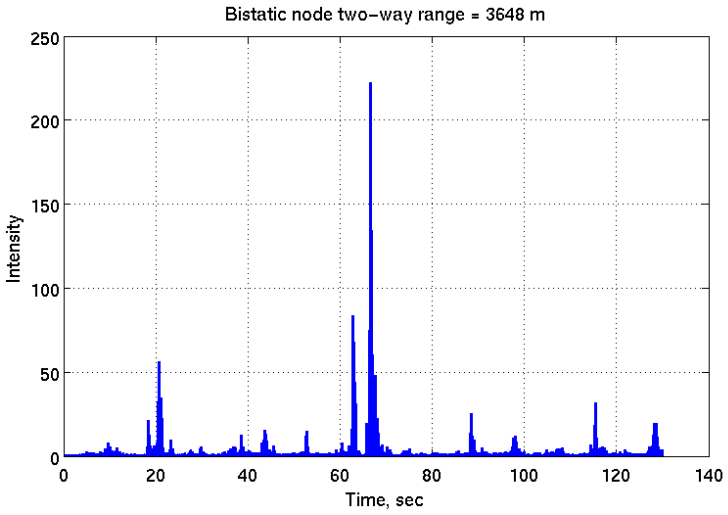

(b) Bistatic, $\beta = 60°$

Figure 6.30: Time history of data collected at 12:20 on 10-Oct-2010.

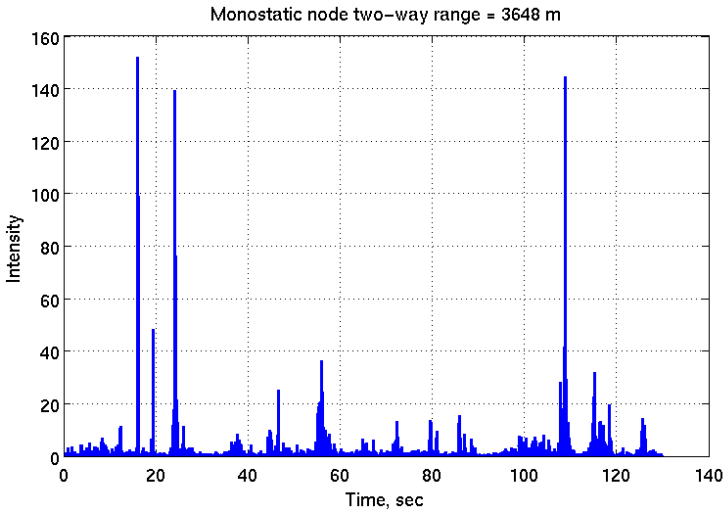

(a) Monostatic

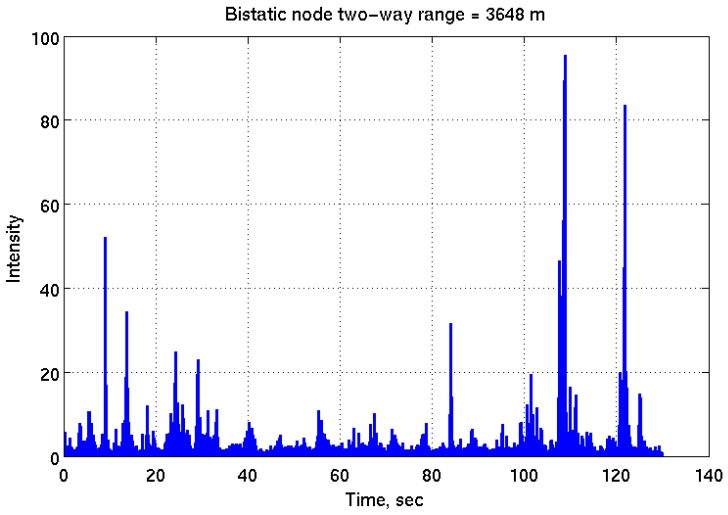

(b) Bistatic, $\beta = 60°$

Figure 6.31: Time history of data collected at 12:33 on 10-Oct-2010.

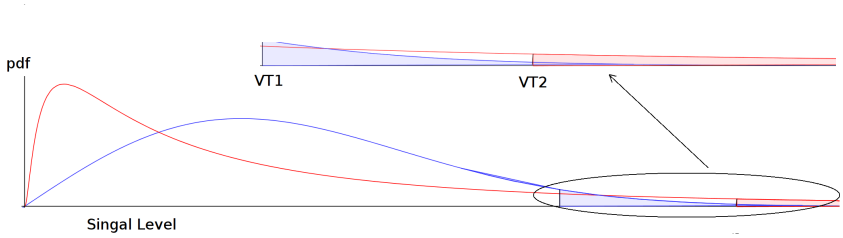

Figure 6.32: Effect of spikiness on threshold level. Note how the threshold (V_{T1}) is much lower for Gaussian noise (blue) compared to that of spiky clutter (red) V_{T2} for the same pfa.

signal, and this leads to false alarms. The probability of detection is given by:

$$\text{Pd} = \int_{V_T}^{\infty} P_{S+I}(x)\, dx \tag{6.38}$$

where P_{S+I} is the pdf of the signal + interference. Obviously the lower the detection threshold the higher the probability of detection. However, this will increase the Pfa. The probability of false alarm is given by:

$$\text{Pfa} = \int_{V_T}^{\infty} P_I(x)\, dx \tag{6.39}$$

where $P_I(x)$ is the distribution of the interference (clutter + the receiver noise). The effect of the tail of the distribution is shown in Fig. 6.32 it can be seen that a lower threshold is required for the short-tailed pdf to have the same pfa as the long-tailed one.

6.3.4.2 Low Sea State Data Set

This data set was recorded on 05-Oct-2010. In this data set bistatic sea clutter was less spiky, this was clear in term of both ν_{BW} and σ_{SP}. In order to compare both the effect of the polarisation and the geometry three cases are presented in this section all at a monostatic range of 294 m and a bistatic angle of 90°. For ν_{BW} and σ_{SP} values refer to Table 6.6. In all cases the data was normalised by its mean intensity. Hence to get the complete picture the calibrated[3] difference in the clutter power must be taken into account. The clutter power values were reported in Table 5.3 and the transmitter gain and loss were reported in Table 3.15.

In the measurements taken at 15:09 both the transmit and receive antennas were vertically polarised. From Fig. 6.33, a SIR of 15 dB was required to achieve a Pd of 80%, while for the monostatic node the required SIR was around 17 dB. While this might not seem like a large difference, taking into account that the clutter power is lower by around 10 dB in the bistatic node the over all reduction in the target RCS for the same Pd is 12 dB. For the cross-polarised measurement the required SIR was similar to that of the vertically polarised clutter around SIR $= 15$ dB, while the required SIR for monostatic node was 18 dB, as shown in Fig. 6.34. This is related to the increase in the spikiness. However, since the

[3]By calibrated it is meant that the differences in gain and losses between the two receivers are taken into account.

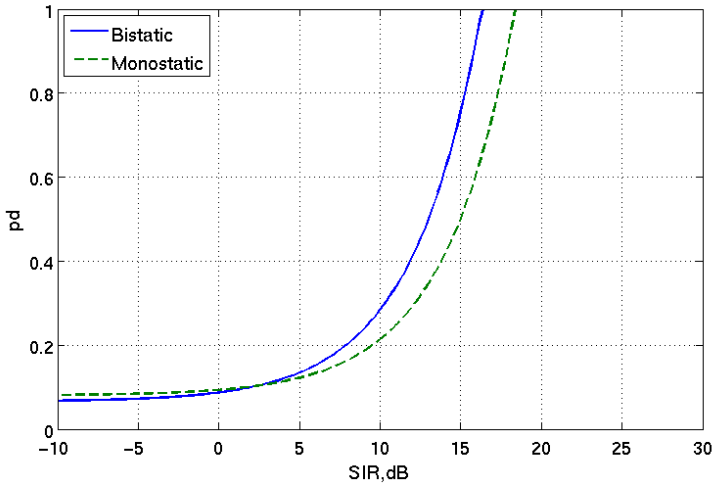

Figure 6.33: Probability of detection vs SIR for a Pfa of 10^{-4}. Both transmit and receiver antennas were vertically polarised. Data collected at 15:09 on 05-Oct-2010.

clutter power was higher for the bistatic node by 8 dB the target bistatic RCS must be higher by 5 dB to achieve the same performance as the monostatic node. From Fig. 6.35 the required SIR for a Pd of 80% increased for bistatic and monostatic sea clutter. For the horizontally polarised sea clutter it was 20 dB, while it was higher by more than 5 dB to more than 25 dB, when taking into account that the calibrated clutter power for bistatic clutter was lower by approximately 15 dB the total reduction in the target RCS was 20 dB.

6.3.4.3 High Sea State Data

This data set was recorded on 10-Oct-2010. For the high sea state data five data sets are presented at monostatic ranges of 1824 m and 2000 m which correspond to bistatic angles of 60° and 120°. For each range both linear polarisations were studied. The KA distribution parameters are listed in Table 6.12, the CNR values were reported in Table 5.6 and the node parameters were reported in Table 3.15. For the measurement taken at 15:51 the transmit and receive antennas were vertically polarised; for the bistatic node $\beta = 60°$. As can be seen from Fig. 6.36 at Pd > 0.6 the required SIR for both channels is almost identical, for a Pd of 80% the required SIR was around 17 dB. However, since the calibrated clutter power was lower by 7 dB for the bistatic channel, the reduction in the necessary target RCS was 7 dB. The data sets recorded at 12:20 and 12:33 had exactly the same configurations; all antennas were horizontally polarised with the monostatic range to the intersection point around 1827 m and $\beta = 60°$ for the bistatic node. However, as can be seen in Table 6.12 ν_{BW} and σ_{SP} values are very different between the two measurements in particular the shape parameters were almost equal for both bistatic and monostatic sea clutter whereas σ_{SP} is much higher in the bistatic case for the measurement taken at 12:20. A stark difference can be seen between the Pd vs SIR plots in both cases. For the data taken at 12:20 the required SIR for a Pd of 80% was 21 dB and 17 dB for the monostatic and bistatic nodes

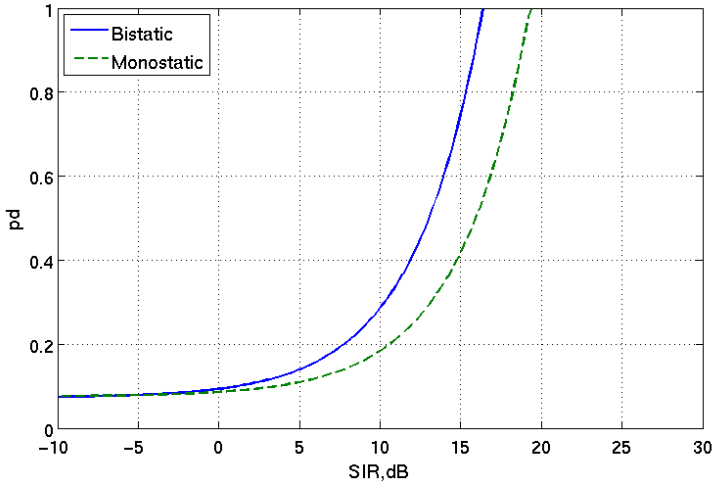

Figure 6.34: Probability of detection vs SIR for a Pfa of 10^{-4}. The transmit was horizontally polarised and the receiver antennas were vertically polarised. Data collected at 16:26 on on 05-Oct-2010.

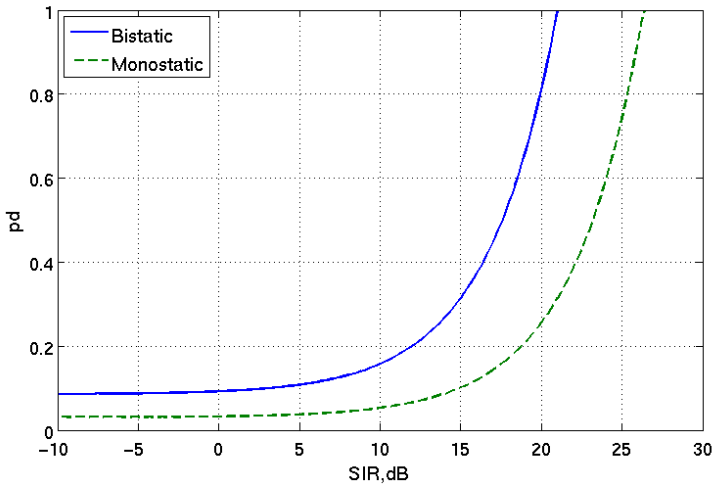

Figure 6.35: Probability of detection vs SIR for a Pfa of 10^{-4}. Both transmit and receiver antennas were horizontally polarised. Data collected at 17:16 on 05-Oct-2010.

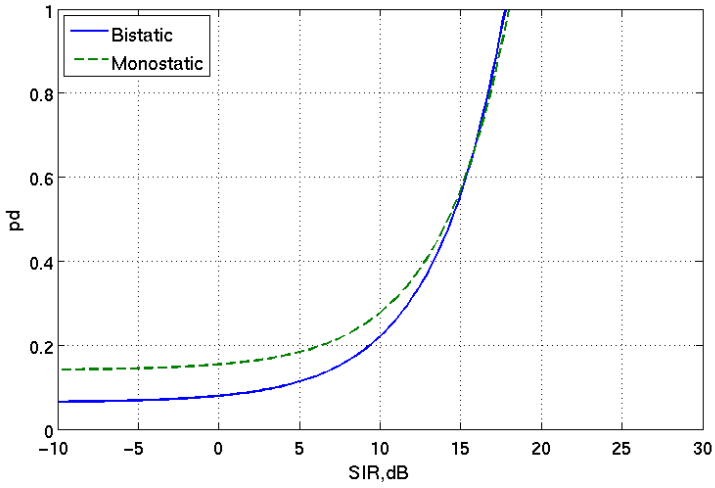

Figure 6.36: Probability of detection vs SIR for a Pfa of 10^{-4}. Both transmit and receiver antennas were vertically polarised. Data collected at 15:51 on 10-Oct-2010.

respectively as shown in Fig. 6.37; while in the data collected at 12:33 the required SIR for the same Pd was 18 dB and 20 dB for bistatic and monostatic sea clutter (Fig. 6.38). These values reflect the changes in ν_{BW} and σ_{SP}. However, the calibrated differences in clutter power were almost equal. Hence to have the same performance as the monostatic node the target RCS must be increased by 4 dB for the data recorded at 12:20, while for the data recorded at 12:33 the RCS of the target can drop by half while maintaining the same Pfa and Pd.

The data sets collected at 12:53 and 16:17 were recorded using horizontal and vertical polarisations respectively. The monostatic range was 1055 m and the bistatic angle was 120°. The required SIR for a Pd of 80% was 13 dB for horizontally polarised bistatic sea clutter and 17 dB for like polarised monostatic sea clutter as shown in Fig. 6.39, hence the reduction in the target RCS in the bistatic case is only 3 dB. For vertically polarised sea clutter required SIR for the same Pd was slightly lower for the bistatic node by 1 dB at 11 dB as can be seen in Fig. 6.40. Taking into account the difference between the node the calibrated clutter power of the two nodes are almost equal as well, hence the reduction in RCS is only 1 dB.

6.4 Summary and Conclusion

In this chapter the amplitude statistics and temporal properties of simultaneously recorded bistatic and monostatic sea clutter were studied. Two data sets were analysed with one recorded when the sea was relatively calm (sea state 2) and the other recorded during a high sea state (sea state 4 – 5).

It has been shown by analysing the temporal autocorrelation function of the recorded data that the compound model still holds for both the monostatic and the bistatic data including those recorded at shallow depths. This being said, because of the large number of spikes, either because of excessive

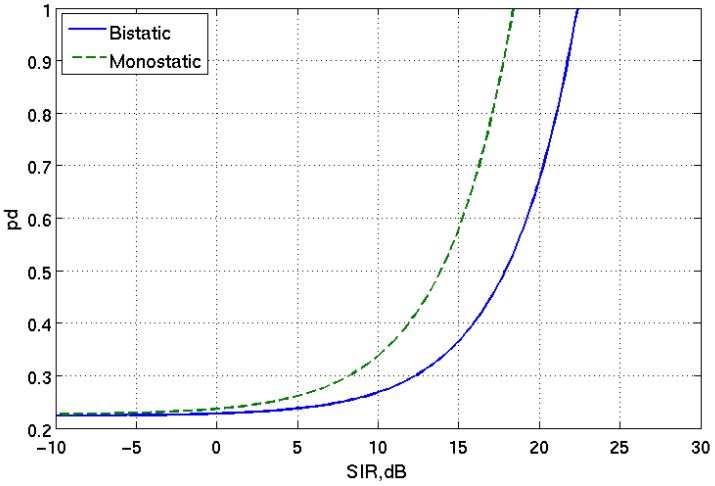

Figure 6.37: Probability of detection vs SIR for a Pfa of 10^{-4}. Both transmit and receiver antennas were horizontally polarised. Data collected at 12:20 on 10-Oct-2010.

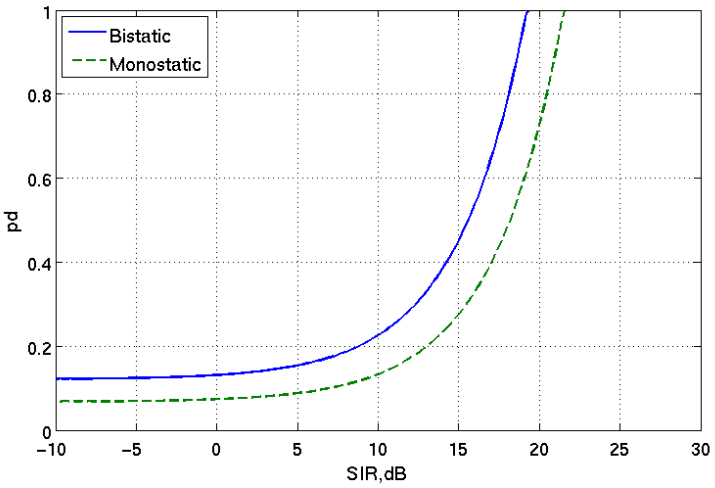

Figure 6.38: Probability of detection vs SIR for a Pfa of 10^{-4}. Both transmit and receiver antennas were horizontally polarised. Data collected at 12:33 on 10-Oct-2010.

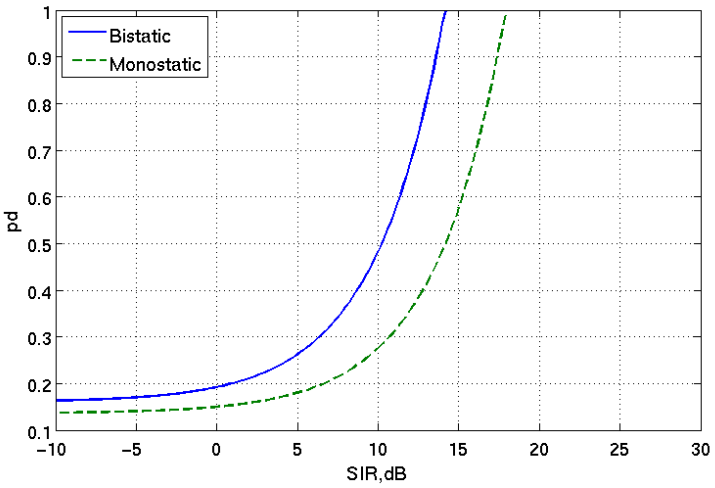

Figure 6.39: Probability of detection vs SIR for a Pfa of 10^{-4}. Both transmit and receiver antennas were horizontally polarised. Data collected at 12:53 on 10-Oct-2010.

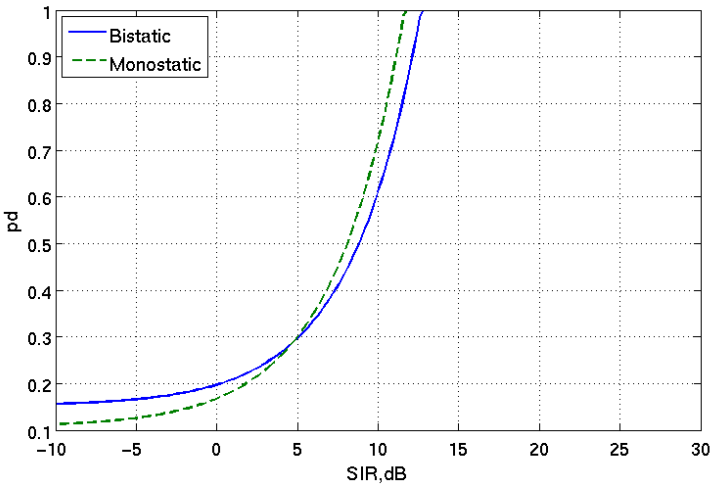

Figure 6.40: Probability of detection vs SIR for a Pfa of 10^{-4}. Both transmit and receiver antennas were vertically polarised. Data collected at 16:17 on 10-Oct-2010.

breaking waves or the weather conditions, the texture deviated from the gamma distribution when the goodness of fit was tested using the Anderson-Darling test. This is not surprising as the data was heavily effected by specular spikes. It was also shown that all the distributions except for the log-normal tended towards the exponential distribution when used to fit thermal noise data. This was a practical check for the implementation of the distributions and the interference removing algorithm.

By analysing the ACF function it was concluded that the speckle decorrelated more quickly in monostatic sea clutter compared to bistatic sea clutter; in all cases the decorrelation time was of the order of tens of milliseconds. However, the differences in the bistatic and monostatic texture and intensity ACF's were not significant and they seemed to be correlated except at times when there were large spikes. By comparing the ACF of the intensity and the texture it was found that the compound model still holds for bistatic and littoral sea clutter.

The intensity of the recorded data was fitted to five different distribution, the log-normal, Weibull, generalised Pareto, K+thermal noise and KA distribution. The parameters of the distributions were determined using the MoM. The KA proved to be the best fit in all most all cases for simultaneously recorded monostatic and bistatic sea clutter. The goodness of fit was tested by taking the mean of the square of difference of the log of the ccdf of the empirical distribution and the theoretical distribution. The log-normal was a reasonable fit when the data was spiky but when the KA failed the log-normal failed as well. The K+thermal noise and the generalised Pareto were able to fit some of the data sets. The Weibull was the worst distribution in terms of the goodness of fit.

Although the KA as used in this work has three free parameters these parameters are not arbitrary and were related to the actual data. By examining the time histories of sea clutter returns, there was clear correlation between the magnitude of the spikes and the parameters of the KA distribution. When a large number or few high amplitude specular spikes were present σ_{SP} of the KA distribution was high, in the absence of such spikes it was very low.

It was shown that in this data set, sea returns from littoral waters were more spiky as the range was decreased because of the increase probability of breaking waves. Bistatic clutter was less effected by these spikes. In the high sea state data set, bistatic clutter was less spiky than monostatic clutter with the exception of one data set, this is believed to be the first such reported measurement.

It was noted from the fits that the bistatic geometry was more effective at reducing the effects of specular spikes but not those due to the modulation and Bragg scattering. The results from the statistical analysis and the average reflectivity from the previous chapter were combined to assess the performance of the bistatic node against the monostatic node. The change in the spikiness was limited in vertical polarisation but more pronounced at horizontal polarisation. It was concluded that the greatest gain was when the radar was horizontally polarised with a bistatic angle around $90°$.

It has been proposed that sea spikes due to non-Bragg scattering are due to multiple bounce spec-

ular reflections [35, 40]. Ward *et al.* [28] proposed that the cause burst scattering was due to specular reflections from the crust of the waves as they break. The radar returns from corner reflector type targets have a smaller amplitude in bistatic geometries. Thus the returns from such spikes will have a smaller amplitude in the bistatic channel. Similar effects have been noticed in SAR where the signal to clutter ratio was higher in bistatic SAR images as compared to monostatic SAR images of the same scene [144]. Similar results were found in [2]. In addition, the clutter was fitted to the K distribution and it was found that the shape parameter was smaller for monostatic clutter.

Chapter 7

Conclusion

In this chapter a summary of this work is presented, together with a discussion of the main contributions to the field of bistatic radar and sea clutter. Possible further developments to NetRAD and other analysis techniques of the clutter and target data are also discussed.

7.1 Summary of Findings

Chapter 2 provided the necessary theoretical background to understand the work presented in this thesis. It started with a concise review of bistatic radar and the bistatic geometry. This was followed by a discussion of the nature of monostatic sea clutter. The last section reviewed bistatic sea clutter. It was shown that there is limited theoretical and experimental information available on bistatic sea clutter and particularly in the out-of-plane geometry.

The development of a novel bistatic/multistatic radar system was documented in chapter 3. This chapter started with a review of the original system design. It was mainly limited by its low output power and the need for cables to distribute the reference clock and start trigger the radar, and data communications. These two issues were treated separately. The output power was increased from $0.2\,\mathrm{W}$ to more than $500\,\mathrm{W}$. Different methods to reduce the effect of the interference between the transmitter and the receivers, particularly the monostatic receiver, were discussed. After a thorough examination the preferred method in terms of cost and performance was the use of two separate antennas for transmission and reception, and an SPST switch in the monostatic receiver chain. Other modifications were carried out to improve the linearity of system. To eliminate the need for cables each node in NetRAD was interfaced with a GPSDO designed by UCT. The GPSDO was used to provide a common frequency reference and simultaneously trigger the different nodes. Wireless microwave links operating at $5\,\mathrm{GHz}$ were used for data communications. Several changes and improvements were made to the software and firmware to accommodate the hardware modifications and improve the system performance. In particular the software interface was changed such that it was possible to control the radar nodes from any PC running the server application with access to the NetRAD network. The new system was calibrated both in the

UK and upon arrival in SA. The repeated tests gave the same results within ± 0.3 dB. The effect of the GPS tracking on the radar performance was also analysed. Simple yet effective methods were devised to eliminate these effects which were discussed in chapter 4. In addition, new antennas were purchased and characterised in UCL near field chamber. New antenna mounts were designed and fabricated. Optical telescope were mounted on the antennas. The optical and EM boresights were calibrated which made it possible to align the antennas using the optical telescopes.

A summary of the field trials carried out in the UK and SA was given in chapter 4. An overview of the technical and logistical challenges in conducting the trials was also provided. Only preliminary trials were conducted at UCL test site on England's south cost, the main trials were conducted in the Eastern Cape in South Africa. An overview of the data collected was also provided. In this chapter the pre-processing applied to the data was discussed. In particular, it was shown that it was possible to eliminate in-band interference by removing less than $0.5\,\%$. Furthermore, the techniques used to deal with the effects of the GPSDO were illustrated. The effect of the drift of the different oscillators and the GPSDO control loop was removed by using the phase of a signal from a fixed target such as that of the sidelobe breakthrough. The time of arrival of sidelobe breakthrough signal was also used to remove the small ambiguity in the trigger mechanism. It was also demonstrated that the effect of extended land clutter was negligible, provided that the mainlobe of the antenna was directed towards the sea. The gathered data was unique in many ways:

1. The bistatic and monostatic data were simultaneously recorded using a coherent radar.
2. The data covered a range of bistatic angles not previously reported in the open literature. Bistatic angles between 30° and 120° were analysed in this thesis.
3. Cross-polarised sea clutter data was analysed in this thesis.
4. This data contained data recorded at shallow depths which is not available in the open literature even for monostatic geometries.
5. The target data contains various examples ranging form large ships to inflatables undertaking various manoeuvres such as spirals and circles.

As a results of conducting and planning these trials many valuable lessons were learnt. The key issues identified are described below:

1. The importance of preparing a detailed and clear trial plan cannot be underestimated. As a minimum the plan should highlight:
   - the duties of the team members,
   - the objectives of the trials,

- a clear step by step schedule

2. Although a trial plan should have a definite objective, it must be flexible enough to adapt to changing circumstances.

3. One day trials were not as successful as those that were composed of several days.

4. Although the trial relied heavily on the help of volunteers from the group, drawing up a trial team was of paramount importance in speeding up the trial setup and execution.

5. Pre-trial training for the core trial team could save valuable trial time.

6. Pre-trial on site meetings are necessary to make sure that all team members are clear on the tasks to be carried out on the day.

7. Post-trial meetings can be used to discuss the day's trial and modify the next day's trial plan if necessary.

8. A detailed trial log is a valuable tool for documenting the trial.

Chapter 5 was devoted to discussing the average normalised radar cross section of monostatic and bistatic sea clutter data. Prior to analysing the gathered data, it was proven that the effect of the finite width of the antenna beams had a negligible effect on the bistatic angle across the clutter patch. This was followed by a description of the numerical method used to estimate σ° and the clutter area.

Two novel data sets were analysed; the first was collected on 05-Oct-2010. The sea was relatively calm and the sea state was approximately 2. Because of the geometry and power limitations most of this data was collected at shallow waters. In all cases the grazing angle was small, thus the bistatic angle was approximately equal to the scattering angle. This is the first time that littoral sea clutter (monostatic or bistatic) has been analysed in such detail in the open literature. The second data set was collected on 10-Oct-2010. The sea was rough with some frontal activities, the sea state was estimated to be 4 – 5. The analysis in this section showed for the first time that for co-polarised sea clutter $\sigma^\circ_B/\sigma^\circ_M$ dropped with increasing bistatic angle until around $\beta \approx 90^\circ$. However, because of the increase in the clutter area as the bistatic angle is increase, the drop in the clutter power is reduced particularly at $\beta > 90^\circ$. It was also shown for the first time that $\sigma^\circ_{HVB} > \sigma^\circ_{HVM}$ at $\beta = 90^\circ$.

The last section of the chapter was devoted to the development of a new bistatic clutter model. The model is applicable to both in-plane and out-of-plane bistatic clutter. It was successfully applied to in-plane sea Domville's data [110]. It was also able to fit the UCL and Ewell and Zehner's [112, 113] out-of-plane data. To model the UCL data only the monostatic normalised co- and cross-polarised radar cross section were needed to predict the bistatic normalised radar cross section. More data is needed to develop models to relate the parameters to the radar parameters and environmental conditions.

In chapter 6 the first reporting of temporal and statistical analysis of bistatic sea clutter was described. It was shown that the compound model still holds for bistatic sea clutter. By analysing the ACF function it was also shown that the speckle decorrelated more quickly in monostatic sea clutter compared to bistatic sea clutter; in all cases the decorrelation time was in the order of tens of milliseconds. However, the differences in the bistatic and monostatic texture and intensity ACF's were not as significant and they seemed to be correlated with the exception of the some of the larger spikes. By comparing the ACF of the intensity and the texture it was found that the compound model still holds for bistatic and littoral sea clutter.

It was shown that in this data set, sea returns from littoral waters were more spiky as the range was decrease. This is believed to be because of the increase probability of breaking waves. It was also demonstrated that the KA distribution provided the best fit to the amplitude statistics of both monostatic and bistatic clutter, compared to the K+thermal noise, generalised Pareto, Weibull and log-normal distributions. The KA distribution was particularly attractive because it treated the spikiness due to the smooth modulation and specular spikes separately. It was shown that the distribution shape parameter was influenced by the look angle with respect to the swell; however, burst spikes were strongly influenced by the bistatic geometry particularly at horizontal polarisation and might provided the niche application for bistatic radar. The amplitude of burst spikes was significantly reduced at with respect to bistatic geometry.

In the last section it was shown that the reduction in clutter power combined with the reduced spikiness provided a potential improvement in target detection particularly at horizontal polarisation.

In summery, this work has reported the analysis and collection of novel simultaneous monostatic and bistatic sea clutter and the target data. The average reflectivity and statistical properties of simultaneous recorded monostatic and out-of-plane bistatic sea clutter data has been analysed. This was achieved by the development of a unique multistatic radar system. This work has resulted in significant advances in both netted radar technology and understanding of bistatic sea clutter.

7.2 Future Work

The proposals in this section are based on the experience gained in the work carried out to prepare this thesis. This section has formed a strong base to push bistatic radar technology and applications further. There are many possible routes to further research in this area. Some possibilities are described below.

7.2.1 System Development

Some of the possible further developments to NetRAD are listed below:

1. Change of radar frequency. Since the system operates at $2.4\,\mathrm{GHz}$ there is a risk of interference particularly in urban areas where there is a wide spread of WiFi access points. A move to another

frequency band could be beneficial. An X-band high power amplifier has been purchased and is currently being tested by the manufacturer[1]. There are also plans to purchase an L-band high power amplifier. In addition to changing the high power amplifier it will be necessary to change the LNA amplifiers, the phase looked loop and the mixer. The IF amplifier and digital acquisition system need not change. In addition, this will allow the study of the clutter and target returns at different frequencies.

2. Change of the acquisition system to a more open system based on software defined radio to enable finer control of the acquisition process and the possibility of some real-time processing, such as displaying the range Doppler map and the RTIs in realtime. UCL is working with UCT on the possibility of using their Rhino [145] platform as the digital back-end for NetRAD.

3. Investigation of using a heterodyne of a low-IF architecture. Using zero-IF in transmission meant that the LO leakage and the lower sideband cannot be removed from the transmitted signal. Furthermore, the DDS transfer function attenuated the amplitude of the higher frequency components. In the receiver chain the use of a single channel to digitise the baseband signal meant the the image could not be remove hence doubling the noise power. These effects can be removed by using a non-zero IF but this would require additional hardware component.

4. Operation in GPS denied environments. Besides the synchronisation and triggering problems caused by the GPSDOs, they require a clear view of the sky. It is worth looking into other methods for synchronising the nodes, such CERN's white rabbit [146], the use of dedicate microwave links to send synchronisation signals, or using highly stable free running oscillators and developing triggering methods that does not depend on the nodes being synchronised in time.

5. Use of a different software platform. The control software was written in C# .NET which meant that the software can only be used on Microsoft Windows based computers. Basing the software interface design on a portable high level language such as Python would make it more portable and easier to maintain and modify. Furthermore, Python can be easily interfaced with C and has mathematical abilities similar to those of Matlab when using NumPy[2] which makes it possible to integrate quick look codes and analysis into the user interface.

6. Automation of antenna alignment. The antennas were steered manually which can introduce human error in reading the vernier. Furthermore, it was found that directing the antennas during strong winds can be difficult. For target measurements the target had to be tracked manually, this was only possible for bistatic nodes due to safety concerns. Replacing the mounts with mo-

[1] Personal communications with Neil Richardson of Microwave Amplifiers limited on 13-Sep-2010.
[2] http://www.numpy.org/, accessed 14-Sep-2010.

torised mounts would speed up the process. If it is possible to integrate the motor control with the NetRAD control software this will greatly improve the accuracy of the experiments.

7.2.2 Data Analysis and Modelling

Some initial work has started on the comparison of the distribution of monostatic bistatic power spectrum density, it was also found that when fitted to the K distribution bistatic clutter was less spiky in the Doppler domain as well [147]. In this publication the UK data was used, this work can be applied to the SA data which contains more geometries and different sea conditions. Furthermore, properties of the Doppler spectrum such as bandwidth and centroid and relate these properties to the physical conditions and Doppler clutter models.

Some of the target data has also been analysed, though this has not formed part of this study. The analysis of the micro-Doppler signature of the selected target, inflatables and sail boats, showed some clear differences between the monostatic and bistatic data. Some were related to the macro-motion and hence to $\cos(\beta/2)$ others were related to the micro-motion and still require more detailed analysis. Much further bistatic and monostatic data collection and analysis can be carried out on low visibility maritime targets.

7.2.3 Radar Trials

More data is still needed to be able to verify and develop models. In particular it is necessary to take repeated measurements of the same clutter patch under the same conditions to be able to assess the statistical significance of what seems like sudden changes in the spikiness and σ°. Furthermore, recording the full scattering matrix would make it easier to further validate the new model for bistatic sea clutter.

Weather stations are usually located at fixed location which is usually a long distance from the measurement point. Being able to recorded the surface data close to the clutter patch will make it much easier to correlate the changes in the reflectivity with the effect of the look angle with respect to wind and sea, wave height and wave depth.

Absolute calibration of the radar nodes will improve the accuracy of the recorded data. One possible solution could be the use of tethered balloons which are covered in a conductive coating. The balloons need to be raised high enough to make the effect of multipath negligible.

It was concluded that using horizontally polarised antennas at a bistatic angle of around 90° offered better detection probability. One possible application could be in port entrance monitoring, since the antennas are fixed the problems associated with pulse chasing and antenna alignment are eliminated. In addition, might well be physically possible to use optical fibre to transmit the common clock. Since the area of interest is relatively small the limited coverage area is advantage of the bistatic geometry rather than a disadvantage. The main aim of such an exercise would be to assess how much gain in detection is achieved against realistic targets whose RCS is likely to drop with increasing bistatic angle [148], and

determine if there is an optimum bistatic angle at which the drop in the RCS of the desired type of targets is smaller than the drop in the clutter power.

Appendix A

The Sea Surface

To model the scattering of electromagnetic waves and to comprehend and quantify the radar echoes from the sea surface, it is necessary to understand the dynamics governing its behaviour. In most cases waves are generated by the wind, both local and non-local, the relationship between the wind and the sea surface is very complex and nonlinear. To aid in understanding of the sea surface some important oceanographic terms will be described below.

A.1 Definitions

The definitions below are based on [29].

Sea state A measure of the roughness of the sea. There are many definitions for the sea state, in radar usually Douglas hydrographic scale is used. It relates the sea roughness to the wind speed and the significant wave height, Table A.1 and [27, 42].

Average wave height The average wave height from crest to trough of the waves. It is denoted by h_{av}.

Root mean square wave height The standard deviation of the wave height. It is used to estimate the roughness of the sea surface. Assuming the wave heights are Rayleigh distributed, it is related to h_{av} by:

$$h_{av} = \sqrt{2\pi}\sigma_h \tag{A.1}$$

Significant wave height The average of the heights of the one-thirds highest waves, more recently it is computed from the standard deviation of the wave height, [149], it is related to h_{av} and σ_h by:

$$H_{1/3} = 1.6h_{av} \tag{A.2}$$

$$H_{1/3} = 4\sigma_h \tag{A.3}$$

Period The time it takes two consecutive crests or troughs to cross a fixed point. It is denoted by T.

Water frequency The water frequency in rad s^{-1} is given by:

$$\omega_w = \frac{2\pi}{T} \tag{A.4}$$

Water wavelength The distance between two consecutive crests from the same wave, it is denoted by λ_w.

Water Wavenumber This is related to the wavelength by

$$k_w = \frac{2\pi}{\lambda_w} \tag{A.5}$$

Fetch and duration They are defined as the horizontal distance (fetch) along which a nearly constant wind has been blowing for a length of time (duration).

Fully developed sea A sea surface which has reached a state of equilibrium after a constant wind has been blowing for a certain fetch and duration. The required fetch and duration can be very long. For example, for a constant wind of $7\,\mathrm{m/s}$ will need to blow for a duration of $20\,\mathrm{h}$ and a fetch of $120\,\mathrm{nmi}$ or $222\,\mathrm{km}$ [42].

Wind waves Waves which are or just have been aroused by local winds.

Swell Waves which were excited by wind but have moved out from the area where they originated.

Gravity waves Waves which the damping mechanism is gravity.

Capillary waves Waves which the restoring force is due to surface tension.

Phase velocity The velocity at which the phase of the waves travel and is given by:

$$v_p = \frac{\omega_w}{k_w} \tag{A.6}$$

Sea state	Description	$H_{1/3}$ m (ft)	V_w m s^{-1} (kn)
1	Calm (Rippled)	0-0.3 (0-1)	0-3.09 (0-6)
2	Smooth	0.3-0.91 (1-3)	3.09-6.17 (6-12)
3	Slight	0.91-1.52 (3.-5)	6.17-7.72 (12-15)
4	Moderate	1.52-2.44 (5-8)	7.72-10.29 (15-20)
5	Rough	2.44-3.66 (8-12)	10.29-12.86 (20-25)
6	Very Rough	3.66-6.1 (12-20)	12.86-15.43 (25-30)
7	High	6.1-12.19 (20-40)	15.43-25.72 (30-50)
8	Very High	>12.19 (>40)	>25.72 (50)

Table A.1: Douglas sea scale

A.2 Sea Spectrum and Wave Height

For gravity waves the dispersion formula relates the wave number to the water frequency ω_w and the water depth

$$\omega_w^2 = g k_w \tanh(k_w d) \tag{A.7}$$

where $g \approx 9.8\,\mathrm{m\,s^{-2}}$ is free fall acceleration for deep waters the equation reduces to

$$\omega_w = \sqrt{g k_w} \tag{A.8}$$

and the phase velocity is given by

$$v_{pg} = \frac{g}{\omega_w} = \sqrt{\frac{g}{k_w}} \tag{A.9}$$

Usually the significant wave height $H_{1/3}$ is used when dealing with gravity waves, thus all the velocities, wavenumber and frequency are those corresponding to $H_{1/3}$.

The ocean can be viewed as being composed of a large number of waves of different frequencies. Each wave can have a different direction, for simplicity, a two dimensional surface is assumed parallel to the x-z plane. This is known as the omnidirectional spectrum. However, this simplification fails in the bistatic radar and a two dimensional spectrum, three dimensional sea, is used. As an example of an omnidirectional wave spectrum the Pierson-Moskowitz (P-M) spectrum will be described briefly below.

The Pierson-Moskowitz spectrum has the general form of [43]

$$S(q) = \frac{b k^{-3}}{2} \exp\left[-0.6\left(\frac{g}{q U_{10}^2}\right)^2\right] \tag{A.10}$$

where $b = 8.1 \times 10^{-3}$, U_{10} is the wind speed $10\,\mathrm{m}$ above the sea surface, sometimes the wind speed $19.5\,\mathrm{m}$ above the sea level is used and it is related to U_{10} by [149]

$$U_{19.5} \approx 1.026 U_{10} \tag{A.11}$$

The square of the rms wave height is equal to the integral of the power spectrum over all possible frequencies

$$\sigma_h^2 = \int_0^\infty S(\omega_w) d\omega_w = 0.146667 \frac{b U^4}{g^2} \approx 35.07 \times 10^{-6} (U_{10})^4 \tag{A.12}$$

and the significant wave height is given by

$$H_{1/3} \approx 23.688 \times 10^{-3} (U_{10})^2 \tag{A.13}$$

To include capillary waves the effect of the capillary waves must be included [43]

$$\omega^2 = gk_B \left[1 + \left(\frac{k_B}{k_m}\right)\right] \tag{A.14}$$

where k_B is the wavenumber responsible for Bragg scattering give by

$$k_B = 2k_r \cos(\psi) \tag{A.15}$$

ψ is the grazing angle and $k_r = \frac{2\pi}{\lambda}$ is the radar wavenumber. k_m is the wavenumber of the slowest wave. It is given by

$$k_m = \sqrt{\frac{\rho_w g}{\gamma_T}} \approx 3.63 \text{ rad/cm} \tag{A.16}$$

where ρ_w is the density of water and γ_T is the surface tension and substituting Eq. (A.14) and (A.16) in Eq. (A.6) gives:

$$v_{pB} = \sqrt{\left(\frac{g}{k_B} + \frac{k_B \gamma_T}{\rho_w}\right)} \tag{A.17}$$

The capillary waves are modulated by the gravity waves, the total observed Doppler shift due to the Bragg scattering must also include the effect of orbital v_o and Stoke drift velocity v_d given by: [93]

$$v_o = \frac{\omega_w H_{1/3}}{2} \tag{A.18}$$

$$v_d = \frac{\omega_w k H_{1/3}^2 \cosh(2k(z+d))}{8\sinh^2(kd)} - \frac{\omega_w H_{1/3}^2 \coth(kd)}{8d} \tag{A.19}$$

where d is the water depth and z is the drift current depth, the second term is due to the conservation of mass in the closed water system. For deep open seas and at the surface, the equation reduces to:

$$v_d = \frac{\omega_w^3 H_{1/3}^2}{4g} \tag{A.20}$$

P-M spectrum assumes a fully developed sea and an infinite fetch, and does not readily include the effects of capillary waves. Fung-Lee spectrum [150] includes the effects of the capillary wave. Fung-Lee model divides the spectrum into two regions gravity and capillary waves, the gravity spectrum is modification of the P-M spectrum. The omnidirectional Fung-Lee is given by:

$$S(k)_1 = \frac{1.4 \times 10^{-3}}{k^3} \exp\left(-\frac{0.74 g^2}{k^2 U_{1.95}^4}\right) \quad k < 4\,\text{rad/m} \tag{A.21}$$

$$S(k)_2 = a_0 \left(1 + 3\bar{k}^2\right) \left[k\left(1 + \bar{k}^2\right)\right]^{(P+1)/2} \quad k \geq 4\,\text{rad/m} \tag{A.22}$$

where a_0, $\bar{k}$, and p are empirical constants that depend on the wind speed and g. It should be noted that

$S_1(4) = S_2(4)$.

All the above mentioned spectra were presented in their 1-D form. The directional or 2-D form can be obtained either by representing k as a victor $\mathbf{k} = \mathbf{k_x} + \mathbf{k_y}$, or use the wavenumber as a scalar and multiply the omnidirectional spectrum by a spectral spreading. Thus the directional spectrum can written as

$$S(\mathbf{k}, \phi_w) = S_{1D}(k) S_{dir}(\mathbf{k}, \phi_w) \tag{A.23}$$

where, ϕ_w is the wind direction. A directional form of P-M spectrum is presented in [43]

$$S(\mathbf{k}, \phi_w) = \frac{b}{4\pi} k^{-4} \exp\left[-0.6\left(\frac{g}{qU_{10}}\right)^2\right] \cos^{2n}\left(\frac{\phi_w - \angle\mathbf{k}}{2}\right) \frac{(2n)!!}{(2n-1)!!} \tag{A.24}$$

where n is the angular spreading factor. By integrating over 2π (A.24) reduces to (A.10). Better results can be achieved if the spreading spectrum is a function of both the wavenumber's amplitude direction and the wind direction [150]. The directional Fung-Lee spectrum is given by

$$S(\mathbf{k}, \phi_w) = S(k)\left[a_0 + a_1(1 - \exp(-bk^2)\cos(2\phi_w)\right] \tag{A.25}$$

where, a_0 and b are constants, and a_1 is a function of wind speed.

The above spectra assumes and infinite fetch, thus they do not include the effect of the wave age Elfouhaily spectrum [43, 151] and JONSWAP [149]. However, JONSWAP does not include the effects of capillary waves, thus not suitable for modelling radar returns at microwave frequencies or above. Elfouhaily spectrum equations are more involved and for the sake of brevity the interested reader is advised to consult the above mentioned references.

The sea surface is generally as a Gaussian surface with a power spectrum given by $S(\mathbf{k}, \phi_w)$; however, such models are not suitable to model the non-linear events such as breaking waves. The breaking wave can occur when any of the following conditions occur:

1. wave steepness $H/L > 0.42$.
2. fluid velocity to phase velocity ratio exceeds 0.47.
3. vertical acceleration > $g/2$.
4. surface slope > 0.58

Generally these thresholds are related and the vertical acceleration criterion is usually used because it is the easiest to model [43]. Using this criterion the area of the sea surface which have vertical acceleration that exceeds $g/2$, this model is called the breaking area model (BAM). causerie the steepness of the waves increases in shallow waters, the probability of breaking waves increases as the waves get closer to

the shore.

Simulation has shown that as the wave steepness the RCS increase in both polarisations, at the point of breaking increases dramatically and overtakes. This increase is attributed to specular reflection near the top of the wave due to the complex multipath. This produces burst spikes. As the water breaks it tumbles down and whitecaps are created. The returns from whitecaps are noise-like and could last for up to a second.

Appendix B

The GIT Model

The treatment in this appendix is based on [59, 138] For frequencies 1 GHz to 10 GHz σ°_{M} is given by:

$$\sigma^{\circ}_{MHH} = 10\log\left(3.9\times10^{-16}\lambda\psi^{0.4}A_iA_uA_w\right) \tag{B.1}$$

for 1 to 3 GHz frequencies σ°_{MVV} is given by:

$$\sigma^{\circ}_{MVV} = \sigma^{\circ}_{MHH} - 1.73\ln(h_{av}+0.015) + 3.76\ln(\lambda) \tag{B.2}$$

and for frequencies from 3 GHz to 10 GHz

$$\sigma^{\circ}_{MVV} = \sigma^{\circ}_{MHH} - 1.05\ln(h_{av}+0.015) + 1.09\ln(\lambda) + 1.27\ln(\psi+0.0001) + 9.7 \tag{B.3}$$

where:

σ°_{MHH} is the horizontally polarised MNRCS in dB,

σ°_{MVV} is the vertically polarised MNRCS in dB,

λ is the radar wavelength in m,

ψ is the grazing angle in radians,

h_{av} is the average wave height in m,

A_i is the interference factor which accounts for multipath effects,

A_u is the upwind-downwind factor,

A_w is the wind speed factor.

A_i is a function of the grazing angle, wave height and the radar wavelength is given by

$$A_i = \frac{\sigma^4_\phi}{1+\sigma^4_\phi} \tag{B.4}$$

$$\sigma^4_\phi = (14.4\lambda + 5.5)\psi h_{av}/\lambda \tag{B.5}$$

A_u is a function of the antenna look angle ϕ_w, the radar wavelength and the grazing angle and is given by

$$A_u = \exp\{0.2\cos(\phi_w)(1 - 2.8\psi)K_\lambda\} \tag{B.6}$$

where

$$K_\lambda = (\lambda + 0.015)^{-0.4} \tag{B.7}$$

It is worth noting that in the model does not include the effects of the swell direction.

A_w depends on the wind speed V_w and the wavelength and is given by

$$A_w = \left(\frac{1.94V_w}{1 + V_w/15.4}\right)^{1.1K_\lambda} \tag{B.8}$$

Appendix C

Variation of Bistatic Angle within the Clutter Cell

In this appendix the mathematical development of a model to find the upper limit of the change of the bistatic angle across the clutter area is described. The effect of range resolution was ignored. In addition, the grazing angle was assumed to be small such that the transmitter, receiver and the isorange surface were coplanar. Without any loss of generality the plane $z = 0$ was used. The weighting of the antenna pattern within the clutter area was ignored. The geometry is defined in Fig. C.1, and the equations below. Positive angles are measured in a counter clockwise direction.

$$Tx = (x_T, y_T) \tag{C.1}$$

$$Rx = (x_R, y_R) \tag{C.2}$$

$$L = \|Tx - Rx\| \tag{C.3}$$

$$Tgt = (x_{Tgt}, y_{Tgt}) \tag{C.4}$$

where Tx, Rx and Tgt are the coordinates of the transmit antenna, receive antenna and the mainlobe intersection point, and L is the baseline. The vector from the transmitter to the target can be written as

$$\mathbf{v_{TxTg}} = r_{TxTg} \left(\cos\left(\phi_T\right) \mathbf{a_x} + \sin\left(\phi_T\right) \mathbf{a_y} \right) \tag{C.5}$$

where ϕ_T and θ_T are the angles the vector makes with the x-axis and y-axis respectively.

Similarly for the receiver:

$$\mathbf{v_{RxTg}} = r_{RxTg} \left(\cos\left(\phi_R\right) \mathbf{a_x} + \sin\left(\phi_R\right) \mathbf{a_y} \right) \tag{C.6}$$

where ϕ_R and θ_R are the angles the vector makes with the x-axis and y-axis respectively.

Let α_T and α_R be half the one way 3 dB beamwidth of transmitting and receiving antennas respectively. The vector from the transmitter/receiver to the 3 dB intersection point is given by:

$$\mathbf{v_{TxTgi}} = r_{TxTgi}\left(\cos\left(\phi_T \pm \alpha_T\right)\mathbf{a_x} + \sin\left(\phi_T \pm \alpha_T\right)\mathbf{a_y}\right) \tag{C.7}$$

$$\mathbf{v_{RxTgti}} = r_{RxTgi}\left(\cos\left(\phi_R \pm \alpha_R\right)\mathbf{a_x} + \sin\left(\phi_R \pm \alpha_R\right)\mathbf{a_y}\right) \tag{C.8}$$

where $i = 1, 2$, and

$$r_{TxTgi} + r_{RxTgi} = r_{TxTg} + r_{RxTg} \tag{C.9}$$

The isorange is an ellipse with semi-major a and semi-minor b given by

$$1 = \frac{x^2}{a^2} + \frac{y^2}{b^2} \tag{C.10}$$

$$a = \frac{r_{RxTg} + r_{TxTg}}{2} \tag{C.11}$$

$$b = \sqrt{a^2 - \frac{L^2}{4}} \tag{C.12}$$

By finding the intersection points of the direction vectors and the isorange ellipse four points can be found. Each intersection point represents the vertex of a different bistatic triangle and could have a different bistatic angle β_i. The deviation from the bistatic angle at the centre $\beta_\circ$ of the patch is given by:

$$\Delta\beta_i = |\beta_\circ - \beta_i| \quad \text{where} \quad i = 1, 2, 3, 4 \tag{C.13}$$

where β_1 to β_4 are the intersection points of between the antennas 3 dB points and the isorange. The maximum deviation is given by $\Delta\beta$:

$$\Delta\beta = \max\left|\Delta\beta_1, \Delta\beta_2, \Delta\beta_3, \Delta\beta_4\right| \tag{C.14}$$

The point corresponding to the bistatic angle with the maximum deviation will have power drop more than 6 dB. an example result is shown in Fig. 5.1.

$$\Delta\beta = \max\left(|\beta_\circ - \beta_i|\right) \tag{C.15}$$

To illustrate the effect of the finite cross range on the variation of the bistatic angle the results of two simulations are presented. In the first case the transmitter and receiver were assumed to be located at $(-200\,\mathrm{m}, 0\,\mathrm{m})$ and $(200\,\mathrm{m}, 0\,\mathrm{m})$ respectively. Both transmit and receive antennas had a 3 dB beamwidth of 1°. The Target was assumed to be at $(50\,\mathrm{m}, y)$ the bistatic angle was varied by sliding the target across the y-axis from $y = 10\,\mathrm{m}$ to $y = 1000\,\mathrm{m}$ in steps of $50\,\mathrm{m}$. The results is shown in Fig. C.2, it

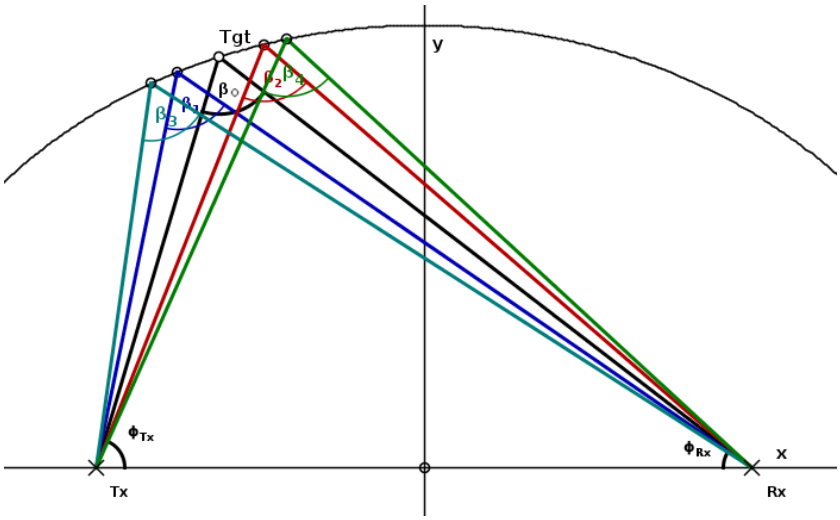

Figure C.1: A sketch showing the variation of the bistatic angle across in a clutter cell, the dimensions are exaggerated for clarity.

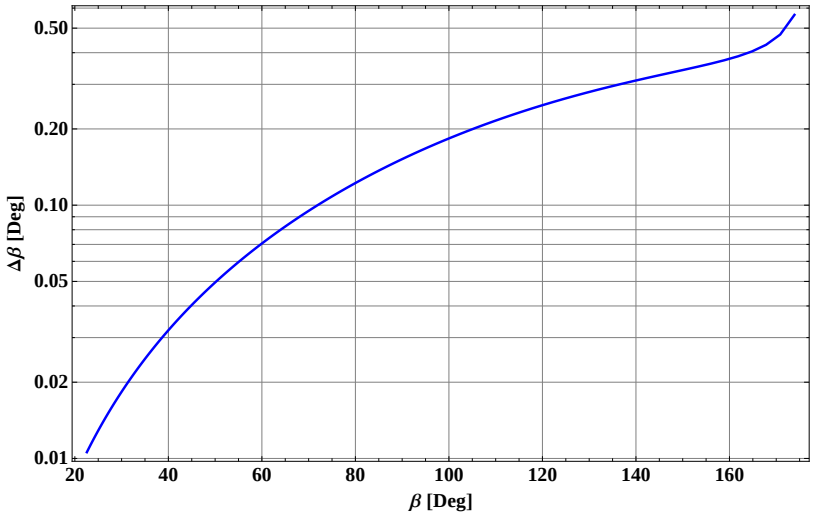

Figure C.2: Maximum variation in the bistatic angle, the antenna beamwidth was assumed to be $1°$.

is clear from the plot that the error is negligible even at large bistatic angles. It should be noted that in forward scattering the approximations used might not be valid. In the second case the beamwidth was assumed to be $10°$, the error remained very small until the $\beta > 150°$, where it increased sharply. This is because as the bistatic angle is increase, the intersection point approaches the baseline and one of the intersection points is on the other side of the ellipse which increases the error. The bistatic angles at the four intersection points are plotted in Fig. C.4. From the plot it is clear that two angles are much smaller than the bistatic angle when $\beta_\circ > 144°$. To understand this a sketch of the geometry was made with $\beta = 144°$, Fig. C.5.The points on the right hand side correspond to bistatic angles around $137°$ and $142°$ which mean that the offset is $\Delta\beta \approx 7°$.

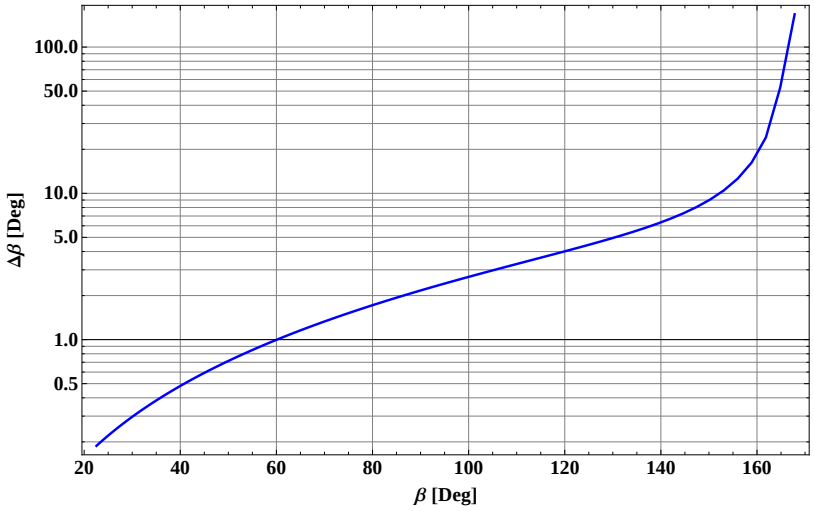

Figure C.3: Maximum variation in the bistatic angle, the antenna beamwidth was assumed to be $10°$.

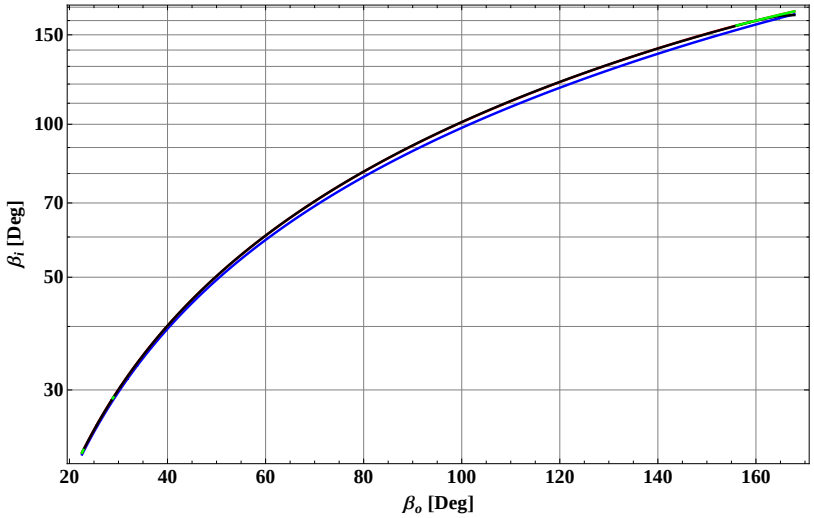

Figure C.4: The bistatic angles at the four intersection points, the antenna beamwidth was assumed to be $10°$.

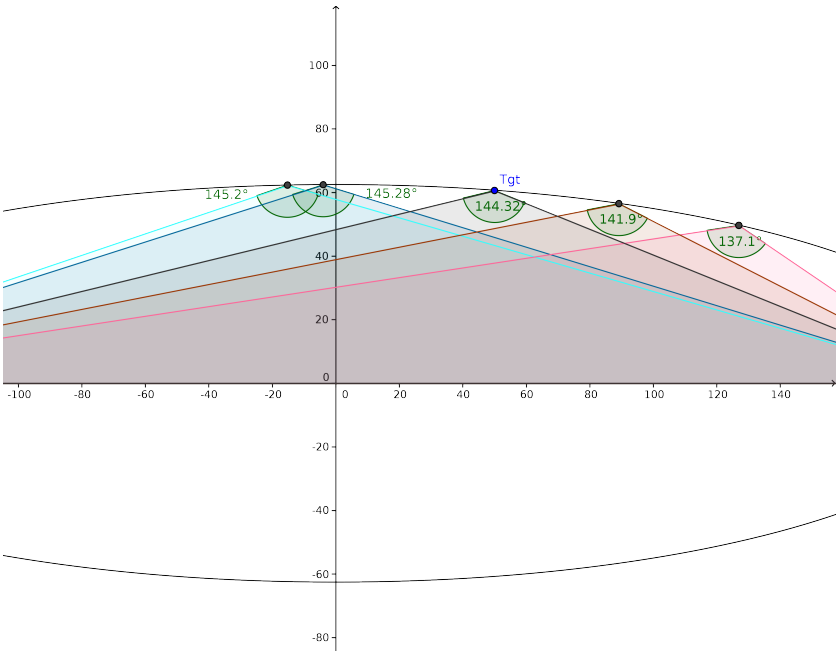

Figure C.5: A sketch showing the variation of the bistatic angle at $\beta \approx 144°$.

Bibliography

[1] N. Willis, *Bistatic Radar*. Scitech, 2005.

[2] G. Yates, "Bistatic synthetic aperture radar," Ph.D. dissertation, University College London, January 2005.

[3] K. Ward and P. Shepherd, "Bistatic radar sea clutter experiments and spatial coherence," in *Proc. Radar Int. Conf.*, Brighton, UK, October 1992, pp. 22 – 25.

[4] N. Willis, *Bistatic Radar*. Scitech, 2005.

[5] ——, "Bistatic radar," in *Radar Handbook*, 3rd ed., M. Skolnik, Ed. Mc-Graw Hill, 2008, ch. 23, pp. 23.1–23.36.

[6] M. Cherniakov, *Geometry of Bistatic Radars*, M. Cherniakov, Ed. John Wiley & Sons, 2007.

[7] M. Jackson, "The geometry of bistatic radar systems," *IEE Proc. Part F*, vol. 133, no. 7, pp. 604 – 612, 1986.

[8] *IEEE Standard Radar Definitions*, IEEE Std. 686, 2008.

[9] V. Kostylev, "Geometry of bistatic radars," in *Bistatic Radar: Principles and Practice*, M. Cherniakov, Ed. John Wiley & Sons, 2007, ch. 11, pp. 244 – 251.

[10] N. Willis, *Bistatic Radar*. Scitech, 2005, pp. 70 – 72.

[11] V. Kostylev, "Scattering fundamentals," in *Bistatic Radar: Principles and Practice*, M. Cherniakov, Ed. John Wiley & Sons, 2007, ch. 10, pp. 193–223.

[12] J. Glaser, "Some results in the bistatic radar cross section (RCS) of complex objects," *Proc. IEEE*, vol. 77, no. 5, pp. 639 – 648, 1989.

[13] R. Kell, "On the derivation of bistatic RCS from monostatic measurements," *Proc. IEEE*, vol. 53, no. 8, pp. 983 – 988, 1965.

[14] R. Hiatt, K. Siegel, and H. Weil, "Forward scattering by coated objects illuminated by short wavelength radar," *Proc. IRE*, vol. 48, no. 9, pp. 1630 – 1635, Sep 1960.

[15] H. Griffiths, "Bistatic and multistatic radar," in *Proc. IEE Military Radar Seminar*, Shrivenham, UK., 2004.

[16] N. Willis, *Bistatic Radar*. Scitech, 2005, pp. 145 – 155.

[17] E. Knott, "Radar cross section," in *Radar Handbook*, 2nd ed., M. Skolnik, Ed. McGraw Hill, 2004, ch. 14, pp. 14.1–14.46.

[18] V. Kostylev, "Advanced scattering," in *Bistatic Radar: Principles and Practice*, M. Cherniakov, Ed. John Wiley & Sons, 2007, ch. 14, pp. 281–391.

[19] N. Willis, *Bistatic Radar*. Scitech, 2005, pp. 131 – 138.

[20] ——, *Bistatic Radar*. Scitech, 2005, pp. 119 – 129.

[21] ——, *Bistatic Radar*. Scitech, 2005, pp. 111 – 114.

[22] M. Weiner, "Clutter," in *Advances in Bistatic Radar*, N. Willis and H. Griffiths, Eds. SciTech Publishing, 2007, ch. 9, pp. 230 – 319.

[23] M. Weiner and P. Kaplan, "Bistatic surface clutter resolution area at small grazing angles," MITRE CORP, Tech. Rep., Nov 1982.

[24] L. Moyer, C. Morgan, and D. Rugger, "An exact expression for resolution cell area in special case of bistatic radar systems," *IEEE Trans actions on Aerospace and Electronic Systems*, vol. 25, no. 4, pp. 548 – 587, July 1989.

[25] N. Willis, *Bistatic Radar*. Scitech, 2005, pp. 157 – 171.

[26] M. Long, *Radar reflectivity of land and sea*, 3rd ed. Artech House, 2001.

[27] L. B. Wetzel, "Sea clutter," in *Radar Handbook*, 3rd ed., M. Skolnik, Ed. McGraw Hill, 2008, ch. 13, pp. 15.1 – 13.43.

[28] K. Ward, R. Tough, and S. Watts, *Sea Clutter: Scattering the K-Distribution and Radar Performance*. The IET, 2006.

[29] F. Nathanson and J. Reilly, "Clutter," in *Radar Design Principles: Signal Processing and the Environment*, 2nd ed., F. Nathanson, Ed. SciTech Publishing Inc, 1999, ch. 7, pp. 269 – 349.

[30] *IEEE Standard Letter Designations for Radar-Frequency Bands*, IEEE Std. 521-2002, 2003.

[31] M. Long, "On the polarization and the wavelength dependence of sea echo," *IEEE Trans. Antennas Propag.*, vol. 13, no. 5, pp. 749 – 754, 1965.

[32] ——, "On a two-scatterer theory of sea echo," *IEEE Trans. Antennas Propag.*, vol. 22, no. 5, pp. 667 – 672, 1974.

[33] J. Wright, "A new model for sea clutter," *IEEE Trans. Antennas Propag.*, vol. 16, no. 2, pp. 217 – 223, 1968.

[34] G. Brown, "Backscattering from a Gaussian-distributed perfectly conducting rough surface," *IEEE Trans. Antennas Propag.*, vol. AP-29, no. 3, pp. 472 – 482, 1978.

[35] P. Lee, J. Barter, K. Beach, B. Lake, H. Rungaldier, H. Thompson Jr., L. Wang, and R. Yee, "What the mechanisms for non-Bragg scattering from water wave surfaces?" *Radio Sci.*, vol. 34, no. 1, pp. 123 – 138, 1999.

[36] L. B. Wetzel, "A model for sea backscatter intermittency at extreme grazing angles," *Radio Sci.*, vol. 12, no. 5, pp. 749 – 756, 1977.

[37] K. Ward, "Compound representation of high resolution sea clutter," *Electronics Letters*, vol. 17, no. 16, pp. 561 – 563, 1981.

[38] S. Watts, "Radar sea clutter modelling and simulation - recent progress and future challenges," in *Proc. IET Seminar on Radar Clutter Modelling*, London, UK, February 2008, pp. 1 – 7.

[39] E. W. Beasley and H. R. Ward, "A quantitative analysis of sea clutter decorrelation with frequency agility," *IEEE Trans. Aerosp. Electron. Syst.*, vol. AES-4, no. 3, pp. 468–473, 1968.

[40] P. Lee, J. Barter, K. Beach, C. Hindman, B. Lake, H. Rungaldier, J. Shelton, A. Williams, R. Yee, and H. Yuen, "X band microwave backscattering from ocean waves," *J. Geophys. Res.*, vol. 100, no. C2, pp. 2591 – 2611, 1995.

[41] D. McLaughlin, N. Allan, E. Twarog, and D. Trizna, "High resolution polarimetric radar scattering measurements of low grazing angle sea clutter," *IEEE J. Ocean. Eng.*, vol. 20, no. 3, pp. 166 – 178, July 1995.

[42] K. Ward, R. Tough, and S. Watts, *Sea Clutter: Scattering the K-Distribution and Radar Performance*. The IET, 2006, p. 16.

[43] ——, *Sea Clutter: Scattering the K-Distribution and Radar Performance*. The IET, 2006, pp. 47 – 54.

[44] ——, *Sea Clutter: Scattering the K-Distribution and Radar Performance*. The IET, 2006, pp. 54 – 88.

[45] G. R. Valenzuela, "Theories for the interactions of electromagnetic and oceanic waves - a review," *Boundary-Layer Meteorology*, vol. 13, no. 1, pp. 61 – 85, 1978.

[46] A. Voronovich and V. U. Zavorotny, "Theoretical model for scattering of radar signals in K_u- and C-bands from a rough sea surface with breaking waves," *Waves Random Media*, vol. 11, pp. 247 – 269, 2001.

[47] K. Ward, R. Tough, and S. Watts, *Sea Clutter: Scattering the K-Distribution and Radar Performance*. The IET, 2006, pp. 88 – 92.

[48] S. Watts, K. Ward, and R. Tough, "The physics and modelling of discrete spikes in radar sea clutter," in *Proc. IEEE international radar conference*, Arlington, VA, May 2005, pp. 72 – 77.

[49] K. Ward and R. Tough, "Modelling radar sea clutter in the littoral," in *IET Seminar on Radar Clutter Modelling*. London, UK: IET, February 2008, pp. 27 – 31.

[50] ——, "Modelling radar sea clutter in littoral environments," in *Proc. Int. Conf. on Radar*, Adelaide, Australia, September 2008, pp. 82 – 87.

[51] M. Long, *Radar reflectivity of land and sea*, 3rd ed. Artech House, 2001, pp. 360 – 366.

[52] M. Katzin, "On the mechanisms of radar sea clutter," *Proc.the IRE*, vol. 45, no. 1, pp. 44 – 54, Jan. 1957.

[53] A. Chaudhry and R. Moore, "Tower-based backscatter measurements of the sea," *IEEE J. Ocean. Eng.*, vol. OE-9, no. 5, pp. 309 – 316, Dec 1987.

[54] M. Donelan and W. J. Pierson, Jr., "Radar scattering and equilibrium ranges in wind-generated waves with application to scatterometry," *J. Geophys. Res.*, vol. 92, no. C5, pp. 4971 – 5029, May 1987.

[55] J. Reilly and G. Dockery, "Influence of evaporation ducts on radar sea return," *IEE Proc. Part F*, vol. 137, no. 2, pp. 80 – 88, Apr 1990.

[56] W. Alpers and H. Hühnerfuss, "Radar signatures of oil films floating on the sea surface and the Marangoni effect," *J. Geophys. Res.*, vol. 93, no. C4, pp. 3642 – 3648, 1988.

[57] R. Moore, Y. Yu, A. Fung, D. Kaneko, G. Dome, and R. Werp, "Preliminary study of rain effects on radar scattering from water surfaces," *IEEE J. Ocean. Eng.*, vol. OE-4, no. 1, pp. 31 – 32, 1979.

[58] E. Conte and M. Longo, "Characterisation of radar clutter as a spherically invariant random process," *IEE Proc. Part F*, vol. 134, no. 2, pp. 191 – 197, 1987.

[59] M. Horst, F. Dyer, and M. Tuley, "Radar sea clutter model," in *IEE Proc. Int. Conf. on Antennas and Propagation. Part 2*, London, UK, November 1978, pp. 6 – 10.

[60] K. Ward, R. Tough, and S. Watts, *Sea Clutter: Scattering the K-Distribution and Radar Performance*. The IET, 2006, pp. 233 – 238.

[61] T. Leonard, I. Antipov, and K. Ward, "A comparison of radar sea clutter models," in *Proc. RADAR 2002*, Oct 2002, pp. 429 – 433.

[62] E. Twarog, D. McLaughlin, and N. Allan, "High resolution polarimetric radar scattering measurements of low grazing angle sea clutter," in *Proc. Int. Geoscience and Remote Sensing Symp. IGARSS '96. 'Remote Sensing for a Sustainable Future.'*, vol. 3, May 1996, pp. 1745 – 1748.

[63] M. Long, *Radar reflectivity of land and sea*, 3rd ed. Artech House, 2001, pp. 228 – 229.

[64] G. V. Trunk and S. F. George, "Detection of targets in non-Gaussian sea clutter," *IEEE Trans. Aerosp. Electron. Syst.*, vol. AES-6, no. 5, pp. 620 – 628, 1970.

[65] G. Trunk, "Radar properties of non-Rayleigh sea clutter," *IEEE Trans. Aerosp. Electron. Syst.*, vol. AES-8, no. 2, pp. 196 – 204, 1972.

[66] G. R. Valenzuela and M. B. Laing, "On the statistics of sea clutter," Naval research lab, Tech. Rep. NRL Rept. 7349, Dec 1971.

[67] M. Sekine and Y. Mao, *Weibull Radar Clutter*. IET, 1990.

[68] D. C. Schleher, "Radar detection in Weibull clutter," *IEEE Trans. Aerosp. Electron. Syst.*, vol. AES-12, no. 6, pp. 736 – 743, 1976.

[69] E. Jakeman and P. Pusey, "A model for non-Rayleigh sea echo," *IEEE Trans. Antennas Propag.*, vol. 24, no. 6, pp. 806 – 814, 1976.

[70] A. Balleri, A. Nehorai, and J. Wang, "Maximum likelihood estimation for compound-Gaussian clutter with inverse gamma texture," *IEEE Trans. Aerosp. Electron. Syst.*, vol. 43, no. 2, pp. 775 – 779, 2007.

[71] I. Blake and J. Thomas, "On a class of processes arising in linear estimation theory," *IEEE Trans. Inf. Theory*, vol. 14, no. 1, pp. 12 – 16, 1968.

[72] K. Yao, "A representation theorem and its applications to spherically-invariant random processes," *IEEE Trans. Inf. Theory*, vol. 19, no. 5, pp. 600 – 608, 1973.

[73] V. Anastassopoulos and G. A. Lampropoulos, "High resolution radar clutter classification," in *Proc. Record of the IEEE 1995 Int. Radar Conf.*, 1995, pp. 662 – 667.

[74] Anastassopoulos, G. A. Lampropoulos, A. Drosopoulos, and N. Rey, "High resolution radar clutter statistics," *IEEE Trans. Aerosp. Electron. Syst.*, vol. 35, no. 1, pp. 43 – 60, 1999.

[75] T. Azzarelli, "General class of non-Gaussian coherent clutter models," *IEE Proceedings Radar, Sonar and Navigation*, vol. 142, no. 2, pp. 61 – 70, 1995.

[76] M. Farshchian and F. L. Posner, "The Pareto distribution for low grazing angle and high resolution X-band sea clutter," in *Proc. IEEE Radar Conference*, May 2010, pp. 789–793.

[77] G. Weinberg, "Assessing Pareto fit to high-resolution high-grazing-angle sea clutter," *Electronics Letters*, vol. 47, no. 8, pp. 516–517, Apr 2011.

[78] J. Hosking and J. Wallis, "Parameter and quantile estimation for the generalized pareto distribution," *Technometrics*, vol. 29, no. 3, pp. 339–349, 1987.

[79] K. Ward and S. Watts, "Use of sea clutter models in radar design and development," *IET Radar, Sonar & Navigation*, vol. 4, no. 2, pp. 146 – 157, April 2010.

[80] W. Stehwien, "Statistics and correlation properties of high resolution x-band sea clutter," in *Proc. Record of the 1994 IEEE National Radar Conf.*, Atlanta, GA, mar 1994, pp. 46 – 51.

[81] T. J. Nohara and S. Haykin, "Canadian east coast radar trials and the k-distribution," *IEE Proceedings F Radar and Signal Processing*, vol. 138, no. 2, pp. 80 – 88, 1991.

[82] A. Farina, F. Gini, M. V. Greco, and L. Verrazzani, "High resolution sea clutter data: statistical analysis of recorded live data," *IEE Proceedings Radar, Sonar and Navigation*, vol. 144, no. 3, pp. 121 – 130, 1997.

[83] M. Sekine, T. Musha, Y. Tomita, T. Hagisawa, T. Irabu, and E. Kiuchi, "Log-Weibull distributed sea clutter," *IEE Proc. Part F*, vol. 127, no. 3, pp. 225 – 228, 1980.

[84] C. Baker, K. Ward, and S. Watts, "Scope of the compound K-distribution model for sea clutter," in *Proc. IEE Radar 87*, London, UK, oct 1987, pp. 207–211, conf. Pub. 281.

[85] K. Ward, C. Baker, and S. Watts, "Maritime surveillance radar. i. radar scattering from the ocean surface," *IEE Proc. Part F*, vol. 137, no. 2, pp. 51 – 62, 1990.

[86] S. Watts, "Radar detection prediction in K-distributed sea clutter and thermal noise," *IEEE Trans. Aerosp. Electron. Syst.*, vol. AES-23, no. 1, pp. 40 – 45, 1987.

[87] T. Lamont-Smith, "Translation to the normal distribution for radar clutter," *IEE Proceedings Radar, Sonar and Navigation*, vol. 147, no. 1, pp. 17 – 22, 2000.

[88] K. Ward, R. Tough, and S. Watts, *Sea Clutter: Scattering the K-Distribution and Radar Performance*. The IET, 2006, ch. 4, pp. 101 – 143.

[89] S. Watts and K. D. Ward, "Spatial correlation in K-distributed sea clutter," *IEE Proc. Part F*, vol. 134, no. 6, pp. 526 – 532, 1987.

[90] K. Ward, R. Tough, and S. Watts, *Sea Clutter: Scattering the K-Distribution and Radar Performance*. The IET, 2006, pp. 36 – 39.

[91] B. L. Hicks, N. Knable, J. Kovaly, G. Newell, J. Ruina, and C. Sherwin, "The spectrum of X-band radiation backscattered from the sea surface," *J. Geophys. Res.*, vol. 65, no. 3, pp. 825 – 837, 1960.

[92] V. Pidgeon, "Doppler dependence of radar sea return," *J. Geophys. Res.*, vol. 73, no. 4, pp. 1333 – 1341, 1968.

[93] D. Trizna, "A model for Doppler peak spectral shift for low grazing angle sea scatter," *IEEE J. Ocean. Eng.*, vol. 10, no. 4, pp. 368 – 375, 1985.

[94] P. Lee, J. Barter, K. Beach, E. Caponi, C. Hindman, B. Lake, H. Rungaldier, and J. Shelton, "Power spectral lineshapes of microwave radiation backscattered from sea surfaces at small grazing angles," *IEE Proc. Radar, Sonar and Navigation*, vol. 142, no. 5, pp. 252 – 258, 1995.

[95] P. Lee, J. Barter, B. Lake, and H. Thompson, "Lineshape analysis of breaking-wave Doppler spectra," *IEE Proc. Radar, Sonar and Navigation*, vol. 145, no. 2, pp. 135 – 139, 1998.

[96] D. Walker, "Modelling and characterisation of radar sea clutter," Ph.D. dissertation, University College London, 2001.

[97] ——, "Experimentally motivated model for low grazing angle radar Doppler spectra of the sea surface," *IEE Proc. Radar, Sonar and Navigation*, vol. 147, no. 3, pp. 114 – 120, 2000.

[98] ——, "Doppler modelling of radar sea clutter," *IEE Proc. Radar, Sonar and Navigation*, vol. 148, no. 2, pp. 73 – 80, 2001.

[99] K. Ward, R. Tough, and S. Watts, *Sea Clutter: Scattering the K-Distribution and Radar Performance*. The IET, 2006, pp. 129 – 142.

[100] A. Khenchaf, "The bistatic scattering from the natural rough surfaces in X and Ku bands," in *Proc. IEEE Int. Geoscience and Remote Sensing Symp. IGARSS '01*, vol. 6, Sydney, Australia, July 2001, pp. 2843 – 2845.

[101] K. Ward and R. Tough, "Theoretical and numerical modelling of bi-static sea clutter," TW Research Ltd., Tech. Rep. TWR/WP097/01, February 2009.

[102] A. Awada, A. Khenchaf, A. Coatanhay, and M. Ayari, "Comparison between small slope approximation and two scale model in bistatic configuration," in *Proc. IEEE Int. Geoscience and Remote Sensing Symp. IGARSS*, vol. 2, Seoul, Korea, 2005, pp. 1341 – 1344.

[103] F. Comblet and A. Khenchaf, "A critical overview of bistatic scattering wave from oceans surface," in *Proc. Oceans 2007*, Vancouver, BC, 2007, pp. 1 – 6.

[104] A. Arnold-Bos, A. Khenchaf, and A. Martin, "Bistatic radar imaging of the marine environment - part i: Theoretical background," *IEEE Trans. Geosci. Remote Sens.*, vol. 45, no. 11, pp. 3372 – 3383, 2007.

[105] ——, "Bistatic radar imaging of the marine environment - part ii: Simulation and results analysis," *IEEE Trans. Geosci. Remote Sens.*, vol. 45, no. 11, pp. 3384 – 3396, 2007.

[106] H. Griffiths, W. Al-Ashwal, K. Ward, R. Tough, C. Baker, and K. Woodbridge, "Measurement and modelling of bistatic radar sea clutter," *IET Radar, Sonar & Navigation*, vol. 4, no. 2, pp. 280 –292, Apr. 2010.

[107] W. G. Stevens and R. Muralidhar, "Statistical properties of bistatic clutter echoes." Rome Lab Hanscom, Tech. Rep., Mar 1994.

[108] V. Pidgeon, "Bistatic cross section of the sea," *IEEE Trans. Antennas Propag.*, vol. 14, no. 3, pp. 405 – 406, 1966.

[109] A. Domville, "The bistatic reflection from land and sea of X-band radio waves, part 1," GEC (Electronics) Ltd, Tech. Rep. Memorandum SLM1802, 1967.

[110] ——, "The bistatic reflection from land and sea of X-band radio waves, part 2," GEC (Electronics) Ltd, Tech. Rep. Memorandum SLM2116, 1968.

[111] T. Kochanski, M. Vanderhill, J. Zolotarevsky, and T. Fariss, "Low illumination angle bistatic sea clutter measurements at X-band," in *Proc. Mastering the Oceans Through Technology OCEANS*, vol. 1, Newport, RI, August 1992, pp. 518 – 523.

[112] G. Ewell and S. Zehner, "Bistatic sea clutter return near grazing incidence," in *Proc. IEE Conf. Radar '82*, London, UK, October 1982, pp. 188 – 192.

[113] G. Ewell, "Bistatic radar cross-section measurements," in *Radar Reflectivity Measurement: Techniques and Applications*, N. Currie, Ed. Artech House, 1989, ch. 5, pp. 139 – 176.

[114] J. Clancy and J. Len, "Bistatic clutter measurement program. phase 3," Decision Science Applications Inc, Tech. Rep., Sep 1995.

[115] V. U. Zavorotny and A. G. Voronovich, "Scattering of GPS signals from the ocean with wind remote sensing application," *IEEE Trans. Geosci. Remote Sens.*, vol. 38, no. 2, pp. 951 – 964, 2000.

[116] Z. U. Zavorotny, A. G. Voronovich, S. J. Katzberg, J. L. Garrison, and A. Komjathy, "Extraction of sea state and wind speed from reflected GPS signals: modeling and aircraft measurements," in *Proc. IEEE 2000 Int. Geoscience and Remote Sensing Symp IGARSS 2000*, vol. 4, 2000, pp. 1507 – 1509.

[117] A. K. Fung, C. Zuffada, and C. Y. Hsieh, "Incoherent bistatic scattering from the sea surface at l-band," *IEEE Trans. Geosci. Remote Sens.*, vol. 39, no. 5, pp. 1006 – 1012, 2001.

[118] M. Martín-Neira, M. Caparrini, J. Font-Rossello, S. Lannelongue, and C. S. Vallmitjana, "The paris concept: an experimental demonstration of sea surface altimetry using GPS reflected signals," *IEEE Trans. Geosci. Remote Sens.*, vol. 39, no. 1, pp. 142 – 150, 2001.

[119] T. Elfouhaily, D. R. Thompson, and L. Linstrom, "Delay-Doppler analysis of bistatically reflected signals from the ocean surface: theory and application," *IEEE Trans. Geosci. Remote Sens.*, vol. 40, no. 3, pp. 560 – 573, 2002.

[120] D. Barton, "Land clutter models for radar design and analysis," *Proc. IEEE*, vol. 73, no. 2, pp. 198 – 204, 1985.

[121] S. R. Doughty, "Development and performance evaluation of a multistatic radar system," Ph.D. dissertation, University College London, 2007.

[122] T. Derham, S. Doughty, K. Woodbridge, and C. Baker, "Design and evaluation of a low-cost multistatic netted radar system," *IET Radar, Sonar & Navigation*, vol. 1, no. 5, pp. 362 – 368, 2007.

[123] *IEEE Standard for Prefixes for Binary Multiples*, IEEE Std. 541-2002 (R2008), Sep 2009.

[124] T. Derham, K. Woodbridge, H. Griffiths, and C. Baker, "The design and development of an experimental netted radar system," in *Proc. Int. Radar Conf.*, Adelaide, Australia, 2003, pp. 293 – 298.

[125] M. Weiß, "Synchronisation of bistatic radar systems," in *Proc. IEEE International Geoscience and Remote Sensing Symposium, IGARSS '04.*, 2004.

[126] J. Sandenbergh and M. Inggs, "A common view GPSDO to synchronize netted radar," in *Proc. IET Int. Conf. on Radar Systems*, Edinburgh, UK, October 2007, pp. 1 – 5.

[127] M. Inggs, H. Griffiths, K. Woodbridge, W. Al-Ashwal, J. Sandenbergh, and G. Inggs, "Experimental coherent networked radar using GPS-disciplined reference oscillators," in *Proc. Cognitive systems with Interactive Sensors (COGIS2010)*, Crawley, UK, Nov. 2010.

[128] M. Cooley and D. Davis, "Reflector antennas," in *Radar Handbook*, 3rd ed., M. Skolnik, Ed. Mc-Graw Hill, 2008, ch. 12, pp. 12.1–12.43.

[129] C. Balanis, "Fundamental parameters and definitions for antennas," in *Modern Antenna Handbook*, C. Balanis, Ed. Wiley-Blackwell, 2008, ch. 2.

[130] L. Marple, Jr., "Computing the discrete-time 'analytic' signal via FFT," *IEEE Trans. Signal Process.*, vol. 47, no. 9, pp. 2600 – 2603, Sep 1999.

[131] J. Sandenbergh, M. Inggs, and W. Al-Ashwal, "Evaluation of coherent netted radar carrier stability while synchronised with GPS disciplined oscillators," in *Proc. IEEE Radar Conference RadarCon2011*, Kansas City, Missouri, May 2011.

[132] M. Tuley, "Antenna RCS and RCSR," in *Radar Cross Section*, 2nd ed., E. Knott, J. Shaeffer, and M. Tuely, Eds. SciTech Publishing, 2004, ch. 10, pp. 407–410.

[133] "UK interface requirement 2006 wireless access systems (WAS) including RLANs operating in the 5150–5725 MHz band," November 2006, Ofcom interface requiements, Acessed 15-Jul-2011. [Online]. Available: http://stakeholders.ofcom.org.uk/binaries/spectrum/spectrum-policy-area/spectrum-management/research-guidelines-tech-info/interface-requirements/uk2006.pdf

[134] W. Al-Ashwal, A. Balleri, H. Griffiths, R. Harmanny, M. Inggs, , M. Miceli, W. Ritchie, J. Sandenbergh, A. Stove, R. Tough, K. Ward, S. Watts, and K. Woodbridge, "Measurement of bistatic radar sea clutter," in *Proc. IEEE Radar Conference RadarCon2011*, Kansas City, Missouri, May 2011.

[135] M. Ritchie, W. Al-AShwal, A. Stove, K. , Woodbridge, and H. Griffiths, "Statistical analysis of monostatic and bistatic sea clutter doppler spectrum," in *Proc. CIE International Conference on Radar Radar2011*, Chengdu, China, Oct. 2011.

[136] W. Al-Ashwal, C. Baker, A. Balleri, H. Griffiths, R. Harmanny, M. Inggs, W. Miceli, M. Ritchie, J. Sandenbergh, A. Stove, R. Tough, K. Ward, S. Watts, and K. Woodbridge, "Statistical analysis of simultaneous monostatic and bistatic sea clutter at low grazing angles," *Electronics Letters*, vol. 47, no. 10, pp. 621 – 622, May 2011.

[137] F. Ulaby, T. Van Deventer, J. East, T. Haddock, and M. Coluzzi, "Millimeter-wave bistatic scattering from ground and vegetation targets," *IEEE Trans. Geosci. Remote Sens.*, vol. 26, no. 3, pp. 229 – 243, 1988.

[138] M. Long, *Radar reflectivity of land and sea*, 3rd ed. Artech House, 2001, pp. 399 – 409.

[139] M. Greco, F. Gini, and M. Rangaswamy, "Statistical analysis of measured polarimetric clutter data at different range resolutions," *IEE Proc. Radar, Sonar and Navigation*, vol. 153, no. 6, pp. 473 – 481, 2006.

[140] K. Bury, *Statistical Distributions in Engineering*. Cambridge University Press, 1999, ch. 3, p. 42.

[141] ——, *Statistical Distributions in Engineering*. Cambridge University Press, 1999, ch. 9, pp. 154–177.

[142] ——, *Statistical Distributions in Engineering*. Cambridge University Press, 1999, ch. 17, pp. 311–358.

[143] R. Bronson, *Schaum's Outline of Theory and Problems of Operations Research*. McGraw-Hill, 1982, ch. 10.

[144] L. M. H. Ulander, B. Flood, P.-O. Froelind, T. Jonsson, A. Gustavsson, J. Rasmusson, G. Stenstroem, A. Barmettler, and E. Meier, "Bistatic experiment with ultra-wideband vhf-band synthetic-aperture radar," in *7th European Conference on Synthetic Aperture Radar (EUSAR)*, 2008, pp. 1–4.

[145] M. Inggs, G. Inggs, A. Langman, and S. Scott, "Growing horns: Applying the Rhino software defined radio system to radar," in *Proc. IEEE Radar Conference*, 2011, pp. 951–955.

[146] P. Moreira, J. Serrano, T. Wlostowski, P. Loschmidt, and G. Gaderer, "White rabbit: Sub-nanosecond timing distribution over ethernet," in *Proc. Int. Symp. Precision Clock Synchronization for Measurement, Control and Communication ISPCS*, 2009, pp. 1–5.

[147] M. Ritchie, W. Al-AShwal, A. Stove, K. Woodbridge, and H. Griffiths, "Satistical analysis of monostatic and bistatic sea clutter doppler spectrum," in *CIE International Conference on Radar*, Chengdu, China, Oct 2011, accepted.

[148] G. Ewell and S. Zehner, "Bistatic radar cross section of ship targets," *IEEE J. Ocean. Eng.*, vol. 5, no. 4, pp. 211–215, 1980.

[149] R. H. Stewart, *Introduction To Physical Oceanography*. Department of Oceanography, Texas A&M University, Aug. 2008, pp. 273 – 292, accessed 22-Mar-2011. [Online]. Available: http://oceanworld.tamu.edu/ocean410/ocng410_text_book.html

[150] A. Fung and K. Lee, "A semi-empirical sea-spectrum model for scattering coefficient estimation," *IEEE J. Ocean. Eng.*, vol. 7, no. 4, pp. 166 – 176, Oct 1982.

[151] T. Elfouhaily, B. Chapron, and K. Katarsos, "A unified directional spectrum for long and short wind-driven waves," *J. Geophys. Res.*, vol. 102, no. C7, pp. 15 781 – 15 796, Jul 1997.